Electron Impact Excitation Studies of Laser-Excited and Ground-State Barium and Ytterbium

By

ShariqUddin Kidwai

A Thesis submitted to the Faculty of Graduate Studies of

The University of Manitoba

in partial fulfilment of the requirements of the degree of

DOCTOR OF PHILOSOPHY

Department of Physics and Astronomy
University of Manitoba
Winnipeg, Manitoba
R3T 2N2

ABSTRACT

The research presented in this dissertation was performed in the Atomic, Molecular and Optical (AMO) physics laboratory at the University of Manitoba. Atomic beams of the two-valence-electron heavy atom systems, barium and ytterbium, were investigated with low energy electron scattering and optical emission studies. Both the ground states and laser excited states were investigated as a function of incident electron beam energy from 10 eV to 50 eV. Measurements of relative cross sections and polarization for 583 nm and 554 nm line emission from the $(6s7p)^1P_1$ and $(6s6p)^1P_1$ states of barium excited by electron impact from both the ground states and the optically pumped metastable $(6s5d)^1D_2$ are reported. Data are normalized to absolute cross sections for the ground state $(6s^2)^1S_0 \rightarrow (6s6p)^1P_1$ state transition due to electron scattering, with corrections for branching ratios and cascading from higher states to deduce the total level excitation cross sections. Results are also presented for the first studies of the 399 nm line emission from laser-excited ytterbium, yielding an upper limit on the apparent cross section for the $(6s6p)^3P_1 \rightarrow (6s6p)^1P_1$ transition. Results are compared with the latest theoretical models and previous data, where available.

ACKNOWLEDGEMENT

I would like to express my sincere appreciation to my new thesis committee members, Dr. Gerald Gwinner (advisor), Dr. Shelley Page (Physics and Astronomy), Dr. George Tabisz (Physics and Astronomy) and Dr. Cyrus Shafai (Electrical and Computer Engineering). Thanks to them for their support, advice and constructive criticism during analysis of my data and the writing of my thesis, leading to the successful earning of the Ph.D. degree from the University of Manitoba.

I would also like to thank my original advisor, Dr. P. Zetner, under whose supervision the research was carried out in the Atomic, Molecular and Optics (AMO) field, along with my previous advisory committee members, Dr. K. Sharma (Physics and Astronomy), Dr. C-M. Hu (Physics and Astronomy) and Dr. S. Kroeker (Chemistry).

My gratitude is extended to Dr. Jeff Hein who introduced me to the AMO lab while doing his research work for his PhD degree and for many fruitful discussions with him. I would also like to thank former AMO lab students who worked on the development of the apparatus in the AMO lab.

Thanks to Mr. Grant Mollard (retired) and Mr. Andrew Pankewycz in the mechanical workshop for fabrication of various experimental parts and also to Mr. Richard Hammel (retired) in the electronics workshop. A very special thank you is owed to Mr. Gilles Roy (retired) for his ever readiness in providing solutions for problems faced in running the experiments.

My gratefulness goes to my mother for her prayers and encouragement and also to my brothers and sister.

My heartfelt thanks to my very supportive wife, Ghazala, for her patience during my studies while looking after our five children, Hamza, Maria, Hisham, Mariam and Hashim. Our children's playful activities were always a source of refreshment and joy; the comments of my wife on running experiments overnight were always delightful.

Finally I want to acknowledge NSERC, the Department of Physics and Astronomy and the FGS for their financial support.

DEDICATION

To my late father, Kalim Kidwai, who received his Masters degree in Civil Engineering back in 1964 at the University of Minnesota, USA and who vigorously promoted higher education in the family.

Contents

List of Figures

List of Tables

Chapter 1

Introduction

1.1 The Electron-Atom Interaction

In a general sense, atomic and molecular optical (AMO) experimental physics has the task to discover and apply the fundamental laws of nature, to acquire further knowledge and to explain the structure of matter on the atomic and molecular level. A prime motivation for experimental research in atomic collisions is to provide benchmark data for assessment of various theoretical models. The improvements in theoretical models by taking into consideration more parameters and the advancement of experimental technology together form the basis of putting forward a complete model of atomic collision which can then be applied to practical use.

In the electron-atom interaction, one of the challenges the theory faces is the many-body problem in the sense that the projectile electron interacts with many electrons of the target atoms. Due to many particles contained in such a system, the number of degrees of freedom increases rapidly, and it becomes difficult to describe the system by using a small number of equations. The general approach to solve many-body problems is to incorporate approximations by ignoring some interactions within the system. This allows the many-body problem to be reduced to a simpler problem, often a set of smaller, independent and easier to solve equations. These approximations are then compared with the experimental results. If the theoretical and experimental results agree, then this

theoretical model is accepted. Thus the role of the experimentalist in the field is to provide sets of measurements as a guide for theoretical development. It is therefore desirable for experimentalists to render information regarding the collision process at the most fundamental level possible.

Theoretical model approximations depend among other parameters also on the regime of incident electron energy. At low energies, from a fraction of eV to a few eV, only a few scattering channels are open which are well approximated by few-state Close Coupling (CC) models [Fursa2002]. This gives rise to a small set of coupled integro-differential equations and can be handled easily by numerical techniques aided by computer programs. The high energy regime of above a few hundred eV to keV opens the possibilities of an infinite number of scattering channels, but these channels are weakly coupled. The Born Approximation (BA) [Fursa2002] based on perturbation theory along with exact treatment of the channel of interest, provides good agreement with the experimental results. However at the intermediate energy range, which is studied in this thesis, electron scattering from the atomic target is much more complicated. In this energy regime, there are too many scattering channels available which cannot be treated by perturbation theory due to strong coupling between these channels. To tackle this problem, new theoretical models are put forward, like Convergent Closed Coupling (CCC) [Fursa1999] with increased number of states and more recently the RCCC model [Bostock2014a b] which introduces relativistic effects in the CCC model. These latest models involving the relativistic contributions are in their infancy and for the reasons stated above, it is a challenge to obtain good agreement with the experimental work in this intermediate electron impact energy regime.

Many fundamental electron-atom collision processes comprising relatively simple atomic targets like hydrogen, helium and alkali atoms having one valence electron are successfully described by various theoretical models. However, there are many more important collision problems to be tackled, with guidance coming from experiments. For example, electron scattering from the heavier alkaline-earth atomic targets which are two-valence electron systems, pose a challenge in defining the target wave function due to a possible two-electron excitation. Also a breakdown of the non-relativistic LS coupling approximation has been observed in heavier atomic targets. In this thesis work, barium and ytterbium are taken as atomic targets in the study of the electron scattering experiments.

In the electron impact ionization experiments, with excitation and double ionization of helium and alkaline-earths, a general accurate treatment of these processes must include an accurate treatment of two-electron excitations. Similarly, spin-resolved experiments provide for very thorough testing of relativistic effects in the scattering theory.

On the applied side, the electron-atom interaction/collision/scattering plays a fundamental role in establishing the characteristics of plasma systems which are in fact partially ionized gases. These plasma systems are present in stellar and planetary atmospheres. They have been studied in astrophysical plasma by Allen [Allen1984] and in auroral plasmas by Massey et al. [Massey1982b]. Interpretation of astrophysical plasmas relies critically on the knowledge of such interactions, and is particularly important at present due to advances in ground-based and space-based telescopes. Artificial plasmas, such as those occurring in fusion research or in the lighting industry,

semiconductor etching plasmas, and laser development in gas discharge modeling also require knowledge of electron interactions with light and heavy atomic and ionic targets. High density gas discharges have been studied by Krivchenkova and Khakaev [Krivchenkova1975], Delcroix et al. [Delcroix1976] and Massey et al. [Massey1982a]. Discharge-pumped lasers have been studied by Massey et al. [Massey1982c]. Quantitative understanding of plasmas requires a vast database of electron interaction data. Only theory can provide all the necessary information with experimental investigations providing the validity of the theoretical models. This is because experiments cannot be performed on each and every atomic species as not all atoms are feasible for laboratory experiments. For example, two-valence atoms like helium, mercury, ytterbium, barium, etc. have been studied and theoretical models are put forward. These theoretical models can be applied to other two-valence electron atoms.

Metastables due to their long lifetimes, extremely large cross sections, and large internal energy are especially important in the understanding and modeling of plasmas (Bogaerts and Gijbels1995). Metastables play a dominant role in plasmas for mainly three reasons. Firstly metastables have longer lifetimes than other excited states, up to milliseconds, as compared to typically nanoseconds. Secondly, being already in an excited state, metastables are easily excited and/or ionized as they require less energy (few eV) to get to the upper levels as compared to the ground state atom. Thirdly, and most importantly, are the large values of the excitation cross sections from metastable levels. These can be up to three orders of magnitude larger compared to the peak excitation cross sections from the ground state [Bogaerts and Gijbels1995, Boffard1999].

Integral cross sections for electron scattering from barium are used in a variety of applications. Mildren and co-workers are extensively investigating the development of barium-vapour lasers where these cross sections are needed for modeling [Mildren1995,1997a,1997b,1997c]. Other practical uses of barium include its role in plasma switches [Yang and Rodrigez1992] and in the manufacture of discharge lamps [Bhattacharya1997]. Barium scattering data are needed to study planetary ionospheres [Wescott1980, Wescott1993, Simons1981, Winske1988, Chapman1989, Shuk1991].

Practical application of ytterbium relates to the potential of the creation of ytterbium-vapour lasers [Cahuzac1968] and practical needs in quantum electronics [Klimkin1975]. The ytterbium scattering data are also required in the methods used for laser isotope separation [Letokhov1978].

1.2 Observables and Experimental Conditions

In this section, a brief introduction is given to experimental observables which are discussed in much greater detail in subsequent chapters. Consider a basic electron-atom collision in which an electron e^- with an initial kinetic energy E_0 interacts with a ground state atom A as,

$$\begin{array}{lll} e^-(E_0) + A \rightarrow & A^* + e^-(E_0 - \Delta E;\, \theta) & \text{(scattered electron)} \\ & \downarrow & \\ & A + \text{photon} & \text{(emitted photon)} \end{array} \qquad (1.1)$$

A part of the impact energy E_0 of the incoming electron is transferred to the atom, which excites the atom to a higher energy state. This energy transfer of ΔE is the excitation energy of the atomic level and is equal to the energy loss of the electron. The electron is then scattered by an angle θ, the scattering angle, and the excited atom generally de-excites spontaneously to the ground level or to a lower level by emitting a photon ($\Delta E = hc/\lambda$) by radiative decay. Detection of the scattered electron and/or the decay photon and measuring the energy/wavelength of these final state particles yields important information about the electron-atom collision process.

1.2.1 Differential Cross Section

One quantity of interest is the differential cross section $\left(\frac{d\sigma}{d\Omega}\right)$ for a particular scattering process. This determines the probability of scattering from a particular initial state to a particular final state of the system. It can be measured by detecting the kinetic energy, hence the momentum, and direction of the scattered electron for a known incident energy and direction of the projectile electron. The electron energy loss spectrum, i.e. a spectrum of the relative intensity of electrons scattered with energy loss ΔE, can be used to map out the energy level scheme of an atom. Electron energy loss spectroscopy (EELS) is an important experimental tool, used in this thesis and discussed further in Chapter 3. Differential cross sections for electron scattering are generally forward peaked and strongly angle dependent.

1.2.2 Integral Cross Section

The integral cross section (σ) for an electron scattering process is literally the integral over all scattering angles of the corresponding differential cross section $\left(\frac{d\sigma}{d\Omega}\right)$. The integral cross section is useful for studies in stellar plasmas, planetary ionospheres, discharge tubes, lasers, fusion reactors, etc., where the scattering angle information is irrelevant. The σ can be measured by detecting the decay photons from a particular electron-excited atomic state, since the photon emission is isotropic. Corrections for decays to other final states and for cascade feeding from higher levels need to be made to deduce the level excitation cross section from the measured photon rates. These details are discussed in Chapter 4.

1.2.3 Photon Polarization

The emitted photons from the decay of an excited atomic state are generally linearly polarized, either parallel or perpendicular to the electron momentum vector. The linear polarization can be measured and related to the magnetic sublevel populations of the excited state prior to the decay. Polarization is discussed in more detail in Chapter 2, and polarization measurements are presented in chapters 3, 4, 5 and 6.

1.2.4 Electron-Photon Coincidence Measurements

In contrast to the single particle detection methods (either scattered electron or decay photon), an electron-photon coincidence measurement yields different information. The photon emission direction defines an axis with respect to the scattering plane. Electron-

photon coincidence measurements depend on the incoming electron energy E_0, the scattering angle θ, the photon emission direction and the photon polarization. In an (e,eγ) coincidence experiment, a complete description of the measurement is achieved by a total of five independent parameters, the absolute differential cross section and the four Stokes parameters which consist of the transferred angular momentum, charge cloud alignment angle, charge cloud height and the charge cloud anisotropy.

1.2.5 Superelastic Scattering

Superelastic scattering from a laser-excited target state is in fact the time-inverse process of the inelastic electron-photon coincidence measurement in which the incoming electron gains energy from the atom and hence deexcites it. A peak in the EELS spectrum with ΔE negative indicates a superelastic collision. Superelastic electron scattering has been used extensively to probe the coherence parameters, which describe the shape and orientation of the excited atomic charge cloud of the p-state. Superelastic scattering was used as a tool to set up the optics of the laser pumping system for the laser-excited experiments in Chapters 5 and 6.

1.3 Context of the Present Studies

The electron-atom excitation process has been widely studied both theoretically and experimentally. A detailed study of the polarization of atomic line radiation due to electron excitation was carried out by Percival and Seaton [Percival1958]. This was

further improved by Fano and Macek [Fano1973], and almost simultaneously Macek and Hertel [1974] gave the first detailed theory of atomic excitation by electron impact on laser-excited atoms. Until the 1970s, experimental work was largely restricted to the determination of cross sections by observing the scattered electrons and measurements of the polarization of light emitted in the radiative decay of excited states. A detailed review on direct electron excitation of atoms has been written by Andersen et al. [Andersen1988] followed by a comprehensive study of electron impact optical excitation functions by Heddle and Gallagher [Heddle1989].

A theoretical topical review by Bray et al. [Bray2002] gives an in-depth discussion of the application of theoretical models to experimental data. The authors claim that the fundamental electron-atom collision processes are considered 'solved' and that guidance is needed from experiment for more challenging collision problems. In a perfect scattering experiment [Andersen1988] all the quantum numbers describing the initial and final states of the target and the projectile are measured, while in a scattering theory various scattering amplitudes are averaged. This provides guidance and a thorough test of the theoretically calculated scattering amplitudes. Thus for complicated processes, experiments are more important to guide the theoretical models as more averaging is done in arriving at the theoretical model.

The first electron-photon coincidence measurements were carried out in 1972 by King et al. [King1972]. In 1979 Blum and Kleinpoppen [Blum and Kleinpoppen] gave a review on initial developments in electron-photon angular correlations resulting from electron impact of atoms and molecules. The first detailed work on coherent low-energy electron scattering was done in 1984 by Slevin [Slevin1984]. After that, with the advent

of supercomputers, the framework for coincidence experiments was created and extensive work has been done since that time. In the following, a survey of related literature is reported for the three experiments carried out in this thesis.

1.3.1 Barium Ground-State Electron Excitation

Among the targets, alkaline-earth atoms have proven to be of considerable scientific interest as targets in electron scattering experiments. The helium atom is by far the most extensively studied target in atomic collision studies due to its simple structure [Bray and Fursa2011, Mikosza1996, VanZyl1980, VanRaan1970, McFarland1967]. The alkaline-earth atoms are essentially two-electron systems, which makes their study a natural extension to the work done with helium and yet still pose a challenge to theory. Barium, being an alkaline-earth atom, can be compared with helium.

Experimentally, Chen and Gallagher [Chen1976] measured the barium 554 nm line emission cross section for the $(6s^2)^1S_0 \rightarrow (6s6p)^1P_1$ transition (shown in Figure 4.5) with electron impact energies from 2.3 eV to 1,497 eV, with results in excellent agreement with the theoretical non-relativistic CCC model [Fursa1999]. Jensen, Register, Trajmar [Jensen1978] measured the relative cross section of the $(6s6p)^1P_1 \rightarrow (6s5d)^1D_2$ transition and then used Chen and Gallagher [Chen1976] data to normalize their results. A similar method is used in the present thesis in chapters 4, 5 and 6. Smirnov [Smirnov2002] measured optical excitation functions of various lines of the barium atom with an uncertainty of 20 – 32%. The excitation functions in barium to n^1P levels and to n^1D levels have been measured by Aleksakhin et al. [Aleksakhin1973].

Theoretically, various models have been put in place and calculations made for scattering channels considered important for practical applications over a wide range of electron impact energies. Theoretical models of Convergent Close Coupling (CCC) and Unitarized First Order Many Body Theory (UFOMBT) have been used to calculate the integral cross section for various barium scattering channels including the $(6s^2)^1S_0 \rightarrow (6s6p)^1P_1$ and $(6s^2)^1S_0 \rightarrow (6s7p)^1P_1$ transitions [Fursa1999] which are relevant to the present experiment. Also the $(6s^2)^1S_0 \rightarrow (6s6p)^1P_1$ cross section was calculated by using different theoretical models such as the non-relativistic two-state CCC model by Fabrikant [Fabrikant1980], Unitarized Distorted-Wave Approximation (UDWA) and UFOMBT by Clark et al. [Clark1989] and the Relativistic Distorted Wave Approximation (RDWA) by Srivastava et al. [Srivastava1992a, Srivastava1992b]. The measured and CCC model calculated differential cross section out of the barium excited states, including the metastable $(6s5d)^1D_2$ state, are in good agreement.

1.3.2 Barium Laser-Excited Metastable State Electron Excitation

Experimentally, electron scattering from laser-excited barium has been studied before at the University of Manitoba AMO lab. The differential cross section $\left(\frac{d\sigma}{d\Omega}\right)$ for 20 eV electron impact excitation to a number of higher states out of the laser-excited $(6s6p)\ ^1P_1$ state was studied by Zetner and Johnson [Zetner2006]. The differential cross section out of laser-excited barium metastable states have also been studied earlier here [Zetner1999,

Li1996]. There is no direct experimental data available for the integral cross section (σ) involving transitions between excited states of barium.

Theoretically, the integral cross section (ICS) has been calculated for the transitions between excited states of barium including the metastable states using CCC and UFOMBT models [Fursa2002] but not for the present work. Recently, relativistic effects were incorporated in the RCCC model and the ICS was calculated for the present study of the $(6s^2)^1S_0 \rightarrow (6s7p)^1P_1$ and $(6s5d)^1D_2 \rightarrow (6s7p)^1P_1$ transitions [Bostock2014a]. ICS calculations for $(6s5d)^1D_2 \rightarrow (6s7p)^1P_1$ transitions have been reported using the Born approximation for 15 eV and 30 eV [Aleksakhin1981].

1.3.3 Ytterbium Laser-Excited ^{3}P state Electron Excitation

Data on the study of electron scattering from laser-excited ytterbium is sparser compared to barium due to the difficulty in producing a reasonable population of laser-excited states. The ytterbium laser-excited $(6s6p)^3P_1$ state has been previously studied at the University of Manitoba. These studies included superelastic electron scattering by Li and Zetner [Li and Zetner1994], differential cross section $\left(\frac{d\sigma}{d\Omega}\right)$ measurements by Hein et al. [Hein2011a] and electron impact coherence parameters (EICP) by Hein et al. [Hein2011b].

The electron excitation of the ytterbium $(6s6p)^1P_1$ state out of the ground state has been investigated, including measured and calculated (using the UDW model) $\frac{d\sigma}{d\Omega}$ by Johnson et al. [Johnson1998]. The optical excitation functions for ytterbium have been extensively studied by Shimon et al. [Shimon1981]. The relative-$\frac{d\sigma}{d\Omega}$ has been measured

by Kazakov and Khristoforov [Kazakov1981]. Srivastava et al. [Srivastava1995] have calculated the $(6s6p)^1P_1$ cross section out of the ground state using the RDW model, and experimentally Predojevic [Predojevic2005] has measured it.

1.4 Dissertation Outline

The work presented in this dissertation is arranged as follows. Chapter 2 deals with the theoretical background, particularly the physics of electron-atom collisions. An overview and general description of the present atomic molecular and optical (AMO) physics laboratory at the University of Manitoba, where all the experiments were carried out, is introduced in Chapter 3 along with details of the experimental set up and the procedures used. The next three chapters, present the experimental techniques, analysis and results. Chapter 4 describes measurements in pursuit of the integral cross section for electron excitation of the barium $(6s7p)^1P_1$ level out of the ground $(6s^2)^1S_0$ level by measuring the 583 nm and 554 nm line transitions. The next two chapters are related to the studies of electron excitation from laser-excited states. Chapter 5 presents first time the integral cross section for electron excitation of the barium $(6s7p)^1P_1$ level out of the laser-excited metastable $(6s5d)^1D_2$ states by observing the 583 nm and 554 nm line transitions. Chapter 6 presents the first attempt to determine the ytterbium $(6s6p)^1P_1$ level cross section for electron excitation out of the laser-excited $(6s6p)^3P_1$ state by studying the 399 nm transition. Finally, a summary and conclusion of the thesis is presented in Chapter 7 where some suggestions for further work are also discussed.

Chapter 2

Theoretical Background

2.1 Introduction

When a neutral atom interacts with an incoming electron, three possibilities can occur. The incoming electron can lose energy, gain energy or pass by without loss or gain in energy. In the first scenario the atom can be excited to a higher level by taking energy from the incoming electron, subsequently decaying to a lower level by emitting a photon or a secondary electron. This type of interaction, in which the incoming electron loses energy, is referred to as an inelastic process. In the second scenario where the incoming electron gains energy, the collision is superelastic. In this superelastic collision, the atom being already in an excited state (e.g. a laser-excited atom) loses some of its excess energy. In the third scenario in which there is no loss of energy in the incoming electron, either an elastic collision occurs between the incoming electron and the atom, or it is possible that no interaction takes place.

This dissertation discusses experiments that were performed on electron collisions with ground state atoms as well as laser-excited atoms. This theoretical chapter is divided into two sections. Section one gives a general background on the electron-atom collision theory, while section two focuses on the collision theory with laser-excited atoms.

Section I: Theory of Electron-Atom Collisions

To study a collision process, an important observable to determine is the scattering cross section. The cross section is related to the probability that under certain conditions, a given type of interaction will happen. Both classical and quantum mechanical scattering phenomena are characterized by their scattering cross sections [McDaniel1989].

2.2 Classical Definition of the Differential Cross section

Consider a collision experiment in which an incident flux of particles J_I bombards a stationary target. The number of particles per unit time scattered into an element of solid angle dΩ in direction (θ,ϕ) are detected. A generic diagram for a scattering experiment is shown in Figure 2.1.

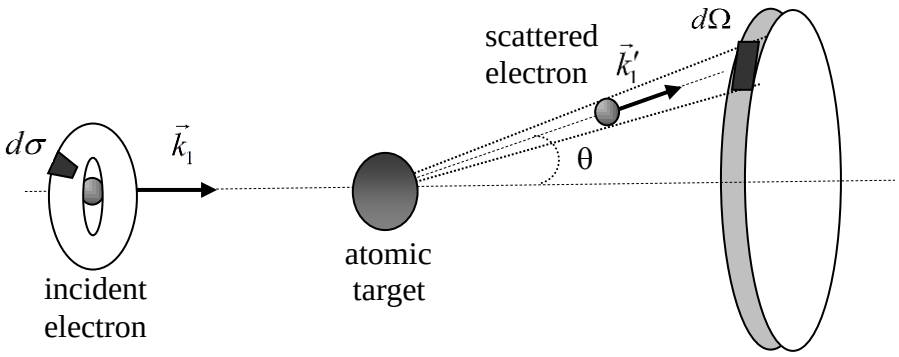

Figure 2.1: Geometry of a scattering experiment showing an incident electron with initial momentum $\vec{k}_1$ being scattered from an atomic target with final momentum $\vec{k}_1'$. If the electron strikes the target atom within a perpendicular area dσ centered on the atom, it will scatter into solid angle dΩ at angle θ to the incoming beam.

These collisions are characterized by the differential cross section $\frac{d\sigma}{d\Omega}$, defined as the ratio of the number of particles scattered into direction (θ,ϕ) per unit time per unit solid angle to the incident flux,

$$\frac{d\sigma}{d\Omega} = \frac{dn/dt}{J_I}, \tag{2.1}$$

where J_I is incident flux of particles defined as the number of particles per unit time crossing a unit area normal to direction of incidence.

From $\frac{d\sigma}{d\Omega}$, the total cross section or integral cross section (σ) can be obtained by integration over all solid angles,

$$\sigma = \int \frac{d\sigma}{d\Omega} d\Omega = \int_0^{2\pi} d\varphi \int_0^{\pi} d\theta \sin\theta \frac{d\sigma}{d\Omega} \tag{2.2}$$

The term total cross section is used in the literature in different ways. It might refer to the sum of all processes such as $\sigma_{elastic}$, $\sigma_{inelastic}$ etc., or to the total cross section (σ) for a particular process. The cross section, which typically depends sensitively on the energy of incoming particles, has dimensions of area. The above expressions indicate how an experimentalist can convert measured count rates and incident particle fluxes to the scattering cross section. The theoretician's task is to calculate such cross sections using the proper quantum mechanical description of the target atom's electronic structure and an appropriate collision model. In the following section, a quantum mechanical description of cross section in terms is discussed.

2.3 Quantum Treatment of the Differential Cross Section

Before discussing the quantum mechanical treatment of $\frac{d\sigma}{d\Omega}$, it is more useful to define the basic nomenclature of quantum mechanics used in scattering theory. In this section the notations used for different particles in the system are 1 and 2 as subscript, 1 being the electron and 2 being the atom. The initial and final conditions are denoted by no prime and prime as a superscript, respectively. The following discussion is based on non-relativistic quantum mechanics.

The energy states of an atom are defined by four quantum numbers, *n, l, m* and *s* which specify the complete and unique quantum state of an atomic electron described by its wavefunction. The principal quantum number, *n* defines the atomic orbital. The magnetic quantum number, *m* refers to the direction of the angular momentum vector *L* with quantum number *l* and does not affect the electron's energy in the absence of an applied magnetic field. There are (2*l*+1) magnetic quantum numbers *m* ranging from -*l* to *+l* in an atomic orbital. The spin quantum number, *s* describes the intrinsic spin of the electron with *s*=1/2. The electron spins *s* interact among themselves and form a total spin angular momentum *S*. The total angular momentum of an atom *J* is thus the vector sum of *L* and *S*. The interaction between *L* and *S* is called LS coupling. In LS coupling the atomic state is specified by *n, L, S and J* along with the magnetic quantum number *m* and the notation of the atomic state is defined by $n\ ^{(2S+1)}L_J$.

2.3.1 Scattering Amplitudes and the Differential Cross Section

A scattering experiment can be viewed as a composition of two parts, preparation of initial state particles and detection of final state particles. The particles here refer to

electrons and atoms. Initial particles are produced, scattering takes place and the final particles are detected. Now consider a projectile electron with a spin angular momentum s_1 and initial momentum $\vec{k}_1$ in a state $\left|s_1\ \vec{k}_1\right\rangle$ scattered from a target atom in a state $\left|\Psi_J\right\rangle$ with angular momentum *J*. After the scattering, the electron is in a state $\left|s_1'\ \vec{k}_1'\right\rangle$ and the atom in a new state $\left|\Psi_J'\right\rangle$. An atomic state Ψ is defined by a certain set of quantum numbers necessary to specify the state completely; after inelastic scattering the atom is left in a different quantum state.

The transition from the initial combined electron-atom system $\left|s_1\ \vec{k}_1\ ,\Psi_J\right\rangle$ to the final combined electron-atom system $\left|s_1'\ \vec{k}_1'\ ,\Psi_J'\right\rangle$ is characterized by the scattering amplitude *f* as,

$$f\left(s_1'\ \vec{k}_1'\ ,\Psi_J';s_1\ \vec{k}_1\ ,\Psi_J\right) = \left\langle s_1'\ \vec{k}_1'\ ,\Psi_J'\left|\hat{T}\right|s_1\ \vec{k}_1\ ,\Psi_J\right\rangle, \tag{2.3}$$

where $\hat{T}$ is the transition operator connecting the initial and final electron-atom system. The scattering amplitude is related to the DCS by,

$$\left|f\left(s_1'\ \vec{k}_1'\ ,\Psi_J';s_1\ \vec{k}_1\ ,\Psi_J\right)\right|^2 = \frac{d\sigma}{d\Omega}\left(s_1'\ \vec{k}_1'\ ,\Psi_J';s_1\ \vec{k}_1\ ,\Psi_J\right), \tag{2.4}$$

where $\frac{d\sigma}{d\Omega}\left(s_1'\ \vec{k}_1'\ ,\Psi_J';s_1\ \vec{k}_1\ ,\Psi_J\right)$ is the differential cross section which gives the probability of exciting an initial atomic state to a final atomic state by measuring the scattered electron detection count rate within a given solid angle. The theoretical description of measurements in which there are unobserved variables requires an average or sum over the calculated scattering amplitudes which connect initial and final states of well-defined quantum numbers. The following sections describe this summation and averaging process.

2.3.2 Observables of an Atomic Target

Consider a scattering experiment in which a beam of incident electrons with a momentum $\vec{k}$ impinges on an assumed stationary atomic target. A good assumption in the scattering experiments is that before and after the scattering, all the interacting particles are spatially separated and cease to interact.

Atomic targets considered in this dissertation are two-electron atoms, with valence electrons spin parallel or opposite to each other, i.e. S=0,1. The orbital angular momentum basis states are represented by $|m_l\rangle$ with values from $-l$ to $+l$. If the atom has $(2l+1)$ unresolved magnetic substates m_l states then the average over the unresolved initial state is given by,

$$\frac{d\sigma}{d\Omega}\left(\vec{k} \to \vec{k}', m_l\right) = \frac{1}{(2l+1)} \sum_{m_l} \frac{d\sigma}{d\Omega}\left(\vec{k}, m_l \to \vec{k}', m_l'\right). \tag{2.5}$$

Now consider the scattering experiment in which the initial atomic states are resolved but there are final unobserved atomic states. The $\frac{d\sigma}{d\Omega}$ for such a process with final unresolved states is given as,

$$\frac{d\sigma}{d\Omega}\left(\vec{k}, m_l \to \vec{k}'\right) = \sum_{m_l'} \frac{d\sigma}{d\Omega}\left(\vec{k}, m_l \to \vec{k}', m_l'\right). \tag{2.6}$$

Finally, combining equations (2.5) and (2.6), the differential cross section for a process in which there are unresolved quantum numbers in both the initial and final states is given by,

$$\frac{d\sigma}{d\Omega}\left(\vec{k} \to \vec{k}'\right) = \frac{1}{(2l+1)} \sum_{m_l} \sum_{m_l'} \frac{d\sigma}{d\Omega}\left(\vec{k}, m_l \to \vec{k}', m_l'\right). \tag{2.7}$$

In a collision experiment for which all the quantum numbers detailing a state are not determined, "coherence" is lost. Full coherence refers to determining all the quantum numbers for both the initial state as well as the final state of the system. The degree to which a system is coherent depends upon the number of quantum numbers known precisely.

2.3.3 Observables of the Electron Beam

In the present dissertation, the incident electron beam spins are not observed and hence the measurements yield only the spin-averaged quantities. Thus the scattering experiment does not distinguish between spin-up and spin-down of an electron, which in turn introduces reflection symmetry about the scattering plane, defined by the incident and scattered electron momenta. An average over initial spin state and sum over the final spin state is therefore taken to describe the incoherent combination of spin states. This is the same procedure described above but now applied to the unobserved quantum numbers of the projectile (electron) rather than the target (atom).

Even though the electron spin may not be directly determined in a collision experiment, the spin still plays role in determining the cross sections. The projectile electron can scatter without changing its spin or its spin can undergo a change in a number of ways. The spin can flip after scattering (spin-flip process), or the projectile electron can be exchanged with the target atomic electron during collision (electron–exchange process). Spin-related processes are relativistic effects and are produced by either the spin-orbit interaction or electron-exchange. The spin-exchange process is most

probable for projectile electron energies in the range of the target electron binding energy which is on the order of eV. Theoretical models generally incorporate an exchange interaction term in low to intermediate energies. More details relating experimental data with the theoretical models will be given in Chapter 4.

The effect of the spin-orbit interaction on the projectile electron is to change the spin polarization. Although changes in spin polarization would not be directly measurable in a spin-insensitive experiment they can manifest themselves even when electron spin is not directly measured. Such effects can be observed in electron-photon coincidence experiments or in superelastic scattering from laser excited targets. A detailed review paper by Andersen, Gallagher and Hertel [Andersen1988] is a good source for understanding electron-photon coincidence experiments on superelastic scattering from laser excited targets.

2.3.4 Connection to Experiments

Now consider the study of collision experiments where an atomic target is excited by the impact of an incident electron. The atom may be excited into a state of well-defined angular momentum with $(2l+1)$ degenerate magnetic sublevels, provided there are no external magnetic fields. Either the scattered electrons are detected or the photons are detected which are emitted due to spontaneous deexcitation of the excited atom[1].

[1] In principle, the electron and photon could be detected in coincidence, but counting rates would be much lower.

If the scattered electron intensity is detected as a function of scattering angle, the differential cross section can be determined. This averages the information of the degenerate magnetic sublevels of the final state and is given by,

$$\frac{d\sigma}{d\Omega} = \frac{\text{scattered electron rate per unit solid angle } d\Omega\ (\theta,\varphi)}{\text{(incident electron rate) . (target area density)}} \qquad (2.8)$$

The angular distribution of photons emitted from an atomic state with equal magnetic sublevel populations is isotropic. Hence, the rate of spontaneous photon emission is proportional to the total cross section for excitation of the atomic state.

2.4 Scattering Theory in Context of the Present Work

A number of theoretical approaches have been applied to the problem of low to intermediate energy electron-atom scattering with varying degrees of success. Some of the relevant background for these theoretical schemes is now given.

2.4.1 Collision Model

Consider an unperturbed atom with number of bound electrons, *N*. The time-independent Schrödinger equation for this unperturbed atom is given as [McDaniel1989],

$$E_n\psi_n = \left[-\frac{\hbar^2}{2m_e}\sum_{i=1}^{N}\nabla_{r_i}^2 + V_a(\boldsymbol{r}_1,...,\boldsymbol{r}_N) \right]\psi_n, \qquad (2.9)$$

where E_n is the energy eigenvalue of the n^{th}-state of the atom[2], ψ_n is the corresponding eigenfunction, $V_a(\boldsymbol{r}_1,...,\boldsymbol{r}_N)$ is the unperturbed Coulomb potential of the atom and r_i the atomic electron coordinate, with the origin at the nucleus.

To describe the projectile electron, its wavefunction $F(\boldsymbol{r})$ is introduced, given as,

$$F(\boldsymbol{r},t) = F(\boldsymbol{r})e^{-iEt/h} \,. \tag{2.10}$$

Then the combined time-independent Schrödinger equation for the projectile electron plus the atom can be written as,

$$E\psi = \left[-\frac{\hbar^2}{2m_e}\left(\nabla_r^2 + \sum_{i=1}^{N} \nabla_{r_i}^2 \right) + V \right] \psi \,, \tag{2.11}$$

where E is the total energy of the combined system (target + projectile), V is the total potential energy including the interaction between the projectile electron and the atom, and ψ is the wavefunction for the combined system. Note that in this time-independent collision theory framework, the total wavefunction describes the coupling of the projectile to all possible states of the atom and is given by,

$$\psi(\mathbf{r}_1,...,\mathbf{r}_N,\mathbf{r}) = \sum_n \psi_n(\mathbf{r}_1,...,\mathbf{r}_N) F_n(\mathbf{r}) \,, \tag{2.12}$$

with $F_n(\mathbf{r})$ is the component of the projectile electron wavefunction that couples to state n of the atom and ψ_n is the unperturbed atomic eigenfunction and the sum is over all the atomic bound states.

The asymptotic form of the projectile electron wave for elastic scattering from the groundstate is given by,

$$F_0 \approx e^{ik_0 z} + \frac{1}{r} e^{ik_0 r} f_0 \,, \tag{2.13a}$$

[2] n=0 is used to denote the ground level.

and the asymptotic form of the inelastically scattered electron wave from the groundstate atom is given by,

$$F_n \approx \frac{1}{r} e^{ik_n r} f_n, \tag{2.13b}$$

where f_n is the inelastic scattering amplitude of the atomic bound state n.

By substituting Equation (2.12) into Equation (2.11) and then subtracting Equation (2.9), it follows,

$$\left(V - V_a\right)\psi = \left[\frac{\hbar^2}{2m_e}\nabla_r^2 + \left(E - E_n\right)\right]\sum_n \psi_n(\mathbf{r}_1,...,\mathbf{r}_N)F_n(\mathbf{r}), \tag{2.14}$$

where $(V - V_a)$ describes the interaction between the projectile and the atom. Multiplying by $\psi_n^*(\mathbf{r}_1,...,\mathbf{r}_N)$ and integrating over the spatial coordinates of the atomic electrons,

$$\int \psi_n^*\left(V - V_a\right)\psi d\mathbf{r}_1 ... \, d\mathbf{r}_N = \left[\frac{\hbar^2}{2m_e}\nabla_r^2 + \left(E - E_n\right)\right]F_n(\mathbf{r}). \tag{2.15}$$

The integrand vanishes for large r. Thus,

$$\begin{aligned} &\left[\nabla_r^2 + \frac{2m_e}{\hbar^2}\left(E - E_n\right)\right]F_n(r) = 0, \\ &\left[\nabla_r^2 + k_n^2\right]F_n(r) = 0, \end{aligned} \tag{2.16}$$

where $k_n^2 = \frac{2m_e}{\hbar^2}\left(E - E_n\right)$ is the wave number squared of the outgoing electron having excited the n^{th} atomic state.

To solve Equation (2.14), consider a matrix V_{mn} describing the interaction of the incident electron beam with the atom when the atom is excited from initial state m to final state n,

$$V_{mn} = \int \psi_n^*\left(V - V_a\right)\psi d\mathbf{r}_1 ... \, d\mathbf{r}_N, \tag{2.17}$$

where ψ_m and ψ_n are the atomic eigenfunctions with eigenvalues E_m and E_n.

Equation (2.15) can be written in terms of the total electron-atom wavefunction by using the matrix notations from Equation (2.17) as,

$$\left[\nabla_r^2 + k_n^2 - \frac{2m_e}{\hbar^2}V_{nn}\right]F_n(r) = \frac{2m_e}{\hbar^2}\sum_{m\neq n}V_{mn}F_m(r)\,. \tag{2.18}$$

The sum on the right hand side leads to an infinite set of coupled differential equations involving the component of the projectile electron wavefunction $F_n(r)$ and thus the scattering amplitudes f_n as given in Equation (2.13). This set of coupled equations has to be reduced by theoretical approximation. Next, the atomic wavefunction is discussed to completely solve the scattering process.

2.4.2 Complex Multi-electron Atomic Model

The Hamiltonian H_{N+1} for the atom-electron system with (N+1) total electrons is given by[3],

$$H_{N+1} = \sum_{i=1}^{N+1}\left(-\frac{\hbar^2}{2m_e}\nabla_i^2 - \frac{Ze^2}{4\pi\varepsilon_0\mathbf{r}_i}\right) + \sum_{i>j=1}^{N+1}\left(\frac{e^2}{4\pi\varepsilon_0\mathbf{r}_{ij}}\right), \tag{2.19}$$

where Z is the atomic number of the target, whose nucleus is considered as the origin of the coordinate system for the collision process, r_i and r_j are the vector coordinates of the i^{th} electron and the j^{th} electron respectively with $r_{ij} = |\,\mathbf{r}_i - \mathbf{r}_j\,|$, and N represents the atomic electrons. The task of the theorist is to solve the Schrödinger equation describing the collision process which can be written as,

$$H_{N+1}\psi = E\psi\,, \tag{2.20}$$

[3] This is a brief summary of the treatment given in chapter 47 and chapter 63 of [Drake2005] with units adapted to be consistent with earlier sections.

with E being the total energy of the system and ψ is the combined wavefunction as in Equation (2.12). The total energy can be written as,

$$E = E_m + \frac{\hbar^2}{2m_e} k_i^2 = E_n + \frac{\hbar^2}{2m_e} k_j^2 , \tag{2.21}$$

with E_m, E_n being the eigenenergies with m and n representing the initial and final state of the atomic target and k are the wave numbers of the incident and scattered electrons.

The differential cross section for a transition from an initial state m to the final state n is given by,

$$\frac{d\sigma_{mn}}{d\Omega} = \frac{k_m}{k_n} \left| f_{mn}(\theta,\phi) \right|^2 . \tag{2.22}$$

The solution of the Schrödinger Equation (2.20) in asymptotic form can be written as [Burke1997; ed. by Drake2005-AMO Handbook Springer2005, Chapter 47],

$$\psi(\mathbf{r}_1,...,\mathbf{r}_N,\mathbf{r}) \overset{\mathbf{r}\to\infty}{\approx} \psi_m(\mathbf{r}_1,...,\mathbf{r}_N)\, \chi_{m_i} e^{ik_m z} + \sum_{n,j} \psi_n(\mathbf{r}_1,...,\mathbf{r}_N)\, f_{mn}(\theta,\phi)\, \chi_{m_j} \frac{e^{ik_n r}}{r} . \tag{2.23}$$

The first term on right hand side of this equation shows the initial atomic target state while the second term represents the sum over all energetically possible final n states. The summation shows the coupling of all the possible channels (states). Thus in the collision model, the sum over all the coupled states in this equation has to be treated in a way that this equation becomes solvable. These atomic eigenstates and their energy eigenvalues satisfy the equation,

$$\left\langle n \left| H_N \right| m \right\rangle = \hbar\omega_n \delta_{nm} . \tag{2.24}$$

To solve for the target states for $N>2$ and to simplify the infinite sum over the coupled states in Equation (2.16), theoretical approximations are used. They are discussed below.

2.5 Specific Theoretical Models

The solution to the infinite set of coupled Schrödinger equations representing the scattering problem is intractable without approximations. A "collision model" is adopted to approximate the V_{mn} in Equation (2.18) and solve this set of equations within the limits of applicability of the chosen collision model. Likewise an approximate structure calculation is used to calculate the required atomic wave functions through Equation (2.24). Any given theoretical scheme must be compared to experimental results to ascertain its validity. If possible, it is desirable to make a connection between the experiment and the theory at the most fundamental level possible, i.e. at the scattering amplitude level. In some cases, electron-photon coincidence experiments or electron scattering from laser-excited atoms can be used to achieve this. Generally, the connection between experiment and theory is made through the collision cross sections.

A number of theoretical approaches have been successfully used to describe low to intermediate energy electron scattering from complex atomic targets. These are:

- Distorted Wave Born Approximation (DWBA)
- Convergent Close Coupling (CCC)
- Born-Bethe Approximation (BBA)

These theoretical models are briefly explained here. *Atomic Collisions* by E.W.McDaniel [McDaniel1989] is suggested for a detailed treatment.

2.5.1 Distorted Wave Born Approximation (DWBA)

In a scattering process, three stages can be defined. Firstly, how the incident particle interacts with the target, secondly what happened to the target due to this interaction and finally, how the scattered particle interacts with the new state of the target. In the First Born Approximation (FBA) the assumption is made that the incident particle weakly interacts with the target, the target is directly excited to the final state, i.e. there is no coupling with the intermediate states (i.e. V_{mn}=0) and finally the wavefunction of the scattered particle is not distorted due to this interaction. With these approximations in FBA, the infinite set of coupled differential equations in Equation (2.18) can simply be written as a single equation for the transition from the initial ground state (m=0) to the final state n as,

$$\left[\nabla_r^2 + k_n^2\right] F_n(r) = \frac{2m_e}{\hbar^2} V_{0n} F_0(r)\,. \tag{2.25}$$

In DWBA, which is a modification of the Born approximation, the incident and the scattered electron wave functions are allowed to distort due to the interaction with the atomic target i.e. in matrix notation both V_{00} and V_{nn} are non-vanishing. This distortion in the electron wave functions is due to the static field of the target atom. But still there is no coupling with the intermediate atomic states i.e. V_{mn}=0 for m≠n. The only allowed scattering is the direct one i.e. $V_{0n}\neq 0$. Applying these conditions to Equation (2.18) results in just two coupled differential equations,

$$\left[\nabla_r^2 + k_0^2 - \frac{2m_e}{\hbar^2} V_{00}\right] F_0(r) = \frac{2m_e}{\hbar^2} V_{0n} F_n(r)\,, \tag{2.26a}$$

and

$$\left[\nabla_r^2 + k_n^2 - \frac{2m_e}{\hbar^2}V_{nn}\right]F_0(r) = \frac{2m_e}{\hbar^2}V_{0n}F_0(r)\,, \tag{2.26b}$$

whose solution give the distorted wavefunction.

DWBA completely depends upon non-relativistic calculations and improves with increasing electron impact energies. The DWBA approach has been previously used in barium collision studies by Clark et al. [Clark1989]. Slight modifications in DWBA gives rise to the First-Order Many-body Theory (FOMBT) which also deals in non-relativistic calculations although some relativistic effects have been included in the atomic state calculation by Srivastava et al. [Srivastava1992].

For complete relativistic effects, the Relativistic Distorted Wave Approximation (RDWA) formulates a completely relativistic approach for the excitation of atoms by electron impact. It is based on Dirac equations in determining the bound state and the scattering wave functions which takes into account the atomic fine structure and the spin dependence of the scattering electron, without further approximation or recoupling of angular momentum. This approach has been studied by Zuo et al. [Zuo1991].

2.5.2 Close Coupling Convergent (CCC) Approximation

This approximation is an extension of the Close Coupling (CC) Approximation. The CC approximation takes into account the intermediate state coupling with target states lying close to the initial and final states. Also, distortions of the incident and the scattered waves are allowed. The number of coupled atomic states is kept low by considering only strongly interacting states, while ignoring weak ones. This is a great difference in

approach compared to previous theoretical models. The CCC approximation allows larger numbers of coupling atomic states by considering pseudo-state levels. It is more appropriate to apply in the low-energy incident electron regime where the atomic energy level spacings are fairly wide. Otherwise the problem of an infinity of final state couplings may arise. It is formulated as a purely nonrelativistic theory in both target structure and electron scattering calculations.

In the CCC approximation, the wavefunction Equation (2.12) can be written in terms of known eigenfunctions ψ_0 of the target Hamiltonian. The expansion coefficients describe the motion of the incident electron relative to the atomic target in various quantum states. If M is the number of coupling atomic states, then the radial partial wave scattering functions satisfy a set of M coupled integro-differential equations. The summation over a small number of M coupled states is then solvable.

Henry and Kingston [Henry1988] and Bray et al. [Bray2002] studied this approximation in detail. Johnson, Bray et al. [Johnson1999] and Fursa et al. [Fursa1999] applied this theoretical approach in describing the collision experiments with barium which is by far the most successful application.

2.6 Experimental Measurement Techniques

The different experimental techniques used to measure scattering observables, such as the cross section and the polarization, are now briefly introduced.

2.6.1 Electron Energy Loss Spectroscopy (EELS)

In an electron energy loss spectroscopy (EELS) experiment, the momentum of the scattered electron is measured directly since the direction and kinetic energy of the scattered electron are known and thus the differential cross section $\frac{d\sigma}{d\Omega}$ can be measured for a known incident energy (E_0) and direction of the scattered electron (θ). Experimentally $\frac{d\sigma}{d\Omega}$ is measured by fixing E_0 and θ and then producing an energy loss spectrum. The energy loss spectrum can be used to map out the energy level scheme of an atom. The intensity of a peak at a particular energy loss value is proportional to the excitation probability of the associated level and hence to $\frac{d\sigma}{d\Omega}$, averaged over target atom sublevels with a defined scattering angle.

2.6.2 Line Emission Measurements

If the photons due to the radiative decay are detected, instead of the scattered electrons, from a collisionally excited atom, the integral cross section (σ) can be measured. An optical band pass filter with an appropriate wavelength corresponding to the radiative decay is used to select the desired photons. The cross section which is measured directly from an experiment is the line emission cross section (σ_{em}). As discussed in Section 4.8, corrections to σ_{em} can be made to deduce the apparent and level excitation cross sections, σ_{ap} and σ_{ex}.

Along with the measurement of the cross section, the polarization of the photons can be also measured. The polarization P of radiation emitted by an atomic excited state due to electron impact, when it deexcites to a lower state, is defined by,

$$P = \frac{(I_{\parallel} - I_{\perp})}{(I_{\parallel} + I_{\perp})}, \qquad (2.27)$$

where $I_{\parallel}$ and $I_{\perp}$ are the intensities of the radiation as shown in Figure 2.3. $I_{\parallel}$ is the intensity of the radiation emitted perpendicular to the electron beam with its electric vector parallel to the z-axis. Conventionally the quantization axis i.e. the z-axis is taken along the electron beam direction, $I_z = I_{\parallel}$. The intensity $I_{\perp}$ of the radiation emitted perpendicular to the electron beam but with its electric vector perpendicular to the z-axis is rotationally invariant and hence $I_x = I_y = I_{\perp}$.

Oppenheimer in late 1920s [Oppeheimer 1927a, 1927b, 1928] and later Penny [Penny1932] treated polarization theory for the cases where the fine structure and the hyperfine structure separations were much smaller or much larger than the line width. In 1958 Percival and Seaton [Percival1958] gave a detailed theoretical approach of the polarization of atomic line radiation resulting from electron beam excitation. Their

treatment included the case where the fine structure and the hyperfine structure separations are comparable to the line width. This gave the polarization as a function of electron energy in terms of magnetic sublevel excitation cross sections and appropriate coefficients. In a second approach, a density matrix formalism is used to determine the polarization of atomic line radiation resulting from electron beam excitation. Details are beyond the scope of this thesis but are found in [Blum1981].

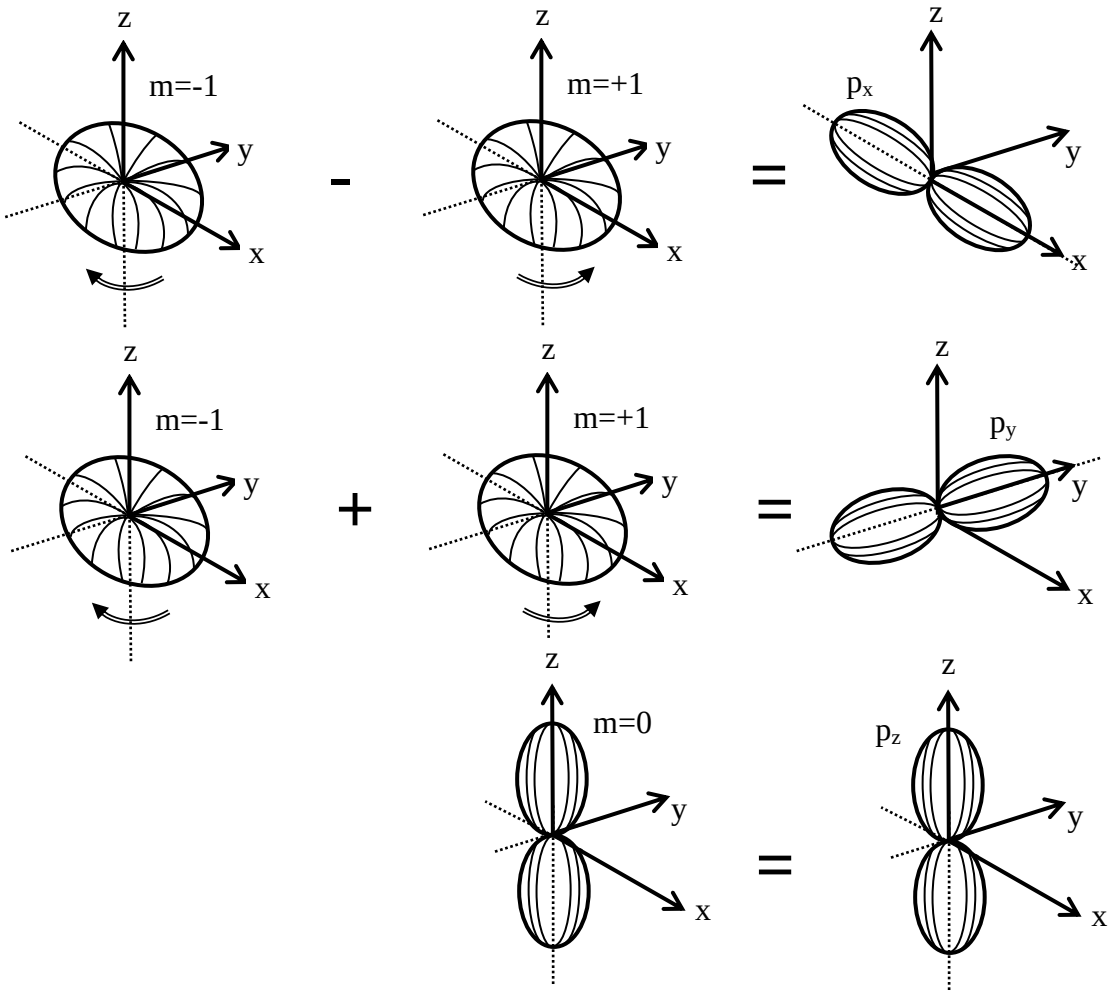

Figure 2.2: Representation of the square of the angular part of wave function for magnetic substates m=-1, m=0, m=+1 of atomic P-state. Also shown on right hand side are the coherent superposition of m=-1 and m=+1 when a linearly polarized laser light is sent along the z-axis.

When an electric dipole transition is the dominant result of an interaction of an electron in an atom with the electromagnetic field, information can be extracted about the magnetic sublevels in the following way. When the electric dipole transitions take place from a higher energy state having total angular momentum quantum number J=1 with total angular momentum magnetic quantum number M_J= 0, ±1 to a lower energy state with J=0 and M_J=0, the linear polarization gives information about the relative population of the magnetic sublevels. For the transitions ΔM_J=0, fluorescence is polarized parallel to the quantization axis taken along the direction of the electron beam, while for transitions ΔM_J=±1, it is polarized perpendicular to the quantization axis. These transitions are depicted in Figure 2.3 for J=1 to J=0.

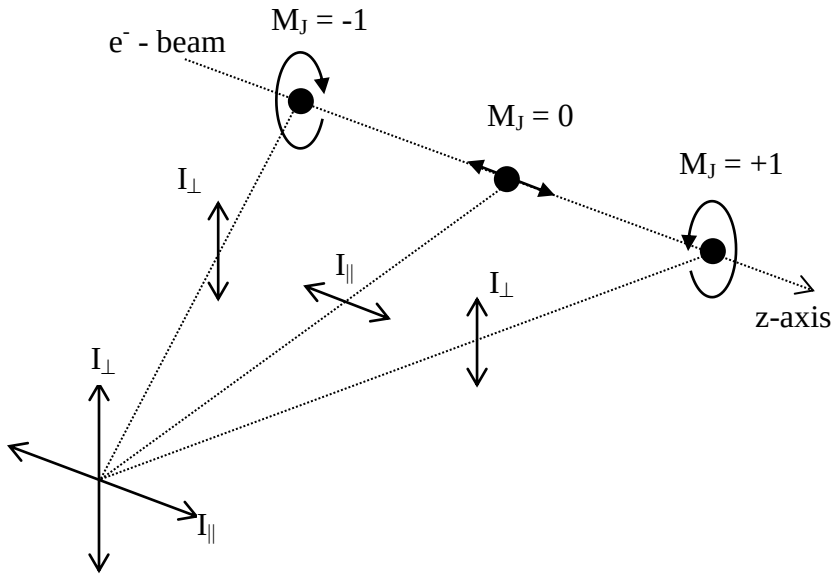

Figure 2.3: Polarization due to magnetic sublevel transitions.

2.6.3 Magneto-Optical Trap (MOT) Experiments

Another experimental technique is to measure the total cross section of electrons scattering off cold atoms confined in a magento-optical trap (MOT). Magneto-optical trapping is used along with laser cooling in order to produce samples of cold, trapped, neutral atoms at micro-Kelvin temperatures. This technique is based on the Doppler effect and conservation of momentum. The trapping or slowing down of atoms is achieved by combining the small momentum of a single laser-photon with a spatially dependent absorption cross section with a large number of absorption-spontaneous emission cycles.

Photons have a momentum $\hbar k$ and the total momentum is conserved in all atom-photon interactions. When a laser beam strikes an atomic ensemble, the spontaneously emitted photons are randomly distributed over all spatial direction. Although each emitted photon transfers $\hbar k$ to the emitting atom, the time-averaged momentum transfer tends to zero. On the other hand when an atom absorbs a photon, it is given a momentum kick in the initial direction of the photon as all absorbed photons come from the same direction. By detuning a laser beam to a frequency less than the resonant frequency, also known as red detuning, the laser photon is only absorbed if its frequency is up-shifted by the Doppler effect, which occurs whenever the atom is moving towards the laser source. This applies a friction force to the atom whenever it moves towards a laser source and thus reducing its speed. For cooling to occur along in all directions, the atom must see this frictional force along all three Cartesian axes. This is achieved by illuminating the atom with three orthogonal, retro-reflected, beams.

Experimental work has been done for several MOT cooled atomic species, such as cesium, rubidium etc. For a detailed approach to the MOT experiment technique the reader is referred to research by the University of Windsor group working on cesium [MacAskill2002, Lukomski2005] and the University of Wisconsin group working on rubidium [Walker1992, Hoffmann1994].

Section II: Collision Theory with Laser-Excited Atomic Targets

2.7 Introduction

The electron collision studies can be extended dramatically by preparing a target atom in a pre-excited state by using the technique of optical pumping. The highly monochromatic, directional and polarized laser photons cyclically pump atomic bound electrons to excite the atom under certain conditions into a coherent superposition state. Thus the wavefunctions of the magnetic sublevels can be combined with a definite phase and amplitude relationship. Scattering experiments are then performed from these coherent superposition states or from a single substate. Measuring the scattered electrons from the isotropic (magnetic substates taken as a single atomic energy state) initial state gives the differential cross section while measuring the scattered electrons from anisotropic (magnetic substates taken as separate energy states) initial state gives the so called partial differential cross section as described in [Hein2011, Hein2012]. In addition, if only the

spontaneous emitted photon is detected from the excited atom, the integral cross section can be deduced.

Generally in a scattering experiment, completely coherent optical pumping may not occur due to a number of natural constraints like power-broadening of the linewidth of a transition, hyperfine structure trapping, radiation trapping, etc. Therefore the orientation of the atom, which means the populations of the magnetic sublevels are not equal, depends generally on the frequency, intensity, polarization, spectral bandwidth of the laser as well as the linewidth and transition probability of the absorbing transition.

The S-P excitations have been studied previously for various atomic targets. These experiments have performed a complete investigation in terms of quantum-mechanical scattering amplitudes. These types of experiments have taken a big step forward by using optical pumping techniques to prepare the excited atomic target states. This includes the work by Hertel et al. [Hertel1977], Herman et al. [Herman1989], Scholten et al. [Scholten1991], Sang et al. [Sang1994], Jiang et al. [Jiang1995] on optically pumped sodium atoms, Hanne et al. [Hanne1993] on Chromium, Law et al. [Law1995] on calcium to name a few. Recently at the University of Manitoba AMO laboratory, electron scattering studies were carried out on ytterbium and barium laser-excited atoms by Zetner, Li, Johnson and Hein, which are referred to at appropriate places in this thesis.

2.7.1 Optically Prepared P-state

The preparation of an initial, excited P-state by laser pumping and subsequent electron scattering from this excited P-state has opened new frontiers to be explored in atomic collision physics. The P-state has three magnetic substates, m=0,±1. With a linearly polarized laser beam used for pumping to the P-state, either the m=0 sub-state or a combination of m=±1 sub-states are selected. Similarly if using a circularly polarized laser beam, either m=+1 or m=-1 sublevel can be selected.

Figure 2.2 shows the atomic P states, with shapes generally referred as "doughnut" and "peanut". The "doughnuts" represent the magnetic sub-states of m=±1 spinning in opposite directions while the "peanut" represents the magnetic substate of m=0 aligned along z-axis. A coherent superposition of m=±1 can be obtained by illumination with a linearly polarized laser light along the z-axis. This is also shown in Figure 2.2 on the right hand side in terms of p-orbitals.

2.7.2 Atomic Level Population Rate Equations

One of the initial estimates that have to be made in a laser-excited scattering experiment is to determine whether enough population of the laser-excited state, which acts as the target atomic state for the incident electron beam, can be achieved. To determine this, the rate equations which govern the rate at which populations of various energy levels change in the presence of laser radiation will be studied. The rate equation approach provides a convenient means of studying the time dependence of the atomic populations of various levels in the presence of radiation at frequencies corresponding to the different

transitions of the atom. A more sophisticated way to determine the atomic level population is by completely describing the atom by quantum mechanics. This approach employs the Optical Bloch Equations [Loudon1983]. In the present work, a rough estimate of the excited atomic population was desired, and a rate equation approach was taken.

Two-Level Atomic System

Consider a two-level atomic system with energy levels E_1 and E_2 as shown in Figure 2.4. This represents a generic S to P state excitation process. The laser pumping process provides the excitation of the atoms into higher energy levels such that the incident laser radiation's frequency υ satisfy the relation,

$$h\upsilon = E_2 - E_1 \text{ , where } E_2 > E_1 . \qquad (2.28)$$

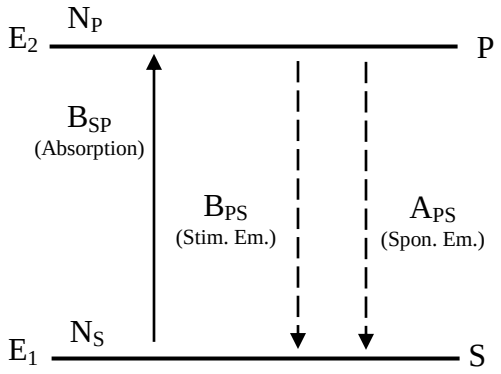

Figure 2.4: Atomic two-level system with ground state S and excited state P. Ns and N_P are the state populations with transitions described by Einstein coefficients A and B. Solid arrow shows the absorption process while the dashed arrows show the two types of emission processes, spontaneous and stimulated emissions

The rate equations describing the processes in Figure 2.4 can be written as [Woodgate1970],

$$\frac{d}{dt}N_S = -\rho(t)B_{SP}N_S + \left(A_{PS} + \rho(t)B_{PS}\right)N_P, \tag{2.29}$$

$$\frac{d}{dt}N_P = \rho(t)B_{SP}N_S - \left(A_{PS} + \rho(t)B_{PS}\right)N_P, \tag{2.30}$$

where N_S and N_P are the populations of the S-level and P-level, respectively. A and B are the Einstein coefficients. A_{PS} (s^{-1}) gives the probability per unit time that an electron in the P-state decays spontaneously to the S-state emitting a photon of energy hυ while B_{PS} (J^{-1} m^3 s^{-1}) gives the probability per unit time per unit spectral energy density due to stimulated emission by the laser and B_{SP} gives the absorption rate. $\rho(t)$ is the spectral energy density per hertz of the laser radiation. In the present application, the time dependence arises from the transit of atoms through the laser beam. Details of the time dependence of $\rho(t)$ are determined by the atomic transit velocity, v, and the transverse spatial profile of the laser beam.

The differential rate equations can be solved and thus give an estimate of the excited state atomic population of a system. In the present work, the two-level atomic system can be applied to the experimental work on the scattering experiment with the ytterbium P-state, which will be discussed in Chapter 6.

Three-Level Atomic System

A three-level atomic system is shown in Figure 2.5. Here the atom is excited by laser pumping from the ground S state to the P state. The P state in turns populates the metastable D state which acts as the target state for the scattering experiment.

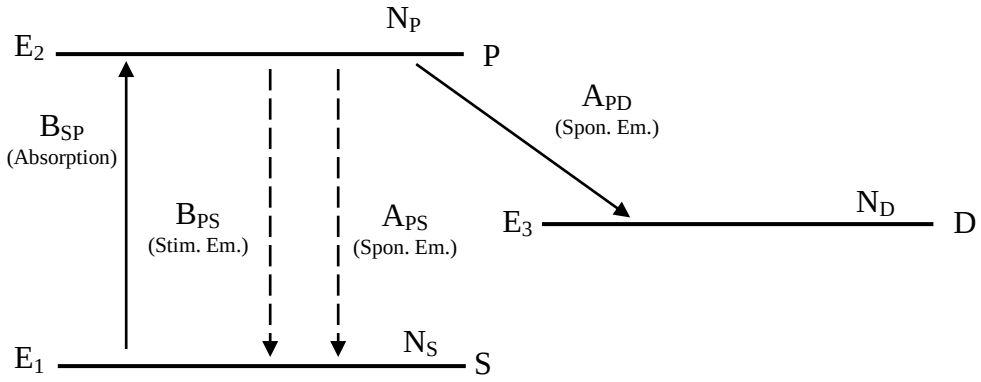

Figure 2.5: Atomic three-level system with state populations Ns, Np, N_D and Einstein coefficients A and B for the transitions indicated. Solid arrow shows the absorption process while the dashed arrows show the two types of emission processes, spontaneous and stimulated emissions.

The rate equations for the above three-level system can be written as,

$$\frac{d}{dt} N_S = - \rho(t)\, B_{SP}\, N_S + \left(A_{PS} + \rho(t)\, B_{PS}\right) N_P \,, \tag{2.31}$$

$$\frac{d}{dt} N_P = \rho(t)\, B_{SP}\, N_S - \left(A_{PS} + A_{PD} + \rho(t)\, B_{PS}\right) N_P \,, \tag{2.32}$$

$$\frac{d}{dt} N_D = A_{PD}\, N_P \,, \tag{2.33}$$

where N_S, N_P and N_D are the respective state populations, and the other notations are similar to as described above in the two-level system.

In the present work, the three-level atomic system is of interest for the barium atom. Electron scattering from the laser-excited D-state of barium will be discussed in Chapter 5. For a three level system, the rate equations are generally solved numerically. The reader is referred to previous work from this lab [Hein2010] for a detailed look at the solutions for this system of equations applied to the barium atom.

2.8 Previous Experimental Studies in Ba and Yb

Previously the experimental results from the University of Manitoba AMO laboratory have been compared with the theoretical models. Experimental studies of electron impact coherence parameters (EICP) from superelastic scattering of laser-excited barium were compared with the unitarized-DWA model [Zetner1992]. Zetner et al. [Zetner1993] have compared experimental results of electron-impact excitation of barium with relativistic and unitarized DWA and the CC theory. Cross section experimental results of ground state barium were compared with two-channel CC, relativistic and non-relativistic DWA theoretical models by Wang et al. [Wang1994]. The experimental results from electron scattering from metastable states of barium were compared with the unitarized-DWA model by Li and Zetner [Li1996]. The electron impact excitation in laser-excited barium experiment was compared with CCC and CC theoretical models [Johnson1999a] and also ground state studies of barium were compared with CCC and unitarized-DWA models [Johnson1999b, Johnson2001]. Johnson et al. [Johnson2002, Johnson2005] have

compared experimental results of electron scattering from laser-excited barium with the CCC approximation.

In ytterbium electron scattering experiments, differential cross section experiments of singlet-P ytterbium have been compared with the unitary DWA model by Johnson et al. [Johnson1998]. Differential cross section and EICP experimental measurements from superelastic scattering from laser-excited ytterbium into the triplet-P level have been compared with unitary DWA by Zetner et al. [Zetner2001]. Hein et al. have compared DCS [Hein2011a] and EICP [Hein2011b] of laser excited ytterbium triplet-P with CCC, relativistic DWA and relativistic CCC.

In general, the comparison between the experiments and the theoretical models summarized above did not give a clear picture of which model was preferred. Recently, relativistic effects were incorporated in the CCC model by Bostock [Bostock2010]. This new RCCC model was applied to barium [Bostock2014a] and ytterbium [Bostock2014b] but has not yet been published. In the experimental chapters these models will be compared with the new results from this work.

Chapter 3

Experimental Setup

3.1 Introduction

In this chapter, components of the apparatus needed to perform an electron-atom collision experiment are described along with their functions. In an electron-atom collision experiment, a projectile electron beam with energy E_0 interacts with an atomic beam target A which is either in the ground state or in a laser prepared excited target state. The electron beam excites the atom A to some higher state A^*, transferring energy ΔE in the process. After the interaction, the scattered electron with a residual energy $E_r = E_0 - \Delta E$ and the emitted photon due to the deexcitation of the atom, can be detected. A schematic of the electron-atom collision is shown in Figure 3.1.

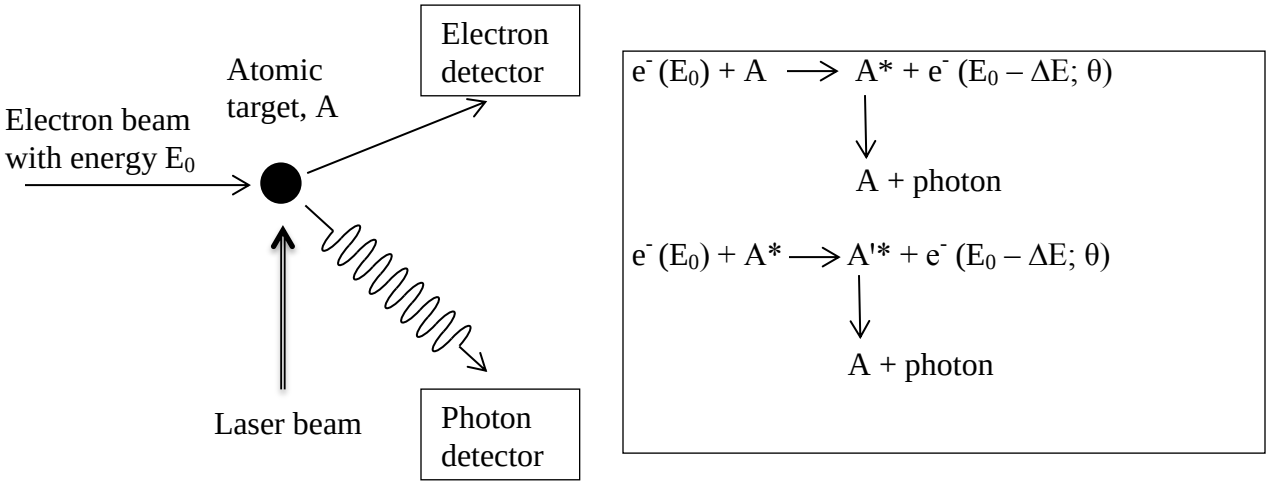

Figure 3.1: A schematic of electron-atom collision showing the particles and the detectors. The target atom can be in the ground state or in a laser-excited state.

3.1.1 Apparatus

The electron-atom collision apparatus can be divided into three main systems, namely: the production system, detection system and data acquisition system. The production system consists of three parts, i.e. production of the atomic beam, laser beam and electron beam, while the detection system includes the electron and photon detectors. The data acquisition system acquires the data for further analysis. The whole experiment was carried out in a vacuum chamber containing the electron gun, the atomic oven assembly and the electron detector. Also inside the vacuum chamber were a gas-jet nozzle, a Faraday cup mounted on the electron detector casing, and a fluorescence-focusing lens assembly. The fluorescence detection system was located outside the vacuum chamber. It includes a holder for interchangeable bandpass optical filters, a rotating assembly containing a polarizer and a quarter-wave plate, and finally the photomultiplier tube detector (PMT) itself. A diagram of the electron-atom collision experiment is shown in Figure 3.2. In the following sections each component of the apparatus is discussed separately in more detail.

3.2 Production of the Atomic Beam

In the present work, two atomic source targets, barium and ytterbium were studied in electron atom collision experiments. Barium is an alkaline earth metal, while ytterbium belongs to the rare earth lanthanides group. Both these metals come in the form of solid metallic pieces. To make them into vapours and use them as atomic source targets requires high temperatures in the range of 700-850°C. For this purpose an oven chamber was used to vaporize the metals.

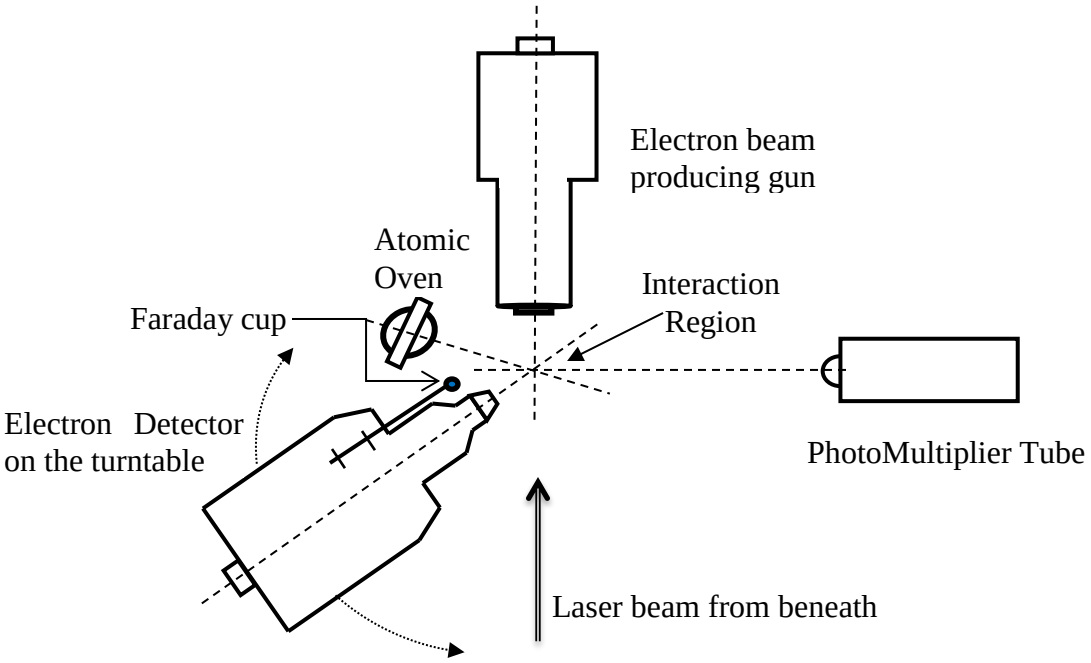

Figure 3.2: Schematic of the electron-atom collision apparatus showing the atomic oven, electron gun, detector with Faraday cup and the PMT.

3.2.1 Atomic Source Oven Chamber

A schematic diagram of the metal vapour source oven assembly is shown in Figure 3.3. The oven chamber was made of stainless steel[4] with a long narrow exit channel of diameter 0.060" and length 0.5". The chamber containing metallic pieces of the source material was sealed by a plug in the filling hole. A power supply[5] supplied current of around 2 A to the coaxial resistive heater[6] wrapped around the chamber. This provided the required temperature of around 800 °C to vaporize the metallic pieces. A

[4] 304 stainless
[5] Alpha 7500 DC
[6] ARI AerOrod BXX06B24-4T

thermocouple[7] was inserted at the top of the chamber to monitor its temperature by a digital voltmeter calibrated in volts/°C. This whole assembly was inserted in the oven holder with a ceramic rod to keep it in place and electrically isolated. The exit channel of the chamber was aligned with the exit hole of the oven holder, producing a collimated atomic beam. A Teflon sleeve was inserted in between the chamber and the oven assembly for thermal isolation and to shield the interaction region from the glow of the heater.

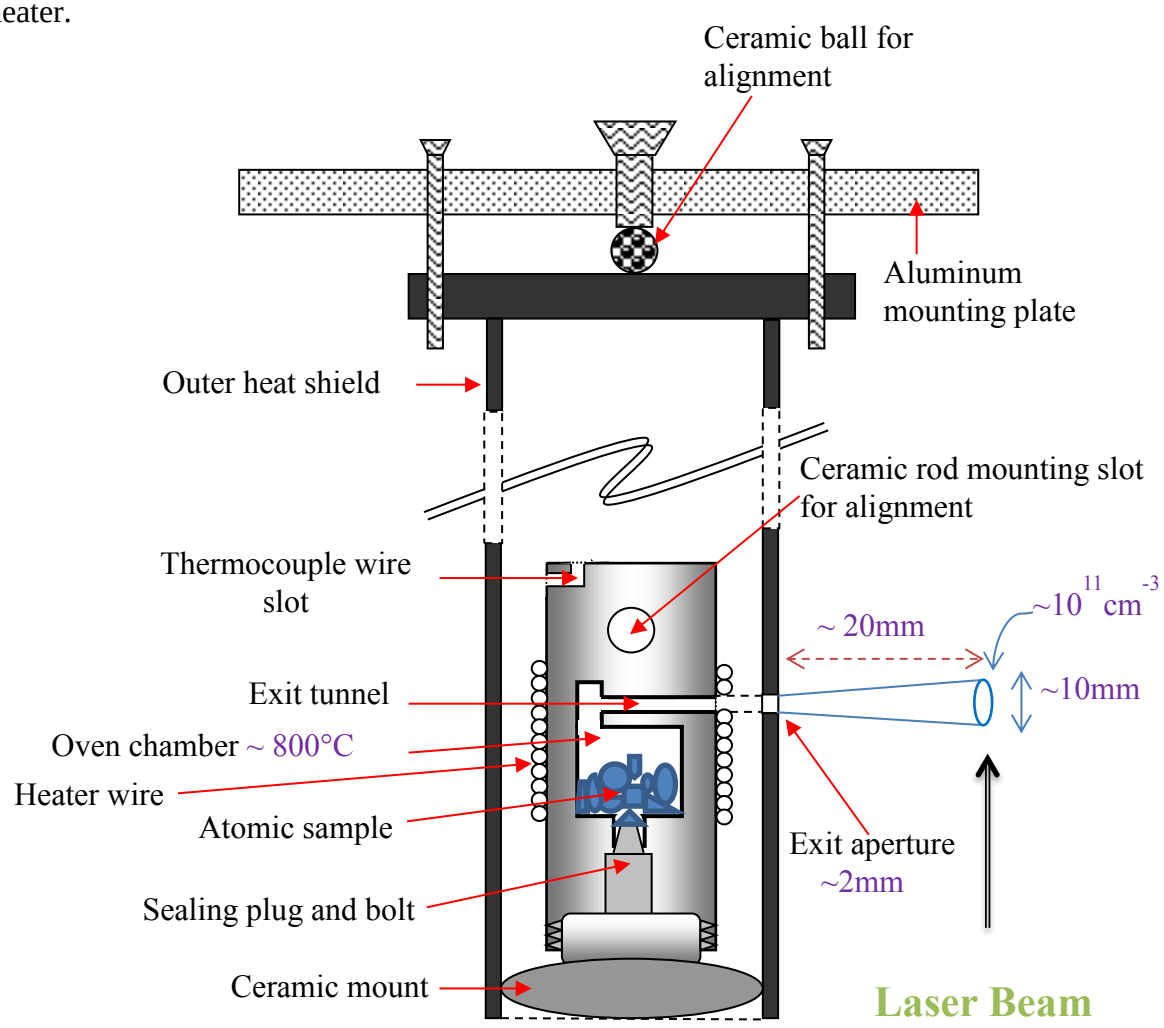

Figure 3.3: A schematic diagram of the metal vapour source oven assembly.

[7] Chromel-Alumel

When the required temperature inside the oven chamber was reached, the atomic beam emerged from the exit channel because the vapour pressure inside the oven-chamber was higher than that outside of the oven.

3.2.2 Atomic Beam Specifications

The atomic beam emerging from the oven travels in the horizontal (scattering) plane. The atomic target density at the interaction region, which was approximately 0.645" away from the outer edge of the oven assembly, was previously measured to be on the order 10^{11} cm^{-3} [Zetner1992] under similar conditions. The atomic beam stability was monitored by observing at the electron energy loss spectrum (Section-3.5). The collimation of the atomic beam was determined by the two apertures of the oven assembly; its size was visually measured to be around 1 cm in diameter by scanning the laser (Section-3.3) across the atomic beam. A photograph showing the interaction of an atomic beam with the laser beam is reproduced in Figure 3.4.

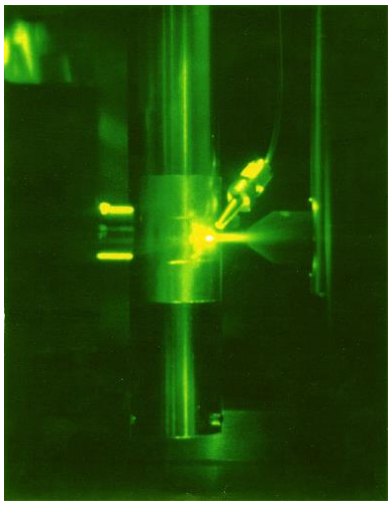

Figure 3.4: A photo taken through a vacuum chamber view port, showing the interaction of the laser beam with the barium beam. The glow in the middle shows the diameter of the atomic beam at the interaction region.

3.3 Laser System

For the experiments discussed in this thesis, a commercial Coherent CR-699-21 ring dye laser system consisting of a tuneable dye laser pumped by an Argon ion laser was used. This system was capable of meeting the following general requirements for performing the laser excitation electron scattering experiments on barium and ytterbium.

- Wavelength consideration: Wavelength must be tuneable to the desired range to excite the ground state atoms to the excited state of interest for the experiments. The present laser system provided stable, unidirectional single wavelength light from 425 – 810 nm, which could be tuned to the present experiment's required wavelengths of 553.7 nm for barium and 555.80 nm for ytterbium.
- Power consideration: Sufficient laser beam power in the range of 50 – 80 mW was needed to populate the excited atomic state of interest.
- Linewidth consideration: The linewidth of the laser should be as narrow as possible; A properly functioning CR-699-21 laser system has a linewidth on the order of 1 MHz; the linewidth was approximately 20 MHz for the present system.

Generally, stability of the laser was monitored by observing the electron energy loss spectrum. Visual checks were also done periodically by sighting the fluorescence spot inside the vacuum chamber. The laser stability requirements were not particularly stringent, since the experiments performed were self-normalizing. The general frequency drift was less than 100 MHz/hour and the power stability of the laser was around 5 %/day. A brief description of the dye laser operational principle is as follows.

3.3.1 Principle of the Dye Laser

Dye lasers are optically pumped lasers. The active media are organic dye molecules dissolved in a liquid. The dye solution is circulated through the oscillator. When the dye solution is irradiated by a pump laser (in the present system by the Argon laser), the molecules are excited from the ground state into one of the vibrational/rotational states of a particular electronic level. Figure 3.5 depicts this excitation of the dye molecules (dark and light lines represent vibrational states and the rotational fine structure, respectively) by the pump laser and subsequent various possible optical transitions. Since the singlet-singlet transitions are allowed, the interaction with the electromagnetic radiation can raise the molecule from the ground level S_0 to one of the vibrational levels of the S_1 state. The excited molecules then decay by stimulated emission into one of the vibrational rotational levels of the ground state, showing a broad-band fluorescence structure.

The light thus emitted by the dye laser has a longer wavelength than the pump laser. Since there are large numbers of vibrational rotational states, a wide band is obtained within the fluorescent spectrum of the dye. This feature makes dye lasers very useful for atomic and molecular spectroscopy, because they can be tuned throughout the emission range of the dye.

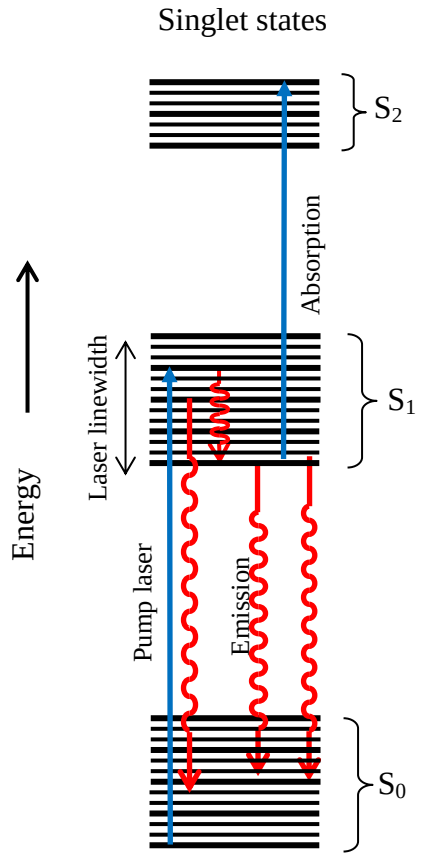

Figure 3.5: Generic energy levels of a laser dye molecule. When the dye molecules are excited by a pump laser (blue), many different optical transitions are possible, leading to a broad range of emission lines (red).

In the present work, a Coherent Innova 90-6 argon ion laser provided the optical pumping to the dye laser. The argon ion laser is capable of high power continuous wave operation from the infrared (IR) through the visible and near ultraviolet UV region, on a few discrete lines. The plasma tube containing the ionized argon gas operates with current densities of 700 A/cm^2 and typical plasma temperatures of 3000 K. It is kept cool by running cold water. The Innova 90-6 has two modes of power regulation: light output power regulation and plasma tube current regulation, with a maximum rated output of

10 W. The dye used was P-556 [8]; with 5W of pump power, the dye can lase from 530 – 624 nm with a peak power at 553 nm [Guggenheimer1993]. This was the ideal wavelength range for the present experiments.

A simple block diagram of the laser system along with an example showing the output spectrum of a similar dye system is shown in Figure 3.6. The technical setup to produce the laser beam at the desired wavelength of 553.70 nm for barium and 555.80 nm for ytterbium was performed based on a previous calibration of the laser system [Zetner1992]. More details of the laser setup and control system are given in [Hein 2010].

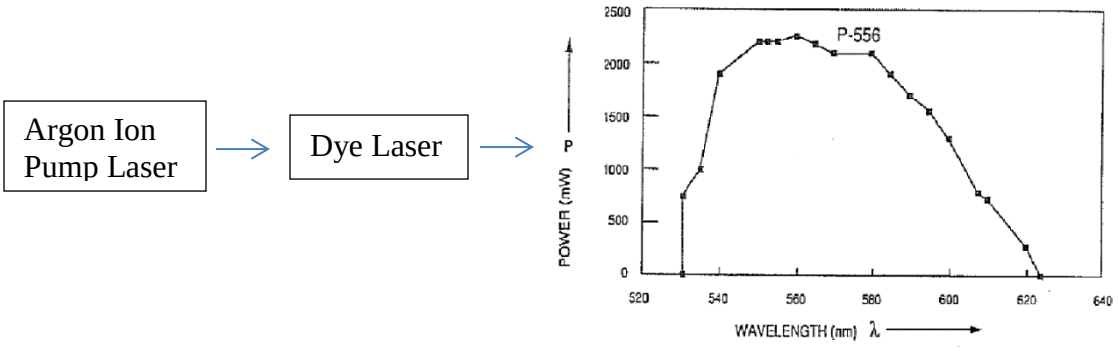

Figure 3.6: Block diagram of the laser system showing the range of output wavelengths achievable with a P556 dye laser system [Guggenheimer1993]. The graph shows the maximum power output is achieved in the range of 550 – 560 nm, as desired in the present work.

[8] Pentamethylpyrro-methene

The laser was introduced into the scattering chamber via an optics system as described in the following section. During the experiments, the laser beam was monitored via the excited state target population deduced by studying an appropriate feature in the electron energy loss spectrum (EELS). This procedure is discussed in detail in Chapter 5. Also the laser beam was visually checked by sighting the fluorescence spot inside the vacuum chamber.

3.3.2 Laser Transportation System

After the laser beam was tuned to the required wavelength and power, it was transported into the vacuum chamber with the aid of optical components. Figure 3.7 is a block diagram of optics used for the laser beam transportation into the vacuum chamber. The laser beam was guided from the laser system to the underneath of the vacuum chamber with a set of mirrors where it encountered a Glan-Taylor prism which was used as a polarizing beam splitter, to ensure that the laser beam was in a well-defined linear polarization state. This linearly polarized laser beam was then directed towards the interaction region. Finally before entering the vacuum chamber, the laser beam was passed through a half-wave retardation plate mounted on a computer-controlled stepper-motor for polarization selection. A computer-controlled shutter was used to switch the laser pumping on or off during an experiment.

3.4 Electron Guns

The function of an electron gun is to focus a beam of electrons from a thermionic emitter onto a fixed point target over a wide range of electron energies. The principle of this focussing is similar to the principle of optics focussing. In charged particle optics, the electrostatic lenses are made of various cylinders and apertures with varying geometries as shown in Figure 3.8, to obtain the desired electron beam [Harting1976]. Electrostatic deflectors are used to steer the electron beam transversely.

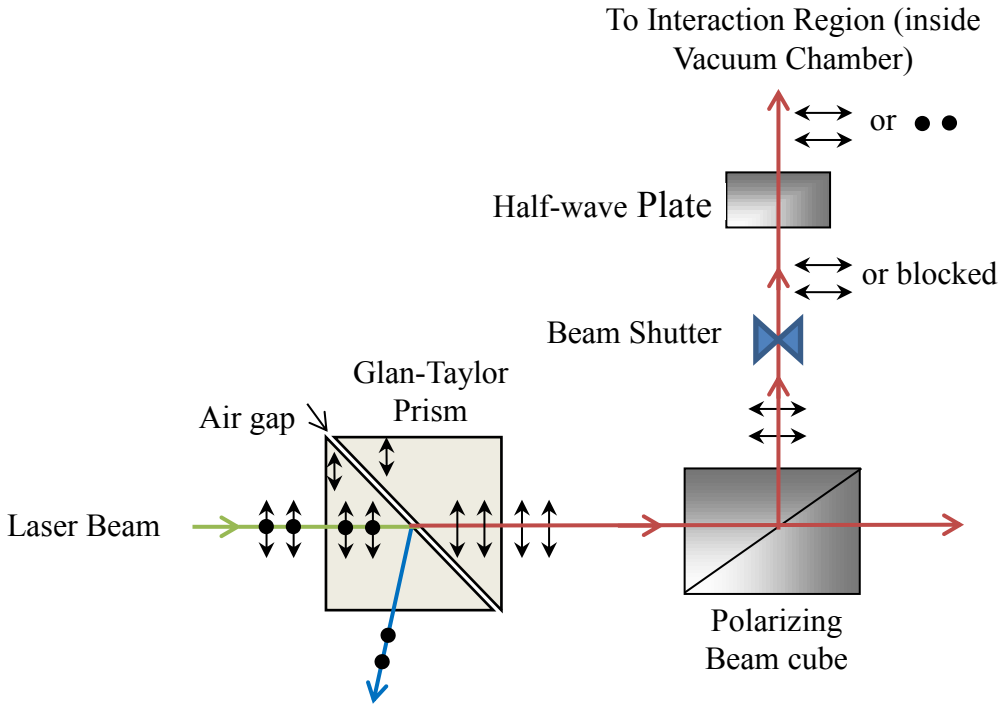

Figure 3.7: Block diagram of optics for transporting the laser beam to the interaction region. The two orthogonal linear polarizations of the laser beam are indicated by arrows and dots.

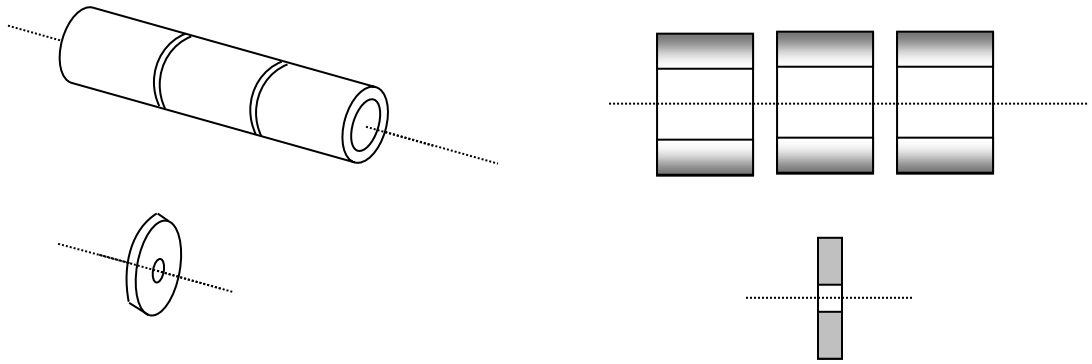

Figure 3.8: Cylinder and circular aperture lenses of an electron gun showing (a) full view (b) cross sectional view with the dashed line showing the electron beam axis.

Two types of electron guns, a high resolution gun (HRG) or a high intensity gun (HIG), were used according to the need of the experiments. In both the guns, electrons were produced by thermionic emission from a tungsten wire filament. The filament emits thermal electrons in all directions, when it is heated due to current passing through it. These electrons have to be immediately accelerated, for example in the present case, by a Pierce-Wehnelt extraction diode [Bernius1988] which is the first element in the electron gun as shown in Figure 3.9. The tapered shape of the cathode element produces initial focussing for the electron beam.

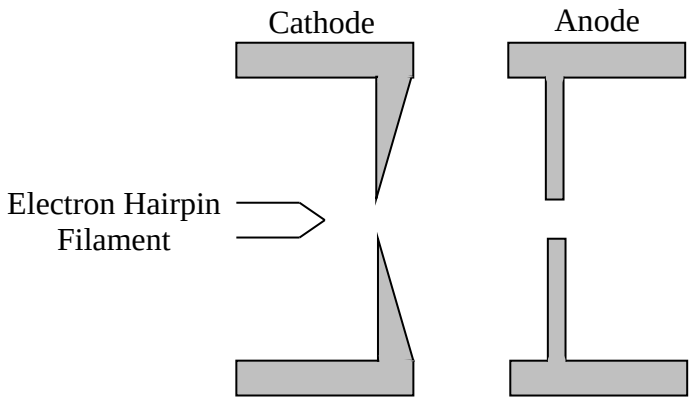

Figure 3.9: Pierce-Wehnelt extraction diode.

The image of the diode extraction aperture serves as the electron source object. This object is focussed at the interaction region by the electron gun lens system.

3.4.1 Basic Principle of Electrostatic Focussing

Electrostatic lenses are used in the electron gun (and also in the electron spectrometer) to focus the beam. One such arrangement is shown in Figure 3.10, consisting of 3 identical metal cylinders at positive electric potentials V_1, V_2 and V_3, with $V_1<V_2>V_3$. If $V_1=V_3$, a special condition known as an Einzel lens, then the beam energy at the output is the same as the input. The electric field distribution deflects the paths of the off-axis electrons by an amount that increases with distance from the symmetry axis, producing a focusing effect.

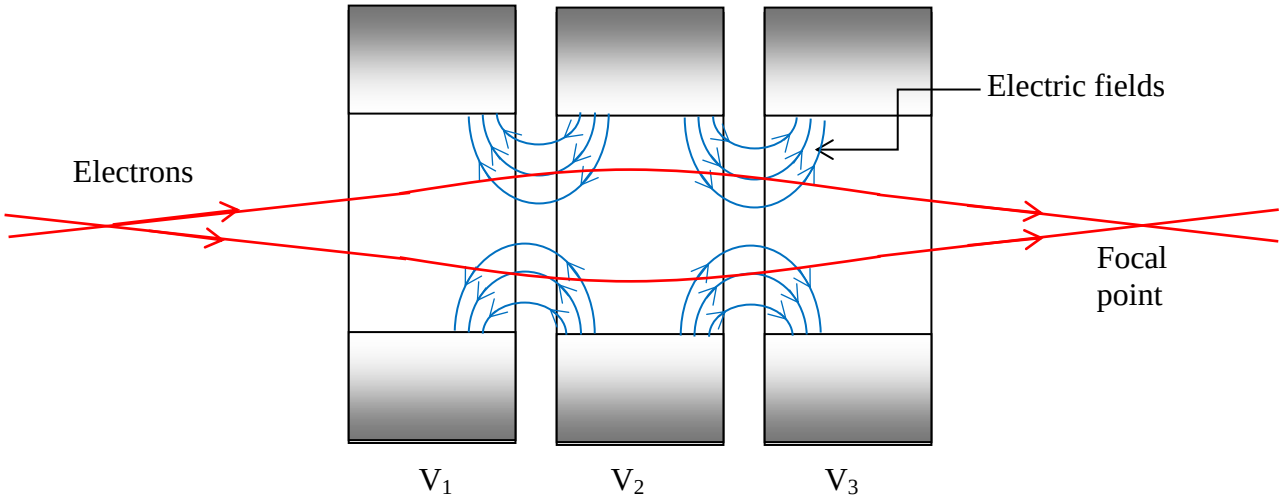

Figure 3.10: Focussing of electrons using a cylindrical electrostatic lens.

3.4.2 Determining the Electron Impact Energy

The interaction region was at ground potential as all components of the apparatus were enclosed in a grounded metal casing. The lens potentials were set with respect to the electron gun common (cathode bias) which was referenced to ground. This determined the impact energy of the electrons at the interaction region, in terms of the negative bias applied to the gun filament: $E_0 = -eV_0$. A schematic showing the cathode bias is shown in Figure 3.11. In the following two sections, the high intensity gun (HIG) and high resolution gun (HRG) used in the experiments, are described separately.

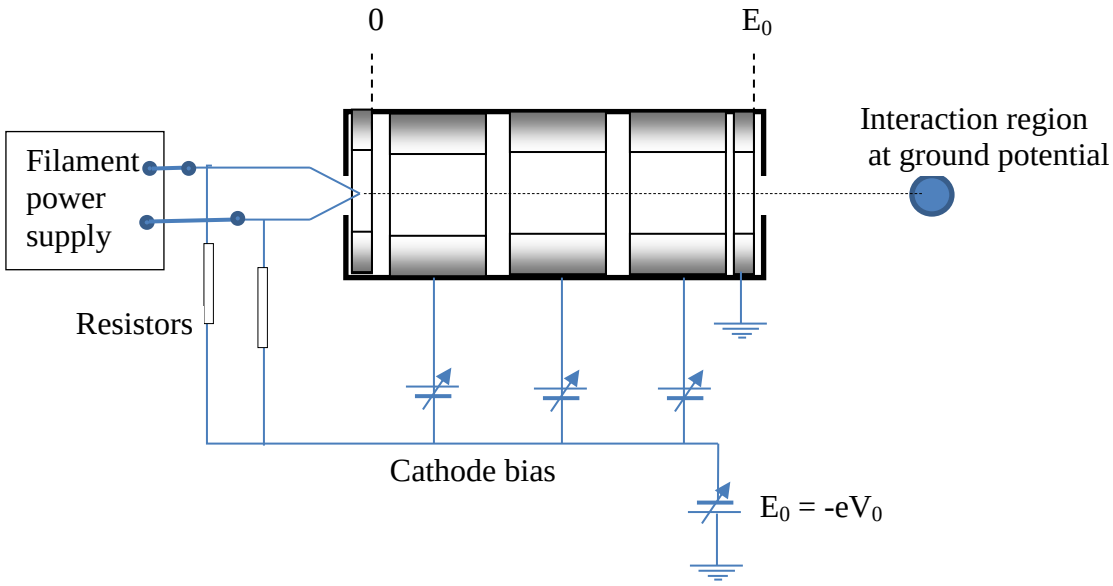

Figure 3.11: Focussing of electrons using electrostatic lens.

3.4.3 High Intensity Gun (HIG)

The high intensity gun (HIG) was used in experiments for which an intense electron beam was required and the electron energy resolution was not so critical. Typically the energy resolution of the HIG at FWHM was 500 meV with an electron beam current of 1-2 μA. This HIG, shown in Figure 3.12, was built at the Jet Propulsion Laboratory in Pasadena, California, USA. It consists of a filament as an electron source, electrostatic lens elements for focussing the beam and deflectors built within the lens elements for transverse steering of the electron beam. Also within the lens elements are the apertures. Initially the lens potential settings of the gun elements were obtained by analytical computer simulations [Chutjian1979] and as used previously in the University of Manitoba AMO laboratory. These initial potentials were then adjusted slightly in order to optimize the electron beam current on the Faraday cup, which was mounted on the

detector and could be moved on the turntable along with the detector, as shown previously in Figure 3.2. The beam size and divergence were estimated by moving the Faraday cup slightly on either side of the beam axis and observing the current on it. The divergence was found to be less than 2° and the size of the electron beam spot was estimated to be approximately 1 cm in diameter. Helium was brought to the interaction region by a gas jet nozzle for the calibration of the electron impact energy and was done with respect to the 19.36 eV helium 2 ^{2}S resonance state.

The electron-producing cathode (Pierce) element was a hairpin tungsten filament located 0.020" behind the very first aperture in the very first element of the gun and held in a ceramic holder. The anode C1 comprised the second aperture in the second element of the gun. The C1 element also had deflectors to guide the electron beam to the next element C2. The fourth element in the gun called Dec1 again contained deflectors to center the electron beam through the final element F1, and ultimately the beam was focussed into the interaction region.

The lens elements and the deflectors of the HIG were made of 304-stainless steel. The filament along with its ceramic holder could be removed for alignment by sighting through the beam axis. The apertures were made of molybdenum because of its high electrical conductivity, non-magnetic properties and low outgassing in vacuum. Where the electron beam passes very close to the surfaces, i.e. when passing through the apertures (diameter in thousandth of an inch) or hemispheres (discussed later in HRG), it is desired to improve the surface conductivity to reduce charge build-up. From experience, a thin layer of carbon soot on apertures and hemispheres was beneficial for this purpose.

For mounting the gun, an aluminum cradle was used along with ceramic rods. First the two ceramic rods were held on the cradle, and then the gun elements were stacked on it. In this way the gun elements were isolated from each other as well as from ground. The whole gun was enclosed by a grounded stainless steel casing so that the gun element potentials did not interfere with the scattering experiment.

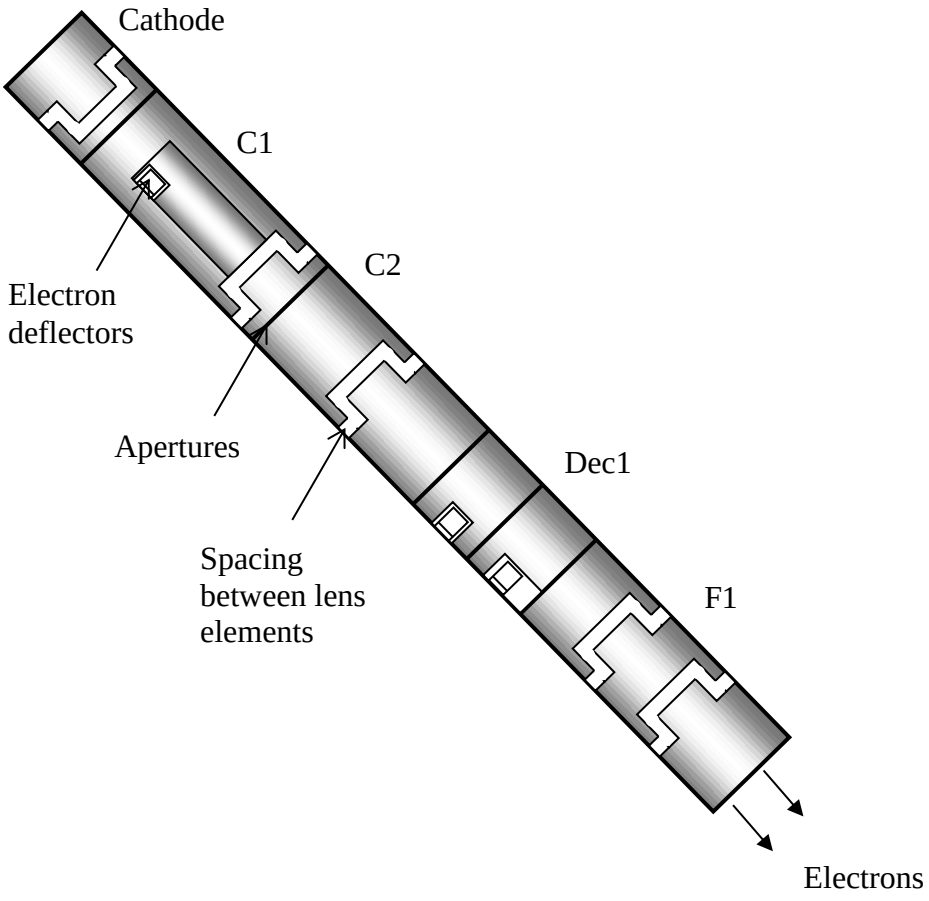

Figure 3.12: Schematic of the High Intensity Gun (HIG).

A current-regulated power supply[9] was used to heat the filament by direct current. The energy of the electron beam was determined by the cathode bias produced by a regulated DC power supply[10] in series with a programmable Digital to Analog Converter (DAC)[11] and an operational amplifier[12]. The DAC also allowed computer control of the impact energy for electron gun tuning and as well as control of the ramping energy in the gun and the electron detector. The lens potential power supply was previously constructed in the AMO laboratory and is discussed in detail by Johnson [Johnson1999]. Adjustable voltage regulators which could be varied by potentiometers, were used to establish the potentials on the gun lens elements. Also each element voltage could be selected by a rotary switch on the lens potential power supply and was measured by an auto ranging multi-meter[13]. The electron beam could be 'shut down' temporarily by applying a negative potential to the last element F1, to facilitate control and background measurements.

Preparation of the HIG

It was important not to have any type of oil residue or any impurity on the gun or detector elements which would greatly compromise its functionality under vacuum. For optimum performance, the HIG needed to be cleaned and reassembled prior to a measurement experiment. This included cleaning of each individual element of the electron gun, i.e. cylinders, apertures, tiny deflectors and insulators. The cleaning process consisted first of all of washing in soapy water and then immersion in an ultrasonic bath for 10-15 minutes.

[9] Lambda LA-200
[10] Kepco HB4AM
[11] Kepco SN500-122
[12] Kepco SN500-122
[13] Keithley-175

Next, the parts were washed with clean water and then immersed in acetone to remove water. Finally the elements were immersed in a solution of methanol and dried by hot air. After cleaning, the gun was reassembled. Great care had to be taken to ensure the correct spacing between the cylindrical lenses and avoid any unwanted electrical contact with other elements of the gun. After assembling the gun, electrical connections were made to individual lenses and deflectors. Finally, the gun was installed inside the vacuum chamber.

3.4.4 High Resolution Gun (HRG)

To improve energy resolution in the HRG, a hemispherical energy analyzer (monochromator) was added. The concentric hemispherical electrodes generate an electric field that deflects electrons along a circular path through its center. If the electron does not have the required energy, it will collide with the outer hemisphere if the energy is too high or with the inner hemisphere if too low. Thus, the overall intensity of the electron beam is reduced but the resolution is increased. A 180° spherical monochromator is used because of its compact geometry, directing the electron beam back through an exit channel parallel to the entrance channel.

Typically the HRG resolution is 100-150 meV at FWHM, at electron currents in the range 200-400 nA. The HRG was built in this AMO laboratory and is described in detail by [Johnson 1999]. The HRG consists of the electron entrance channel, the electron analyzer and the electron exit channel. The first element in the entrance channel as in the HIG is the filament Pierce element. After that there are three aperture lens elements which focus the electron beam onto the entrance of the electron analyzer

(monochromator). The selected electron energy beam then is focussed on the aperture of the exit channel. A general view of the HRG is depicted in Figure 3.13.

The monochromator consists of two hemispherical electrodes. The inner hemisphere has a radius of curvature (R_1) of 1.313", while the outer one has a radius (R_2) of 1.688". The center path of the electron beam through the monochromator has a radius (R_0) of 1.495".

The HRG lens elements were made of Oxygen-Free High Conductivity (OFHC) copper, as were the electrodes of the monochromator. The lens apertures and the Pierce element were constructed exactly the same as the HIG, of molybdenum and stainless steel, respectively. Also the lens stacks of the HRG were mounted in a similar way to the HIG on ceramic rods held in aluminum cradles. Both the entrance and exit lens stacks along with the monochromator were mounted on an aluminum plate. Ceramic spacers and washers were used for electrical isolation where needed. Two holes on the outer spheres of the monochromator, one each for entrance and exit lens stack, were used for the alignment between the stacks and the monochromator as well as with the interaction region. A coaxial heater[14] was fixed at the back of the outer sphere to reduce the effect of ambient metal vapour deposition on the spheres. Also the whole gun was enclosed in a grounded aluminum chassis so that the lens potential did not interfere with the scattering experiments.

The HRG power supply used the same kind of potential regulators as the HIG. The same power supplies for the cathode bias and as well as the filament power supply were used in both the guns. As in the HIG, the last lens element in the exit stack could be used as an electron beam shutter by switching off its power supply. The voltages on the

[14] ARI AerOrod BXX06B24-4T

spheres were supplied by ten-turn potentiometers on the HRG supply using a power supply[15].

Preparation of the HRG

The tasks for preparation and assembly of the HRG were similar to those of the HIG, but with more components including the cleaning, sooting and alignment of the monochromator. The monochromator had to be aligned with the electron beam entrance and exit stacks before installing the last component of the filament assembly in the entrance stack. After electrically connecting all the components, the gun was ready to be installed inside the vacuum chamber.

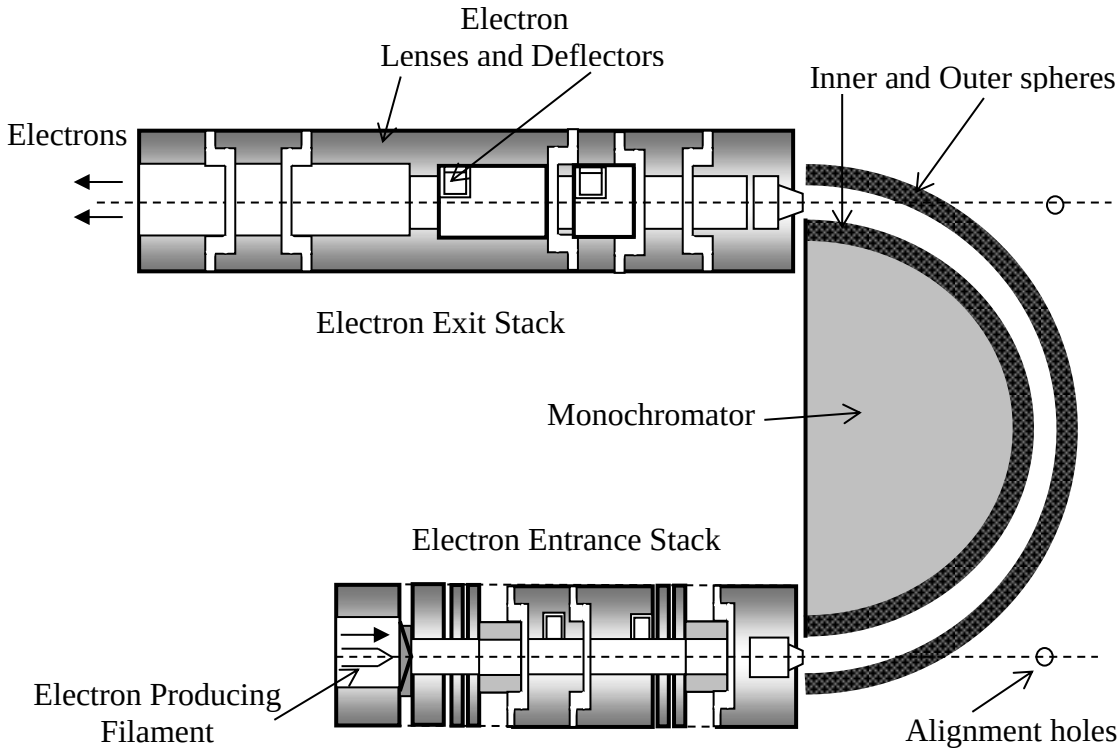

Figure 3.13: High Resolution Gun (HRG).

[15] Lambda LSC-A-02

3.5 Electron Detector

The electron detector was also built at the Jet Propulsion Laboratory in Pasadena, California. The function of the electron detector is 3-fold, to collect electrons at a certain electron scattering angle, to discriminate against electrons that are not of the desired energy and finally detect them and process them into a digital signal proportional to the rate of the electrons passing through the system. Individual scattered electrons are counted as data pulses for a pre-specified 'dwell time'.

The electron detector as shown in Figure 3.14 can be roughly visualized as a reversed HRG. It consists of a collection stack, an electron energy analyzer and an electron multiplier in the detection stack. The apertures in the nose cone of the detector and the first element in the collection stack limit the angle of view from the interaction region. The scattered electrons with a residual energy E_r which are within this view-cone enter the collection stack where they are accelerated/deaccelerated by the various lens potentials scanned with time such that,

$$E_r \rightarrow E_r + \Delta E_{lens}(t)$$

where, ΔE_{lens} is the 'boosted' energy provided by the accelerating potential V, such that $eV = \Delta E$. The monochromator 'pass energy' E_M is fixed by the hemispheres potentials. Thus only those scattered electrons pass through the monochromator and enter the detection stack which satisfy $E_r + \Delta E_{lens}(t) = E_M$. The electrons reaching the detection stack are finally accelerated to some nominal fixed kinetic energy to hit the channeltron detector at the end of the detection stack for optimum efficiency.

Two types of electron multiplier were used in the experiments. The function was the same for both of them. One of them was a channeltron electron multiplier[16] with continuous dynodes while the other was a Channel Electron Multiplier (CEM)[17] with discrete dynodes. In either electron multiplier, an incident electron generates a current pulse due to cascading emission of electrons in the presence of a strong DC bias field. The signal is extracted through an AC decoupler circuit.

As in the HRG, all lens elements of the detector system were made of OFHC copper, but the hemispherical surfaces of the monochromator were made of aluminum and were gold-plated. The apertures within the lens elements and the nose-cone were made of molybdenum and were carbon-sooted. The view-cone of the detector was approximately 6.3°. Both the collection and detection stacks, as in the electron guns, were mounted on ceramic rods held in aluminum cradles. Both cradles were then attached to the hemispheres with a brass mounting plate using Macor washers for electrical isolation. The inner and outer hemispheres have a radius of 2.250" and 2.750" respectively. The power supply for the detector was similar to that of the HRG which supplied the potential to the detector lens elements with respect to the analyzer common, which was biased with respect to ground. This arrangement is called the analyzer bias similar to the cathode bias as discussed earlier in Section 3.4 (refer to Figure 3.11).

Preparation of the Detector

The preparation and assembly of the electron detector was very similar to that of the HRG. The final stage was to install a channeltron, after the alignment of the monochromator with the electron collection and detection stacks.

[16] Galileo 4039 Channeltron
[17] ETP AF-14151 CEM

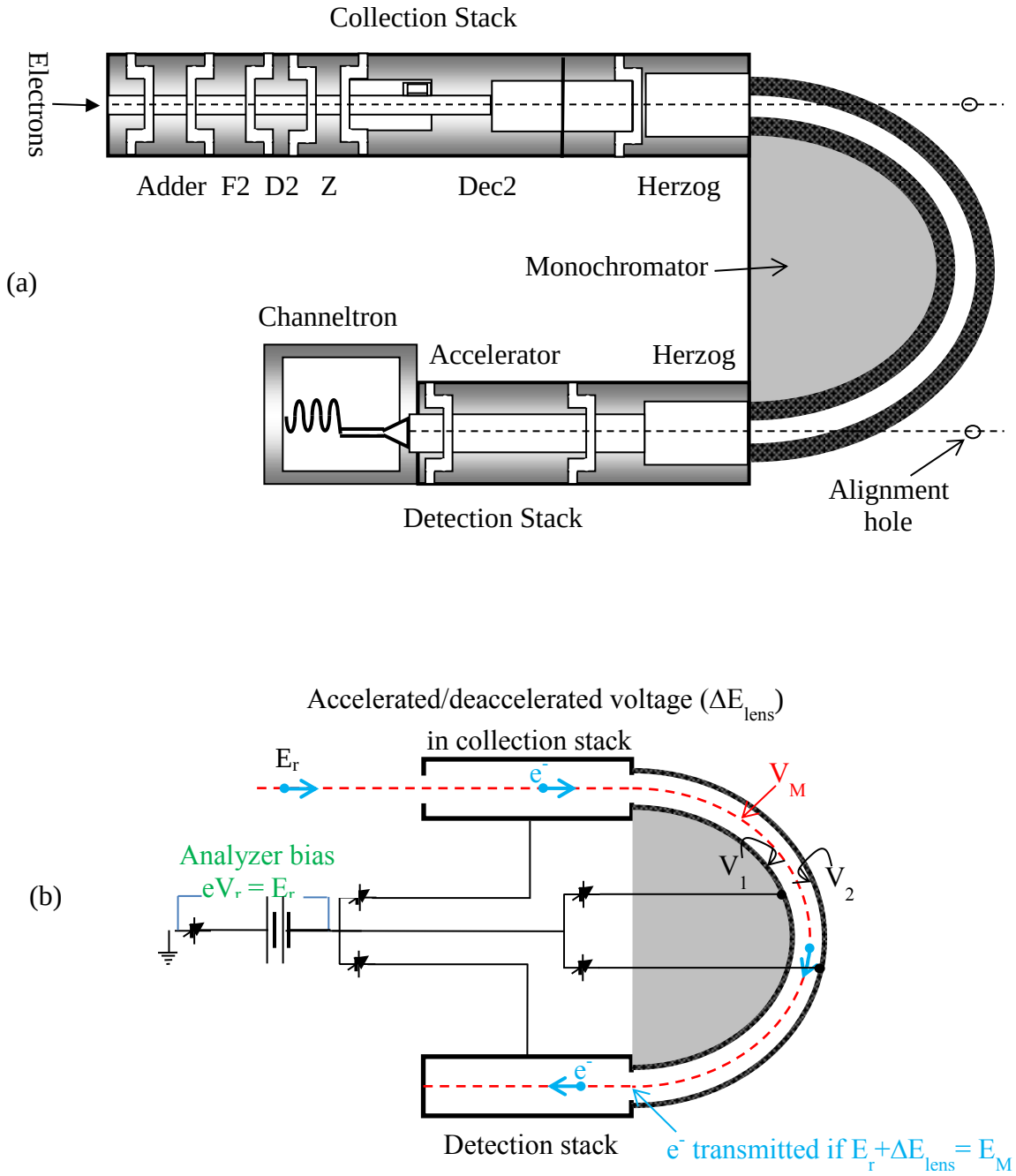

Figure 3.14: (a) Details of the electron detector. (b) working of the monochromator explained.

3.6 Working of the Electron Spectrometer

The apparatus described above produced an incident electron beam of energy (E_0) which intersected the target atomic beam, either in its ground state or in a laser-prepared target state. The scattered electrons with residual energy (E_r) from the target were collected and analysed by the electron detector to obtain the electron energy loss (ΔE) spectrum as discussed below. Referring to Figure 3.1, the impact energy E_0 and the energy loss ΔE are related by,

$$\Delta E = E_0 - E_r.$$

As stated earlier, the interaction region was at ground potential, and both the cathode and the analyzer potentials were biased with respect to the ground. To generate an electron energy loss spectrum (EELS), the analyzer bias was ramped, keeping the incident energy fixed. A sample EELS spectrum for barium is reproduced in Figure 3.15 with $\Delta E = 0$, showing the elastic peak and $\Delta E = 2.24$ eV ($^1S_0 \rightarrow {}^1P_1$ transition), the most prominent inelastic peak.

The impact energy of the electrons produced by the electron gun was determined by the absolute value of the negative bias applied to the filament with respect to the grounded interaction region. This cathode bias can be varied by the computer-controlled data acquisition system. With the DAC and the op-amps, the cathode and the analyzer biases could either be held constant or ramped continuously. With the cathode bias fixed and the analyzer bias ramped, an electron energy loss spectrum (EELS) can be obtained. The electron detector mounted on the turntable inside the vacuum chamber thus collected, analysed and counted the scattered electrons. This EELS was used for calibration

purposes or for the laser-excited target population determination. The excited atoms de-excite by emitting photons; photons of particular wavelength λ selected by the filtering system were then detected by the PMT situated outside the vacuum chamber.

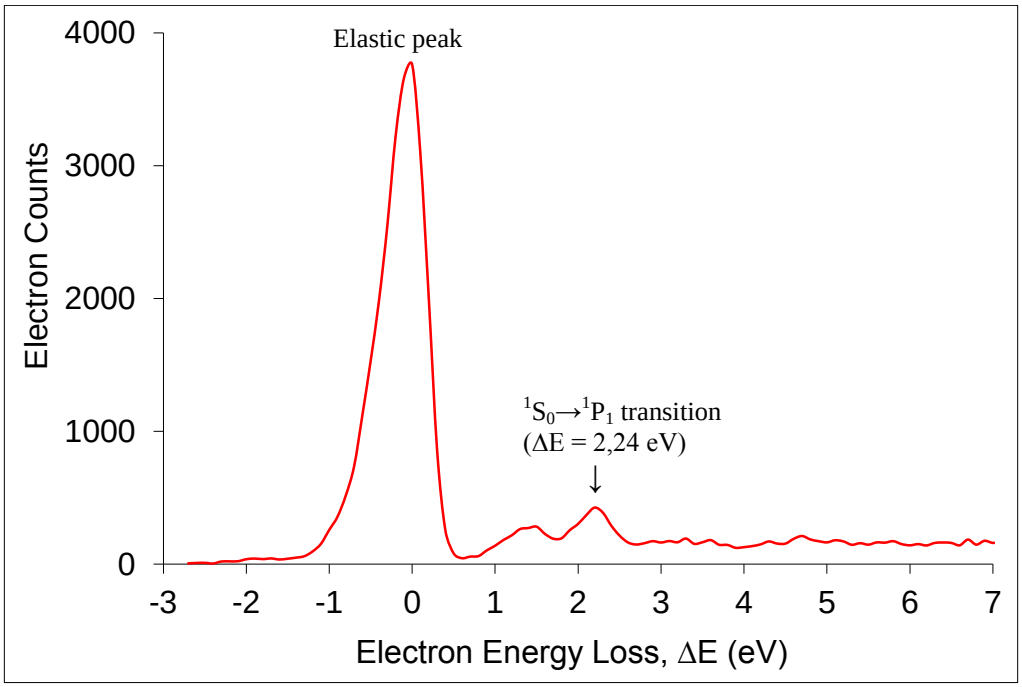

Figure 3.15: Sample EELS for Ba with 40 eV incident electron energy.

3.7 Photon Detection System

The line emission fluorescence from the interaction region was measured by a photomultiplier tube (PMT)[18] situated outside the vacuum chamber. To make sure that only the fluorescence of interest reached the PMT, a series of optical components were placed in between the interaction region and the PMT. The first optical element was a 7

[18] EMI 9658R

cm focal length lens mounted on stainless cylinder tube inside the vacuum chamber at approximately one focal length. It collected the light from the interaction region and directed it towards the PMT. A cylindrical tube along with two pin-hole apareture discs was used to align the PMT with the interaction region. Outside the vacuum chamber, between the viewport of the vacuum chamber and the PMT, there was a series of line transmission filters, so as to select the wavelength of interest and block the unwanted light from entering the PMT. This setup is shown in Figure 3.16.

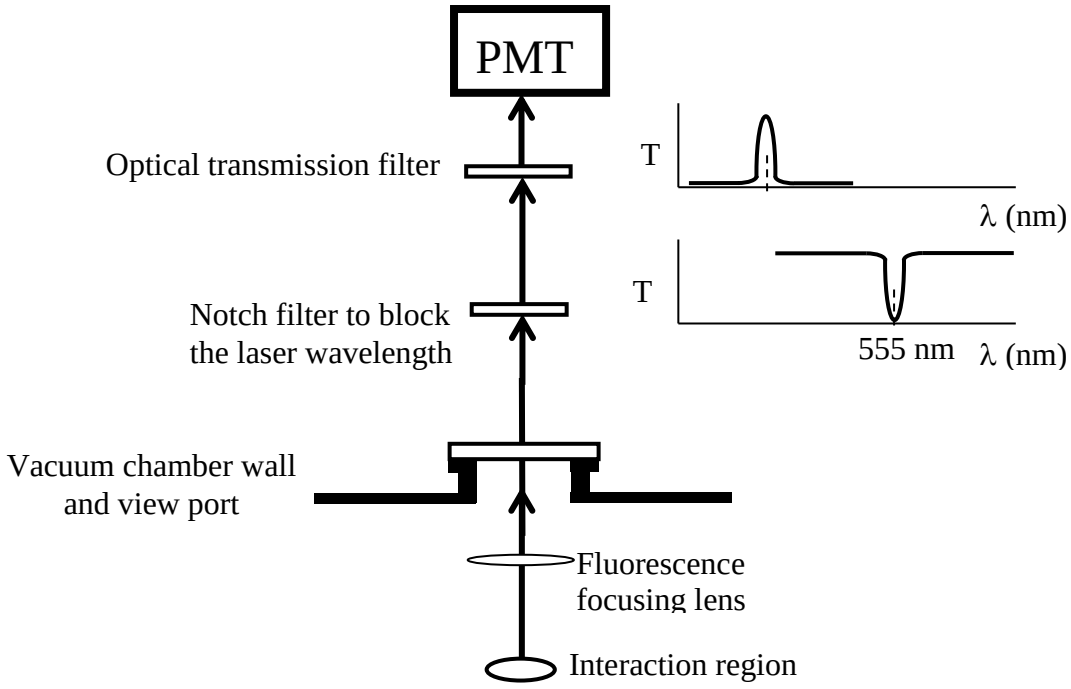

Figure 3.16: Optical fluorescence transport and detection system.

In the present work, linear polarization of the emitted photons was detected. This was achieved by a computer-controlled stepper motor system, consisting of a polarizer and a quarter-wave plate as shown in Figure 3.17. The function of the polarizer was to

identify the linear polarization of the emitted photons. The quarter-wave plate was used to convert this linear polarization into circular polarization. This latter step was taken on the advice of the PMT manufacturer to eliminate a small polarization dependence of the PMT efficiency.

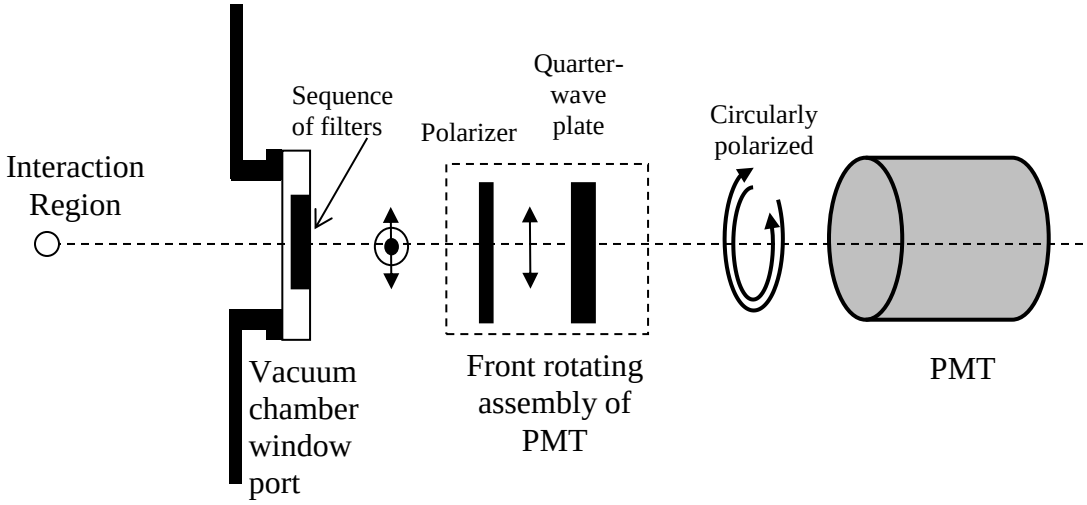

Figure 3.17: Polarizer and quarter-wave plate rotating assembly to convert the linear polarization to circular polarization before being measured by the PMT.

A sample fluorescence modulation spectrum is shown in Figure 3.18, obtained by continuously rotating the polarizer. Maxima and minima correspond to the polarizer aligned parallel and perpendicular to the polarization axis of the incident light. A detailed discussion of the analysis procedure to extract the fluorescence polarization from the modulation spectra is given in Chapter 4.

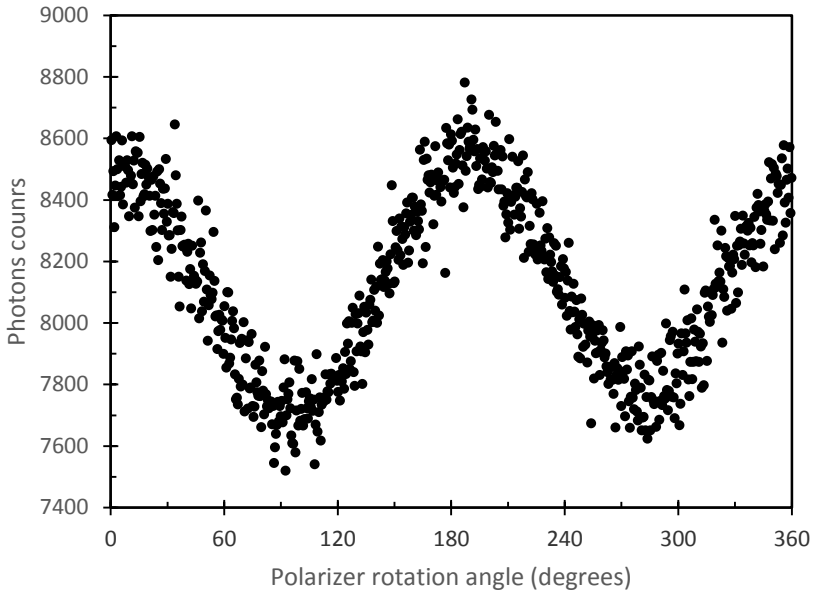

Figure 3.18: Sample fluorescence modulation spectrum for 583 nm barium at 40 eV incident electron energy obtained by continuously rotating the PMT polarizer.

3.8 The Vacuum Chamber

All atomic beam experiments were carried out inside a vacuum chamber. The vacuum chamber was made of a non-magnetic stainless steel bell-jar resting on a stainless steel base plate, making a dome of 27" in height and 36" in diameter. A groove at the bottom of the bell jar hold a Vitron O-ring which sealed the chamber when in contact with the base plate. Inside the vacuum chamber there was a turntable on which the detector was mounted. This turntable was used to select the scattering angle and could be rotated mechanically from outside the chamber. The vacuum chamber had in total eight view ports. These window ports were used for different purposes, such as to transport the laser

beam into the chamber, as a viewport for the detection of photons by a photomultiplier, and for visual inspection of the interior of the chamber. The electrical connections inside the chamber to the electron gun, electron detector, Faraday cup and the atomic oven assembly were provided by electrical feedthroughs. A gas-jet nozzle inside the chamber provided different gases for calibration purposes.

The vacuum inside the chamber was achieved by a two-step process. First a mechanical fore pump[19] was used to establish rough vacuum, lowering the pressure inside of the chamber to about 10^{-3} Torr. Then an oil diffusion pump[20] located at the bottom of the vacuum chamber took over the job of further evacuating the chamber. In all the experiments, the vacuum inside the chamber was below $5x10^{-7}$ Torr. The mechanical pump was also used to rough-pump the gas jet supply line. A ionization gauge tube[21] was mounted directly on the vacuum chamber, and the pressure of the system was monitored by a ionization gauge controller[22]. A schematic diagram of the vacuum system is shown in Figure 3.19.

A number of safety trips were incorporated in the vacuum system. The pressure trip point set on the ion gauge was $7x10^{-5}$ Torr. If the pressure increased above this safety trip point, the diffusion pump heater would shut off, and the ionization gauge and all the voltage supplies operating inside the chamber were automatically switched off. The other two safety trips related to floor water flooding and excessive diffusion pump heating. In both emergency cases, the main safety trip would be activated due to shut down of the supply of cold water or electrical supply to the diffusion heater.

[19] Varian SD-700
[20] Varian VHS-6
[21] Varian 0571-K2471-303
[22] Varian 843

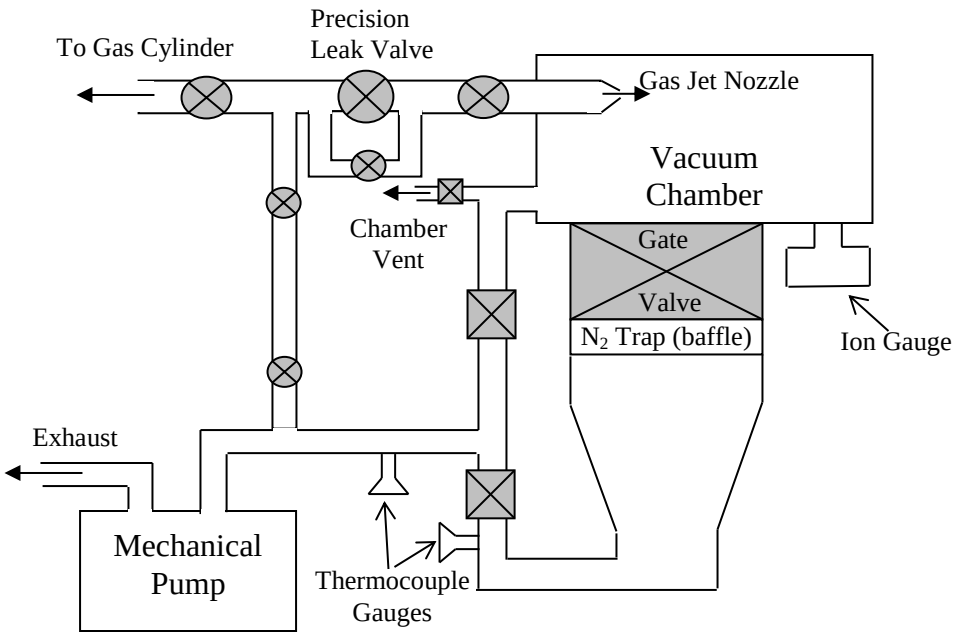

Figure 3.19: Schematic diagram of the vacuum system.

3.9 Experimental Assembly

After assembling and installing the electron gun, the electron detector and the atomic oven assembly inside the vacuum chamber, each of them were aligned to the interaction region with a two-pin platform. In the two-pin platform, one metallic pin was centered at the interaction region while the other pin was on the edge of the platform, approximately 10 cm from the interaction region. The alignment was done by shining torch light beam from the back of the electron gun along the electron beam axis onto the interaction region, and the two pin shadows were aligned. The same procedure was

repeated with the alignment of the electron detector and the atomic oven assembly. Once all alignments were made, the gun, the detector and the atomic oven were connected to the electronics for data acquisition. The whole scattering apparatus was enclosed within a mu-metal cylinder inside the vacuum chamber which was degaussed by applying a varying high AC voltage across the μ-metal shield and the ground. Finally the bell-jar was lowered on the μ-metal shield cylinder and the evacuation process started.

3.10 Data Acquisition System

The data acquisition system controlled the motors in the optical systems, recorded and processed the signals from all components, and ran the control programs for the two ramp generators of the spectrometer, the electron gun and the electron detector as shown in Figure 3.20.

The Stamp Data Acquisition System (SDAQ) replaced the older MCS-based data acquisition system in the University of Manitoba AMO laboratory. The system is based on microcontrollers[23] and other electronics. It communicates using a RS232 or a USB connection and interfaces easily with all the components like stepper motors, shutters and the DAC[24]. The microcontrollers work with other electronics to perform the required tasks of the data acquisition, dwell time generation, device manipulation and communication. This system is described in detail by Hein [Hein2010].

Two signals come from the measurement apparatus, one from the electron detector and the other from the PMT. The electron detection by the channeltron/CEM

[23] Parallax BS2P40 BASIC
[24] Kepco SN 500-122

was turned into a measurable current pulse by a cascading effect of secondary electrons within the channeltron/CEM. The high voltage to the channeltron was supplied by an Ortec 446 high voltage power supply through a high voltage vacuum feedthrough. An AC filter circuit was connected to the output of the channeltron to isolate any AC component of the high voltage from the detector signal. The sharp negative pulses leaving the filter were fed into a pre-amplifier[25] and then to an amplifier[26]. These amplified signals were passed into a timing single channel analyzer SCA[27] which shaped the pulses and also acted as a discriminator. After the SCA, the signal was split. One was sent through a gate in the interface NIM module to the SDAQ for data collection and the other was sent to an Ortec 441 ratemeter for visual monitoring. In a similar fashion, using another set of NIM modules, the photon signal from the PMT passed to the SDAQ for data collection and to a separate ratemeter.

[25] Ortec 113
[26] Ortec 572
[27] Ortec 551

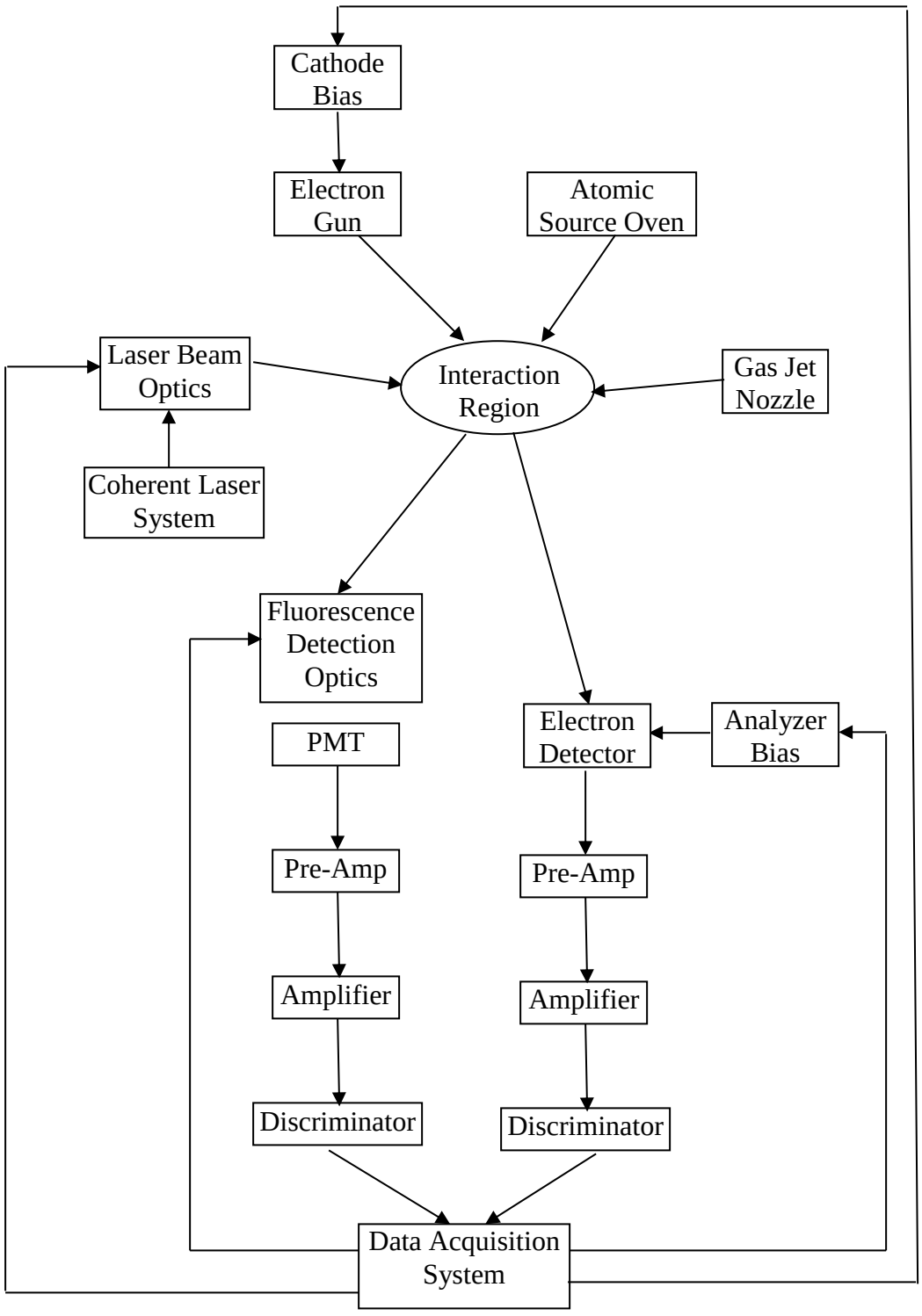

Figure 3.20: Block diagram of the University of Manitoba AMO apparatus and data acquisition system.

Chapter 4

Characterization of the 583 nm Transition due to Electron Impact Excitation of the Barium Ground State

4.1 Introduction

In this chapter, a particular radiative transition between low lying states of barium was studied, excited by electron impact on ground state barium atoms. The experimental strategy of combining EELS and direct observation of decay fluorescence for the 583 nm $(6s7p)^1P_1 \rightarrow (6s5d)^1D_2$ transition, normalized to a known transition of 554 nm, was attempted to estimate the line emission cross section for 583 nm. Further corrections for cascading from the upper levels to the $^1P_1$ excited state, based on recent theoretical calculations, and a branching ratio correction for decays of the $^1P_1$ to other lower states were made to arrive at an estimate for the electron impact excitation cross section: σ_{ex}. The experimental technique is described, and results are compared with previous measurements and with theory for σ_{ex}.

4.1.1 Optical excitation function

The energy dependence of the cross section is referred to as the optical excitation function, which is essentially an unnormalized cross section. Calculations for the ground state excitation of helium, the simplest two-valence-electron atom, are shown in Figure 4.1.

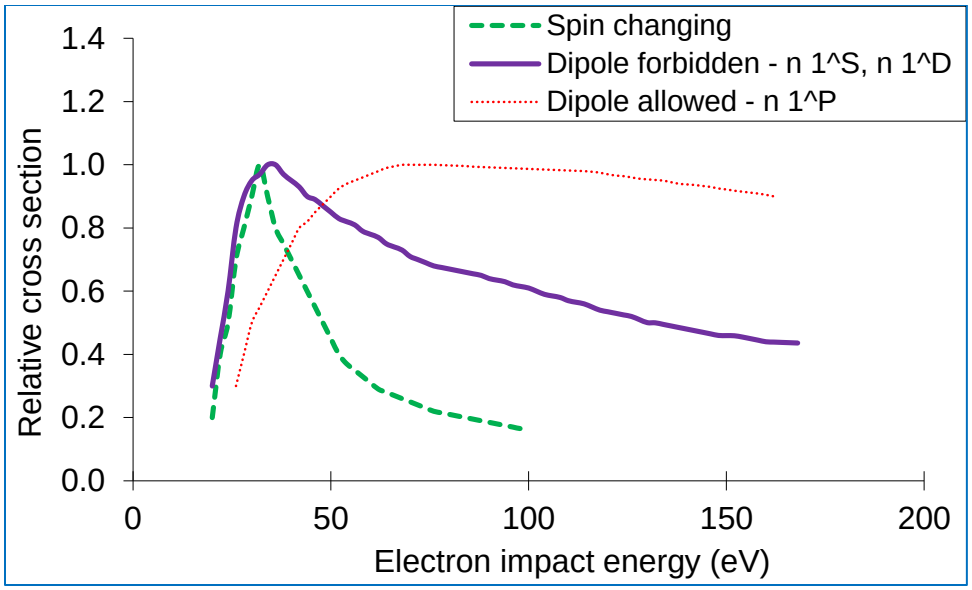

Figure 4.1: Optical excitation function for various transitions from the ground state of helium [Lin1991].

For optically allowed transitions, the cross section rises relatively slowly from threshold energy to a broad maximum at approximately five times the threshold energy. At higher energies, the cross section is more usually expressed as a function of $\frac{ln(E)}{E}$. In an electron exchange process where there is excitation from a singlet ground state to a triplet state, the cross section peaks sharply close to the threshold electron energy and then falls off at high energies as a function of $\frac{1}{E^3}$. If the excitation is spin allowed but optically forbidden, then at higher energies Bethe theory predicts a $\frac{1}{E}$ dependence of the cross section [Drake2006].

For dipole allowed transitions in helium, the largest cross section for electron excitation out of the ground 1^1S state comes from excitation into n^1P levels with the maximum n^1P levels cross section at energy a few times the threshold energy. The cross section for n^1P levels decreases slowly after reaching a maximum as the energy increases.

For the dipole forbidden transitions, the cross sections of n^1S and n^1D from the ground state are not as large as for n^1P levels, and decrease more rapidly at higher energies above their peak values compared to n^1P. For spin-flip transitions, smaller excitation cross sections out of the ground state into triplet levels are found compared to spin conserving electron excitations. The spin-flip cross section peaks at slightly above threshold energy unlike the n^1P cross section, and decreases more rapidly from the peak as energy increases.

4.1.2 Polarization of Emitted Radiation

Along with the study of the optical excitation functions for an electron-impact atomic excitation, the polarization associated with the radiative decay can also be studied. By convention, the polarization of light is described by specifying the orientation of the electric field at a point in space over one period of the oscillation. When light travels in free space, it propagates as a transverse wave i.e. the polarization is perpendicular to its direction of travel. In this case, the electric field may be oriented in a constant direction (linear polarization), or it may rotate about the propagation axis (circular or elliptical polarization).

Experimentally, polarization of the emitted light can be measured as a function of electron impact energy to yield a polarization function for that particular transition. When an atom is excited by a collision with an electron beam, the electron beam axis is the polarization reference axis for the subsequent radiative decay. The polarization of radiation excited by a monoenergetic beam of electrons is defined as,

$$P = \frac{(I_{\parallel} - I_{\perp})}{(I_{\parallel} + I_{\perp})} \tag{4.1}$$

where $I_{\parallel}$ and $I_{\perp}$ are the radiation intensities with electric field vectors parallel and perpendicular to the electron beam axis respectively, as shown in Figure 4.2. The total radiation intensity emitted by the atom is $(I_{\parallel} + 2I_{\perp})$.

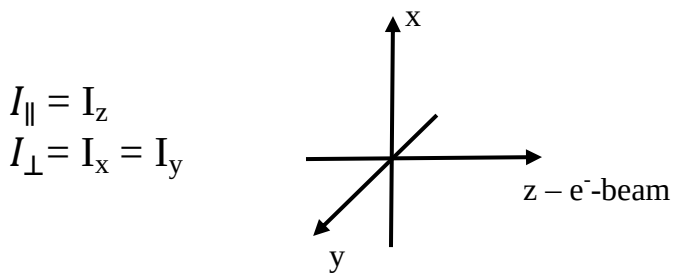

Figure 4.2: Radiation intensities with electric field vectors parallel and perpendicular to the electron beam axis.

Qualitatively, the phenomenon of polarization of the atomic radiation due to electron impact can be explained by considering the simplest conceivable case of a spinless hydrogen atom in its 1s ground state being struck by a spinless electron [Lamb1957]. When an incoming electron has just sufficient threshold energy, either the atomic 1s electron is excited, called a direct excitation, or the incoming electron is excited, called an exchange excitation, to the 2p state. Here the direct excitation process is considered. The incoming electron, with a linear momentum along the electron beam axis and having exactly the threshold energy, stops after exciting the atom to the 2p state.

This incident electron imparts a certain angular momentum with respect to the centre of the atom, perpendicular to its axis of motion. In other words, there is no angular momentum parallel to the electron beam axis. This situation corresponds to the excited 2p state with only m=0 substates. When the atom deexcites to the 1s ground state (with only m=0), the change in the magnetic quantum number is zero. Thus the only polarization would be in the direction parallel to the electron beam. This indicates that at threshold, the polarization is large ~100% and is positive i.e. the electric field is aligned along the electron beam axis. Now as the incident electron energy increases, the scattered electron does not stop but moves along after exciting the atom and also carries off some of the angular momentum. This implies that the angular momentum along the electron beam axis starts to increase indicating the increase in the population of the m=±1 magnetic quantum substates of the excited level. This in turn decreases polarization from ~100% polarization along the electron beam axis (m=0) to some polarization perpendicular to the electron beam (m=±1). As the incident electron energy is increased further, the percentage polarization keeps on decreasing, reaches zero, and becomes negative when more and more energetic electrons preferentially populate m=±1 magnetic quantum substates. A sample polarization function graph for a helium P-S transition is shown in Figure 4.3.

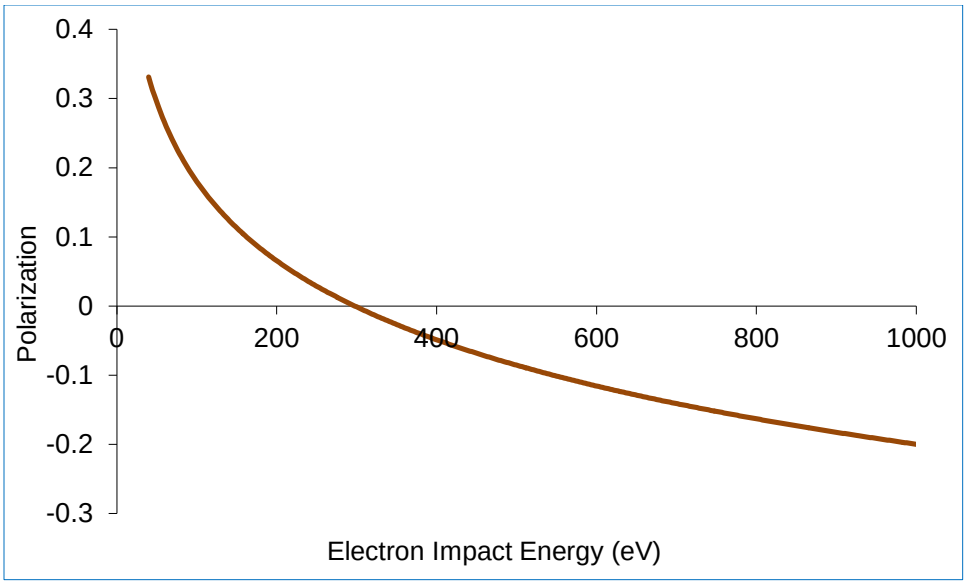

Figure 4.3: Sample helium polarization function for a 501.6 nm ($3^1P \rightarrow 2^1S$) transition [Raan1971].

Theoretical expressions for the polarization of fluorescence emitted due to de-excitation of the excited state by electron impact are given by Percival and Seaton [Percival1958]. Theoretically the maximum of the polarization should be at the threshold energy as discussed above, but experimentally the maximum is found a few electron-volts above threshold. This shifted behaviour of the polarization was first observed in mercury. This is due to the fact that at the threshold energy and below, the low energy incident electrons, lingering in the vicinity of the atom, temporarily combine with the excited state electrons making the atom temporarily negatively charged. This coupling and decoupling of electrons, mixes the states of m=0,±1, resulting in the reduced polarization at lower than threshold energies [Schultz1973].

4.1.3 Context of the Present Study

Barium, being a complex two valence-electron target, provides a natural extension to the extensive helium electron scattering studies in the literature, as described in Chapter 1. The atomic target barium, with atomic number Z=56 and electronic configuration ([Kr] $4d^{10}$ $5s^2$ $5p^6$) $6s^2$ $^1S_0$ belongs to the alkaline group. A barium energy level diagram showing relevant energy levels along with electron ground state excitation and subsequent radiative decay is depicted in Figure 4.4.

The experiment reported here was carried out for two scattering channels from the ground state electron excitation to the 2.24 eV state and to the 3.54 eV state. The dominant mixed-state configurations for the relevant states as calculated in the CCC model [Fursa1999] are given in Table 4.1 with the atomic states labelled by the major configuration for a certain energy level in the last column (by which they will now be referred). Note that the ground state is about 89% of ($6s^2$ $^1S_0$); the 2.24 eV state is 64% of (6s6p $^1P_1$), the 3.54 eV state is 47% of (6s7p $^1P_1$) and the 1.41 eV state is 80% of (6s5d $^1D_2$) state in this model[28].

[28] Here it refer to probability densities, which reflect the square of the dominant configurations in Table 4.1.

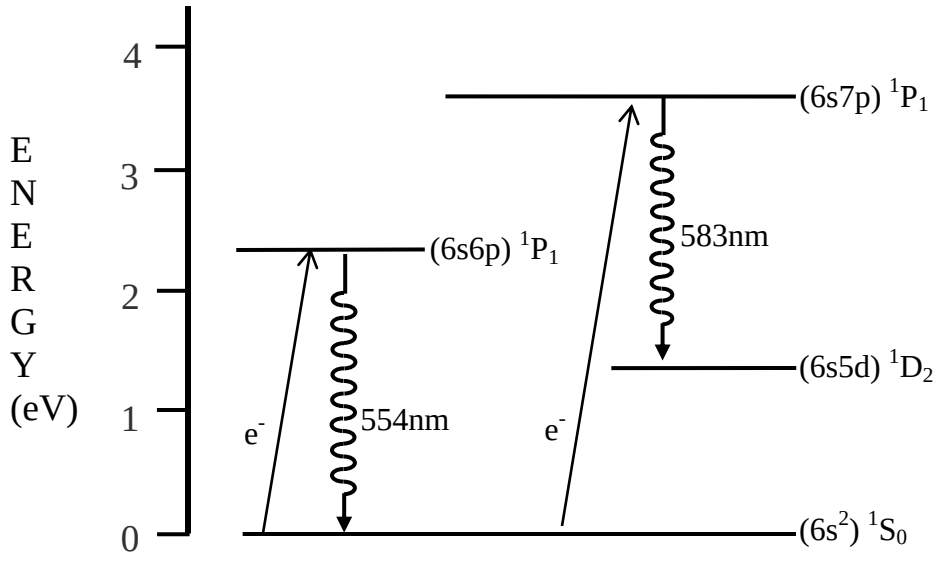

Figure 4.4: Relevant barium energy levels and fluorescence deexcitations.

Table 4.1: Barium mixed-states configuration given by CCC model [Fursa1999].

Atomic state energy (eV)	Dominant mixed-state configurations	State label
0.00	$0.944(6s^2\ ^1S) + 0.228(6p^2\ ^1S) - 0.191(6s7s\ ^1S)$	$6s^2\ ^1S_0$
1.41	$0.896(5d6s\ ^1D) - 0.226(5d7s\ ^1D) - 0.226(5d^2\ ^1D)$	$6s5d\ ^1D_2$
2.24	$0.800(6s6p\ ^1P) - 0.504(5d6p\ ^1P) - 0.256(7p6s\ ^1P)$	$6s6p\ ^1P_1$
3.54	$0.688(6s7p\ ^1P) - 0.550(5d6p\ ^1P) + 0.331(5d7p\ ^1P)$	$6s7p\ ^1P_1$

4.1.4 Experimental Considerations

Because the 554 nm line emission from excitation of the 2.24 eV state has been well studied, previous results can be used for absolute normalization along with the measurements of both 554 nm and 583 nm emission excited by electron beam impact in the present work. The ground state barium atomic beam ($\leq$ 0.8% strontium impurity) was prepared as described in Chapter 3. The atomic beam was subjected to an electron beam at 20, 30, 40 and 50 eV. The subsequent optical radiation intensities and their polarizations, resulting from the spontaneous radiative transitions of 554 nm and 583 nm by deexcitation to lower levels, were measured.

Measurements of the line emission from atomic states are challenging due to the fact that the interaction rates are low, and the photon detector intercepts only a small fraction of photons produced. A few experiments have been previously performed to measure emission cross sections in helium [VanZyl1980] and in hydrogen [Williams1975, 1976, 1988]. The Optical emission spectrum due to bombardment of barium atoms by monoenergetic 30 eV electrons was reported by [Aleksakhin1975, Smirnov2003].

4.1.5 Cross Sections Explained

In an electron-atom collision study, a number of processes take place simultaneously. Experimentally, a window is set with the help of detectors and filters to measure a certain process. Other processes which are not directly measured but which effect the interpretation of the data must be taken into consideration. There are three types of cross

sections studied in this thesis which are depicted in Figure 4.5 and are subsequently explained. These are:

- The *line emission cross section* σ_{em}; apart from normalization factors, this is the directly experimentally measured quantity, deduced from the fluorescence yield at a particular wavelength.
- The *Apparent level excitation cross section* σ_{ap}; this is deduced from σ_{em}, taking into consideration the branching factor for decays to other final states.
- The *Electron impact level excitation cross section* σ_{ex}; this is deduced from σ_{ap} after correcting for cascade feeding from higher states.

In the three experiments studied in this thesis, the electron beam excites the target atom, and the subsequent fluorescence line emitted due to deexcitation of the atomic level is measured. This fluorescence line intensity is proportional to the line emission cross section σ_{em}. When the excited atomic state decays, it can deexcite to more than one lower state. The relative probability of decay to a particular final state is referred to as the branching ratio for that transition. This branching ratio factor (more in Section 4.6.3) has to be taken into consideration to determine the apparent cross section σ_{ap}. Also, decays from higher excited states can feed the upper level of the transition of interest; an amount referred to as the cascading correction (more in Section 4.6.5), has to be subtracted from σ_{ap} to obtain the level excitation cross section σ_{ex}. The ultimate goal in the atomic collision studies is to determine the latter cross section, σ_{ex}.

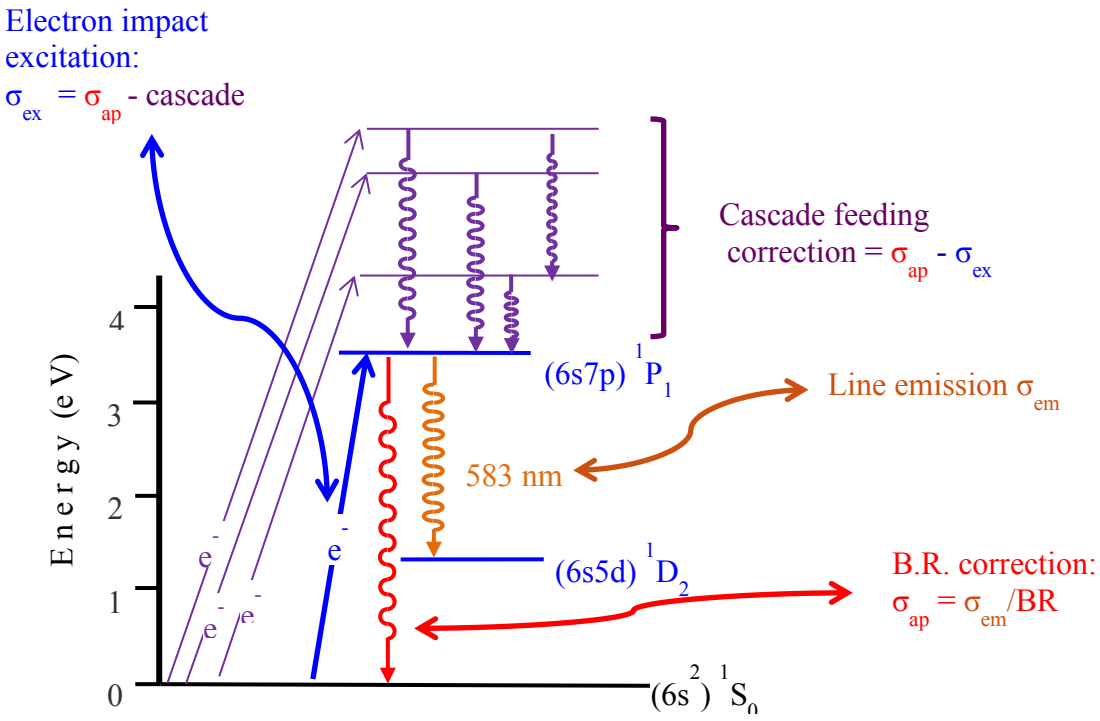

Figure 4.5: Three types of cross sections shown; σ_{em} , σ_{ap} and σ_{ex} along with the two types of corrections; branching ratio and cascading for the $^1P_1$ state and the 583 nm line transition in Ba.

4.2 Experimental Setup and Procedure

The preparation for electron-atom collision experiments is described in detail in Chapter 3. A general schematic for the current experiment is shown in Figure 4.6. Note that the fluorescence measurement system was aligned at θ=45° to the incoming electron beam.

The initial check of the system to determine whether it was working properly was to tune the electron beam on the Faraday cup downstream of the interaction region. Typically, the high intensity gun, with a newly cleaned system, produced around 1.5 μA current. Helium was brought through the gas-jet nozzle to the interaction region for energy calibration with the well-known inelastic peaks of helium. This procedure also

checked the performance of the electron detector. Finally the barium oven out-gassing was done by switching on the oven heater and very gradually increasing the heater current, typically in steps of 0.25 A over a period of 30 – 40 minutes. While out-gassing, it was crucial to monitor the pressure of the vacuum chamber. Generally out-gassing was done over 2–3 days depending upon the variation of pressure inside the chamber. Once the pressure inside the vacuum chamber stabilized around or below 10^{-6} Torr, the whole system was ready for the experiment.

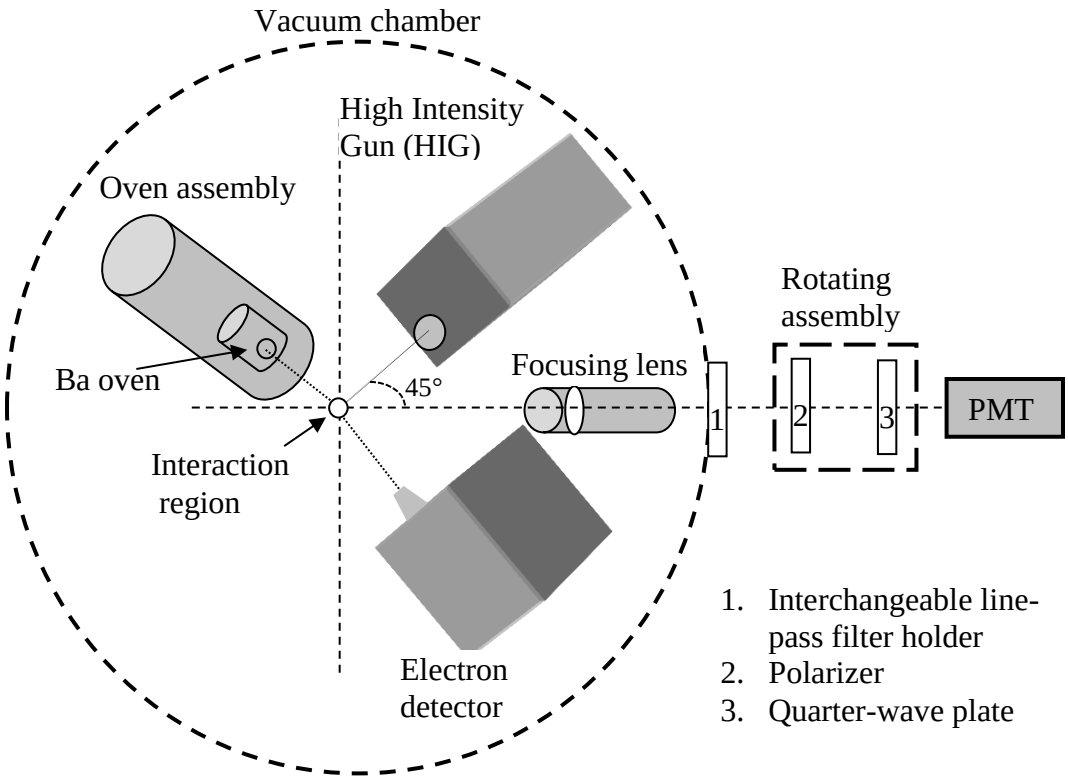

Figure 4.6: Experimental setup.

With the atomic beam and the electron beam colliding at the center of the vacuum chamber, fluorescence measurements could then be undertaken. The first observation with the nominal PMT high voltage setting for the 554 nm fluorescence was an unexpectedly high background counting rate. This problem was also present, but less significant, at 583 nm. As a precaution, the PMT high voltage (HV) was reduced for the 554 nm measurements which decreased the counting rate. Unfortunately, this procedure introduced a rate-dependent calibration factor which is not well understood. The systematic error associated with the PMT HV adjustment is discussed in detail in Section 4.8.

The procedure then used was to set the electron beam energy and acquire simultaneous EELS and fluorescence data, alternating between the 554 nm and 583 nm settings for the line pass filter and the PMT HV. The MCS based data acquisition system was used to collect the electron and fluorescence signals simultaneously. The PMT polarizer was rotated through a full 360° in 720 steps (channels) of the stepper motor to acquire fluorescence data for the specific line transition (554 nm or 583 nm). Simultaneously, the electron signal was acquired to generate the EELS spectrum of barium, first with the electron gun ON and then repeated with the gun OFF for the background data. Data were acquired for 200 ms for each stepper motor channel thus giving a total run-time of around 5 minutes for each pass through the polarizer cycle. To acquire good statistics for all electron impact energies studied, 100 – 200 passes were acquired for the 554 nm and 583 nm fluorescence signals separately. The length (in passes through the PMT polarizer rotation cycles) of each data run was varied according

to the experimental conditions; accumulated MCS spectra were saved at the end of each data run.

The fluorescence signal data for the 554 nm and 583 nm line transitions in barium were taken for four electron impact energies from 20 – 50 eV, in steps of 10 eV. In all fluorescence data, there was significant background rate. This was attributed to the glow from the electron gun filament and the barium oven heater, which presumably through many metallic reflections entered the PMT.

4.3 Fluorescence Data

The rotation of the polarizer in front of the PMT gives a modulation of the detected intensity that depends upon the polarization of the incident light. This follows the well-known Malus law: for a perfect polarizer with incident intensity I_0 polarized at an angle ϕ to the axis of the polarizer, the transmitted intensity is given by,

$$I=I_0 \cos^2 \phi. \qquad (4.2)$$

A rotating polarizer with light incident along the z-axis (perpendicular to the page) and polarizer transmission axis at angle $\phi=\omega t$ to the x-axis is shown in Figure 4.7(a). The fluorescence of interest has intensity components I_x and I_y polarized in the x and y directions respectively. From above Equation (4.2) the transmitted intensity can be written as,

$$I(\phi)=I_x \cos^2 \phi + I_y \sin^2 \phi \qquad (4.3)$$

Note that if $I_x = I_y$, the fluorescence is unpolarized and the detected intensity is independent of ϕ. For $\phi=0$, $I=I_x$ and for $\phi=\pi/2$, $I=I_y$, giving an oscillating pattern e.g. as depicted in Figure 4.7(b) (with $I_x>I_y$ in this figure).

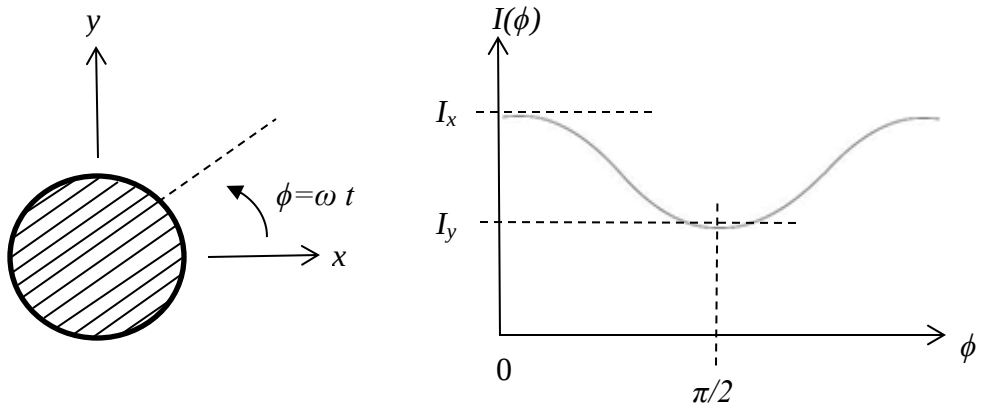

Figure 4.7: (a) A rotating polarizer with its transmission axis at an angle ϕ. (b) Oscillating pattern of PMT output downstream from a rotating polarizer with $I_x > I_y$.

The measured polarization is given as,

$$P_{meas} = \frac{(I_x - I_y)}{(I_x + I_y)}. \tag{4.4}$$

To determine this from the intensity pattern, note that the latter can be rewritten as,

$$I(\phi) = \tfrac{1}{2}(I_x + I_y) + \tfrac{1}{2}(I_x - I_y)\cos(2\phi) \tag{4.5}$$

$$= a + b\cos(2\phi),$$

where the first term corresponds to the average intensity and the second describes the oscillating pattern. The measured polarization is then given by the ratio b/a and the total intensity by $2a$. Allowing for an arbitrary angle offset, and expressing the angle in DAQ channel numbers, equivalent information can be extracted from a sine fit of the form,

$$I(x) = y_0 + A\sin(\pi(x - x_c)/w). \tag{4.6}$$

Figure 4.8 shows the parameters of the fitted equation. Note that the intensity maxima occur when the polarizer pass axis is in the horizontal plane for this experimental setup. Physically, $2y_0$ is the total intensity and A/y_0 is the polarization measured at this fluorescence detection angle (45°).

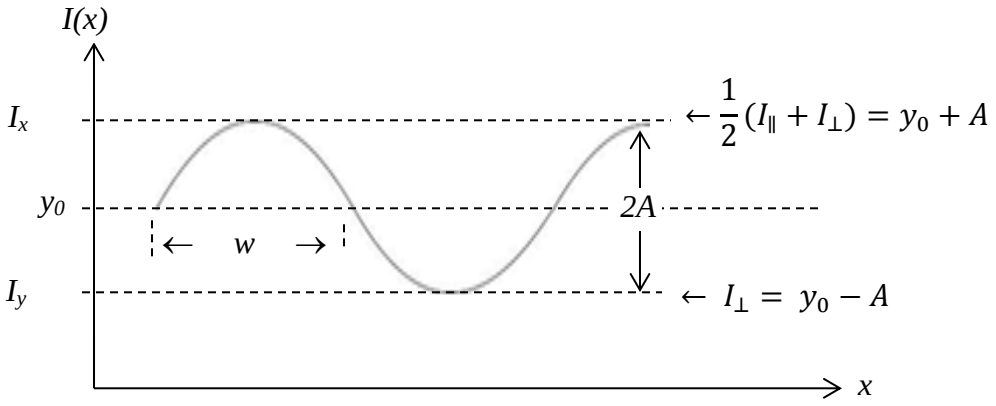

Figure 4.8: Sine wave pattern showing the fitted parameters of Equation (4.6).

Conventionally, the photons are measured at a right angle to the electron beam axis as shown in Figure 4.9. With the PMT at θ=45° to the electron beam axis[29], the intensity maxima and minima of Figure 4.7 correspond to,

$$I_x = \frac{1}{2}(I_\parallel + I_\perp)$$

$$I_y = I_\perp,$$

Therefore, the total intensity in terms of the fundamental intensities defined in Figure 4.2 is deduced in terms of the fitted parameters as,

$$I = (I_\parallel + 2I_\perp) = 3y_0 + A, \qquad (4.7)$$

[29] Chapter5; Equation (5.4)

and the polarization is,

$$P_{meas} = \frac{(I_{\parallel} - I_{\perp})}{(I_{\parallel} + I_{\perp})} = \frac{2A}{(y_0 + A)}\,. \qquad (4.8)$$

As an example, the fitted fluorescence signals for the 554 nm line transition for 50 eV are shown in Figure 4.10. Data have been accumulated for 15 full passes of the polarizer rotation cycle. Each channel represents; 15 x 200 ms = 3 s of data taking. Thus the counting rates are about 2.5 kHz. The vertical scale has a suppressed zero; the polarizations are clearly quite small. The gun ON and gun OFF fluorescence rates are almost identical, illustrating the very large background problems encountered for the photon signals. Notice also that the background data exhibit comparable polarization to the electron gun ON data. These features illustrate the challenges associated with extracting the true signal parameters (intensity and polarization) from the measured photon data.

To verify that the choice of statistical error bars $\sqrt{N}$ was appropriate, the residuals are plotted in Figure 4.11 for the weighted fit to the data of Figure 4.10(a) . The residuals follow a Gaussian distribution with a width consistent with the assumed statistical errors on the data points. A similar fit to the 583 nm fluorescence data is shown in Figure 4.12. The fitted parameters of Figure 4.10 and Figure 4.12 are summarized in Table 4.2. Note the much larger data acquisition time for 583 nm to obtain a comparable number of photon counts; the 583 nm rate is only ~1/10 of the 554 nm rate.

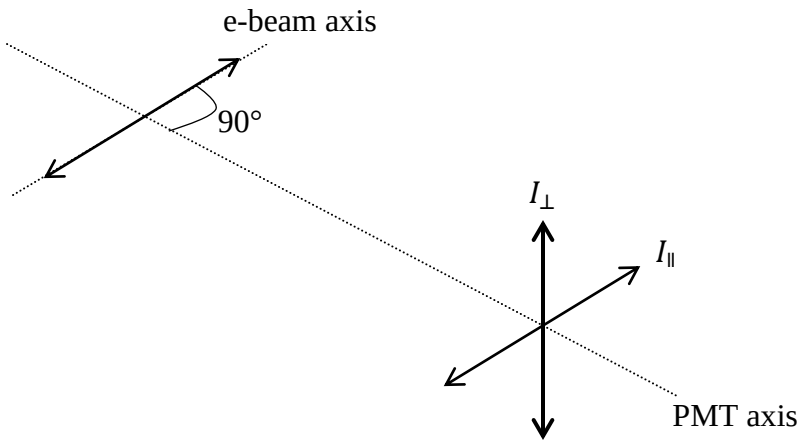

Figure 4.9: conventional setup with the PMT at 90° to the electron beam axis showing the fluorescence polarization geometries.

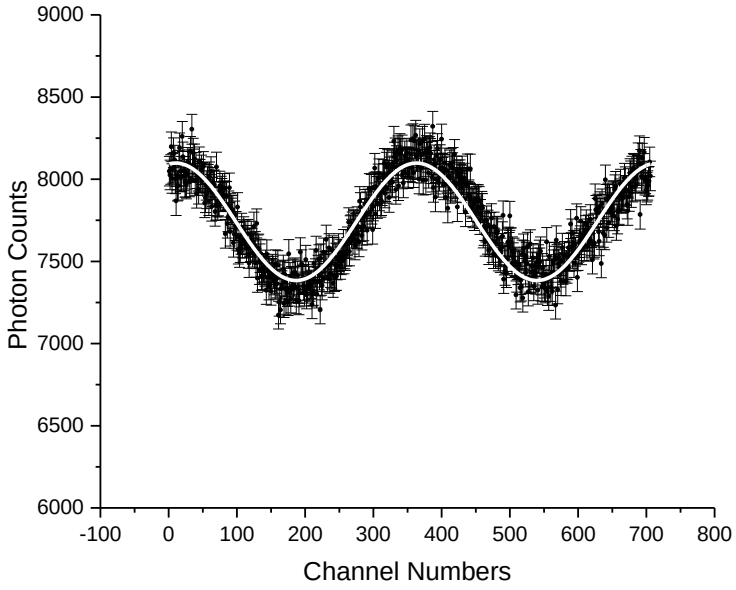

(a)

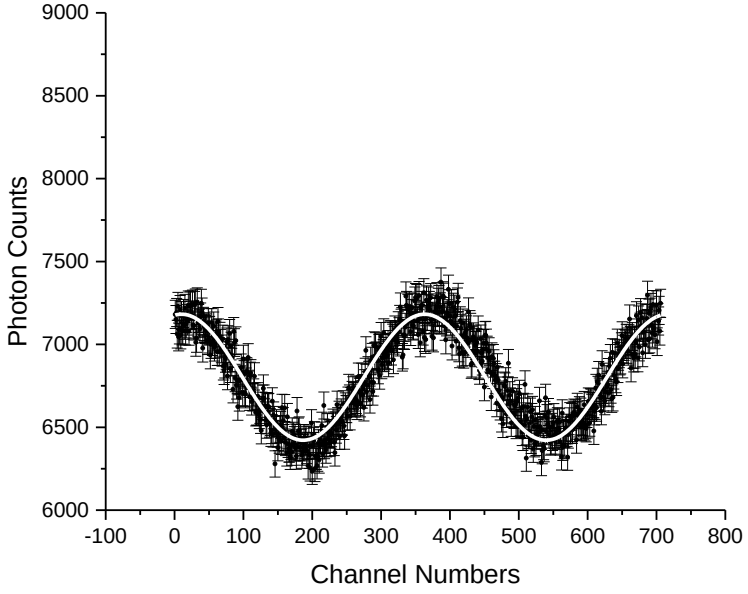

(b)

Figure 4.10: Fitted experimental fluorescence data for 554 nm accumulated for 15 passes at 50 eV electron energy with electron gun (a) ON and (b) OFF.

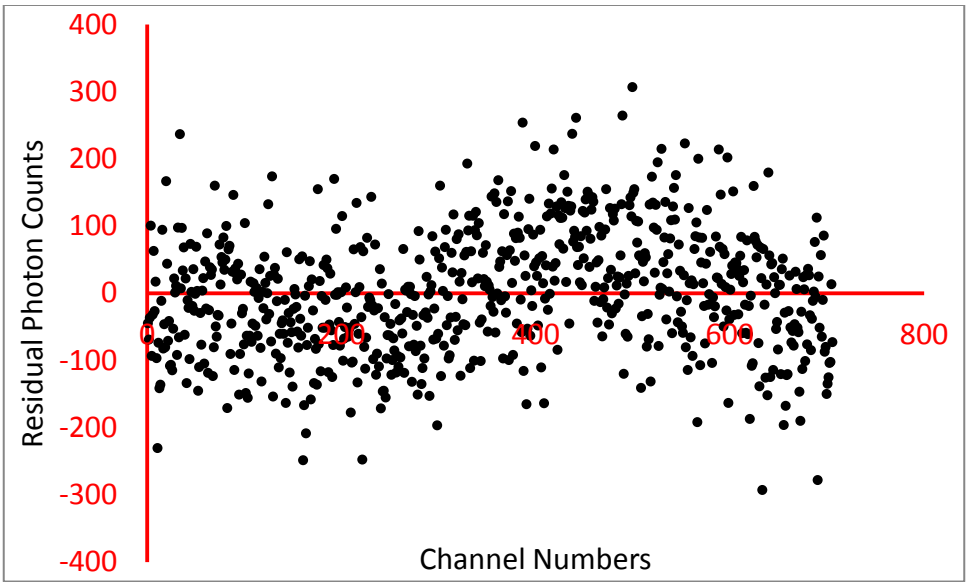

(a)

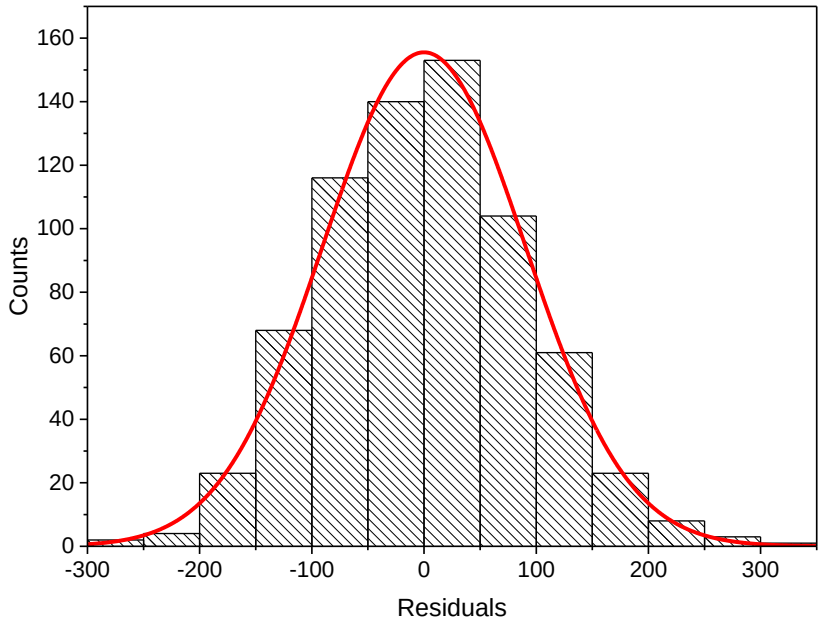

(b)

Figure 4.11: (a) Residual data set and (b) Gaussian fit to residuals histogram, for the same data set as in Figure 4.10(a).

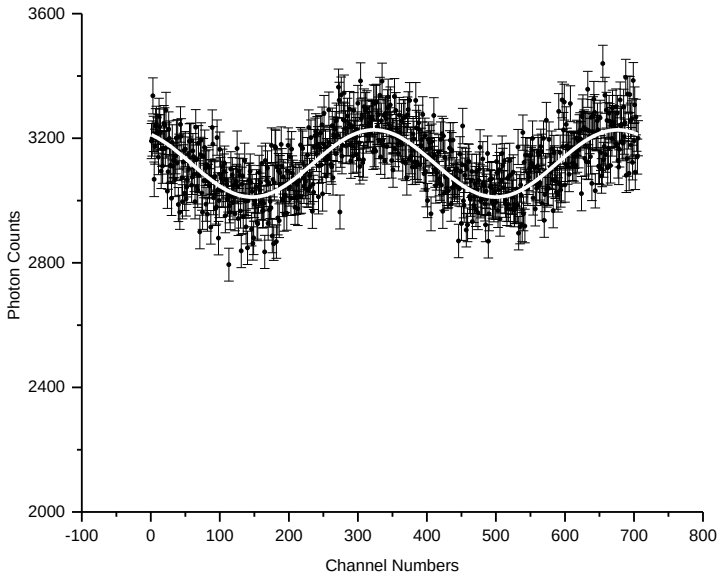

(a)

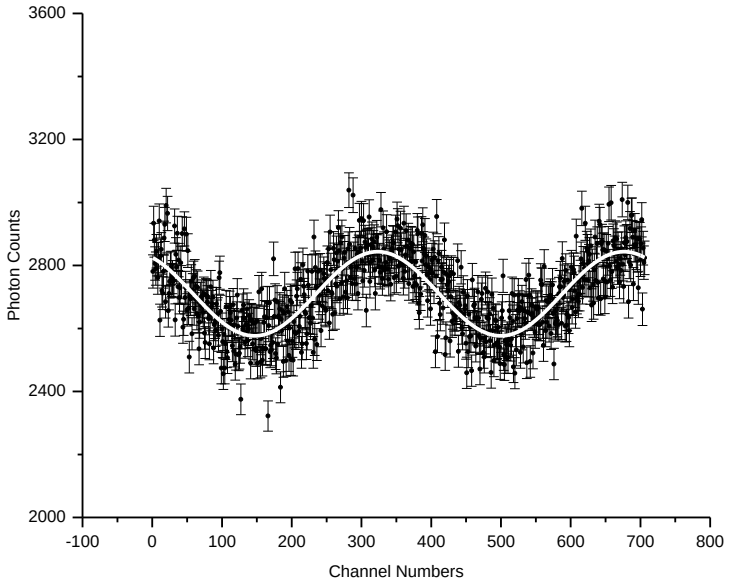

(b)

Figure 4.12: Fitted experimental fluorescence data for 583 nm accumulated for 76 passes at 50 eV electron energy with electron gun (a) ON and (b) OFF.

Table 4.2: Fitted sine-model parameters at 50 eV for the data of Figure 4.10 and Figure 4.12. Units of y_0 and A are (counts/200ms)xN, where N is the number of passes through the PMT polarizer cycle.

Sine-model equation : $I = y_0 + A\sin(\pi(x - x_c)/w)$				
Fitted parameters	554nm@50eV with electron gun:		583nm@50eV with electron gun:	
	ON	OFF	ON	OFF
Number of passes	15	15	76	76
Reduced χ^2	1.1	1.2	1.9	2.3
y_0	7741 ± 4	6802 ± 4	3119 ± 3	2710 ± 3
A	358 ± 5	380 ± 5	108 ± 4	134 ± 4

At some stages of the data taking, the PMT stepping motor was found to be slipping on its rotation axis, and the data taking was paused to correct this mechanical problem. In the subsequent analysis, it was found that some of the longer data runs did not fit well to the sine model of Equation (4.6). This might be due to axis of rotation of the polarizer being offset to the fluorescence detection axis, giving the appearance of a 'damped' modulation due to nonuniformity of the polarizer; in some cases it appeared that a small amount of stepping motor slippage may have occurred during a run. In these problem cases, a reduced sample of the PMT data was used to fit the sine model.

4.4 Calculations of the 554 and 583 nm Relative Intensities

The fluorescence data with electron gun ON and OFF were fitted separately to Equation (4.6) for each data run. To extract the intensity signal, the fitted PMT graph parameters were first converted to counting rate in Hz with ON and OFF signals defined as;

Electron gun ON: $I(x) = y_0 + A \sin(\pi (x - x_c) / w)$, (4.9a)

Electron gun OFF: $I'(x) = y_0' + A' \sin(\pi (x - x_c) / w)$. (4.9b)

The difference gives the intensity signal $I_s(x) = I(x) - I'(x)$ as,

$$I_s(x) = (y_0 - y_0') + (A - A') \sin(\pi (x - x_c) / w). \quad (4.10)$$

The total radiated intensity is deduced from Equation (4.7):

$$I = 3(y_0 - y_0') + (A - A'), \quad (4.11)$$

and the polarization from Equation (4.8) as,

$$P = \frac{2(A - A')}{(y_0 - y_0') + (A - A')}. \quad (4.12)$$

A graph of these parameters versus run number at 20 eV for 554 nm is shown in

Figure 4.13. Notably, the signal intensity parameter, $(y_0 - y_0')$, includes some values that are an order of magnitude different from the others, while the polarization parameter, $(A - A')$, values are much more consistent with each other. The reasons for this are not clear.

Data were combined for all runs at a given energy, by calculating the weighted average of fitted parameters, $(y_0 - y_0')$ and $(A - A')$. The weighted averages were

calculated from the expression: $\bar{x}_{wt} = \frac{\sum_i x_i w_i}{\sum_i w_i}$ with weights $w_i = \frac{1}{\delta x_i^2}$. This procedure is appropriate for combining measurements with varying statistical uncertainties δx_i. The uncertainty in the weighted average is generally calculated as $\delta \bar{x}_{wt} = \frac{1}{\sqrt{\sum_i 1/\delta x_i^2}}$. Given that the individual measurements x_i varied by more than their assigned statistical errors δx_i, the resulting $\delta \bar{x}_{wt}$ gave a statistical uncertainty estimate that was too small. This was evidenced by the reduced χ^2 statistic being significantly larger than 1, as seen in Table 4.3. The χ^2 distribution [Taylor1997] is used to check for goodness of fit of an observed distribution to a theoretical one, in this case:

$$\chi^2 = \sum_i \left(\frac{x_i - \bar{x}_{wt}}{\delta x_i} \right)^2$$

The reduced-χ^2 is defined by dividing the χ^2 by number of degrees of freedom,

$$df = N - (n+1)$$

where *N* is number of data points, and *n* is the number of coefficients in the fit formula.

For the present data, the errors in the weighted averages were evaluated as $\delta \bar{x}_{wt} = \sqrt{\chi^2 / df}$; this is equivalent to using the standard deviation of the x_i distribution instead of δx_i in the calculation of $\delta \bar{x}_{wt}$, which is appropriate given the additional run-to-run variation in the experimental conditions.

Runs were discarded for which $(y_0 - y_0')$ was many error bars away from the mean. These same data runs were also discarded from the averaging of *(A – A')*. This selection improved the reduced χ^2 as can be seen in the summary of Table 4.3, an

indication of greater consistency in the reduced data set. Nonetheless, the signal intensity parameters for the reduced data set still show large variations in some cases, e.g. 554 nm at 50 eV.

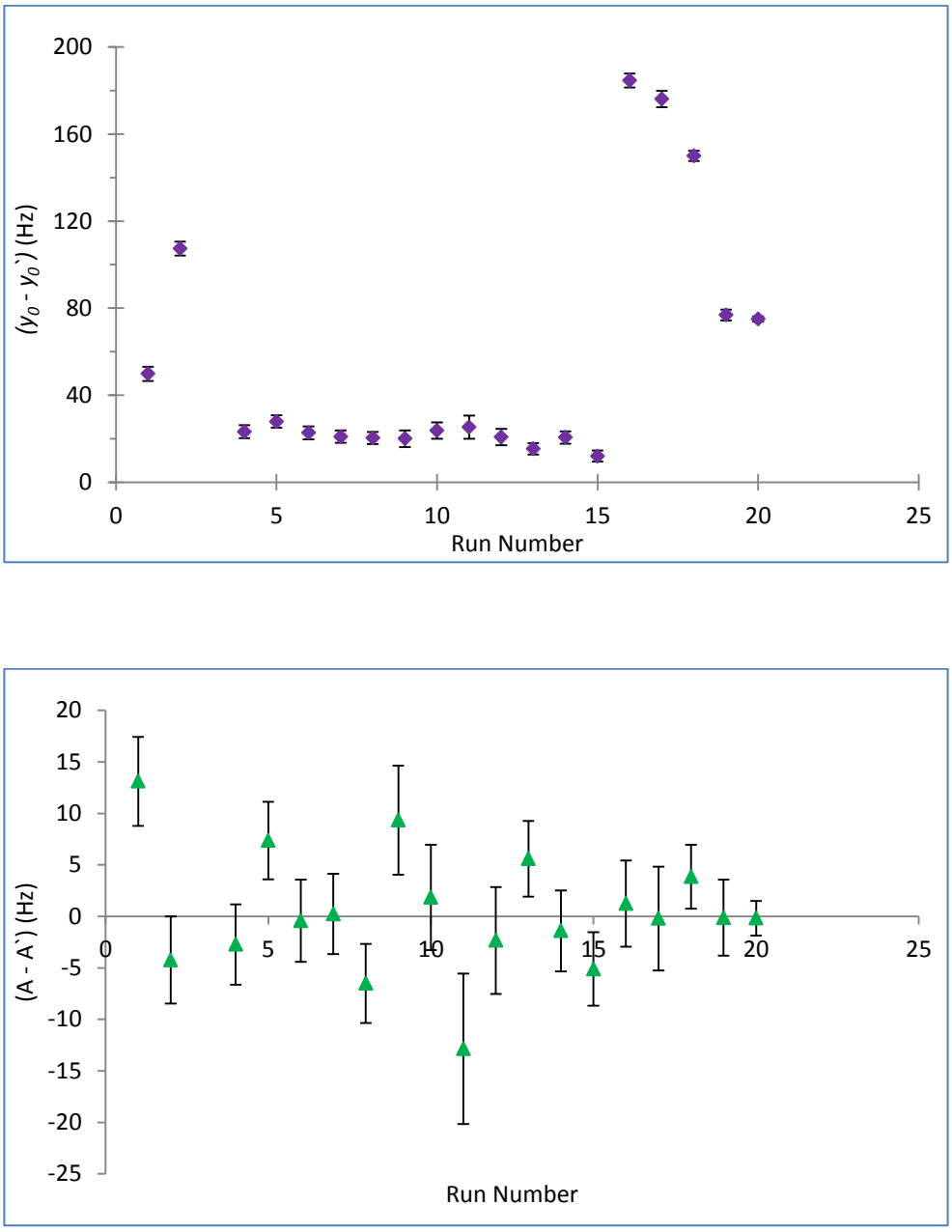

Figure 4.13: Graph of the two fitted intensity parameters at 20 eV for 554 nm before any cuts (a) $(y_0 - y'_0)$ (b) $(A - A')$ vs run number.

Table 4.3: Weighted average parameters $(y_0 - y'_0)$ and $(A - A')$ along with χ^2/df and degrees of freedom for the full data set in comparison with reduced data sets after cuts, showing improved χ^2/df.

Energy (eV)	λ (nm)	Full Data Set			Reduced Data Set		
		$(y_0 - y'_0)$ (Hz)	χ^2/df	df	$(y_0 - y'_0)$ (Hz)	χ^2/df	df
20	554	61 ± 12	354	18	20 ± 1.4	2.3	10
	583	16 ± 2	44	12	6.3 ± 0.68	1.1	7
30	554	104 ± 19	985	25	16 ± 1	1.5	12
	583	28 ± 5	271	17	4.6 ± 1.2	1.4	5
40	554	328 ± 31	1376	15	343 ± 3	5.5	5
	583	21 ± 8	1060	18	80 ± 4	61	8
50	554	610 ± 29	450	7	582 ± 27	324	5
	583	54 ± 2	9.0	8	54 ± 2	9.0	8
Energy (eV)	**λ (nm)**	**$(A - A')$ (Hz)**	**χ^2/df**	**df**	**$(A - A')$ (Hz)**	**χ^2/df**	**df**
20		0.53 ± 1.1	1.6	18	0.20 ± 1.5	1.5	10
	583	1.5 ± 1.4	3.9	12	1.4 ± 1.9	4.8	7
30	554	1.1 ± 0.9	1.2	25	1.8 ± 1.2	0.66	12
	583	-1.0± 2.1	2.2	17	0.97 ± 1.4	0.82	5
40	554	-3.5 ± 1.9	2.7	15	-0.77 ± 2.4	2.8	5
	583	-2.0 ± 0.5	2.7	18	-4.4 ± 1.3	3.4	8
50	554	-16 ± 2	1.1	7	-15 ± 2	1.3	5
	583	-3.4 ± 0.8	0.30	8	-3.4 ± 0.8	0.30	8

The fluorescence intensity calculated from Equation (4.11) from the reduced data set of Table 4.3 is proportional to the emission cross section. Results are listed in Table 4.4 and are plotted in Figure 4.14. The weighted average intensity of the 554 nm line is about 10x larger than that of the 583 nm line. For both lines, the intensities increase dramatically above 30 eV.

Table 4.4: The weighted average intensity signal for both fluorescences.

Electron Energy (eV)	I_{554} Hz	I_{583} Hz	$\frac{I_{583}}{I_{554}}$
20	60 ± 6	20 ± 6	0.34 ± 0.11
30	50 ± 5	15 ± 5	0.30 ± 0.10
40	1028 ± 11	236 ± 13	0.23 ± 0.01
50	1731 ± 81	159 ± 7	0.09 ± 0.01

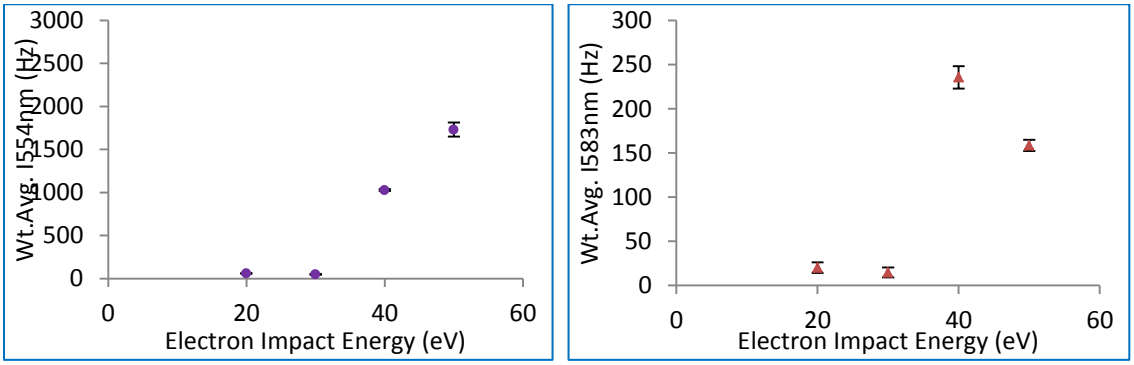

(a) (b)

Figure 4.14: The weighted average intensity of the photon signal for (a) 554 nm (b) 583 nm. Note that the vertical scale of the 554 graph is 10x that of 583 nm graph.

Figure 4.15 shows the ratio $\frac{I_{583}}{I_{554}}$ which is proportional to the relative cross section, as will be discussed in the next section. Since the photon rates were much smaller at 20 eV and 30 eV as seen in Figure 4.14, those points have larger statistical uncertainties than the points at 40 eV and 50 eV. The intensity ratio shows a smoothly decreasing trend with increasing electron impact energies. The line polarization of 554 nm and 583 nm was calculated by using Equation (4.12) and is shown in Figure 4.16. Both polarizations are small, almost consistent with zero at most electron impact energies.

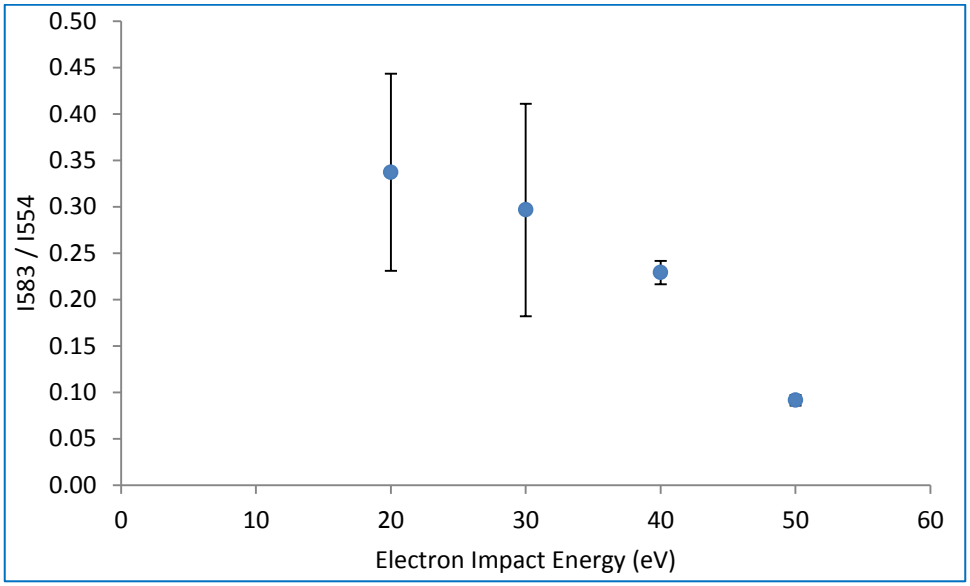

Figure 4.15: Ratio of intensities of 583 nm and 554 nm from Figure 4.14.

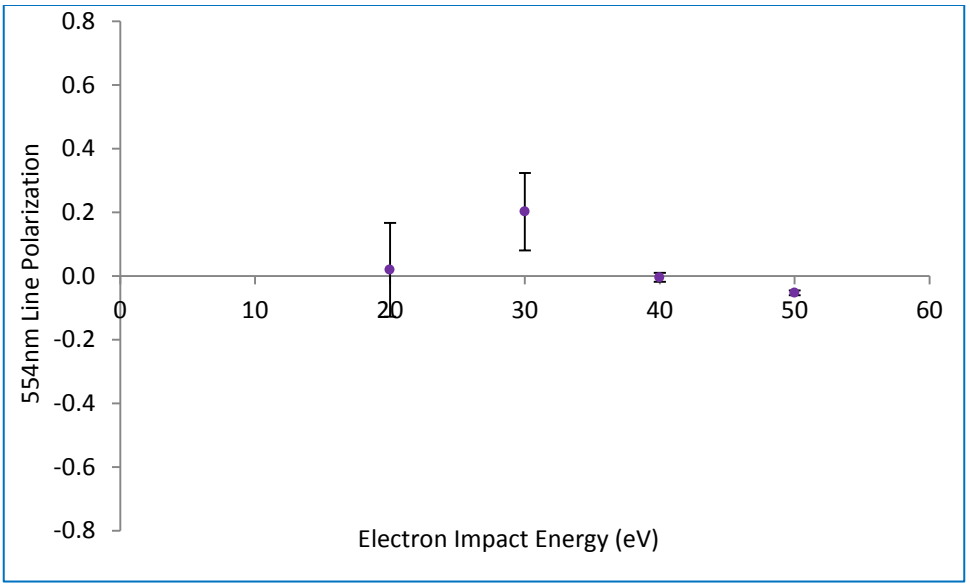

(a)

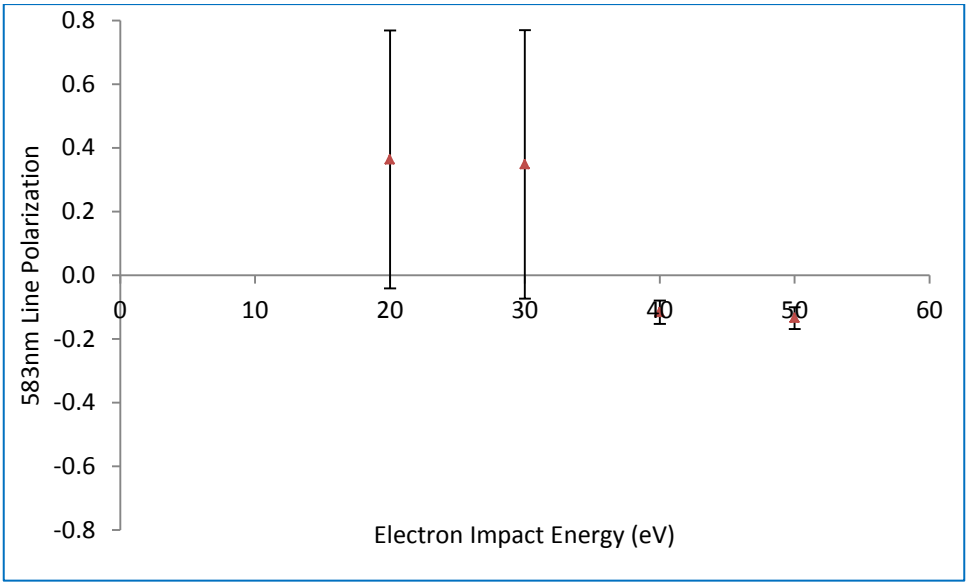

(b)

Figure 4.16: Measured line polarization of (a) 554 nm (b) 583 nm.

4.5 Normalization to EELS Data

Concurrently with the fluorescence intensity data, barium electron energy loss spectra (EELS) were also acquired. The purpose of these spectra was for normalization, since the scattered electron rate is proportional to the product of atomic beam and electron beam intensities, which also determine the overall line emission rate. Figure 4.17 shows a portion of the EELS for one run (10 passes) at 30 eV electron impact energy as an example. In total more than 500 EELS graphs were plotted. The 2.24 eV peak was used for normalization. For each data run, the 2.24 eV peak was selected and integrated, with background determined from the tails of the peak and subtracted by the integration program. The background-subtracted 2.24 eV counts, with errors calculated as $\delta S = \sqrt{\delta T^2 + \delta B^2}$ where $S=(T-B)$ are the signal counts and T, B are the total and background counts respectively, were examined to check for the expected scaling of the photon signals with electron scattering rates.

A careful examination of the 554 and 583 nm photon rates compared to the 2.24 eV EELS rates was made. It was expected that the photon signal rates would be proportional to the EELS rates and vice versa. This turned out not to be the case, for reasons which are unclear, likely associated with the very large photon background rates encountered in the measurements. As an example, the photon signal rates are plotted versus the EELS 2.24 eV rate for 50 eV in Figure 4.18. Clearly, these two experimental signals do not track with each other. Therefore, it was decided not to use the intended EELS normalization scheme to account for variations in the beam and target parameters between measurements. Rather it had to be assumed that the relatively large number of

interleaved 554 and 583 nm photon data sets would have provided adequate sampling of the beam and target conditions so that on the average no net correction was necessary.

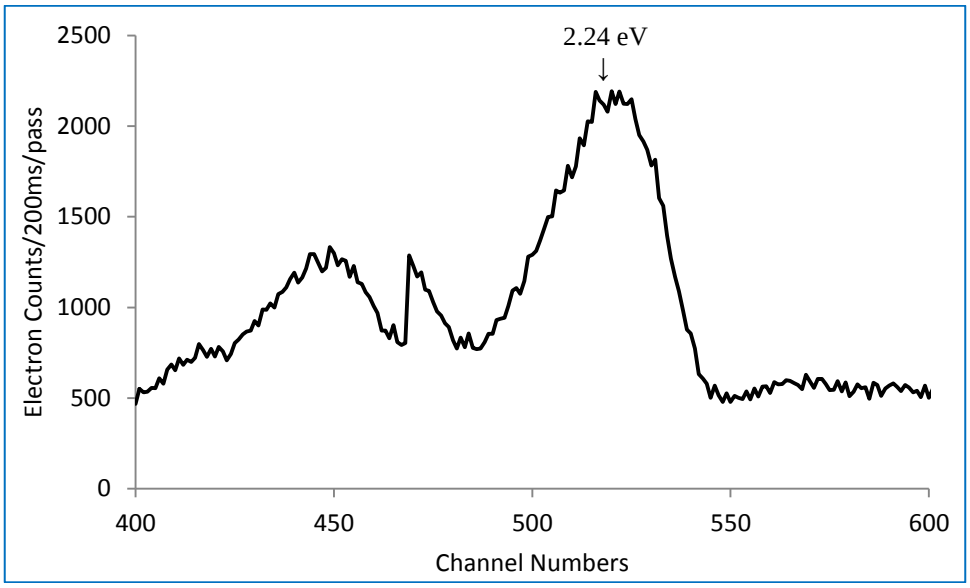

Figure 4.17: Sample EELS for 10 passes at 30 eV.

4.6 Corrections for Instrumental Effects

By measuring the ratio of the fluorescence intensities with the same apparatus under similar conditions (with the exception of the PMT HV setting as discussed earlier), most instrumental effects cancel. This is a significant advantage of the method in principle. As discussed in the previous section, unfortunately the intended EELS normalization scheme was not successful. However, there are well determined instrumental effects that are not the same at both wavelengths which must still be corrected for. These are briefly discussed below.

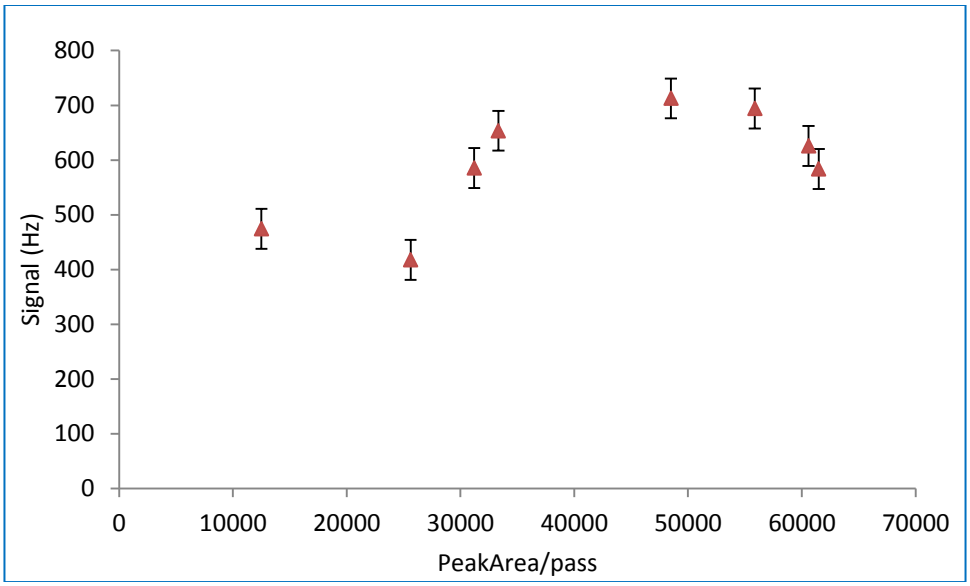

(a)

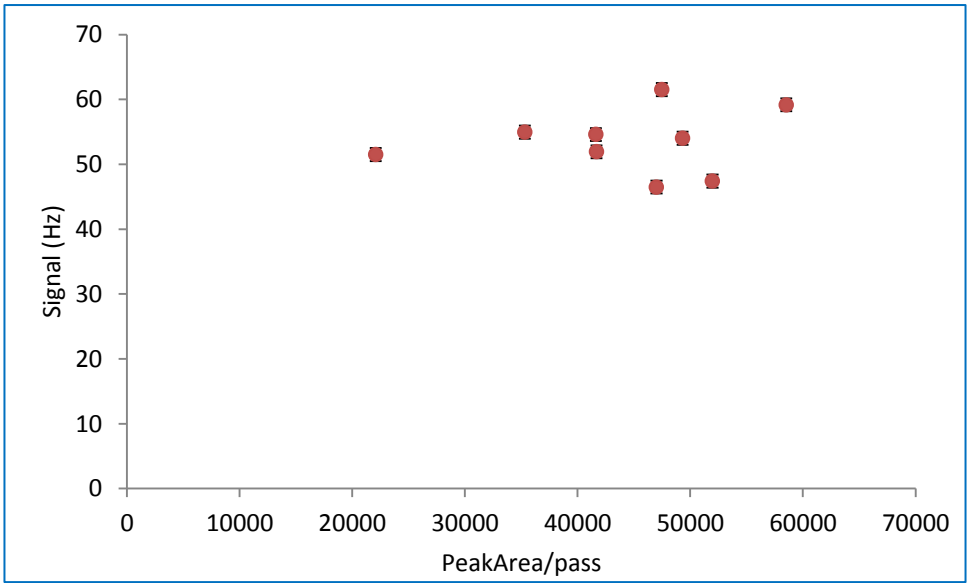

(b)

Figure 4.18: Comparison of photon signal rate and the 2.24 eV EELS rates at 50 eV electron energy for (a) 554 nm and (b) 583 nm.

4.6.1 PMT Photocathode Response

The quantum efficiency (QE) of the PMT photocathode varies with wavelength as shown in Figure 4.19. It can be seen from this figure (multialkali response line) that the QE of the photocathode at 554 nm is about 20% greater than at 583 nm. From a detailed analysis of Figure 4.19, the factor of 1.22±0.02 must be applied to the EELS-normalized line emission intensity ratio to account for this effect.

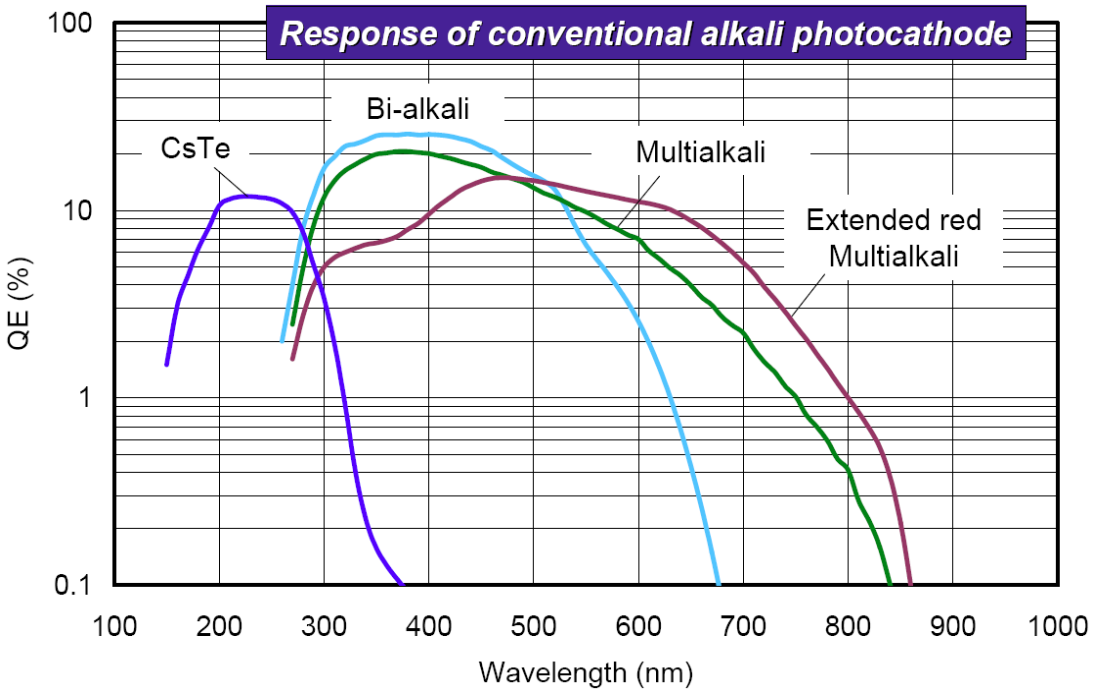

Figure 4.19: Quantum efficiency of conventional alkali photocathode.

4.6.2 Line Filter Transmission

The transmission graphs [Andover Corporation] for the two line filters as used in the measurements are shown in Figure 4.20. From these, the transmission ratio $\frac{T_{554}}{T_{583}}$ was calculated to be 0.91±0.07 and must be applied to the line emission intensity ratio.

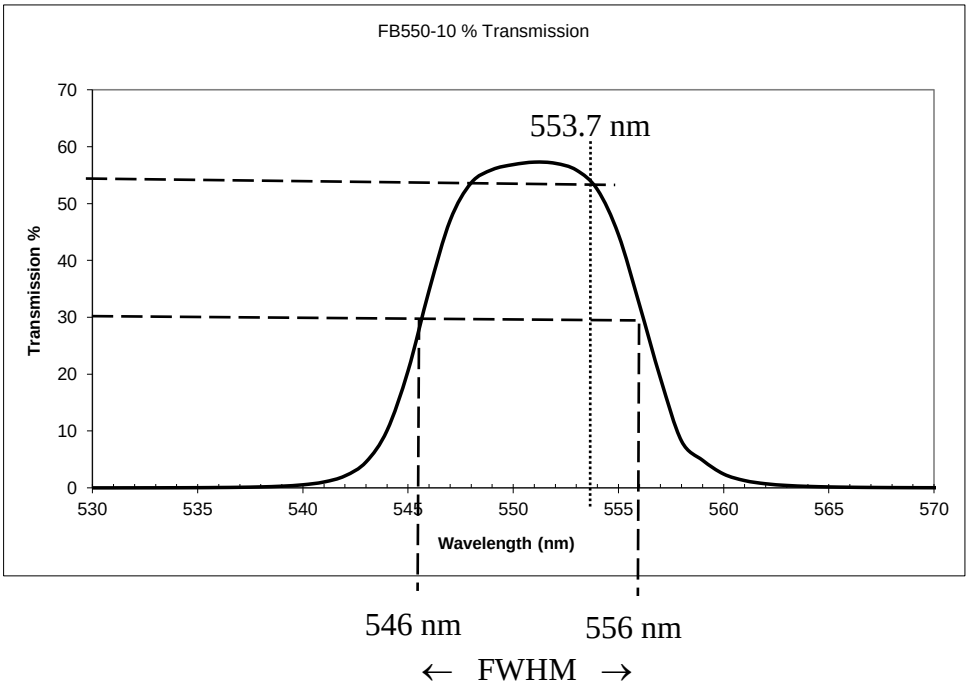

(a)

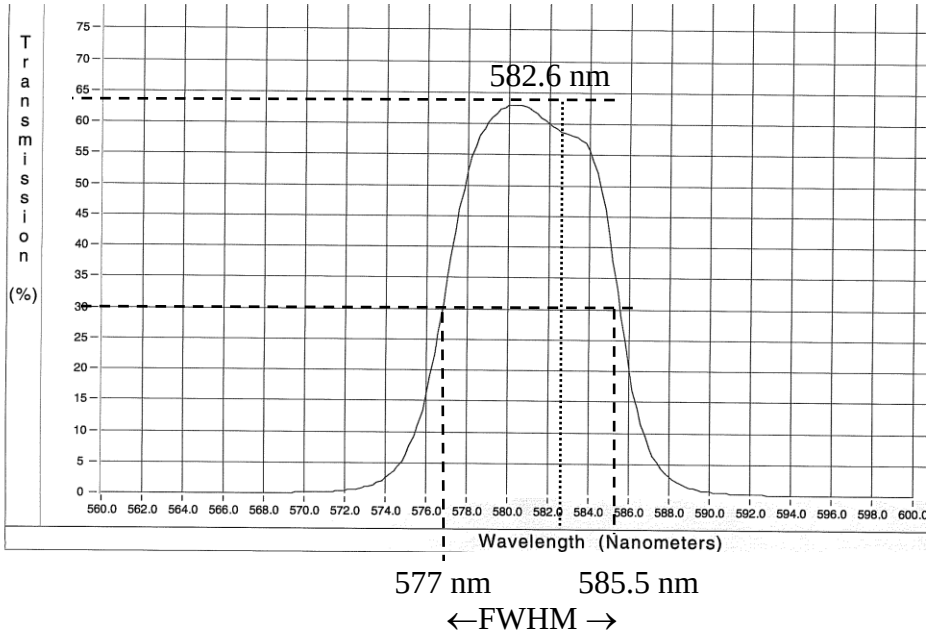

(b)

Figure 4.20: Transmission curves for (a) 550 nm and (b) 581 nm line transmission filters [Andover Corporation].

An additional consideration is whether any other known spectral lines of barium fall within the transmission windows of the line filters and could have diluted the experimental signals. Aleksakhin et al. [Aleksakhin1975] measured electron impact line emission cross sections for a number of spectral lines in barium. Their results for spectral lines closest in wavelength to the 554 nm and 583 nm lines in barium are tabulated in Table 4.5. It can be seen that the transitions observed by Aleksakhin et al. are easily filtered out by these two line transmission filters.

Table 4.5: Strongest closest effective excitation cross section σ_{ex} for spectral transitions to the present studied 554 nm and 583 nm transitions (shown with an *) in barium.

λ (nm)	Transition	σ_{ex}(x10^{-19} cm^2) @30eV
472.6	$5\ ^1D_2 \rightarrow 7\ ^1P_1$	500
553.5*	$6s^2\ ^1S_0 \rightarrow 6\ ^1P_1$	25,000*
582.6*	$5\ ^1D_2 \rightarrow 6s7p\ ^1P_1$	460*
648.3	$5\ ^1D_2 \rightarrow 5d6p\ ^1F_3$	560

4.6.3 PMT High Voltage Differences

The PMT gain correction is a rate-dependent and poorly determined multiplicative factor assumed to be constant with a generous error bar. This factor affects the 554 nm photon data, and hence the ratio of (583 nm / 554 nm) photon intensities could not be reliably determined. To account for this effect in an approximate manner, the observed 554 nm intensities were scaled up by a factor of 10 in subsequent analysis, and a systematic error of 50% for the PMT HV adjustment was included in the final analysis.

4.6.4 Summary of the Corrections for Instrumental Effects

An instrumental correction factor f=1.11±0.09 was applied to the measured fluorescence intensity ratio to account for the PMT photocathode response and line filter transmission. A separate PMT HV correction factor of x(10±5) was applied to the 554 nm fluorescence intensity.

4.7 Blended Features

There are several lines, not measured by Aleksakhin et al., whose emission wavelengths fall within the 8.5 nm FWHM passband of the 581 nm filter. The electron impact excited transitions giving rise to these additional lines are $(6s^2)^1S_0 \rightarrow (5d6p)^1F_3$, $(6s^2)^1S_0 \rightarrow (6s6d)^3D_2$ and $(6s^2)^1S_0 \rightarrow (6s6d)^3D_3$. These are given in Table 4.6 [http://physics.nist.gov/ PhysRefData/ ASD/ lines_form.html]. The quantity gA is the radiating level degeneracy multiplied by the spontaneous emission rate – a measure of the line intensity. These all correspond to strongly dipole forbidden transitions and were expected to be weak enough that their corresponding line emission cross sections are negligible. Thus to a good approximation, it was initially concluded that the 583 nm filtered detector was sensitive to the desired $(6s^2)^1S_0 \rightarrow (6s7p)^1P_1$ excitation alone. Later, Bostock's [Bostock2014a] new calculations showed non-negligible cross sections for the above mentioned three transitions, i.e. $^1S_0 \rightarrow ^1F_3$, $^1S_0 \rightarrow ^3D_2$ and $^1S_0 \rightarrow ^3D_3$. The contributions from these three wavelengths are referred to as 'blended' features in this chapter as well as in Chapter 5 and depicted in Figure 4.21.

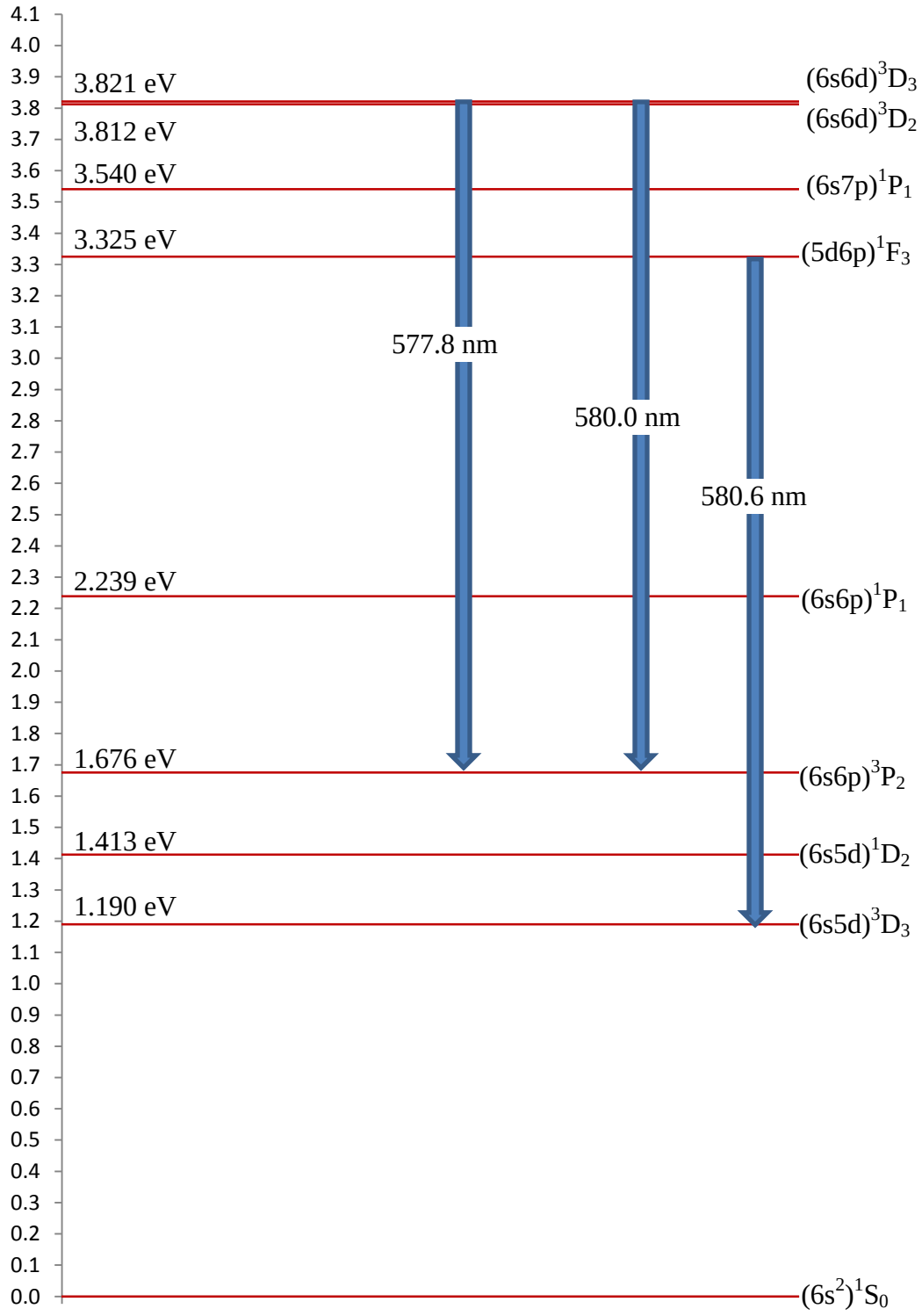

Figure 4.21: The three 'blended' wavelengths which can pass through the 581 nm passband filter.

Table 4.6: Emission wavelengths within the 8.5 nm FWHM passband of 581 nm filter along with the present studied line at 582.6 (shown with an *).

Wavelength (nm)	Radiating Level	Level energy (eV)	Line Intensity, gA ($x10^8$ s^{-1})
582.6*	$6s7p\ ^1P_1$	3.5403	1.8*
580.6	$5d6p\ ^1F_3$	3.3247	0.26
580.0	$6s6d\ ^3D_2$	3.8126	1.0
577.8	$6s6d\ ^3D_3$	3.8209	5.7

4.8 Results and Discussion

4.8.1 Line Emission Cross Section Ratio

Applying the instrumental corrections to the measured intensity ratio, the line emission cross section ratio $\frac{\sigma_{583}}{\sigma_{554}}$ was determined. The results are summarized in Table 4.7. The first column shows the uncorrected ratio obtained from the fitted fluorescence parameters as discussed in Section 4.4. The second column shows the applications of the instrumental correction factor f=1.11±0.09. the last column shows the results after rescaling the 554 nm rate ×(10±5) to account for the PMT HV adjustment.

Table 4.7: Emission cross section ratio $\left(\frac{\sigma_{583}}{\sigma_{554}}\right)$ showing raw and corrected results as discussed in the text.

E (eV)	$\frac{I_{583}}{I_{554}} \propto \frac{\sigma_{583}}{\sigma_{554}}$	$\frac{\sigma_{583}}{\sigma_{554}} \times f$	$\frac{\sigma_{583}}{\sigma_{554}} \times \frac{f}{HV_{corr}}$
20	0.34 ± 0.11	0.37 ± 0.12	0.037 ± 0.022
30	0.30 ± 0.10	0.33 ± 0.13	0.033 ± 0.021
40	0.23 ± 0.01	0.25 ± 0.02	0.025 ± 0.013
50	0.09 ± 0.01	0.10 ± 0.01	0.010 ± 0.005

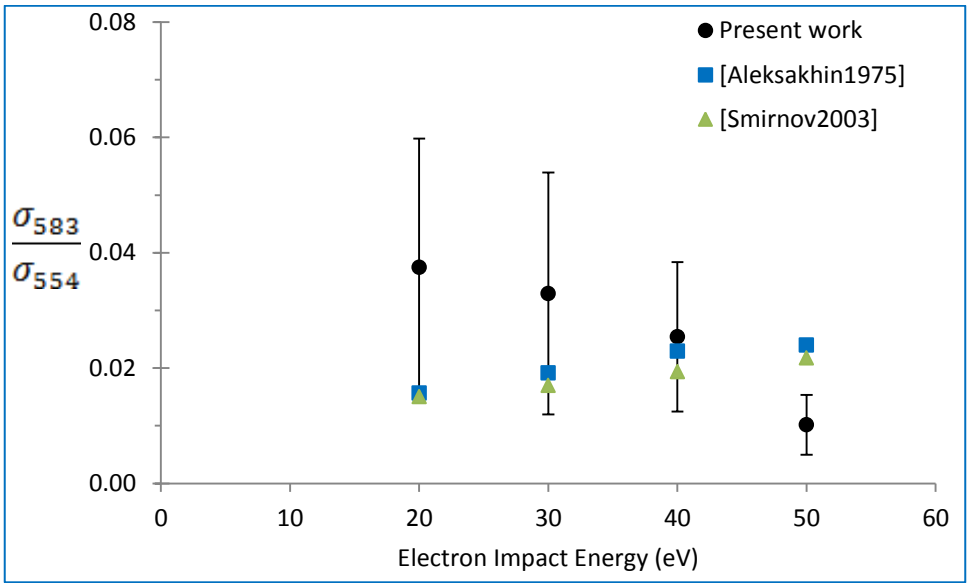

Figure 4.22: The $\frac{\sigma_{583}}{\sigma_{554}}$ line emission cross section ratio compared with previous experiments.

Results are plotted in Figure 4.22 using the full uncertainties of Table 4.7 (last column). The present work finds a smooth decreasing trend of the cross section ratio with increasing electron energy. This is in contrast to the trend found in previous measurements, also plotted in the figure. Unfortunately the error bars on the present work are relatively large. However, results obtained are generally in agreement with previous measurements, neither of which actually reported their experimental uncertainties.

4.8.2 583 nm Line emission Cross Section

To obtain the line emission cross section of the 583 nm transition ($\sigma_{583\text{-em}}$), the experimental ratio of $\frac{\sigma_{583}}{\sigma_{554}}$ determined above was normalized to the 554 nm line emission cross section $\sigma_{554\text{-em}}$ measured by Chen and Gallagher [Chen1976]. These authors have measured $\sigma_{554\text{-em}}$ for various electron impact energies (including cascade and branching contributions) with an uncertainty of 5%, and their results are in excellent agreement with the theoretical CCC-model [Fursa1999]. By interpolation of Chen's graphical data, $\sigma_{554\text{-em}}$ was obtained for the four energies studied in this experiment. These results are tabulated in Table 4.8. Note that the experimental $\sigma_{583\text{-em}}$ is not corrected for cascade population from higher levels, nor for unobserved decays to other low lying states.

Table 4.8: Experimental line emission cross section $\sigma_{583\text{-em}}$.

Electron Energy (eV)	[Chen1976]	Present Work	
	σ_{554} x10^{-16} cm^2	$\frac{\sigma_{583}}{\sigma_{554}}$	$\sigma_{583\text{-em}}$ x10^{-16} cm^2
20	38.6 ± 1.9	0.037 ± 0.022	1.4 ± 0.86
30	34.2 ± 1.7	0.033 ± 0.021	1.1 ± 0.72
40	29.4 ± 1.5	0.025 ± 0.013	0.75 ± 0.38
50	27.6 ± 1.4	0.010 ± 0.005	0.28 ± 0.14

Aleksakhin et al. [Aleksakhin1975] and Smirnov [Smirnov2003] had studied excitation of barium by electron impact. Both have obtained an optical emission spectrum (OES) by bombardment of target barium atoms by monoenergetic 30 eV electrons, a technique completely different from the present experiment. The present and previously reported values of $\sigma_{583\text{-em}}$ are plotted in Figure 4.23. Figure 4.23 shows the same trend as that in Figure 5.22. The two data sets agree within the error bars of each other. On average, there is reasonable agreement with the CCC model prediction.

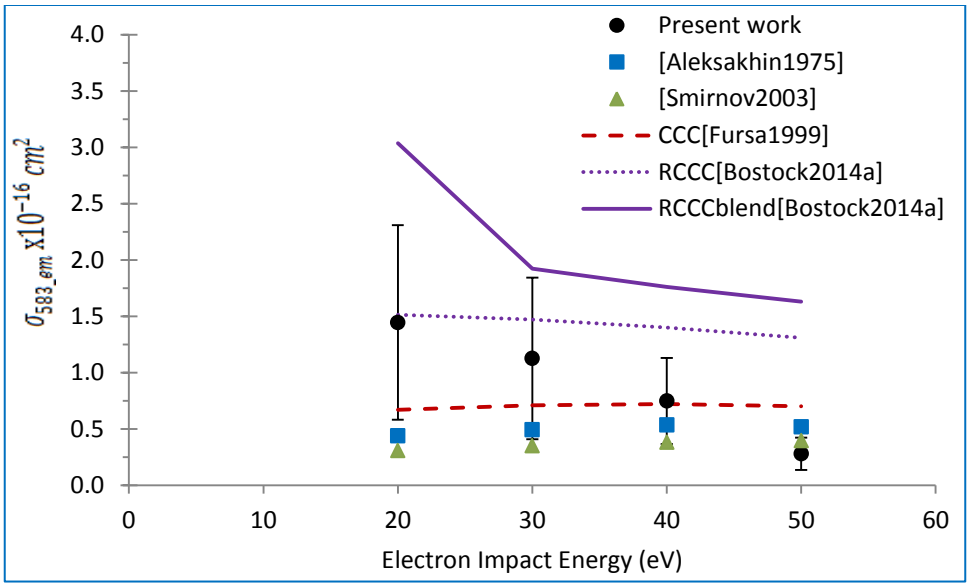

Figure 4.23: Present work σ_{583_em} along with previous experiments and models.

To this point, the experimentally measured line emission cross section $\sigma_{583\text{-}em}$ includes contributions from branching ratio and cascading factors. In the following sections these two factors are discussed and are applied to the experimental data to obtain the electron impact excitation cross section $\sigma_{583\text{-}ex}$, also referred to as the direct level excitation cross section in the literature.

4.8.3 Branching Ratio Contributions

An excited level can deexcite to a number of lower levels, with relative atomic transition probabilities referred to as branching ratios. If A_{jk} is the Einstein A coefficient i.e. the probability of spontaneous transition from state j to lower state k per atom per unit time, then the branching ratio for this transition is defined as,

$$\text{Branching Ratio} = \frac{A_{jk}}{\sum_i A_{ji}}. \qquad (4.12)$$

In order to determine the apparent level excitation cross section σ_{ap} for the 3.54 eV state giving rise to the 583 nm emission, σ_{em} must be divided by the branching ratio to account for decays to other lower states which were not observed.

The branching ratio for the $(6s6p)^1P_1 \rightarrow (6s^2)^1S_0$ (554 nm line) transition was calculated as 0.998 [McCavert1974]. Thus, the $(6s6p)^1P_1 \rightarrow (6s^2)^1S_0$ line emission cross section ($\sigma_{554\text{-}em}$) is effectively identical to the $(6s6p)^1P_1 \rightarrow (6s^2)^1S_0$ apparent level excitation cross section, $\sigma_{554\text{-}ap}$. This $\sigma_{554\text{-}ap}$ can form a standard for normalizing other experimental electron collision cross sections obtained by relative measurements, as done in the current work.

The transition probabilities out of the $(6s7p)^1P_1$ level (also referred to as the $(5d6p)^1P_1$ level) to lower levels are given by [Kulaga2001]; the corresponding branching ratios were calculated using Equation (4.12). The experimental reference [Niggli1987] given by [Kulaga2001] yielded a branching ratio of 0.56 while the theoretical works mentioned by the same author yielded a branching ratio in the range of 0.43 – 0.65. Other branching ratio factors mentioned in earlier work are 0.606 [Smirnov2003], 0.0326 [Aleksakhin1975] and 0.782 [Niggli1987]. The branching ratio factor from [Aleksakhin1975] seems anomalously low. Considering the wide range of different values, the experimental branching ratio 0.56±0.07 was adopted in order to obtain the apparent (level excitation) cross section, σ_{ap} as presented in Table 4.9.

Table 4.9: Branching ratio and cascade contributions to the cross sections to obtain σ_{ap} and σ_{ex}.

E (eV)	σ_{em} $x10^{-16}cm^2$	Exp. Branching Ratio [Kulaga2001]	σ_{ap} $x10^{-16}cm^2$	$f_{cascade}$ [Bostock2014a]	σ_{ex} $x10^{-16}cm^2$
20	1.4 ± 0.86	0.56	2.6 ± 1.5	0.62	0.99 ± 0.59
30	1.1 ± 0.72	0.56	2.0 ± 1.3	0.66	0.69 ± 0.44
40	0.75 ± 0.38	0.56	1.3 ± 0.68	0.56	0.59 ± 0.30
50	0.28 ± 0.14	0.56	0.50 ± 0.26	0.49	0.25 ± 0.13

The errors arrived at for the final results for σ_{ex} in Table 4.9 include the quadrature sum of the following contributions: (i) a statistical uncertainty of 5% - 30% based on the fitting procedures outlined in Section 4.4; (ii) a 10% uncertainty in the instrumental correction factor f (Section 4.8.1); (iii) a 50% uncertainty in the HV correction factor for the 554 nm rates (iv) a 12% uncertainty in the branching ratio correction. The single largest contribution is the HV correction factor, as discussed in the text. Following that, the dominant statistical uncertainty is associated with run-to-run variations in the 583 nm and 554 nm rates due to changing experimental conditions. No additional uncertainty is assigned for the fractional cascade contribution assessed from the predictions of RCCC model [Bostock2014a].

4.8.4 Apparent Cross Section σ_{ap}

To obtain the apparent cross section $\sigma_{583\text{-}ap}$ for the (6s7p) $^1P_1$ state, the emission cross section $\sigma_{583\text{-}em}$ was divided by the experimentally measured branching factor of 0.56±0.07 [Kulaga2001] This gave the total fluorescence emission from the (6s7p) $^1P_1$ state and this σ_{ap} is shown in Figure 4.24 along with the theoretical predictions. The experimental works of [Smirnov2003] and [Aleksakhin1975] referenced earlier did not report the apparent cross section, so they are not shown in the figure.

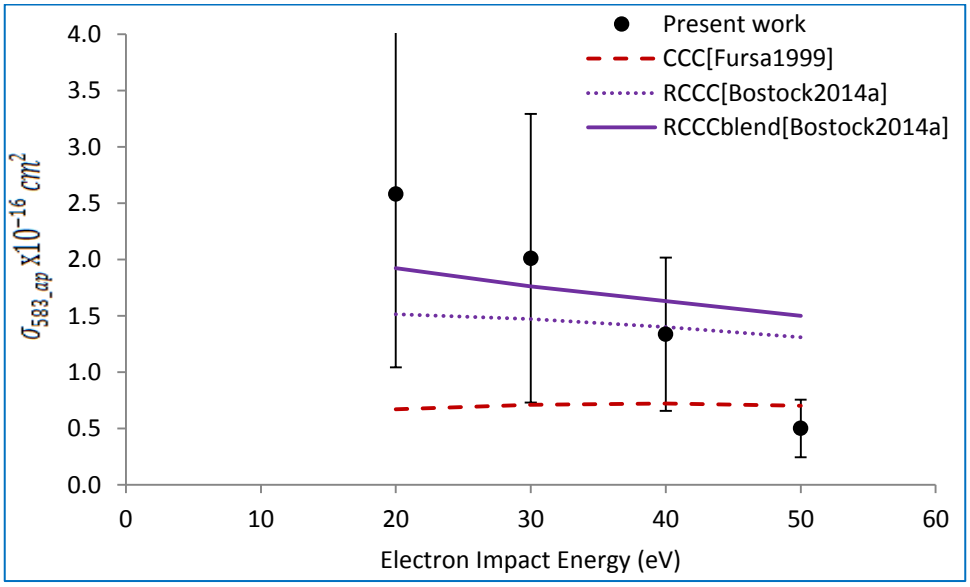

Figure 4.24: Present σ_{583_ap} comparison with theoretical models of CCC and RCCC.

The RCCC-model [Bostock2014a] reported a very high electron excitation cross section of the $(5d6p)^1F_3$ level out of the ground state. This $(6s^2)^1S_0 \rightarrow (5d6p)^1F_3$ electron excitation is a strongly dipole forbidden transition. Also other dipole forbidden transitions (previously discussed in Section 4.7) were found to have non-negligible electron excitation cross sections in the RCCC-model [Bostock2014a]. These 'unexpected' cross sections gave rise to a 'blended' cross section which included contributions from electron excited $^1F_3$, $^3D_2$ and $^3D_3$ states as discussed in Section 4.7. The calculations in this 'blended' scheme are also shown in Figure 4.24; their effect is generally to increase the apparent cross section by about 20%, improving the agreement at all energies except at 50 eV.

4.8.5 Cascade Contributions

In the cascade effect, higher energy levels which can also be excited by electron impact can deexcite to populate the upper level of the transition of interest. The population of the upper state and thus any measured cross section is the sum due to the direct ground state excitation as well as cascading from higher energy levels. To obtain the electron impact excitation cross section (σ_{ex}) of the line $(6s7p)^1P_1 \rightarrow (6s5d)^1D_2$, ideally cascading cross sections from all higher levels to $(6s7p)^1P_1$ should be measured experimentally and subtracted from σ_{ap}. The measurement of cascading cross sections is an enormous task. Currently there is no experimentally measured cascade cross section available in the literature for the $(6s7p)^1P_1$ level.

Fortunately, the theoretical cascade contribution to the $(6s7p)^1P_1$ state has been studied by an Australian research group [Fursa1999] using the Convergent Close

Coupling (CCC) model and the Relativistic-CCC (RCCC) model [Bostock2014a]. Their work shows that the cascading contribution is energy dependent, especially at the lower energies. An American research group [Csanak1971a, Csanak1971b, Csanak1988] proposed another theoretical model, the Unitarized First Order Many-Body Theory (UFOMBT) model to incorporate the branching ratio factor and the cascade factor. In the present work the CCC and RCCC theoretical models were used because of their relativistic approach, which is in principle more appropriate for the case of heavy atoms.

4.8.6 Electron Impact Excitation Cross Section

Theoretical models were used to estimate the cascade contribution for each electron beam energy. The fractional cascade contribution was found from RCCC model [Bostock2014a] via;

$$f_{cascade} = \frac{\sigma_{ap} - \sigma_{ex}}{\sigma_{ap}}. \quad (4.13)$$

This theoretically calculated cascade contribution fraction was subtracted from the apparent cross section to obtain the electron impact excitation cross σ_{ex}. Results are reported in Table 4.9. Figure 4.25 compares the present excitation cross section σ_{ex} with the three theoretical models of UFOMBT [Csanak1971a], CCC [Fursa1999] and RCCC [Bostock2014a]. The UFOMBT-model shows a different trend in cross section compared

to the RCCC and CCC models. The present experimental excitation cross section $\sigma_{583\text{-}ex}$ agrees with all models within the error bars except at 50 eV where it is a factor of 2-3 smaller than predictions.

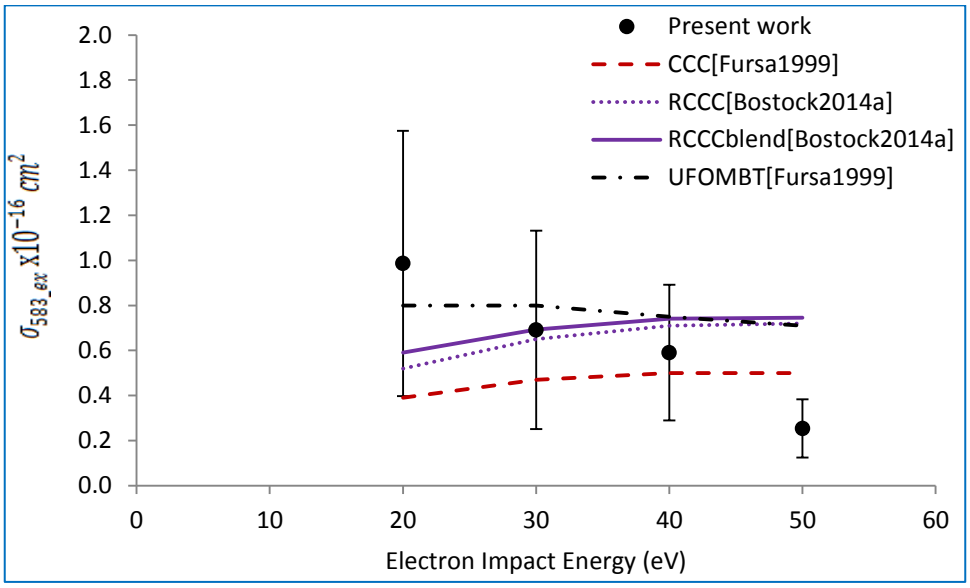

Figure 4.25: Experimental σ_{ex} comparison with theoretical models.

4.9 Conclusion

In this chapter, experimental techniques were developed that could be used to measure the relative line emission cross sections for electron excitations from ground state barium in an atomic beam. The procedures for acquiring and analyzing electron energy loss (EELS) spectral data and fluorescence polarization intensities were demonstrated and described. These techniques were applied to measure the relative line emission cross section for the 583 and 554 nm transitions in barium at a range of electron beam energies.

Unfortunately, several difficulties were encountered during the data taking and subsequent data analysis which limit the impact of this new work in light of existing data. These included a PMT high voltage adjustment to the 554 nm (reference transition) data, which introduced a relatively large normalization uncertainty; large backgrounds in the PMT signals at both wavelengths, and a lack of scaling of the photon and scattered electron signals which precluded the use of EELS data for beam and target normalization purposes.

Nevertheless, when appropriate uncertainties were taken into account, the present results agreed within errors of previously published experiments. The presentation of these data, along with the associated conclusions for the apparent and excitation cross sections of the $(6s7p)^1P_1$ state in barium, allowed the full analysis technique to be described, and the new calculations of Bostock et al. [Bostock2014a] (so far unpublished) to be presented for the first time in comparison with experimental data.

Chapter 5
Measurement of the Cross Section for 583 nm Line Emission from Barium due to Electron Excitation from the Laser-Excited Metastable D state

5.1 Introduction

In the last chapter, electron excitation of the barium $(6s7p)^1P_1$ state out of the ground state was studied. In this chapter, experimental work on the barium 583 nm line transition with excitation out of the laser excited metastable $(6s5d)^1D_2$ is undertaken. In general the atomic target state is prepared by optically pumping the ground state by using a tuneable dye laser producing the required resonance wavelength.

Electron impact on excited target states offers a new regime of collision studies. The challenge to theoretical approaches can be more severe than for ground state scattering because of the presence of many more scattering channels which should not be neglected. The proper calculation of two-electron excitations and (relativistic) singlet-triplet mixing becomes critical for these transitions. Previous studies have shown [Zetner1999] that scattering from the barium $(6s5d)^1D_2$ level cannot be well-described by the nonrelativistic approximation, mainly due to the presence of the relativistic effect of singlet-triplet mixing in the atomic wave functions [Bray2002]. Until now theoretical models such as the convergent close-coupling (CCC model), which can be considered as

a ‘pseudo-relativistic’ approach, have been applied to the available experimental data with partial success. A more fully relativistic theoretical model (RCCC model) is under development by theoretical groups, which will shed more light on the effects of the singlet-triplet mixing in the barium $(6s5d)^1D_2$ level after comparison with the current experimental data.

In barium there are two 6s valence electrons in the singlet-S ground state. The ground state excitation to the $(6s6p)^1P_1$ state at 2.24 eV is predominantly a one-electron excitation while the ground state excitation to the $(6s7p)^1P_1$ state at 3.54 eV has a good chance of a two-electron excitation also [Fursa1999]. This feature also makes the study of barium (6s7p) singlet-P state more interesting. In this chapter, the integral cross section (σ) is determined for electron excitation of the barium $(6s7p)^1P_1$ state out of laser excited metastable state of $(6s5d)^1D_2$ via measurements of the 583 and 554 nm line emission and normalizing to previous measurements of the 554 nm cross section.

The use of laser optical pumping to produce the excited state atom naturally gives rise to a target ensemble which is anisotropically distributed in magnetic sublevel population. This anisotropy depends on the laser polarization and incidence direction with respect to the quantization axis defined by the electron beam direction. This feature allows additional information about the scattering cross section dependence on magnetic substate to be extracted; the ideal goal of precisely defining the initial quantum mechanical state of the target is thereby approached.

Barium has a convenient level structure for the purpose of optical pumping with conventional dye laser systems; details are discussed in the next section. Generally it is difficult to produce sufficiently high number densities of the laser excited atoms for

scattering experiments, but pumping of the barium metastable state can be quite efficient, in the range of 20-40% [Hein2010].

The incident electron impact energies in the present study are from 10 eV to 50 eV in steps of 10 eV for the line transition between barium levels $(6s7p)^1P_1 \rightarrow (6s5d)^1D_2$ with energies of 3.54 eV and 1.41 eV respectively. This low-intermediate electron impact energy range was selected to challenge theoretical models which make approximations to the atomic wave function, to the interaction potential between various particles, and to the infinite set of differential (integral) equations, as discussed in Chapter 2. At low-intermediate energies, certain electron-atom collision problems have been described reasonably well using the CCC and R-matrix theoretical models in hydrogen, helium, alkali atoms (Li, Na, K) and alkaline-earths (Ca, Sr, Mg, Ba) [Bray2002]; at higher energies, UDWA and RDW are more compatible with the experimental data [Zetner1993].

5.2 Background to the Measurements

To perform a laser-excited scattering experiment, the first step is to make sure that the laser is tuned to excite a desired level of a specific isotope. The relevant energy level diagram for the dominant isotropic species ^{138}Ba is shown in the previous chapter, Figure 4.21, and the optical pumping scheme is illustrated in Figure 5.4. The barium $(6s6p)^1P_1$ level at energy 2.24 eV is pumped by the laser.

The barium beam contains the naturally occurring isotopic mixture (71.7% ^{138}Ba, 11.3% ^{137}Ba, 7.8% ^{136}Ba, 6.6% ^{135}Ba, 2.4% ^{134}Ba, 0.1% ^{132}Ba, and 0.1% ^{130}Ba). The even

isotope ^{138}Ba $(6s^2)^1S_0$ is by far the most prevalent in the naturally occurring mixture of barium. It has zero nuclear spin (I = 0), and, consequently, a level scheme uncomplicated by hyperfine structure. The total angular momentum of a level, including nuclear spin, is $\boldsymbol{F} = \boldsymbol{I} + \boldsymbol{J}$ (vector sum of nuclear spin *I* and electronic angular momentum, *J*). Thus, a $^1P_1$ level has *F*=1 for all even numbered (*I*=0) isotopes and *F*=1/2, 3/2, 5/2 for the odd numbered barium isotopes (*I*=3/2). The hyperfine structure for the $(6s6p)^1P_1$ level is shown in Figure 5.2 [Register1983].

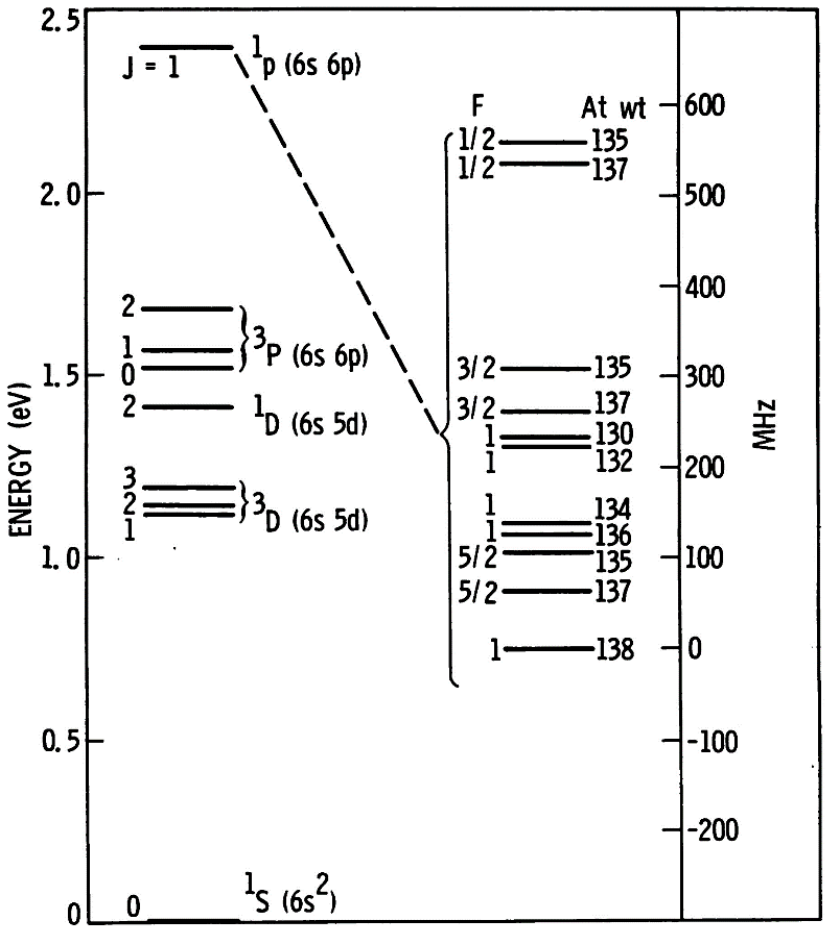

Figure 5.1: Hyperfine structure for the $(6s6p)^1P_1$ level for barium isotopes [Register1983].

For the $^1S_0$ ground state, the total angular momentum is F=0 for even numbered isotopes, and *F*=1/2, 3/2 for the odd numbered isotopes. Thus it can be seen that if odd isotopes are excited by optical pumping from a $^1S_0$ to $^1P_1$ level, it would excite multiple sublevels of $^1P_1$ resulting in depolarization of the target population. Figure 5.2 depicts the difference between a complicated pumping scheme of an odd isotope resulting in the depolarization of the target population versus a simple pumping scheme of an even isotope giving a polarized target population. In a depolarized target, magnetic substates are equally populated, while in a polarized atomic target, the magnetic substates are populated according to selection rule and thus unequal population of substates can be achieved.

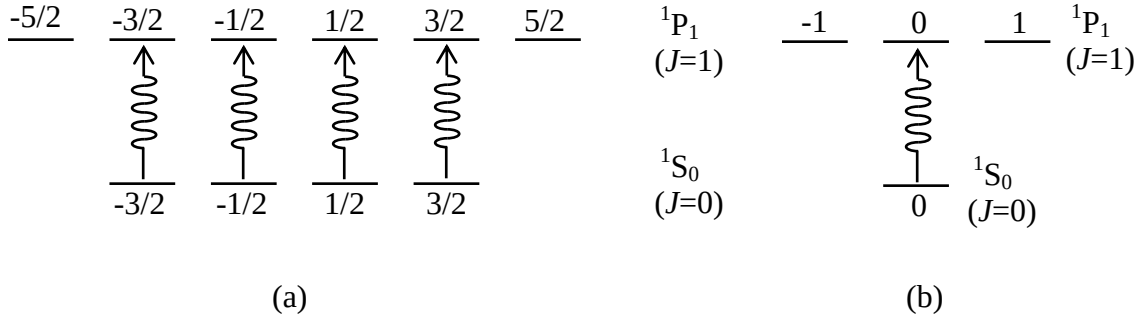

Figure 5.2: Optical pumping scheme showed for (a) Odd isotopes (b) Even isotopes.

A recent study was carried out in the University of Manitoba AMO laboratory to determine the contribution of various barium isotopes to laser induced fluorescence (LIF) with the use of data from van Wijngaarden and Li [vanWijngaarden1995] to fit the LIF spectrum [Hein2010]. It was found that for LIF with the fluorescence polarizer oriented parallel (ϕ=0°) to the electron-atomic beam plane[30], 98% of the fluorescence intensity was from the ^{138}Ba isotope line with the remaining contribution coming from other isotopes. This can be seen in a plot of the LIF spectrum against the laser tuning frequency in Figure 5.3(a), where the odd isotope ^{137}Ba contribution is negligible while that of another odd isotope ^{135}Ba is significant but lies on the shoulder of the composite isotope fit and well outside the line shape fit to the ^{138}Ba isotope. Thus no significant contribution from other isotopes can be seen for the ϕ=0° orientation. For LIF with the fluorescence polarizer oriented perpendicular (ϕ=90°) to the electron-atomic beam plane, some contribution from odd isotopes can be seen in Figure 5.3(b). This contribution of odd isotopes with ϕ=90° orientation is approximately 18 times less than that from the ϕ=0° orientation. Nevertheless this contribution from odd isotopes would result in a slightly depolarized P state for fluorescence polarization with ϕ=90° and this depolarization would be reflected in metastable D states also.

[30] The polarizer orientations are indicated in Figure 5.6.

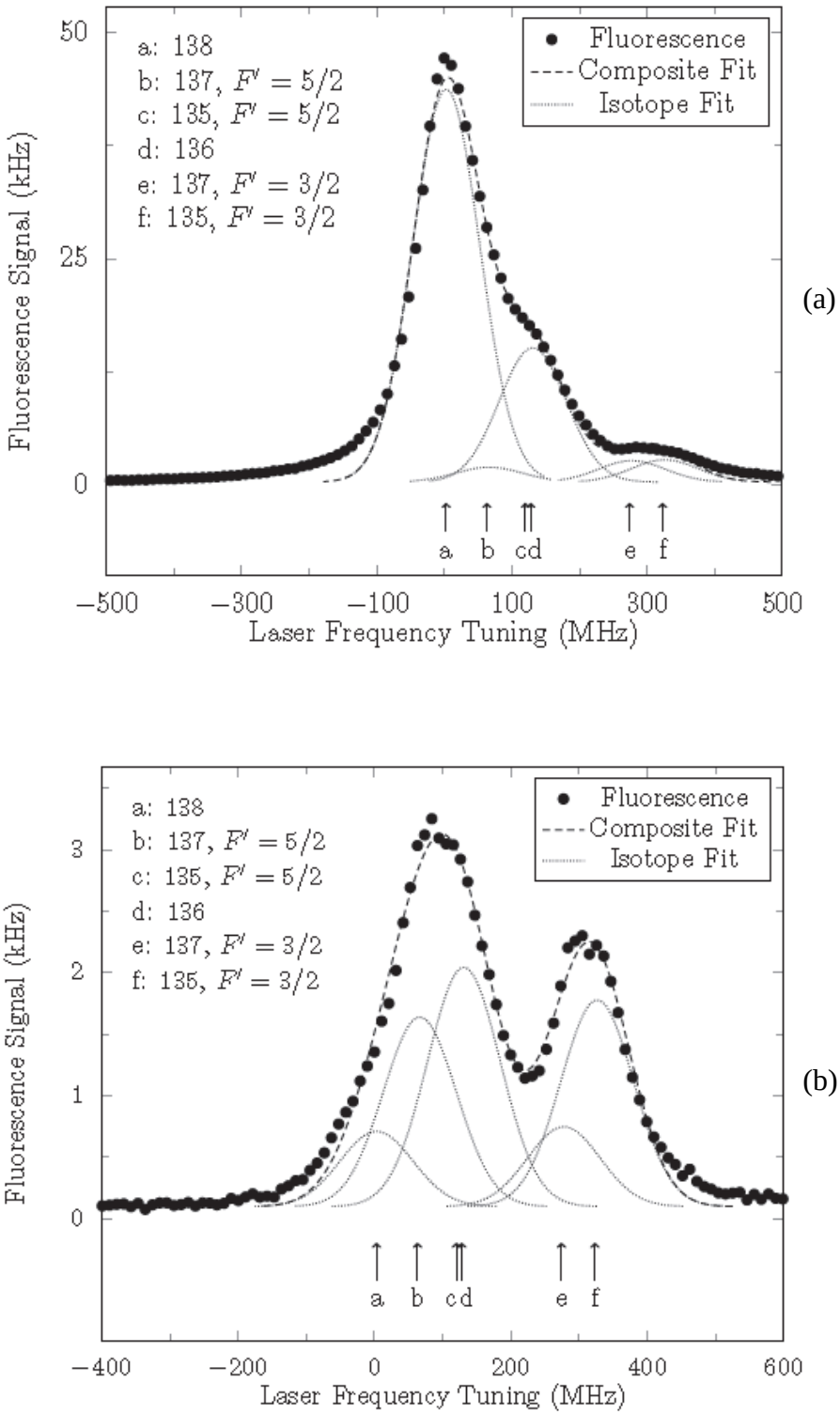

Figure 5.3: LIF as a function of laser frequency for various barium isotopes tuning for fluorescence polarizer oriented at (a) ϕ=0° (b) ϕ=90° [Hein2010, vanWijngaarden1995].

A number of checks can be made to verify that mainly the ^{138}B isotope is laser pumped. The separation between the $^{138}Ba(6s6p)^1P_1$ and $^{137}Ba(6s6p)^1P_1$ is 63 MHz while between the $^{138}Ba(6s6p)^1P_1$ and $^{135}Ba(6s6p)^1P_1$ is 105 MHz [Register1983]. If the absorption line width approaches the hyperfine level spacing, then both the even and odd isotopes can be simultaneously pumped by the laser. Absorption and emission lines are broadened by a number of processes. These processes can be grouped under the following mechanisms;

(i) Natural broadening: is intrinsic to the transition and results from the Heisenberg uncertainty principle.

(ii) Doppler broadening: is due to random thermal motions of the atoms.

(iii) Power broadening: The line profile can also be affected by the radiation intensity.

(iv) Pressure broadening: The width of the spectral line can also be affected by vapour density.

The first three (i – iii) broadening mechanisms were studied earlier for barium by Zetner et al. [Zetner1997] in this AMO lab with laser power of around 80 mW and atomic density of 10^{11} atoms/cm^3 in the interaction region with atomic beam divergence of ±6°. These experimental conditions are similar to the present work. They reported broadening widths of 19 MHz, 108 MHz and 84 MHz for (i), (ii) and (iii) respectively with a combined absorption FWHM of 140 MHz. From a comparison of these with the findings of [Register1983] above, it was assumed that it is a good approximation to isolate the ^{138}Ba isotope in the laser pumping process.

There is no contribution from the broadening mechanism (iv), as conditions in the effusive atomic beam are, to a good approximation, collisionless. From the studies of

[Register1983] and [Zetner1997] it is clear that only tails of the unwanted absorption lines will see the laser radiation tuned to the ^{138}Ba transition. Furthermore since all other barium isotopes are less than 12% abundance, the contribution from isotopes other than ^{138}Ba will be additionally supressed.

Once the desired ^{138}Ba $(6s6p)^1P_1$ state is pumped by the laser, the excited atoms can decay to lower energy states. It can be seen that there are three groups of states below the $(6s6p)^1P_1$ state in addition to the ground state: the $(6s6p)^3P_{0,1,2}$ state series, $(6s5d)^1D_2$ state and the $(6s5d)^3D_{1,2,3}$ state series. Decay to the $(6s6p)^3P_{0,1,2}$ state series is the electric-dipole forbidden by the selection rules for parity and spin. Also, decays to all D states, except to $(6s5d)^1D_2$, are prohibited due to electric-dipole spin selection rule, $\Delta S = 0$, in an LS coupling scheme. The LS coupling scheme for these levels in barium is a good approximation but some singlet-tripling mixing exists (Fursa1999). Consequently, the selection rule for the total angular momentum, $\Delta J = 0, \pm 1$ has to be taken into account. This would eliminate the possibility of decay to $(6s5d)\ ^3D_3$ state. Thus, decays from the optically pumped $(6s6p)^1P_1$ state to $(6s5d)^3D_1$, $(6s5d)^3D_2$ and $(6s5d)^1D_2$ states and to the ground state $(6s^2)^1S_0$ are possible. The $(6s6p)^1P_1$ state predominantly decays to the ground state (99.7%) and only 0.3% decays to the three allowed D states. The branching ratios of the transitions from $(6s6p)^1P_1$ state to these three D states of $(6s5d)\ ^3D_1$, $(6s5d)\ ^3D_2$ and $(6s5d)\ ^1D_2$ are 0.01, 0.29 and 0.69 respectively [Bizzarri1990]. Thus the transition to the $^3D_1$ level can be ignored with 70% of the D state transitions to the $^1D_2$ level and 30% to the $^3D_2$ level.

The D states are metastable states since the transitions from the D states to the ground state are electric-dipole forbidden. The metastable D states have a lifetime of ~

10^{-3} s as compared to ~10^{-9} s for spontaneous emission from the P states. The D states can deexcite by a number of ways, for example, by optical radiation, rare quenching or other types of collisions, such as with the walls of the vacuum chamber.

In this way the pumping cycle continues as the laser pumps the ground state atoms to the P state from where they deexcite to D states, and the remaining P state atoms deexcite back to the ground state to be re-pumped again. Thus the D states become significantly populated. Figure 5.4 shows the process of populating the metastable D states through optical pumping of the P state.

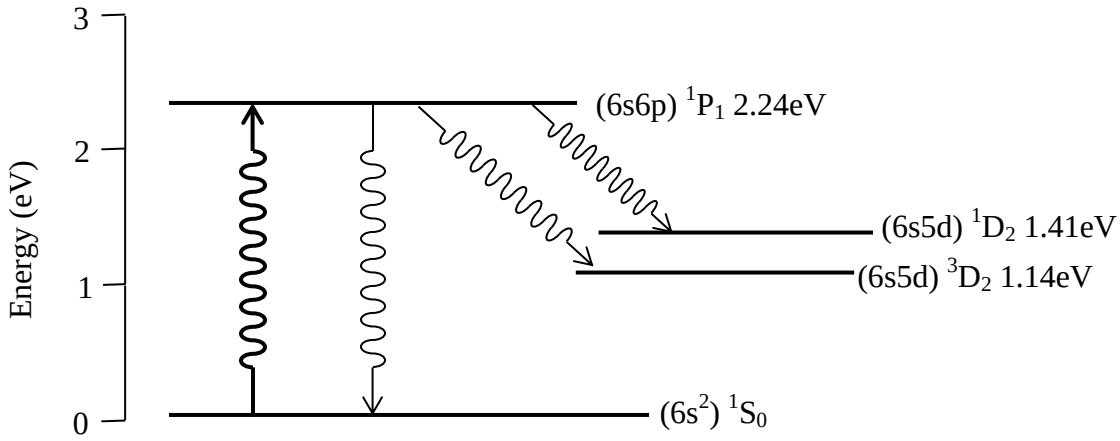

Figure 5.4: Populating metastable D states by optical pumping of the P state.

Due to a well-defined laser linear polarization and propagation direction with respect to the electron beam (quantization) axis, an anisotropic target P state is prepared, where anisotropy means magnetic sublevels are unequally populated. *Alignment* of the anisotropic target P state is said to occur when population of magnetic sublevels, *m* are equal i.e. $n(|J,m\rangle) = n(|J,-m\rangle)$, while *orientation* of the anisotropic target P state occurs

when population of magnetic sublevels are not equal i.e. $n(|J,m\rangle) \neq n(|J,-m\rangle)$. The nature of the target population anisotropy is determined by the polarization state and the direction of the pump laser beam.

Theoretically, the anisotropic target P state should also produce anisotropy of the target D state, since radiative relaxation of the P(m) sub-state to the lower level D(m´) sub-state is determined by the magnetic quantum numbers; m, m´ (as encountered in the Zeeman effect). In fact, the magnetic sublevel populations produced by the radiative P – D relaxation will be determined by the relative line intensities observed in the Zeeman effect, as discussed below.

To be more precise, in the so-called *photon (or light) reference frame* for linearly polarized laser light the quantization axis is along the direction of the electric field vector E of the light beam. Here the pump transition maintains the magnetic sublevel state through the selection rule $\Delta m=0$. So in the present case the m=0 level of the $^1P_1$ state is pumped from $^1S_0$ ground-state. However the electron scattering cross sections are conventionally analyzed, calculated and observed in the *collision reference frame* where the quantization axis is along the direction of the incident electron beam. Thus to describe the results of the present experiment, a rotation needs to be carried out to transform one reference frame to the other. After the rotation to the collision reference frame is performed, the population in the pumped $^1P_1$ state is seen to reside in the m=0 level when the laser polarization lies in the scattering plane and parallel to the incident electron beam direction. When the laser polarization is perpendicular to the incident electron beam direction, the m=+1 and m=-1 levels of the $^1P_1$ state are pumped [Hertel and Stoll1994, Mauk and Hertel1994].

The above mathematical argument of the excitation process to magnetic substates can be explained by taking a more physical view of this excitation process. Consider laser polarization to be defined relative to the axis used to define the magnetic quantum number m, which here is the axis of the incident electron beam. The laser light linearly polarized in this direction can only produce transitions following the selection rules $\Delta l=\pm 1$, $\Delta m=0$ [Grynberg2010]. The laser light polarized perpendicular to this direction can be considered to result from the superposition of right- and left-circularly polarized beams propagating along the quantization axis. These two beams respectively lead to the selection rules $\Delta l=\pm 1$, $\Delta m=+1$ and $\Delta l=\pm 1$, $\Delta m=-1$.

5.2.1 Relative Intensities of Transitions from the $^1P_1$ -state

Theoretically the relative intensities of the magnetic substates are obtained by squaring the matrix element in the transition probability of an electric dipole radiation from an upper state $|J\ m\rangle$ to a lower state $|J'\ m'\rangle$ and is given as,

$$\omega_m \propto \left|\langle J'\ m'|\mathbf{r}|J\ m\rangle\right|^2, \tag{5.1}$$

where **r** connects the substates $m' = m\pm 1$. The non-zero matrix elements squared of these components of **r** has to be determined, as discussed below.

In the present experiment, to populate of the magnetic sublevels of the D state, the laser initially excited the ground state (m=0) atoms to the P state. When the laser polarization was parallel to the electron beam axis (the L0 configuration), it pumped the ground state to m = 0 of the P state. This laser-excited P state can then decay to m = 0, ±1 of the D state. Similarly when the laser polarization was perpendicular to the electron

beam axis (the L90 configuration), it pumped the ground state to $m = \pm 1$ of the P state assumed in the *collision frame*. This laser excited $m = \pm 1$ of the P state can then decay to $m = 0, \pm 1, \pm 2$ of the D state.

The relative populations of magnetic substates in the D state can be determined by the relative intensities of the Zeeman components of a line in electric dipole radiation. As an example, detailed work is shown for relative intensities from $m = +1$ (P state) to $m' = 0, +1, +2$ (D state) transition, followed by a statement of the final results for the relative intensities from$m = -1$ and $m = 0$ of the P state to the allowed magnetic substates of the D state with the condition $\Delta m = 0, \pm 1$.

From $m = +1$ (P state) to $m' = 0, +1, +2$ (D state) transition:

$$\begin{aligned} \omega_0 &\propto \left|\langle J'm'|r|J\ m\rangle\right|^2 \quad m' = 0,\ m = +1 \\ \omega_{+1} &\propto \left|\langle J'm'|r|J\ m\rangle\right|^2 \quad m' = +1,\ m = +1\ . \\ \omega_{+2} &\propto \left|\langle J'm'|r|J\ m\rangle\right|^2 \quad m' = +2,\ m = +1 \end{aligned} \tag{5.2}$$

Considering ω_0 explicitly [Woodgate1970, Table 8.1].

$$\begin{aligned} \omega_0 = \left|\langle 2\ 0|r|11\rangle\right|^2 &= \left|\langle 2\ 0|z|11\rangle\right|^2 + \left|\langle 2\ 0|r_{+1}|11\rangle\right|^2 + \left|\langle 2\ 0|r_{-1}|11\rangle\right|^2 \\ &= 0 + 0 + \frac{1}{2}(\text{J-m+1})(\text{J-m+2})\text{B} \\ &= \frac{1}{2}(\text{1-1+1})(\text{1-1+2})\text{B} \\ \omega_0 &= \text{B} \end{aligned} \quad ,$$

where the quantity B is a function of all quantum numbers (other than m and J) and the radial integral, necessary to describe the state. Furthermore this quantity B will cancel out when finding the relative intensities of the magnetic substates, and hence its specific value is not important in the present context. Similarly,

$\omega_{+1} = 3\mathrm{B}$
$\omega_{+2} = 6\mathrm{B}$

with the condition that,

$$\omega_0 + \omega_{+1} + \omega_{+2} = 1 = 10\mathrm{B} \Rightarrow \mathrm{B} = \frac{1}{10},$$

This gives,

$$\omega_0 = \frac{1}{10};\ \omega_{+1} = \frac{3}{10};\ \omega_{+2} = \frac{6}{10}\ .$$

From *m* = -1 (P state) to *m*′ = 0, +1, +2 (D state) transition:

Likewise from m = -1 (P state) to m' = 0, -1, -2 (D state), with $\Delta m = 0, \pm 1$, the relative intensities are:

$$\omega_0 = \frac{1}{10};\ \omega_{+1} = \frac{3}{10};\ \omega_{+2} = \frac{6}{10},$$

From *m* = 0 (P state) to *m*′ = 0, +1, +2 (D state) transition:

Similarly from m = 0 (P state) to m' = 0, +1, +2 (D state), with $\Delta m = 0, \pm 1$ the relative intensities are:

$$\omega_{-1} = \frac{3}{10};\ \omega_0 = \frac{4}{10};\ \omega_{+1} = \frac{3}{10}.$$

The relative Zeeman intensities discussed above determine the relative m-substate populations in the D state and are tabulated in Table 5.1 and depicted in Figure 5.5. From the table it is clear that theoretically, $n(|J,m\rangle) = n(|J,-m\rangle)$ for the D state and, hence, the D target state population will be aligned by radiative cascade from the P state pumped by linearly polarized laser light.

Table 5.1: Relative population of D state magnetic substates from laser excited P state magnetic substates.

Magnetic substate relative population of D state $\omega_m=N(m)/N(D)$	From P state, $m = -1$	From P state, $m = 0$	From P state, $m = +1$
ω_{-2}	6/10	-	-
ω_{-1}	3/10	3/10	-
ω_0	1/10	4/10	1/10
ω_{+1}	-	3/10	3/10
ω_{+2}	-	-	6/10

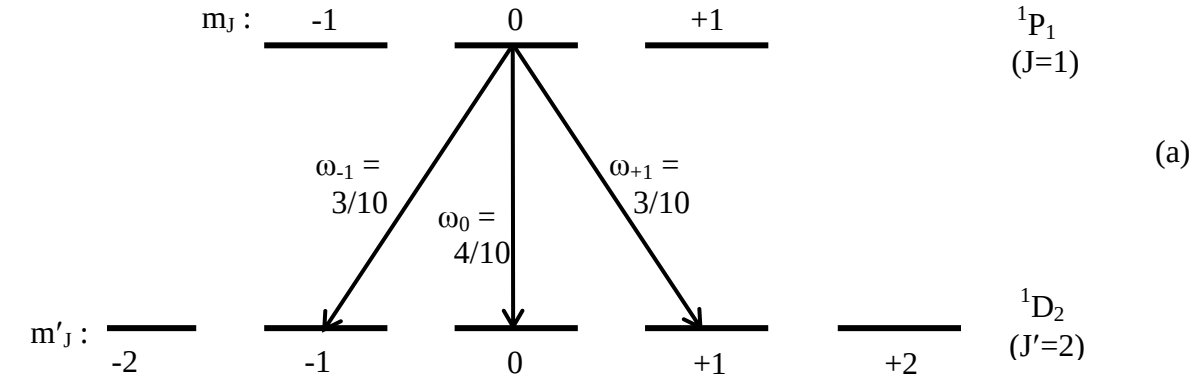

(a)

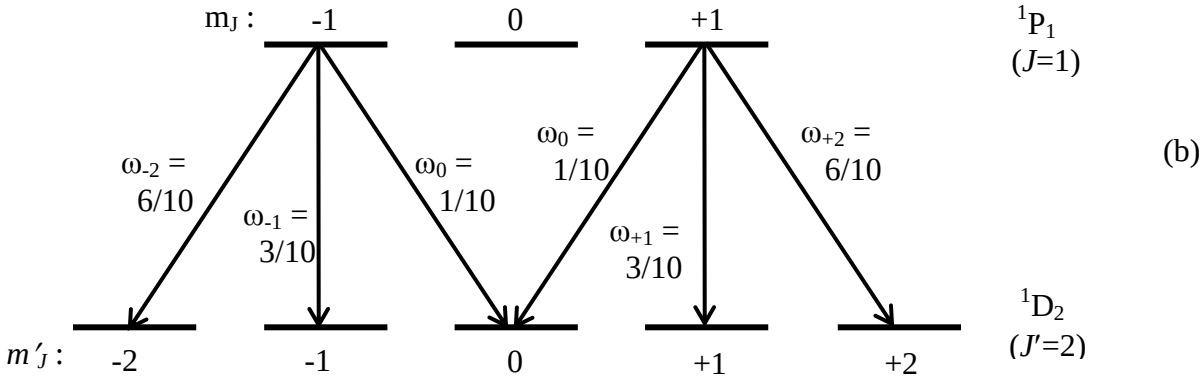

(b)

Figure 5.5: Relative substates intensities of transitions from $^1P_1 \rightarrow {}^1D_2$ with (a) $m = 0$ (b) $m = \pm 1$.

Figure 5.5 summarizes the laser-excited population of substates of the D state. Figure 5.5(a) shows the L0 laser polarization orientation populating 40% of $m'=0$ and 60% of $m'=\pm1$ substates while Figure 5.5(b) shows a more complicated populating scheme for the L90 laser polarization orientation. Here L90 is populating 60% of $m'=\pm2$, 30% of $m'=\pm1$ and 10% of $m'=0$ substates. Note that $m'=0, \pm1$ are populated with either laser polarization.

5.3 Experimental Set up

The general description of the experimental set up is as described in Chapter 3. In this experiment the high intensity gun (HIG) was fixed at 45° to the fluorescence detection axis, and the electron detector was mounted on the turntable of the vacuum chamber. The barium oven was mounted roughly at 90° to the electron gun. The 554 nm laser beam tuned to the S – P transition entered the vacuum chamber from beneath after passing through the optics system as discussed in Chapter 3 and shown in Figure 3.4; it entered the chamber perpendicular to the scattering plane defined by the electron beam axis, atomic beam and the photon detection axis.

The fluorescence detection set up was as follows. The photomultiplier tube (PMT) located outside of the vacuum chamber was aligned to the fluorescence detection axis defined by the 7 cm focal length lens using the two-pin assembly. Details are given in Chapter 3. A sequence of optics was mounted in front of the PMT to select the fluorescence reaching the PMT. An interference filter with a 581 nm centre wavelength (CWL) and a 1.0 nm bandpass passed the fluorescence from the P to D state, while a

notch filter with a 555 nm CWL and a 5 nm band-reject width blocked the laser-induced fluorescence (LIF). The last elements before the PMT were the polarizer and the quarter-wave plate to detect the polarization of the detected fluorescence. The reason for this assembly of polarizer and quarter-wave plate is explained earlier in the experimental chapter, Section 3.7.

The 583 nm line fluorescence observation state is denoted by Pϕ, with P0 referring to the polarizer oriented parallel and P90 with the polarizer oriented perpendicular to the electron-photon (583 nm photon) plane. Similarly for the polarization selection of the 554 nm laser-excited P state, Lψ denotes the laser polarization state with respect to the electron beam axis. The desired laser polarization is selected by a λ/2-plate; L0 refers to laser polarization parallel and L90 refers to polarization perpendicular to the electron beam axis. Figure 5.6 shows all four polarization geometries. In Figure 5.6(a) the current set up is shown where the 583 nm fluorescence detection axis i.e. the PMT axis is at 45° to the electron beam axis. Conventionally, the PMT axis is set at 90° with respect to the electron beam axis as shown in Figure 5.6(b). Thus to compare the present work with other experiments and with the theory, a transformation from 45° to 90° angle between the PMT axis and the electron beam axis was carried out.

The transformation relation of measured line emission intensity at θ=45° to line emission intensity at θ=90° is explained in detail by [Hein2010] and given by:

$$I_{90}^{P0} = \frac{1}{sin^2\theta}\left[I_{\theta}^{P0} - I_{\theta}^{P90}cos^2\theta\right], \text{ and} \tag{5.3a}$$

$$I_{90}^{P90} = I_{\theta}^{P90} \equiv I^{P90}, \tag{5.3b}$$

with $I_{90}^{P0} = I_{\parallel}$; $I_{90}^{P90} = I_{\perp}$ as in Figure 4.2.

With θ=45°, as in the present experiment, Equation (5.3a) reduces to:

$$I_{90}^{P0} = [2I_{45}^{P0} - I_{45}^{P90}]. \tag{5.4}$$

This relation was used in subsequent data analysis.

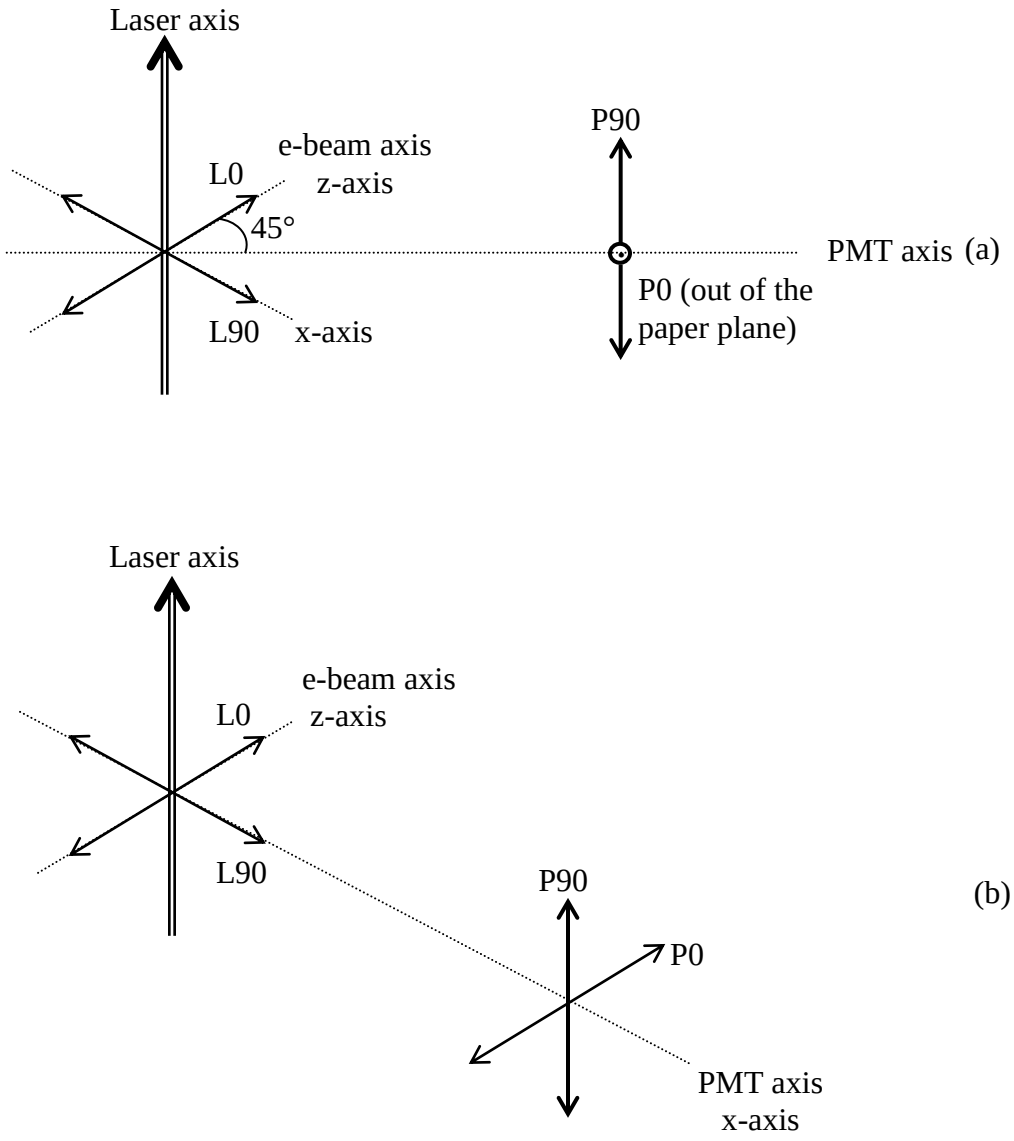

Figure 5.6: Laser and fluorescence polarization geometries in the (a) present experiment (b) Conventional set up.

In order to prepare the laser-excited D state target atoms, a special laser alignment procedure was introduced. Since the optically pumped P state atoms are short lived, the principle was to do the optical pumping upstream in the atomic beam and allow the excited atoms to drift downstream before encountering the electron beam at the interaction region. The longer-livedD state atoms would then be the predominant excited state species probed by the electron beam.

Before the experimental data were taken, the laser beam was introduced into the vacuum chamber and focused on the interaction region. The superelastic scattering feature of the $(6s6p)^1P_1 \rightarrow (6s^2)^1S_0$ [ΔE = -2.24 eV] transition could be seen in the energy loss spectrum, indicating successful optical pumping of the $(6s6p)^1P_1$ state. Gradually the laser beam axis was translated upstream along the barium atomic beam axis using the mirrors until the superelastic scattering feature of $(6s6p)^1P_1 \rightarrow (6s^2)^1S_0$ disappeared from the energy loss spectrum. This was verified by comparing the EELS spectra with the pumping laser ON and OFF. At this position of the laser then, there were no $(6s6p)^1P_1$ state atoms in the interaction region. Thus, the atomic beam target consisted of metastable D state atoms as well as ground- state atoms at the interaction region with the electron beam.

Table 5.2: Measurement Scheme: L0 and L90 denote laser polarization parallel and perpendicular to the electron beam direction, while P0 and P90 denote the polarizer oriented parallel and perpendicular to the electron-photon plane.

Data Sequence Number	Laser Polarization Configuration	583 nm Fluorescence Polarization Configuration	Comments	Electron Gun ON / OFF
1	L0	P0		ON
2	L0	P90		
3	L90	P90		
4	Loff	P90		
5	L90	P0		
6	Loff	P0		
7	L0	P0	redundant	
8	L0	P0		OFF
9	L0	P90		
10	L90	P90		
11	Loff	P90		
12	L90	P0		
13	Loff	P0		
14	L0	P0	redundant	

5.3.1 Data Acquisition

The multi-channel-scaler (MCS) based data acquisition system was used to collect and process the data. A measurement protocol was developed to include all combinations of laser and fluorescence polarizations and redundant checks. Table 5.2 shows the measurement sequence used in the current experiment. The experiment was carried out for five electron impact energies from 10 – 50 eV in steps of 10 eV.

The electron energy loss spectrum (EELS) was recorded simultaneously with the photon counts in an independent MCS. A sample barium EELS for 1 data run at 40 eV electron impact energywith laser ON and OFF is shown in Figure 5.7 . As shown in the figure, the energy resolution here is approximately 0.5 eV FWHM as determined by the HIG, with a typical electron beam current of 1.5 μA. To determine the population of the laser-excited barium metastable D state, the $(6s^2)^1S_0 \rightarrow (6s6p)^1P_1$ at 2.24 eV feature was used. According to the analysis outlined in Section 5.5, the D state population for the single run (5 minutes) at 40 eV data shown in Figure 5.7 was (13 ± 2) %.

In principle, any feature that indicates depletion of the ground-state in an EELS can be used to estimate the D state population as long as there are no unresolved laser-excited transitions to confuse the interpretation. It can be seen in Figure 5.8 that the other feature $(6s^2)^1S_0 \rightarrow (6s5d)^1D_2$ at 1.41 eV is not depleted by the same ratio as feature $^1S_0 \rightarrow {}^1P_1$. The explanation is that there are unresolved laser-excited transitions contributing to the $(6s^2)^1S_0 \rightarrow (6s5d)\ ^1D_2$ feature which can be seen in the high-resolution spectrum of Figure 5.8 [Register1978], also taken with a similar optical pumping scheme. In Figure 5.8, feature 19 is the ground-state $(6s^2)^1S_0 \rightarrow (6s5d)^1D_2$ (1.41 eV) transition where it is isolated somewhat when the laser is OFF (upper figure), but when the laser is

ON (lower figure), there are several additional laser-excited features within ~ 0.5 eV shown in the dashed box in the figure. In contrast, feature 27 which is the $(6s^2)^1S_0 \rightarrow (6s6p)^1P_1$ (2.24 eV) transition, is by far the dominant transition in both laser OFF and ON spectra within ~ 0.5 eV, again shown in the dashed box in the figure. Thus the depletion ratio of the $(6s^2)^1S_0 \rightarrow (6s6p)^1P_1$ (2.24 eV) feature due to laser ON and OFF was taken to determine the population of the laser-excited barium metastable D state as the target state for electron excitation.

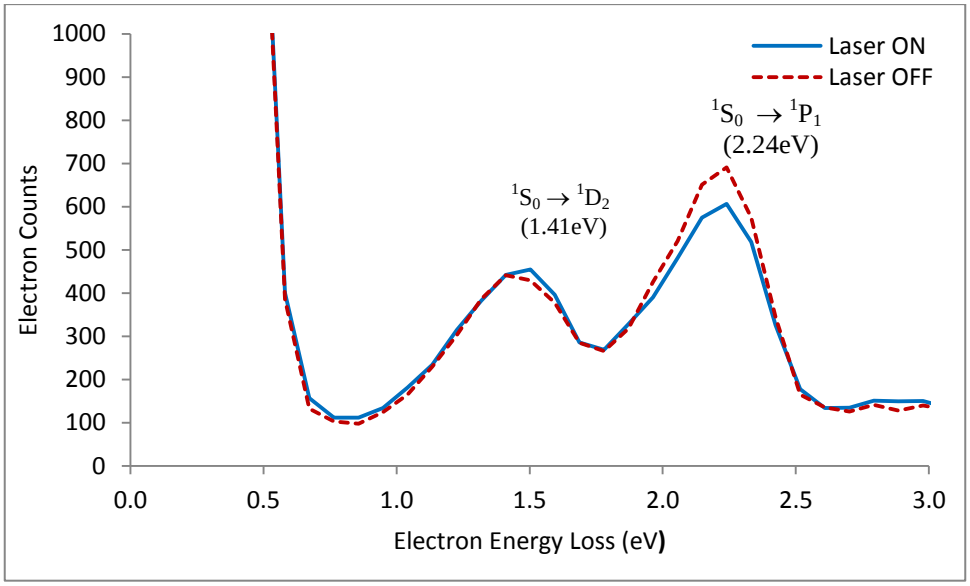

Figure 5.7: Sample EELS of barium at 40 eV electron impact energy.

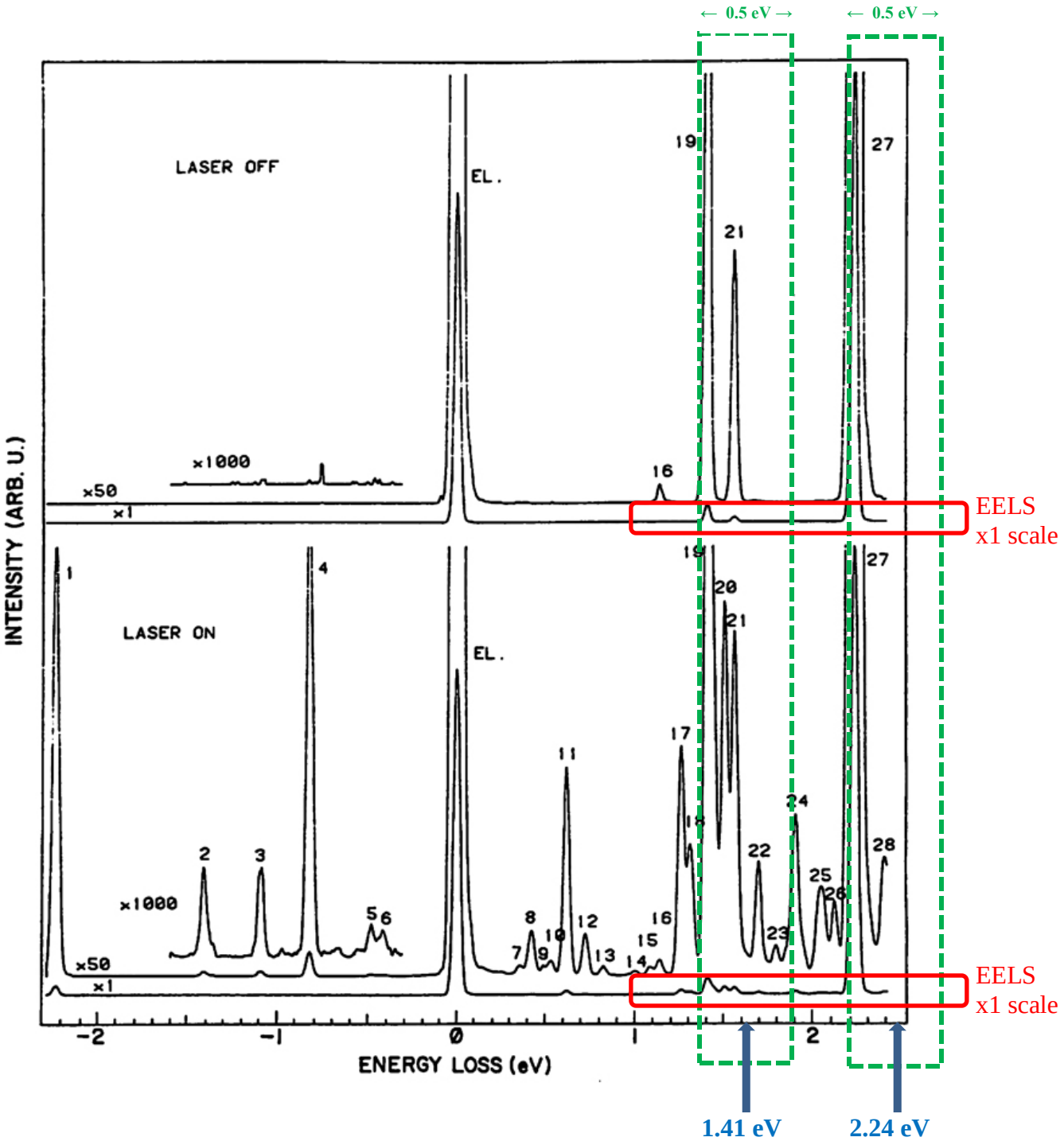

Figure 5.8: High resolution EELS of optically pumped barium with pumping laser OFF (upper) and ON (lower) along with magnifications [Register1978]. The central feature at zero energy loss corresponds to the elastic scattering peak, and the bold arrows show the peaks of interest for the present experiment. The dashed boxes show 0.5 eV energy spread, and the solid boxes highlight the EELS on x1 scale.

The photon counts of the 583 nm $(6s7p)^1P_1 \rightarrow (6s5d)^1D_2$ transition were collected in the other MCS. A typical fluorescence data sequence run is shown in Figure 5.9. Each data run consisted of 14 sampling intervals with selected laser and fluorescence polarizer settings with both electron gun on and off. Each sampling channel was 200 ms duration, hence taking around 5 minutes to complete one measurement cycle (Table 5.2); instantaneous counting rates were on the order of 1.2 – 1.5 kHz. These fluorescence data were used in studying the polarization and in calculating the integral cross section of the 583 nm radiative line.

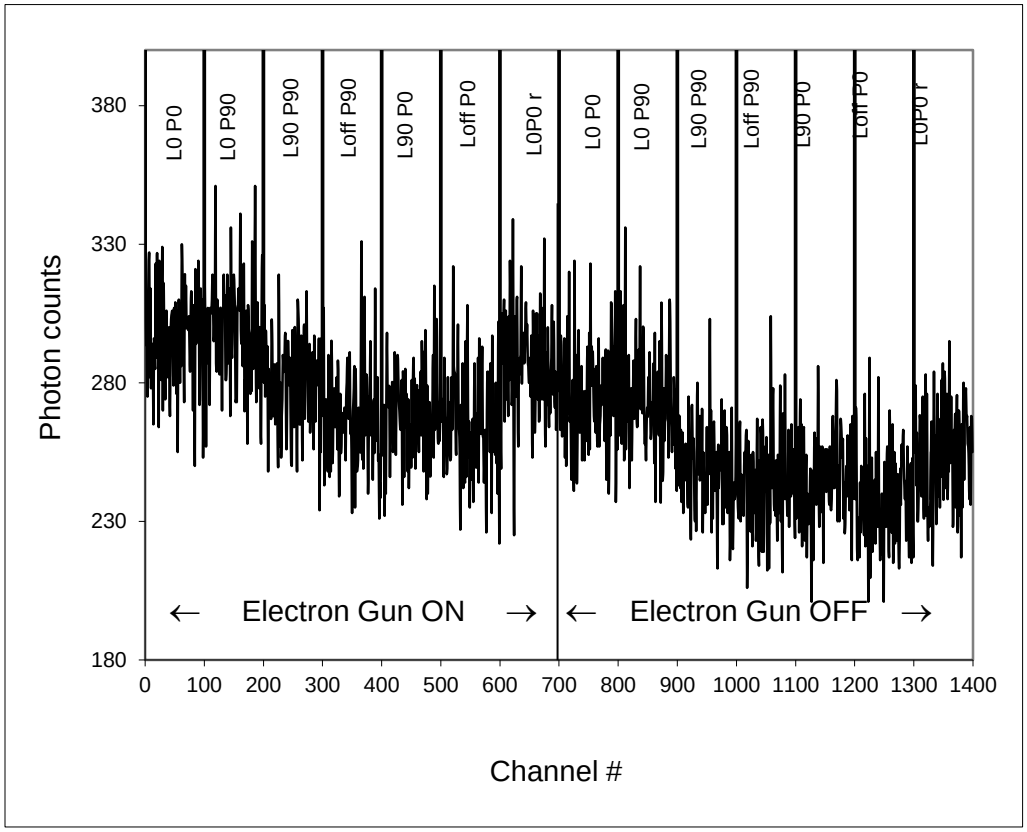

Figure 5.9: Raw 583 nm fluorescence MCS data at 40 eV incident electron energy, with the data sequence as specified in Table 5.2. The vertical bands at 100 channel increments separate the different experimental polarization configurations. Counting time: 200 ms/channel.

5.3.2 Determination of Laser and Fluorescence Polarization Angles

The high intensity electron gun (HIG) beam energy was calibrated by using the helium ^{2}S elastic scattering resonance at 19.37 eV [Schultz1973]. The calibration showed a value of 19.14 eV, which is less than the resonance energy by 0.23 eV. This offset was taken into account for all incident electron energies during the experiments.

For calibrating the laser polarization orientation Lψ, the laser induced fluorescence (LIF) at 554 nm was observed by the PMT system through highly attenuating neutral density filters with the PMT polarizer fixed. A stepping motor attached to a λ/2-plate rotated the plane of polarization of the laser beam. The resulting laser induced fluorescence (LIF) intensity as a function of the laser polarization orientation is shown in Figure 5.10. The minima and maxima indicate the alignment of the laser polarization parallel to and perpendicular to the PMT axis respectively, as illustrated in Figure 5.6(a). The sinusoidal intensity function, Equation (4.6), was fitted to the data of Figure 5.10 to determine the polarization and locations of intensity maxima and minima. Using statistical error bars $\sqrt{N}$ for each data sample, the fit yielded $\sqrt{\frac{\chi^2}{df}}$ of 2.2 with polarization of 0.43±0.01. The minima and maxima positions occur at channel 25 and 77 respectively with periodicity of 100 channels.

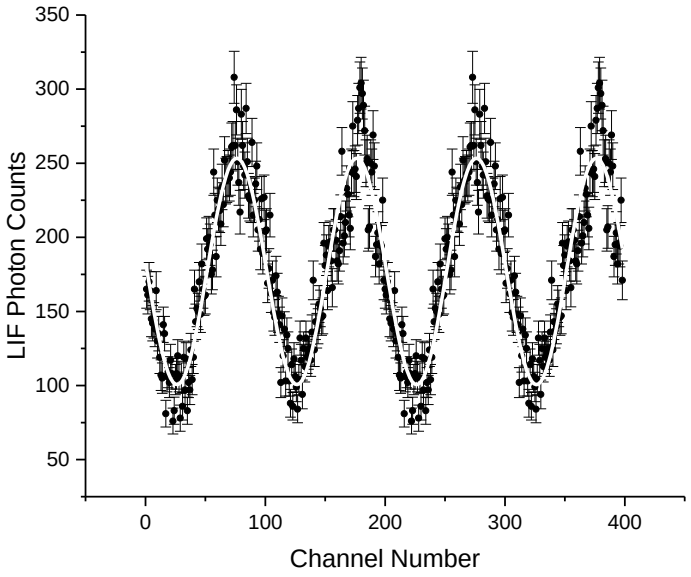

Figure 5.10: Fitted 554 nm laser induced fluorescence (LIF) intensity as a function of the laser polarization orientation. Horizontal axis: 1 channel number = 1.8°.

Similarly, in order to calibrate the fluorescence Pϕ angles, the PMT polarizer was rotated by its associated stepper motor to obtain the LIF sinusoidal intensity function for a fixed laser polarization direction. Figure 5.11 shows the measured LIF as a function of PMT polarizer angle. The minima show the PMT-polarizer pass-axis parallel to the laser propagation direction, while the maxima show the PMT-polarizer pass-axis perpendicular to the laser propagation direction. From these measurements, the polarizer angle settings for P0 and P90 were determined. The sinusoidal intensity function, Equation (4.6), was fitted also to the data of Figure 5.11, to determine the polarization and locations of intensity maxima and minima. Using statistical error bars $\sqrt{N}$ for each data sample, the fit yielded $\sqrt{\frac{\chi^2}{df}}$ of 2.2 with polarization of 0.67±0.01. The minima and maxima positions occur at channel 130 and 312 respectively with periodicity of 355 channels.

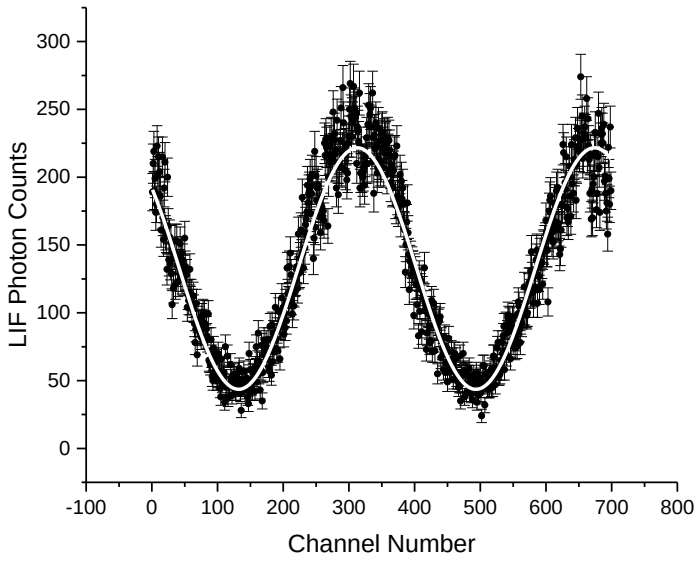

Figure 5.11: Fitted 554 nm laser induced fluorescence (LIF) intensity as a function of the PMT polarizer orientation. Horizontal axis: 1 channel number = 0.51°.

The laser induced fluorescence (LIF) measurements in Figure 5.10 and Figure 5.11 were set up with the PMT polarizer angle adjusted for maximum intensity during the laser scan, and with the laser polarization angle set for maximum intensity during the PMT scan. Ideally both sets of scans should yield the same value of the LIF polarization. A misalignment of the fixed polarization axis for either case yields a measurement that is systematically low by a factor of $\cos^2\alpha$ where α is the angle between the actual and optimal alignment settings. Taking the alignments to be optimal for Figure 5.11, $P_{LIF} = 0.67 \pm 0.01$ was taken for the measurements.

5.4 Derivations of Equations for Relative Population of the Laser-Excited D state and Relative Cross Section

In the following sections, the population (Δ) of the laser-excited barium metastable D state is discussed, followed by a discussion of determination of the relative cross section $\sigma_{DS} = \frac{\sigma_D}{\sigma_S}$ for the 583 nm line transition excited by electron impact out of the metastable D state. A schematic of the relevant atomic states of barium indicating the energy levels and fluorescence transitions, electron excitation cross sections (σ_S and σ_D) and atomic state populations (Σ and Δ) is shown in Figure 5.12.

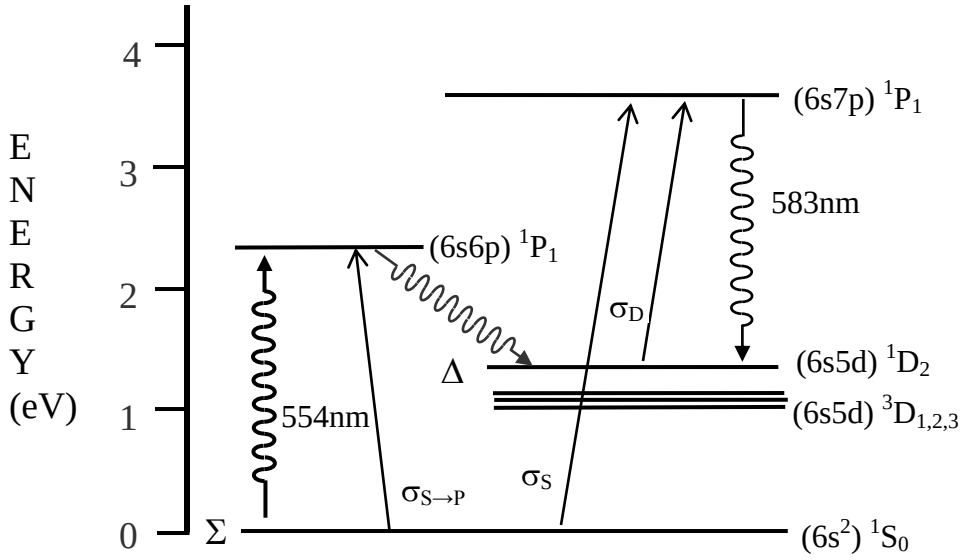

Figure 5.12: Energy level diagram of barium showing relevant fluorescence and electron impact excitation transitions. Σ and Δ are the fractional population of atoms in S and D states and σ_S and σ_D are the corresponding electron excitation cross sections respectively, while $\sigma_{S\rightarrow P}$ is the ground state electron excitation cross section of the optically pumped $^1P_1$ state.

5.4.1 Population of the Laser-Excited Metastable D State

Let the fractional population of atoms in S and D states be denoted by:

$$\Sigma = \frac{N_S}{N} \quad \text{and} \quad \Delta = \frac{N_D}{N}, \tag{5.5}$$

$$\text{with} \quad N_S + N_D = N, \tag{5.6}$$

where, N is the total atomic target population
N_S is the S-state population
N_D is the D state population.

The above ratios are bounded by the constraint:

$$\Sigma + \Delta = 1. \tag{5.7}$$

When the laser beam is OFF, the number of ground-state atomic targets in the interaction region is N and when the laser beam is ON, this number is depleted by the amount N_D. To use the EELS as a measure of fractional D state population, Δ, the following procedure was applied.

Let the integral of the 2.24 eV peak in the EELS spectrum (Figure 5.7) be denoted by i (2.24), which corresponds to the $^1S_0 \rightarrow {}^1P_1$ transition indicated with cross section $\sigma_{(S\rightarrow P)}$ in Figure 5.12 . Then,

$$i_{ON}^{L\Psi}(2.24) = K\ \Sigma^{L\Psi}\sigma_{(S\rightarrow P)}, \text{ and} \tag{5.8}$$

$$i_{OFF}(2.24) = K\ \sigma_{(S\rightarrow P)}, \tag{5.9}$$

where, assuming stable electron and atomic beams for the laser ON and OFF measurements, the common factor K accounts for the electron and atomic beam densities, the electron spectrometer acceptance and efficiency, and the data acquisition time.

Dividing Equation (5.8) by Equation (5.9), yields:

$$\Sigma^{L\Psi} = \frac{i_{ON}^{L(\psi)}(2.24)}{i_{OFF}(2.24)}, \tag{5.10}$$

and thus from Equation (5.7):

$$\Delta^{L\Psi} = 1 - \frac{i_{ON}^{L(\psi)}(2.24)}{i_{OFF}(2.24)}. \tag{5.11}$$

Equation (5.11) will be used to determine the laser-excited metastable D state population in the data analysis.

5.4.2 583 nm Line Emission Cross Section from the Laser-Excited D State relative to the Ground-State

The laser ON fluorescence signal for laser state Lψ and fluorescence polarizer state Pϕ is given by:

$$I_{ON}^{L\psi P\phi} = K'\,(\,\Sigma^{L\psi}\sigma_s^{P\phi} + \Delta^{L\psi}\sigma_D^{L\psi P\phi}), \tag{5.12}$$

where K′ is an experimental proportionality constant accounting for the laser intensity, the incident electron flux, the atomic target density, the PMT solid angle, fluorescence detection efficiency and data acquisition time. $\Sigma^{L\psi}$ and $\Delta^{L\psi}$ are the relative populations of the ground-state and D state respectively for the various laser-polarization geometries, and σ_s, σ_D are the electron excitation cross sections as indicated in Figure 5.13.

Now, since:

$$\Sigma^{L\psi} + \Delta^{L\psi} = 1, \tag{5.13}$$

when the laser is OFF, $\Sigma = 1$ (i.e. $\Delta = 0$), Equation (5.12) becomes:

$$\mathrm{I}_{\mathrm{OFF}}^{\mathrm{P}\phi} = \mathrm{K}'\,\sigma_s^{\mathrm{P}\phi}\ . \tag{5.14}$$

Accounting for the 45° PMT measuring angle as discussed in Section 5.3, the polarization-averaged ground state cross section is given by:

$$\langle \sigma_s \rangle \equiv \frac{2\sigma_s^{\mathrm{P0}} + \sigma_s^{\mathrm{P90}}}{3}. \tag{5.15}$$

Using Equation (5.14) and Equation (5.15) we can define the polarization-averaged line intensity by excitation out of the ground state as:

$$\langle I_{OFF} \rangle \equiv \frac{2I_{OFF}^{\mathrm{P0}} + I_{OFF}^{\mathrm{P90}}}{3} = K' \langle \sigma_s \rangle. \tag{5.16}$$

Dividing Equation (5.12) by Equation (5.16) gives:

$$\frac{\mathrm{I}_{\mathrm{ON}}^{\mathrm{L}\psi\mathrm{P}\phi}}{\langle I_{OFF} \rangle} = \frac{\Sigma^{\mathrm{L}\psi}\sigma_s^{\mathrm{P}\phi}}{\langle \sigma_s \rangle} + \frac{\Delta^{\mathrm{L}\psi}\sigma_D^{\mathrm{L}\psi\mathrm{P}\phi}}{\langle \sigma_s \rangle}. \tag{5.17}$$

Rearranging Equation (5.17) with equations (5.13) and (5.14), gives the relative cross section as:

$$\sigma_{DS}^{\mathrm{L}\psi\mathrm{P}\phi} \equiv \frac{\sigma_D^{\mathrm{L}\psi\mathrm{P}\phi}}{\langle \sigma_s \rangle} = \frac{1}{\Delta^{\mathrm{L}\psi} \langle I_{OFF} \rangle} \left[\mathrm{I}_{\mathrm{ON}}^{\mathrm{L}\psi\mathrm{P}\phi} - \left(1 - \Delta^{\mathrm{L}\psi}\right) I_{OFF}^{\mathrm{P}\phi} \right]. \tag{5.18}$$

The above Equation (5.18) gives the relative line emission cross section in terms of the fluorescence intensities and the relative population of the laser excited metastable D state, determined earlier through Equation (5.11).

5.4.3 Correction for Laser Polarization

Ideally the 554 nm laser induced fluorescence (LIF) should be 100% polarized, indicating 100% laser polarization, but in the present experiment the polarization was significantly lower (67% as seen in Figure 5.11). Assuming that the LIF and laser polarizations were

identical the measured relative cross sections obtained from Equation (5.18) were corrected for the laser polarization using the relation [Hein2010]:

$$[\sigma_{DS}^{L\psi P\phi}]_{Measured} = P_{Laser}[\sigma_{DS}^{L\psi P\phi}]_{True} + (1 - P_{Laser})[\sigma_{DS}^{P\phi}]_{Average}, \qquad (5.19)$$

with $P_{Laser} = P_{LIF}$ assumed and where $[\sigma_{DS}^{L\psi P\phi}]_{True}$ is the corrected relative cross section reported in the present work as $\sigma_{DS}^{L\psi P\phi}$.

5.5 Data Analysis

The data analysis was carried out separately for the electron data and the photon data. From the electron data, the population of the laser-excited target D states was determined. The D state populations were used along with the photon data to determine the cross sections. These two data analyses are described first, and then the analysis in determining the relative cross section is described.

5.5.1 Electron Data Analysis

As discussed in Section 5.3.1, the depletion ratio of the 2.24 eV peak with laser ON and laser OFF determines the laser-excited D state population, the target state of interest for electron excitation studies. For each of the five electron impact energies studied, there were approximately 30 measurement data files, and each data file contained 14 separate experimental configurations (Table 5.2). Thus for each energy, more than 200 EELS graphs were analysed and 2.24 eV EELS peaks were integrated. Signal to background

ratios in the windows of integration were typically 0.10. As an example, an L90 EELS sample for 30 eV, configurations L90P0 and L90P90 along with LoffP0 and LoffP90 is shown in Figure 5.13. Since the target population is independent of the fluorescence polarization, EELS data for the two fluorescence polarization configurations were averaged and substituted in Equation (5.9) to obtain the population Δ^{L90}. For this example, $\Delta^{L90} = 0.194 \pm 0.213$.

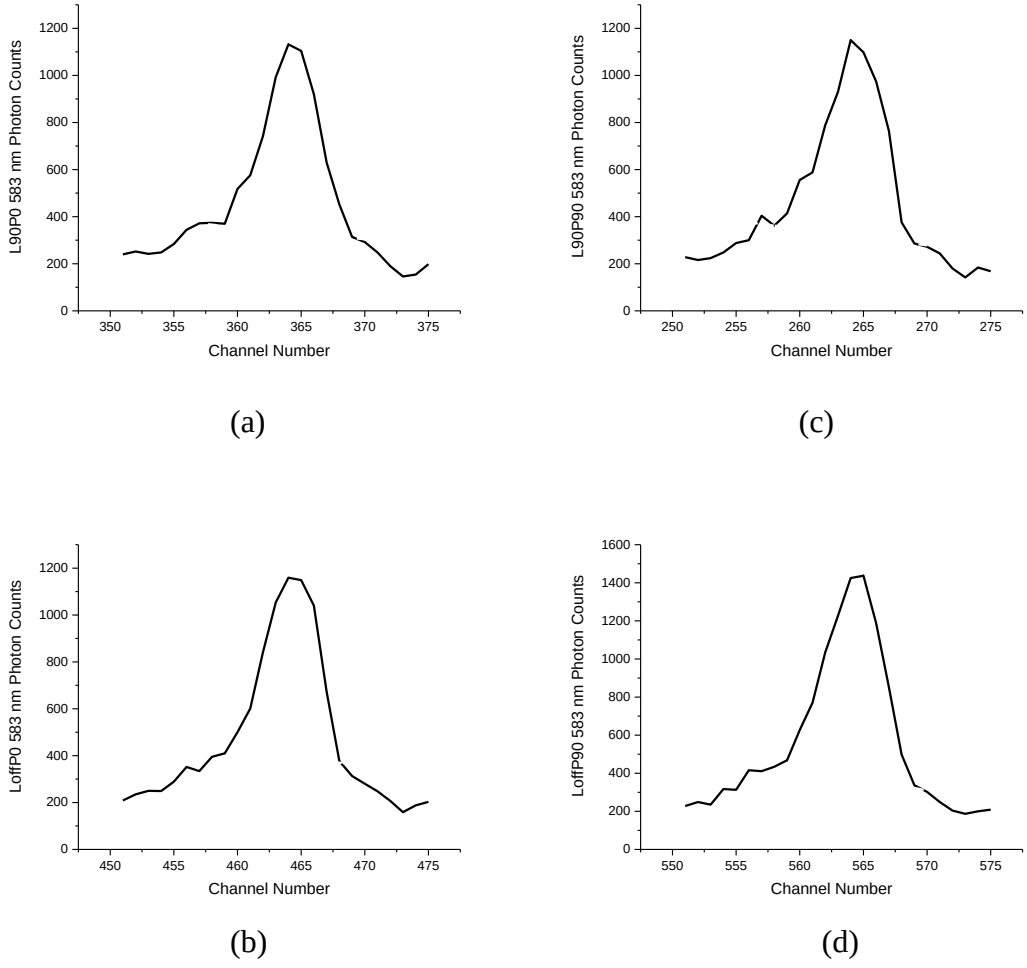

Figure 5.13: EELS sample showing the 2.24 eV peak used to determine the target D state population for a typical data run at 30 eV. Panel (a) L90P0 configuration; (b) LoffP0; (c) L90P90; (d) LoffP90.

Figure 5.14 presents a typical data run at 10 eV showing the integrated electron peak counts for each laser polarization state of the data sequence. One can see evidence of randomly varying counting rates that change at several times the assigned statistical error bars. Since the photon counts of interest are acquired simultaneously, the most important variation is that in the laser off electron rate, measured in states 4 and 6 of the sequence. To account for the extra variability, the errors in the laser OFF measurements were taken as a quadrature sum of the statistical counting error and the spread in the integrated counts for laser OFF in two supposedly identical runs, determined as half the difference between the two. The horizontal dashed band shows the spread in laser OFF in Figure 5.14.

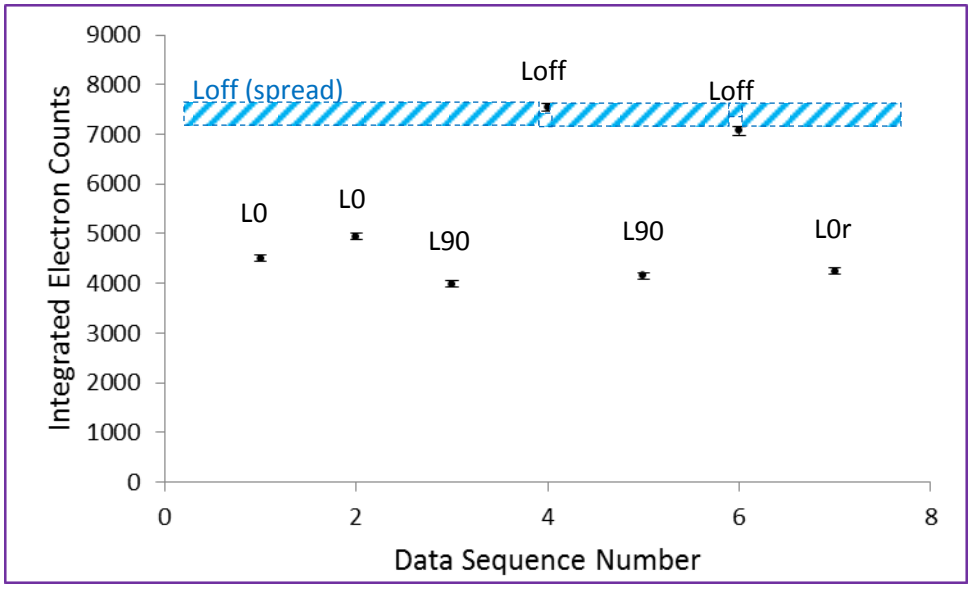

Figure 5.14: Typical measurement run of the data sequence at 10 eV showing the integrated 2.24 eV electron peak for each laser polarization state.

The laser-excited D state populations for both laser polarizations, L0 and L90, were calculated using Equation (5.11) for each measurement with errors as described above. Figure 5.15 shows a typical Δ^{L0} population data set for electron impact energy of 50 eV. From the experiments carried out previously on laser-excited barium from this AMO laboratory [Hein2010], the D state population can be up to 20%. In Figure 5.15 some runs show a higher population, but the majority of them lie between 0 – 20 % within error. Any measurement with a negative population was discarded from further analysis as those results are unphysical.

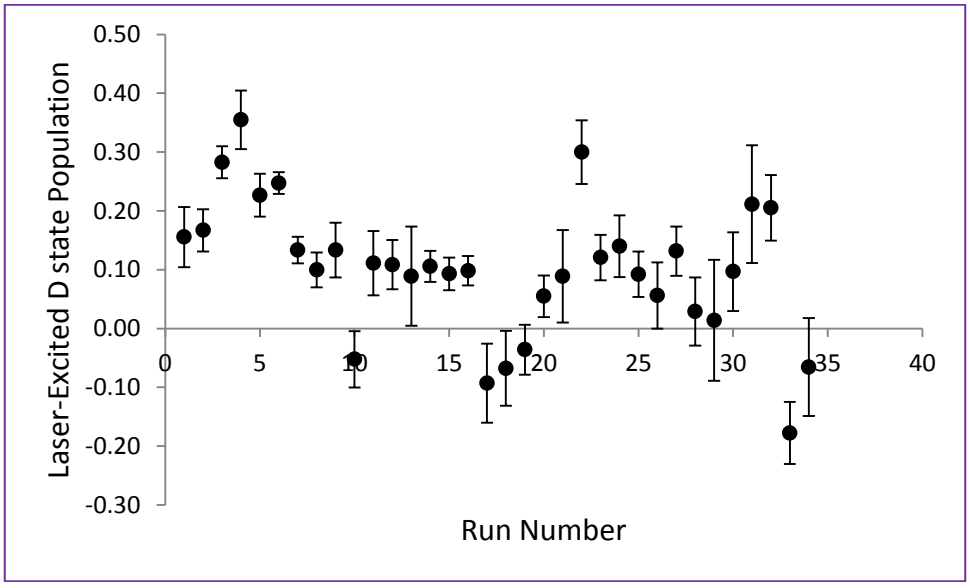

Figure 5.15: Full 50 eV data set of laser-excited D state population Δ^{L0}.

5.5.2 Photon Data Analysis

Recall that photon data were collected simultaneously along with the corresponding electron data in a separate MCA. The photon analysis was carried out by first summing all counts in a certain measurement configuration for each data run. Figure 5.16(a) shows typical photon summed counts at 10 eV for a particular data run, and Figure 5.16(b) shows the corresponding background-subtracted photon-summed signal. The integration time is 20 sec for each data point (100 channels x 200 ms/channel). Error bars are based on counting statistics for the summed photon counts in each data sequence state. It is evident that there is a large background at 583 nm measured with the electron gun off for these data.

For the present barium photon data because of the substantial background, it was deemed important to investigate the photon signal-to-background (S/B) ratio. The photon S/B ratio is shown in Figure 5.17(a) for the L90P90 configuration of the 50 eV dataset, which exhibited the most stable running conditions. The S/B ratio shows almost a constant average ratio of around 12%. As another example, Figure 5.17(b) shows the same S/B ratio for the 10 eV data set. Reasons for the additional variation at 10 eV are not clear.

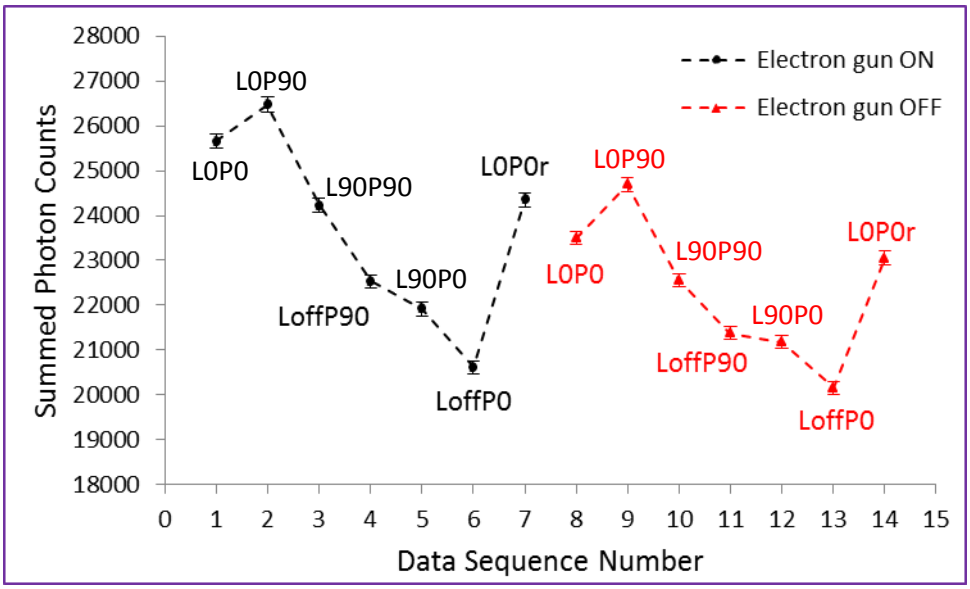

(a)

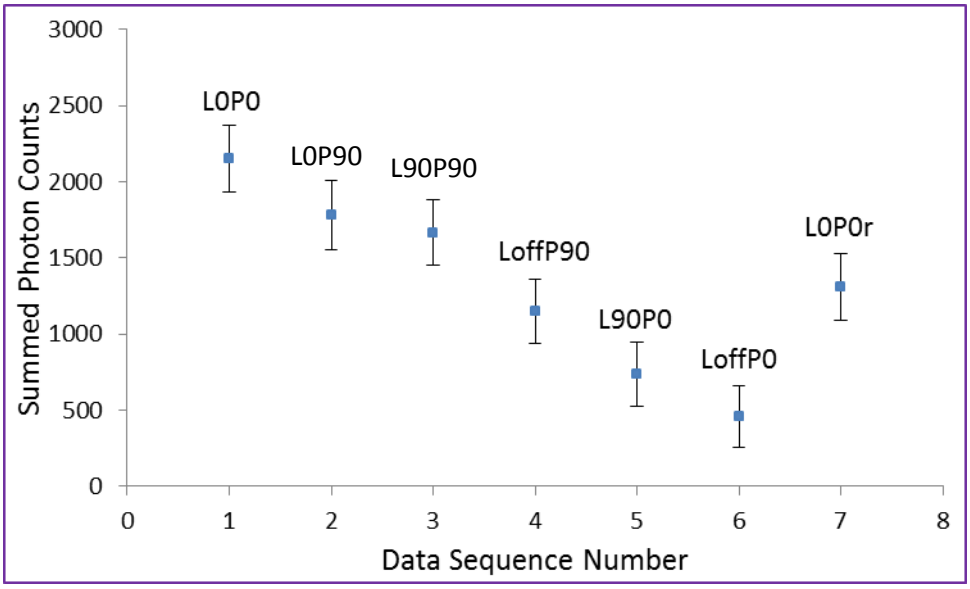

(b)

Figure 5.16: Summed 583 nm photon counts for a typical data run at 10 eV versus data sequence number, with labels corresponding to Table 5.2. Integration time: 20 sec per state. Panel (a) Full 14-state data sequence; panel (b) Background-subtracted counts by subtracting gun OFF from gun ON data.

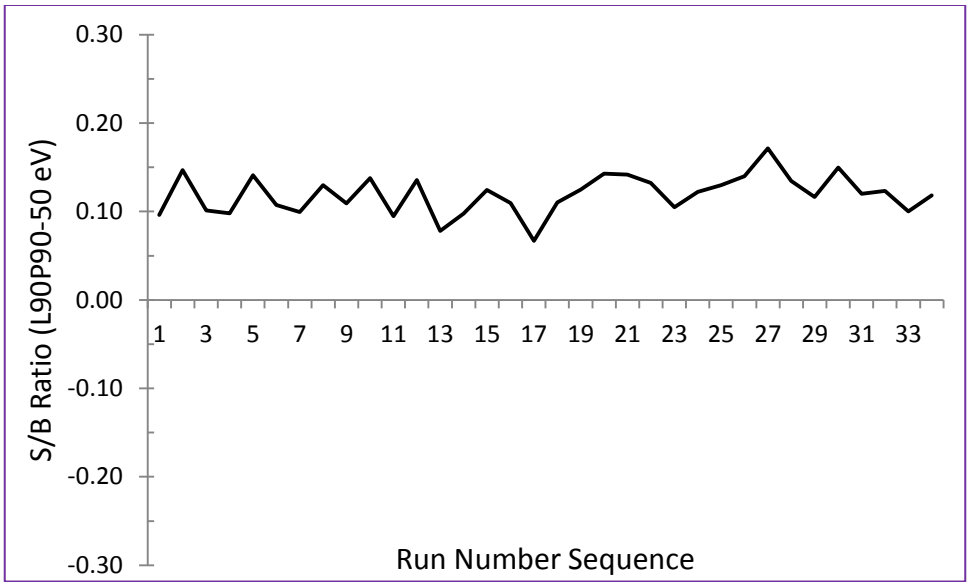

(a)

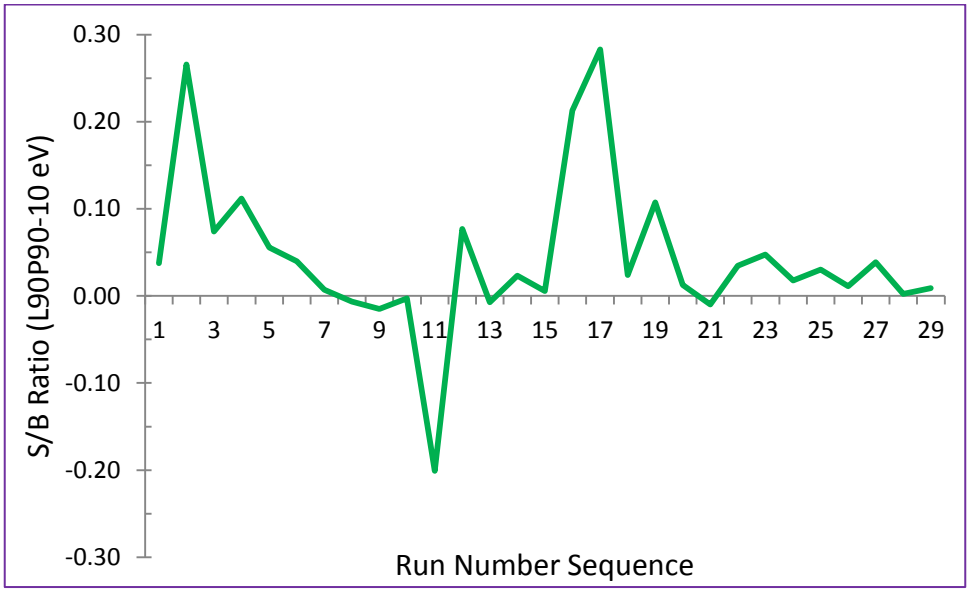

(b)

Figure 5.17: (a) L90P90 graph of 583 nm signal-to-background ratio for the 50 eV dataset. (b) L90P90 graph of 583 nm signal-to-background ratio for the 10 eV dataset.

Equation (5.18) indicates that for stable running conditions,

$$I_{ON}^{L\psi P\phi} = \left[\sigma_{DS}^{L\psi P\phi}\left\langle I_{OFF}\right\rangle - I_{OFF}^{P\phi}\right]\Delta^{L\psi} + I_{OFF}^{P\phi} \qquad (5.20)$$

A graph of the photon signal counts for all 40 eV data in the L90P0 configuration versus laser-excited D state population Δ^{L90} is shown in Figure 5.18. For the integration time of 20 sec per point, the average signal rate for these data is about 75 Hz (1500 counts/20 sec). The signal rate scales approximately with population as expected from Equation (5.20) and indicated by the fitted line in Figure 5.18. From all of the above analysis it was deemed fit to calculate the relative cross section on a measurement by measurement basis.

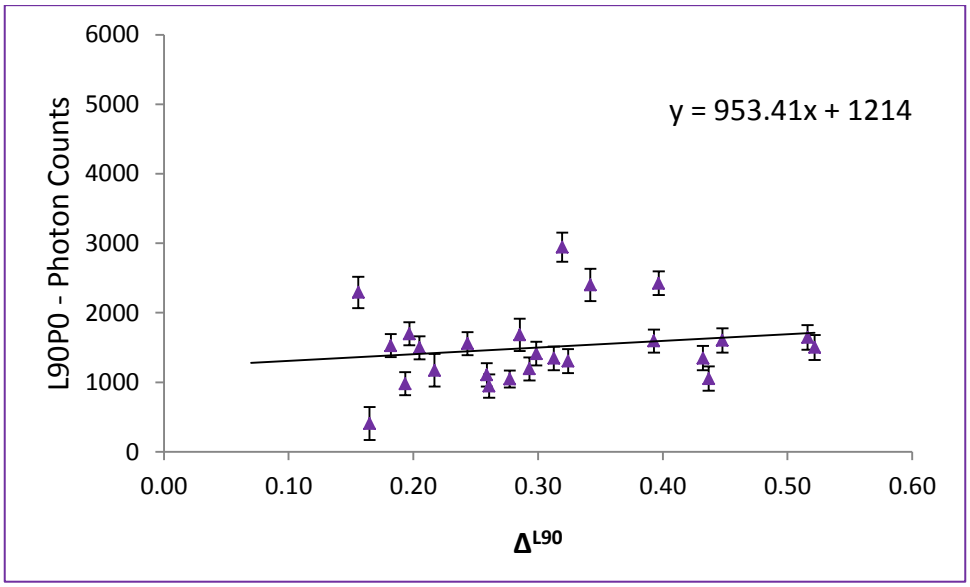

Figure 5.18: Photon signal counts for the L90P0 configuration versus laser-excited D state population for 40 eV. Solid line shows the linear fit of Equation (5.20).

5.5.3 Calculation of the Relative Cross Section

After calculating the relative population of the laser-excited D state and analyzing the photon data, the relative cross section (RCS) was calculated. This was done for each of the four laser and 583 nm fluorescence polarization combinations on a measurement by measurement basis for all energies using Equation (5.18). A graph of the relative cross section for all 40 eV data in the L90P0 configuration versus run number is shown in Figure 5.19.

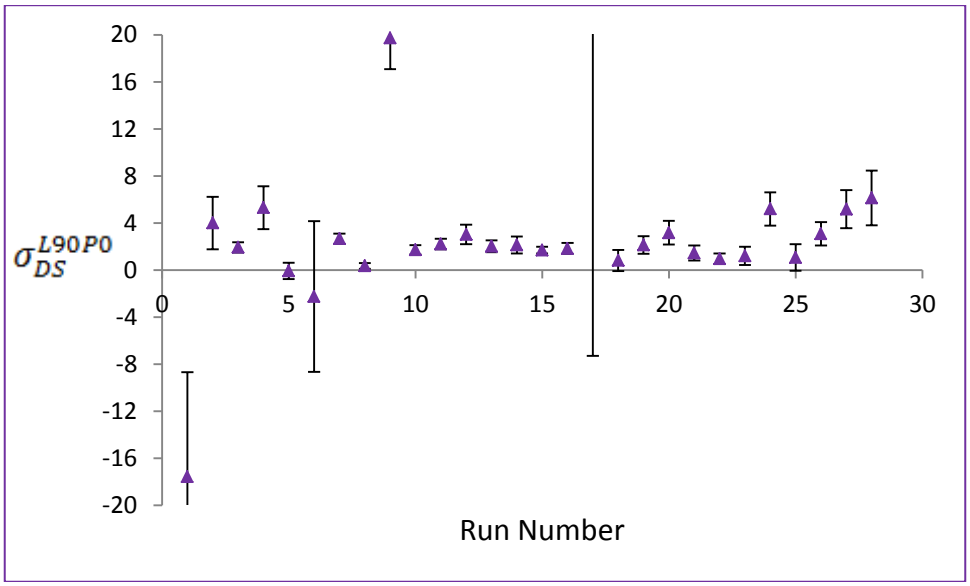

Figure 5.19: Relative cross section (RCS) for the L90P0 configuration versus run number for 40 eV i.e. for same dataset as in Figure 5.18.

It can be seen in Figure 5.19 that there is a cluster of data points with an average RCS near 2.0 as well as anomalies with both negative and lager positive values of the RCS. Two steps were taken to discard unreasonable data. First, all runs with negative D state populations were discarded, and the RCS was determined for each remaining measurement at a given energy. According to the procedure described in Section 4.4, a

weighted mean of all remaining measurements was calculated; accounting appropriately for the different uncertainties in the individual measurements, and the reduced-χ^2 of the measurements was also calculated. Second, those cross sections were discarded which were many error bars away from the mean, specifically discarding data with negative RCS by more than 1σ. This selection improved the reduced-χ^2 as can be seen from Table 5.3, an indication of greater consistency in the reduced data set. The weighted average cross section was calculated for the remaining data, and to account for additional non-statistical spread in the data, the uncertainty was scaled by a factor of $\sqrt{\frac{\chi^2}{df}}$.

5.6 Results and Discussion

From Table 5.3, it can be seen that the relative cross sections generally show little polarization dependence and are fairly consistent with each other. The 20 eV measurements gave a negative cross section for the L0P90 configuration, but was consistent with zero within its error bars. Also at this energy, the comparison between various polarizations configurations does not follow the same trend as observed at other energies.

The weighted average relative 583 nm line emission cross sections $\sigma_{DS}^{L\Psi P\Phi}$ calculated from Equations (5.18) and (5.19) are shown in Figure 5.20. As a general comment, the higher energy data are more reliable, as they had larger photon signal-to-background ratios and more consistent experimental conditions. For same number of data runs, the smaller $\sqrt{\frac{\chi^2}{df}}$ of the 50 eV data yields a smaller adjusted error bar on the

weighted average. In general, the cross sections σ_D and σ_S are comparable, resulting in the ratio σ_{DS} on the order 1 – 3 except for the L90P0 configuration at 50 eV. The relative cross sections do not vary dramatically with energy and are generally smaller at 50 eV. σ_{DS} is generally independent of the laser polarization orientation indicating isotropic population of the laser-excited D states, suggesting that the D state excitation process is insensitive to the laser polarization.

Table 5.3: Relative cross section and $\sqrt{\frac{\chi^2}{df}}$ for the data set with cuts described in the text.

Electron Energy (eV)	Polarization Configuration	Data Set (Δ<0 cut)		Reduced Data Set (Δ<0 and -1σ cuts)	
		RCS	$\sqrt{\frac{\chi^2}{df}}$	RCS	$\sqrt{\frac{\chi^2}{df}}$
10	L0P0	-1.2 ± 0.6	5.8	2.7 ± 0.7	1.6
	L0P90	2.7 ± 0.4	3.7	2.7 ± 0.4	1.0
	L90P90	3.7 ± 0.8	2.3	4.0 ± 0.7	3.3
	L90P0	1.6 ± 0.7	2.4	2.1 ± 0.6	3.5
20	L0P0	3.0 ± 1.0	8.8	3.8 ± 0.4	0.6
	L0P90	-3.9 ± 0.7	4.8	-1.2 ± 1.9	0.7
	L90P90	0.6 ± 0.7	1.8	0.7 ± 0.6	2.2
	L90P0	2.0 ± 1.4	2.5	3.8 ± 0.6	0.6
30	L0P0	0.8 ± 0.3	3.0	1.1 ± 0.2	1.3
	L0P90	0.4 ± 0.6	4.2	1.2 ± 0.7	6.5
	L90P90	-0.5 ± 0.7	1.3	1.3 ± 0.5	0.7
	L90P0	-0.5 ± 0.7	1.3	1.6 ± 0.5	0.6
40	L0P0	1.0 ± 0.2	2.4	1.1 ± 0.2	3.5
	L0P90	1.6 ± 0.3	3.0	1.6 ± 0.3	5.0
	L90P90	1.7 ± 0.4	5.1	1.7 ± 0.4	9.4
	L90P0	1.6 ± 0.2	3.2	1.6 ± 0.2	4.7
50	L0P0	0.8 ± 0.1	1.1	0.9 ± 0.1	1.2
	L0P90	1.2 ± 0.1	1.2	1.2 ± 0.1	0.8
	L90P90	1.1 ± 0.1	1.2	1.1 ± 0.1	1.2
	L90P0	0.3 ± 0.1	1.0	0.5 ± 0.1	1.0

Figure 5.21 (a) and (b) show the relative line emission cross section out of the D state averaged over the fluorescence polarizations with the weighted averages calculated as:

$$\sigma_{DS}^{L\psi} = \frac{1}{3}\left[2\sigma_{DS}^{L\psi P0} + \sigma_{DS}^{L\psi P90}\right], \tag{5.21}$$

and averaged over the laser polarizations with the weighted averages calculated as:

$$\sigma_{DS}^{P\phi} = \frac{1}{2}\left[\sigma_{DS}^{L0P\phi} + \sigma_{DS}^{L90P\phi}\right]. \tag{5.22}$$

The 20 eV data showed some inconsistencies, which is reflected in Figure 5.21(b). An error box around the 20 eV data points indicates the relatively larger uncertainty at that energy.

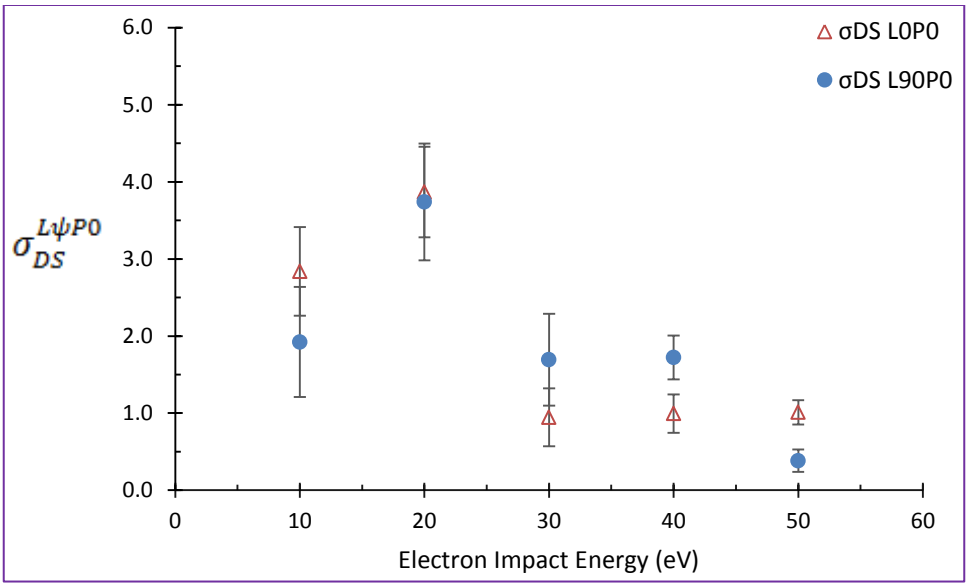

(a)

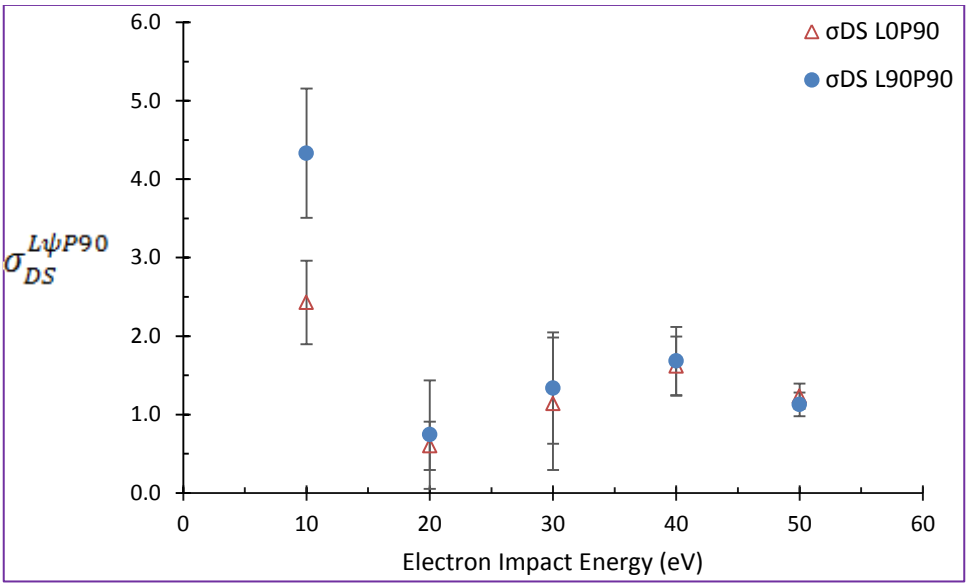

(b)

Figure 5.20: Relative 583 nm line emission cross section $\sigma_{DS}^{L\psi P\phi}$ for different laser and fluorescence polarizations. (a) $\sigma_{DS}^{L\psi P0}$ (b) $\sigma_{DS}^{L\psi P90}$.

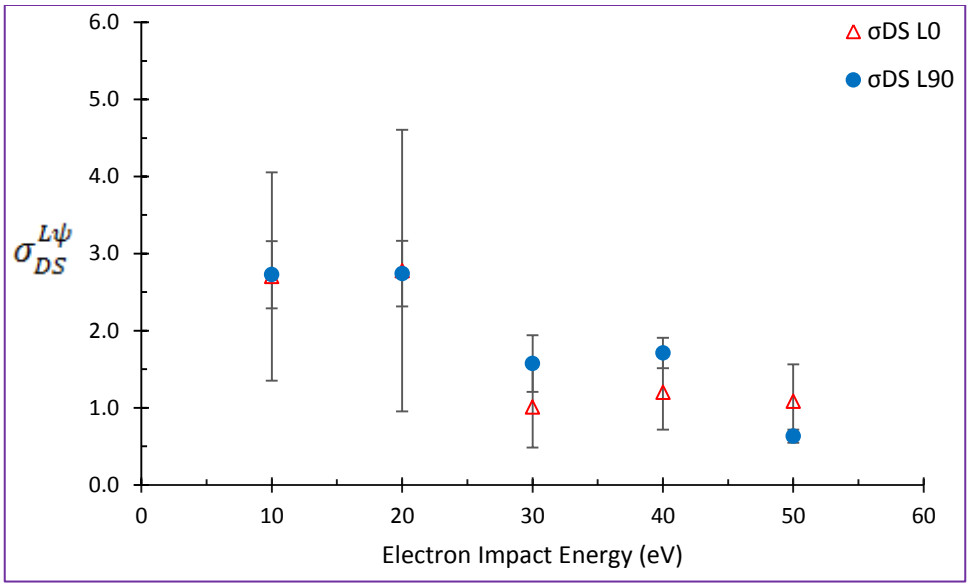

(a)

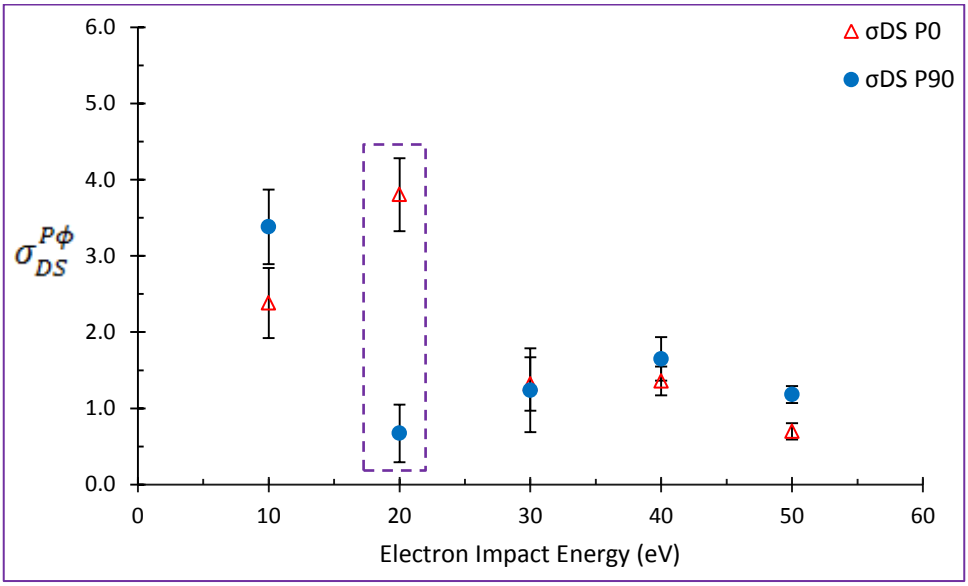

(b)

Figure 5.21: Relative 583 nm line emission cross section out of the D state averaged over (a) fluorescence polarizations and (b) laser polarizations. The dashed box in panel (b) highlights the disagreement within the 20 eV data set.

In Figure 5.21(a) where σ_{DS} is averaged over the fluorescence polarizations shows $\sigma_{DS}^{L\psi}$ independent of laser polarization. Figure 5.21(b) where σ_{DS} is averaged over the laser polarizations shows $\sigma_{DS}^{P\phi}$ independent of fluorescence polarization apart from the anomalous 20 eV data points and reflects the same isotropic trend in the D state as in Figure 5.20. Finally, averaging over the both laser and fluorescence polarizations yields the unpolarized relative cross section as:

$$\sigma_{DS} \equiv \frac{\sigma_D}{\sigma_S} = \frac{1}{2}\left[\sigma_{DS}^{L0} + \sigma_{DS}^{L90}\right] = \frac{1}{3}\left[2\sigma_{DS}^{P0} + \sigma_{DS}^{P90}\right], \tag{5.22}$$

and is shown in Figure 5.22 and tabulated in Table 5.4. The cross section is almost constant from 30 – 50 eV, while at lower energy of 10 – 20 eV it is higher approximately by a factor of 2.5.

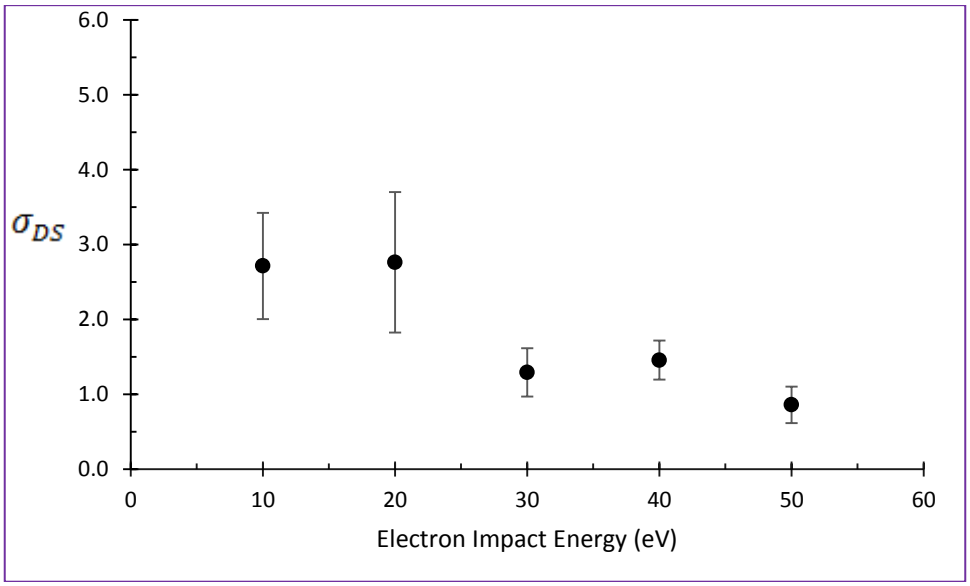

Figure 5.22: Relative 583 nm line emission cross section σ_{DS} averaged over laser and fluorescence polarizations.

The polarization P of the 583 nm line emission is defined after averaging over the laser polarization[31] as in Equation (5.22), as:

$$P \equiv \frac{\sigma_{DS}^{P0} - \sigma_{DS}^{P90}}{\sigma_{DS}^{P0} + \sigma_{DS}^{P90}} . \tag{5.22}$$

The polarization is plotted in Figure 5.23 showing polarization consistent with zero at lower energies and around -15% at higher energies; the anomalous 20 eV point is not shown. The higher 583 nm polarization at higher energy indicates that the magnetic substates are not equally populated (refer to Figure 5.6) i.e. an anisotropically distributed population in magnetic substates [Percival and Seaton1958].

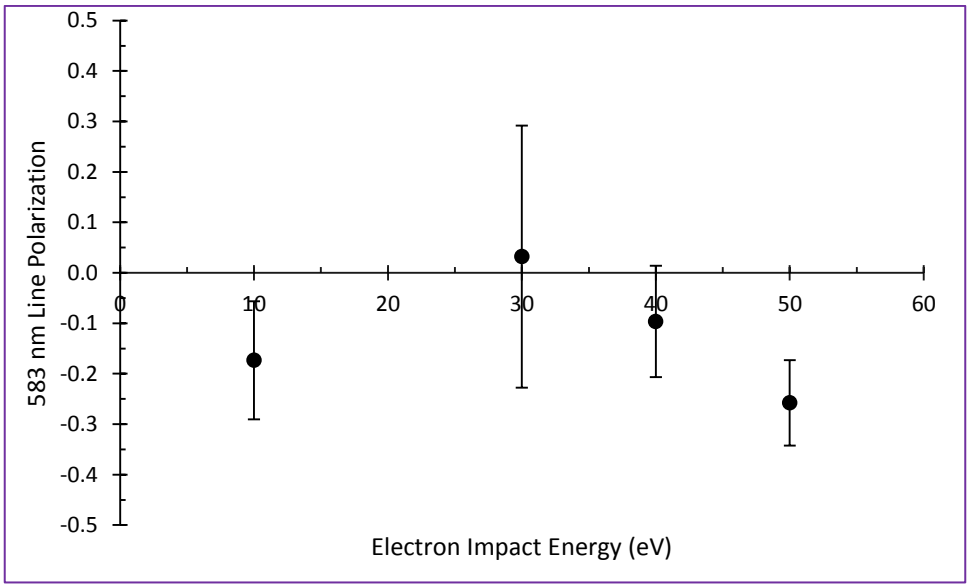

Figure 5.23: Polarization of the 583 nm emission for excitation from metastable D state.

[31] These expressions account for the 45° PMT angle as described in Section 5.3.

Theoretically there should be polarization of the D state as discussed in Section 5.2.1, but under realistic experimental conditions, a potential problem associated with the laser excitation process should be considered. During the passage of the atoms from the laser interaction (upstream of atomic beam) to the interaction region, the photons deexciting spontaneously from P state to the ground-state might be reabsorbed by another atom due to the fact that spontaneous photons are emitted in random directions. This is known as radiation trapping. If this effect is large, it would depolarize the excited P state population as the atomic ensemble will interact with photons of random linear polarizations and propagation directions. This would result in incoherent excitation of the P state and subsequent isotropic population of the metastable D state. Radiation trapping has been found to be negligible for pumping of the short-lived P state [Zetner1992, Zetner1993, Li1994a]; however the continued optical cycling responsible for the generation of the D state population may lead to depolarization of these metastable states [Li1995] which is observed also in the present experiment.

Table 5.4: Experimental relative emission cross sections of the ^{138}Ba 583 nm line out of laser excited metastable $^1D_2$ state.

Electron Energy (eV)	σ_{DS}
10	2.71 ± 0.71
20	2.76 ± 0.94
30	1.29 ± 0.32
40	1.45 ± 0.26
50	0.86 ± 0.24

5.6.1 The Apparent Cross Section $\sigma_{D\text{-}ap}$

The apparent cross section $\sigma_{D\text{-}ap}$ of $(6s7p)^1P_1$ level out of the laser excited metastable $(6s5d)^1D_2$ level, was obtained by normalizing the present experimental relative cross section σ_{DS} with the various published $(6s7p)^1P_1$ apparent cross sections out of the ground state excitation, $\sigma_{S\text{-}ap}$. This $\sigma_{S\text{-}ap}$ was taken from previous experimental work of Smirnov [Smirnov2003], and also from the theoretical models of CCC [Fursa1991] and RCCC [Bostock2014a]. These $\sigma_{S\text{-}ap}$ are plotted in Figure 5.24. Unfortunately, theoretical predictions disagree with each other varying up to a factor of 5 over the energy range considered. Also, all predictions disagree with the only available experimental data. For $\sigma_{S\text{-}ap}$ the most recent calculations by Bostock [Bostock2014a] show the largest disagreement with experiment [Smirnov2003]. In the following discussion, the experimental value of $\sigma_{S\text{-}ap}$ from [Smirnov2003] will be used to normalize the present relative cross section σ_{DS} data to obtain $\sigma_{D\text{-}ap}$.

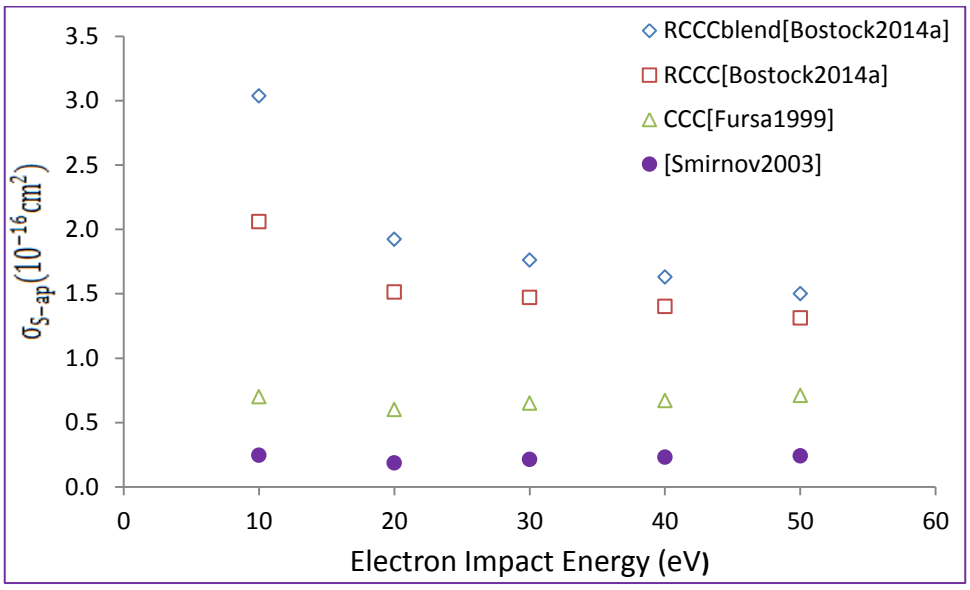

Figure 5.24: Ground state excitation cross section $\sigma_{S\text{-}ap}$ from previous experimental work and theoretical models. Open symbols: theoretical models; closed symbols: experiment.

Recall that the branching ratio factor has to be taken into account when determining the apparent cross section $\sigma_{D\text{-}ap}$ from the experimentally measured emission cross section $\sigma_{D\text{-}em}$. In Chapter 4 (Section 4.6.3), the experimental branching ratio factor of 0.56 was used, but a range of 0.43 – 0.65 is reported in the literature Kulaga [Kulaga2001]. Thus depending upon the value of branching ratio factor taken, the result for $\sigma_{D\text{-}ap}$ can be shifted. In Figure 5.25, $\sigma_{D\text{-}ap}$ is obtained by normalizing the present work σ_{DS} with the experimental value of $\sigma_{S\text{-}ap}$ [Smirnov2003] and results are shown in Table 5.5. To show the range of the branching factor, two dashed curves are also drawn in Figure 5.25. This same present result for $\sigma_{D\text{-}ap}$ is also shown in Figure 5.26 along with the only other available $\sigma_{D\text{-}ap}$ calculated in the RCCC model for comparison purpose. In Figure 5.26, the two RCCC model curves are calculated with and without the contributions of blended lines at 577.8 nm, 580.0 nm and 580.6 nm, as discussed in section 4.7. The "RCCC blend" curve can be considered as an upper limit prediction for the observed cross section assuming that each of these additional lines had the same transmission as the 583 nm line of interest through the optical filter. Similarly, the "RCCC" curve can be considered as a lower limit prediction for the observed cross section.

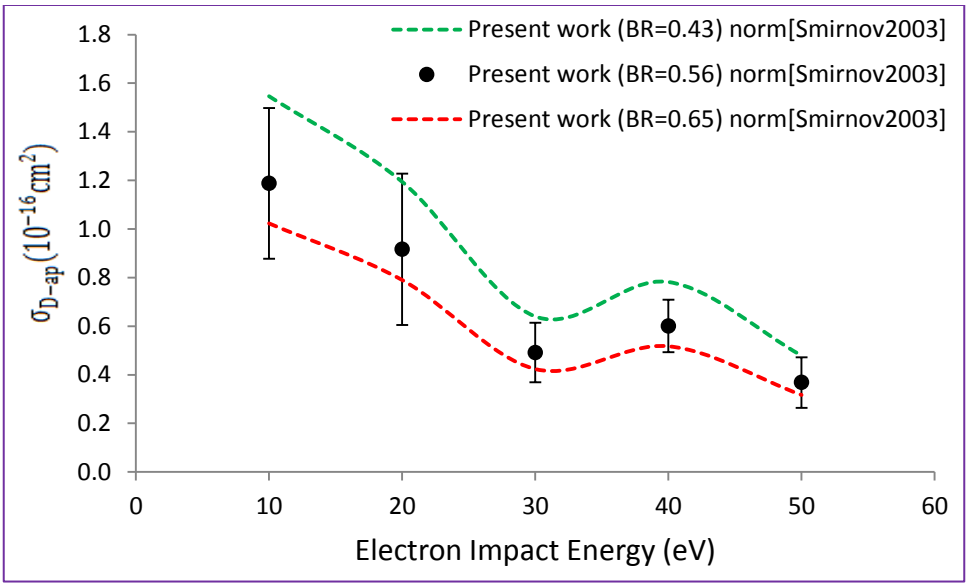

Figure 5.25: $\sigma_{D\text{-}ap}$ obtained by normalizing the present work $\sigma_{DS\text{-}ap}$ with the experimental value of $\sigma_{S\text{-}ap}$ [Smirnov2003]. The two dashed curves show the range of the branching factor discussed in the text.

Table 5.5: Comparison of the apparent cross section $\sigma_{D\text{-}ap}$ of the ^{138}Ba 583nm line out of the metastable $^1D_2$ state with different normalization data for $\sigma_{S\text{-}ap}$.

Electron Energy (eV)	Present work σ_{DS}	$\sigma_{D\text{-}ap}$ x 10^{-16} cm^2 $(\ldots 6s5d)^1D_2 \rightarrow (\ldots 6s7p)^1P_1$
		Present work normalized to
		Exp [Smirnov2003]
10	2.71 ± 0.71	1.19 ± 0.38
20	2.76 ± 0.94	0.92 ± 0.29
30	1.29 ± 0.32	0.49 ± 0.16
40	1.45 ± 0.26	0.60 ± 0.19
50	0.86 ± 0.24	0.37 ± 0.12

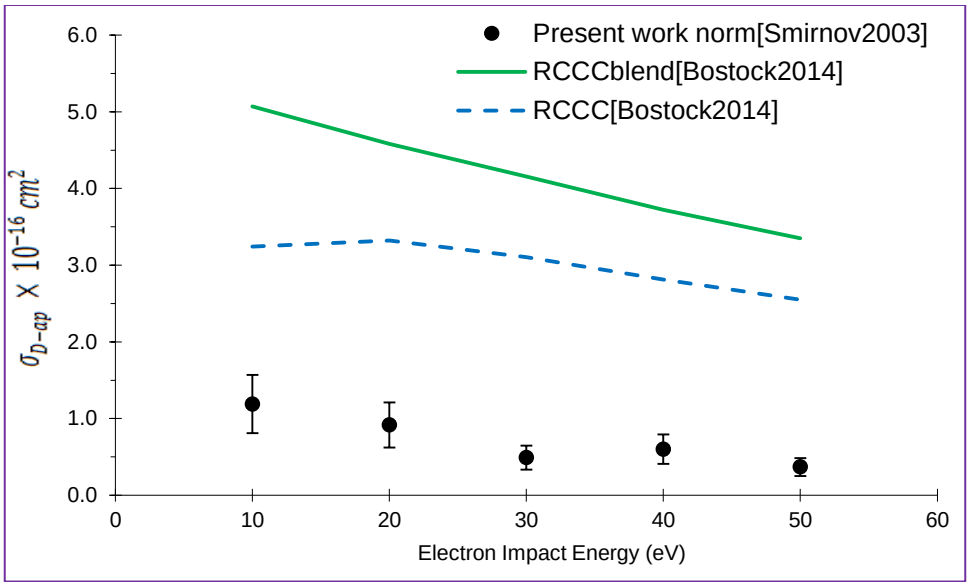

Figure 5.26: Comparison of $\sigma_{D\text{-}ap}$ between present experimental data and theoretical RCCC model calculations [Bostock2014a].

The graphs in Figure 5.26 show that the measured $\sigma_{D\text{-}ap}$ is approximately 4x lower than that of the RCCC-blend model at lower energies and approximately 9x lower at higher energies. The trend is almost the same, with $\sigma_{D\text{-}ap}$ decreasing with electron energy. The RCCC-blend model shows a decrease by a 1.5 factor between 10 eV and 50 eV, while the measured $\sigma_{D\text{-}ap}$ decreased by a factor of 3. The RCCC model $\sigma_{D\text{-}ap}$, i.e. without contributions from the blended lines resulting from of $^1S_0 \rightarrow {}^3D_2$, $^1S_0 \rightarrow {}^3D_3$, and $^1S_0 \rightarrow {}^1F_3$ excitations, does not follow the same trend as the RCCC-blend model; rather it is flat at lower energies.

A previously reported cross section $\sigma_{D\text{-}ap}$ using Born approximation calculations by Aleksakhin [Aleksakhin1983] shows values more than 40 times higher than the values in the Table 5.4. This shows that a relativistic approach, such as the RCCC model, is

more in agreement with the experimental results and indicates a failure of non-relativistic models in heavy atoms like barium at medium-low incident electron energies.

5.6.2 Excitation Cross Section $\sigma_{D\text{-}ex}$ out of the Metastable D state

The apparent cross section $\sigma_{D\text{-}ap}$ obtained in the above section is converted into the excitation cross section $\sigma_{D\ ex}$[32] by taking into account the cascade contribution (refer to Section 4.6.4) by the RCCC model [Bostock2014a]. This $\sigma_{D\text{-}ex}$ is compared with the theoretical excitation cross sections and shown in Figure 5.27. Since the cascade contribution is subtracted from the respective apparent cross section, the shape of the excitation cross sections in Figure 5.27 shows the same trend as given in Figure 5.26, but with smaller values.

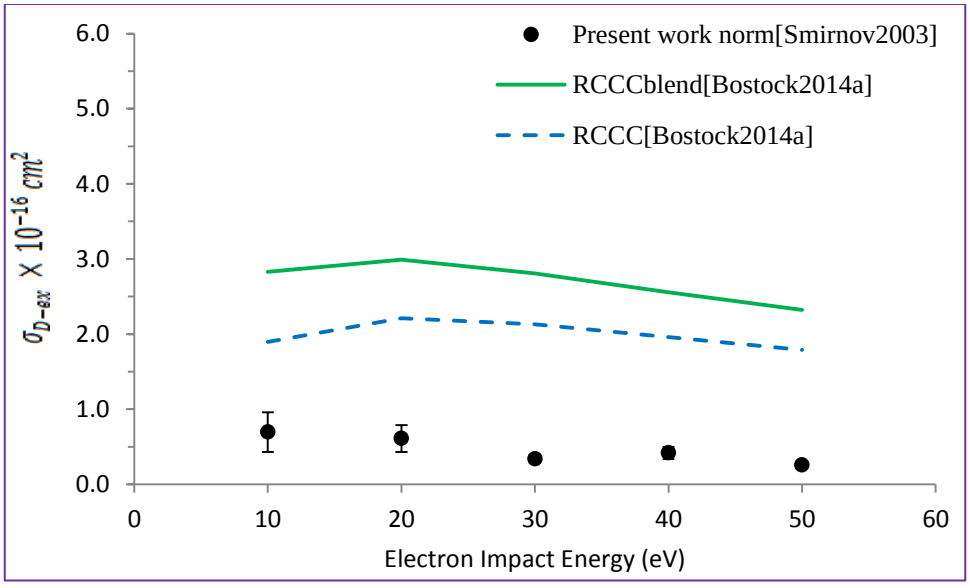

Figure 5.27: Comparison of present work (experimental) and RCCC (theoretical) excitation cross section $\sigma_{D\text{-}ex}$.

[32] Also called the level or direct excitation cross section.

5.7 Conclusion

In the present chapter, the electron impact excitation process has been studied on the laser excited barium $(6s5d)^1D_2$ level by measuring the intensity of the 583 nm transition from the $(6s7p)^1P_1$ state to the metastable $(6s5d)^1D_2$ state. This measured relative line emission cross section σ_{DS} was used to determine the level excitation cross section $\sigma_{D\ ex}$ of the $(6s7p)^1P_1$ state out of the metastable $(6s5d)^1D_2$ state by taking into consideration the branching ratio and the cascade contribution.

The excited metastable states were populated by the $(6s7p)^1P_1 \rightarrow (6s5d)^1D_2$ radiative cascade, an incoherent process dependent on spontaneous emission from the $(6s7p)^1P_1$ state, and thus the $m = +1$ and $m = -1$ substates bore no phase relationship to each other.

There is a general agreement in the trend between the experiment and the relativistic RCCC theoretical model of relative cross sections. The present work shows a lower cross section than the RCCC model. Since the RCCC model was very recently developed and the present work gives the first experimental data for the 583 nm line cross section, further work is needed to make a good connection between theory and the experimental results.

Chapter 6

Polarization-Dependent Cross Sections for Electron Excitation of the 3.11 eV $^1P_1$ state in Ytterbium from the Laser-Excited 2.24 eV $^3P_1$ state by Measuring the 399 nm Line

6.1 Introduction

The previous two chapters were devoted to experimental studies of barium. In this third and last experiment, laser-excited ytterbium was selected for the electron scattering experimental studies. Studies of laser-excited ytterbium are interesting from both experimental and theoretical viewpoints. The relative ease in producing a vapour beam of ytterbium and the availability of a cw dye laser to transfer ground-state population to the excited state make it a feasible target. Experimentally, ytterbium opens up a new frontier in electron-atom collision experiments with laser excited atoms since the P state laser excitation can generate a coherent magnetic sublevel population.

Ytterbium (Z=70) is a heavy atomic target with electronic configuration ([Kr] $4d^{10}$ $5s^2$ $4f^{14}$ $5s^2$ $5p^6$ $5p^6$) $6s^2$ $^1S_0$ and belongs to the rare earth metal, lanthanide group. Unlike the well-studied ground to P state electron excitation in helium which is theoretically well-described in an LS coupled framework, electron impact excitation of similar transitions in a heavy two-electron system such as ytterbium involves excitation of states in which the spin-orbit interaction plays a strong role. One notable consequence

of the breakdown of LS coupling is the presence of strong intercombination radiative transitions. These intercombination lines are electric dipole semi-forbidden transitions for which the spin selection rule is violated. In the present work, an attempt is made to measure the cross section from one of these electric dipole semi-forbidden transitions of $^3P \rightarrow {}^1P$. The non-negligible spin-orbit interaction in heavy atoms necessitates a fully relativistic theoretical approach to the electron scattering description. Hence, electron scattering from the ytterbium atom provides a useful tool for testing relativistic approaches to the scattering problem, several of which are now under development. One goal of the study of electron-Yb scattering is thus to provide benchmark data for assessment of theoretical approaches.

To further complicate the theoretical problem, the states of the Yb atom are not well-described by unique two-electron configurations. The most prominent mix of two-electron configurations in the low-lying ytterbium states is given in Table 6.1 [Johnson1998, Zetner2001].

Table 6.1: Dominant mixed-state configurations of ytterbium.

Atomic state energy (eV)	Dominant mixed-state configurations	State label
0.00	$0.9766(6s^2)^1S_0 + 0.1875(6p^2)^1S_0 - 0.0682(5d^2)^1S_0$	$(6s^2)^1S_0$
2.24	$0.9906(6s6p)^3P_1 - 0.07914(6s6p)^1P_1$	$(6s6p)^3P_1$
3.11	$0.9358(6s6p)^1P_1 - 0.3112(5d6p)^1P_1 - 0.1261(6s7p)^1P_1 + 0.0758(6s6p)^3P_1$	$(6s6p)^1P_1$

Ytterbium can be compared with the heavy target mercury (Z=80), which has been the subject of a number of theoretical [Srivastava1995, Bostock2010] and experimental [Shimon1981, Johnson1998, Predojevic2005a,2005b] studies, but not has been as extensively studied as barium. Mercury also has a two-valence-electron structure ($6s^2$ in the ground state). Like ytterbium, mercury exhibits a strong breakdown of LS coupling and strong intercombination transitions are clearly observed. An added interest in the study of scattering from ytterbium is the possibility of using laser excitation techniques which are difficult to employ in studies of mercury, where suitable laser excitation transitions lie in the ultraviolet region. For ytterbium, it is feasible to probe more features of the scattering dynamics in a relativistic system and investigate these dynamics in greater detail by scattering from laser-excited states. In the present case, the strong intercombination line between the ground state and the ^3P state (556 nm) is easily accessible to cw dye laser excitation.

Electron-atom collision studies in ytterbium are relatively scarce. Shimon [Shimon1981] measured the optical excitation functions (OEF) for 36 atomic transitions in ytterbium for electron incident energies ranging from 20 – 300 eV. In 1983, the electron energy loss spectrum (EELS) of ytterbium was published along with the $(6s6p)^1P_1$ and $(6s6p)^3P_{0,1,2}$ excitation functions at 14 eV [Kazakov1983]. In 1993, the ytterbium EELS spectrum was studied below 10 eV incident electron energy [Mandy1993]. Recently, Predojevic et al. [Predojevic2005a,2005b] measured the differential cross section for electron impact excitation of $(6s6p)^1P_1$ and $(6s6p)^3P_1$ states with incident electron energy ranging from 10 – 80 eV in ytterbium. Previously from the present AMO lab, Johnson et al. [Johnson1998] measured the differential cross section

for the excitation of the $(6s6p)^1P_1$ state for incident electron energies ranging from 5 – 80 eV with scattering angle from 2° – 65°. Zetner et al. [Zetner2001] measured the relative differential cross section for $(6s6p)^3P_1$ and $(6s6p)^3P_2$ states for incident electron energies ranging from 10 – 40 eV with scattering angle up to 60°, and Hein et al. [Hein2011] measured the differential cross section for 20 eV electron impact excitation from the laser excited $(6s6p)^3P_1$ state to $(6s7s)^3S_1$ state and to the $(6s6p)^1P_1$ and $(6s5d)^3D_{1,2,3}$ combined state.

6.2 Background to the Measurements

In this chapter, 399 nm radiation originating from the ytterbium $(6s6p)^1P_1$ state was observed in order to measure the relative line emission cross section σ_{PS} for medium to low electron impact energies. The notation σ_{PS} denotes the cross section for excitation of the ^1P state out of the laser-excited ^3P state relative to that out of ground state: $\sigma_{PS} = \frac{\sigma_P}{\sigma_S}$ for the transitions shown in Figure 6.1. The ^3P state was excited with linearly polarized laser light at 556 nm; the laser polarization and 399 nm polarization dependence were both studied.

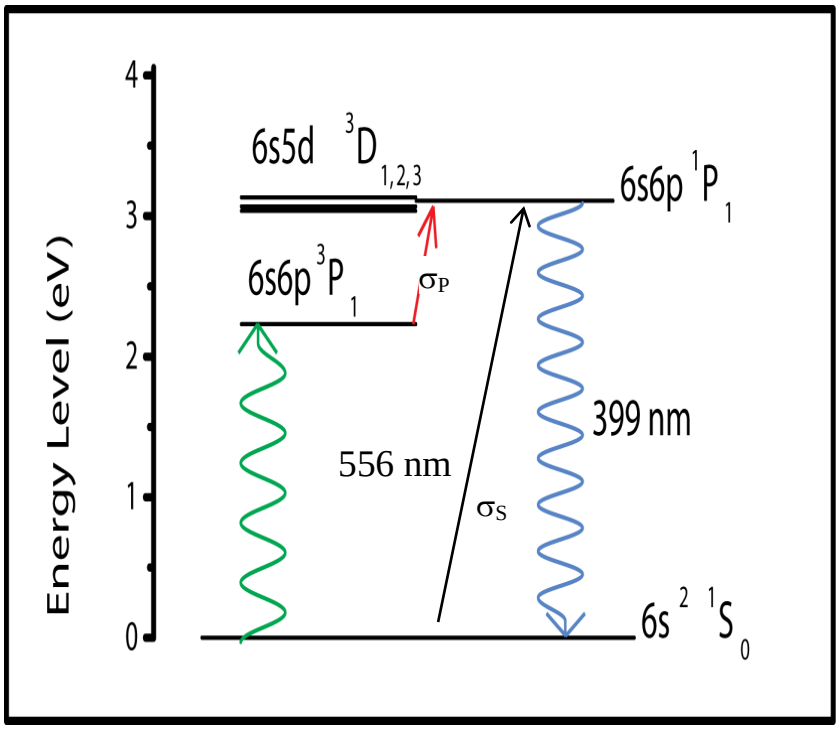

Figure 6.1: Low lying energy level diagram of Yb showing the dominant electron state configurations, the optical pumping transition to the $^3P_1$ state (556 nm) and the radiative decay of the $^1P_1$ state (399 nm) studied in this chapter. Electron excitation cross sections are indicated by solid arrows.

The ^3P state has three magnetic sub-states, m=0,±1. With linearly polarized laser light used for pumping to the P state, either the m=0 or a quantum mechanical superposition of the m=±1 sub-states are selectively populated, with reference to a quantization axis pointing along the electron beam direction. Alternatively, circularly polarized laser light propagating along the electron beam direction could be used to selectively populate either the m=+1 or m=-1 sublevel of the ^3P state. In either case, whether linearly or circularly polarized laser light is used, the target atom sub-states are completely defined by quantum numbers. This is a consequence of the coherent nature of the laser excitation of a P state. This process differs significantly from the process used to populate the barium metastable D state described in Chapter 5. In the barium case, the

excited metastable D state was populated by a P – D state radiative cascade, an incoherent process dependent on spontaneous emission from the P-state. In that scheme, a target population was produced in the D state m=+1 and m=-1 substates but the m=+1 and m=-1 substates bore no phase relationship to each other. In the present excitation of the P state m=+1 and m=-1 substates, there is a well-defined phase relationship between the two laser-excited substates.

6.2.1 Optical Pumping of ^{174}Yb

Ytterbium has 7 naturally occurring stable isotopes, with the most abundant being ^{174}Yb at 31.8%. A laser-induced-fluorescence (LIF) scan of the optically pumped $(6s^2)^1S_0 \rightarrow (6s6p)^3P_1$ transition is shown in Figure 6.2 [Pandey2009]. ^{174}Yb is the most intense, due to its relative abundance, and has no hyperfine structure due to absence of nuclear spin. The transitions in neighbouring isotopes are at least 1 GHz apart and therefore ^{174}Yb can be cleanly selected for optical pumping.

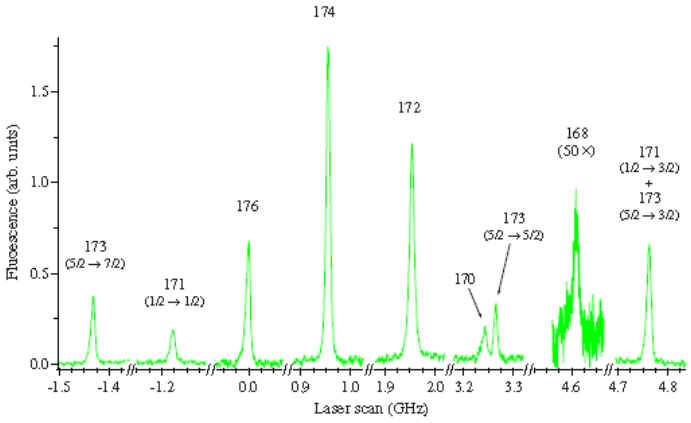

Figure 6.2: Laser-induced-fluorescence from the $^3P_1 \rightarrow {}^1S_0$ transition in ytterbium. The relative intensities of the peaks are consistent with the relative abundance of the naturally occurring Yb isotopes. The odd isotopes have hyperfine structure while even isotopes do not [Pandey2009].

6.2.2 Optical Fanning Technique

The ^{174}Yb isotope represents only 31.8% of the naturally occurring mixture of ytterbium, making it more difficult than barium to produce high number densities of laser-excited atoms. Under conditions of complete optical saturation of the $^1S_0 \rightarrow {}^3P_1$ transition, only around 15% of the vapour beam is pumped to the P state. This represents a hard upper limit to the excited state population. On average, around 3% of the atoms in the vapour beam were measured to be laser-excited in the present experiment, as discussed in Section 6.6.

In a conventional method of laser excitation, the laser light is transported into the interaction region in a parallel beam where it interacts with a divergent atomic beam, Figure 6.3(a). The conventional laser interacts with a small portion of the divergent atomic beam for the following reason. Although the $^1S_0 \rightarrow {}^3P_1$ intercombination transition is relatively strong, it is much weaker than a typical $^1S_0 \rightarrow {}^1P_1$ atomic resonance line. In the ytterbium case, the $^1S_0 \rightarrow {}^3P_1$ transition has a natural linewidth of just ~182 kHz in contrast to the much stronger $^1S_0 \rightarrow {}^1P_1$ transition with ~28 MHz natural linewidth (similar to the transition pumped in the Ba experiments). As a consequence of the very narrow absorption linewidth of $^1S_0 \rightarrow {}^3P_1$ transition, a small transverse velocity component of the atoms in the vapour beam will cause Doppler de-tuning out of resonance with the laser. In other words, the laser will resonantly interact with a very small "velocity group" of the overall atomic beam. This, again, is quite different from the barium case in the previous chapter where the relatively large absorption width of the $^1S_0 \rightarrow {}^1P_1$ transition spanned a large range of velocity groups and, hence, large fractions of the target beam population.

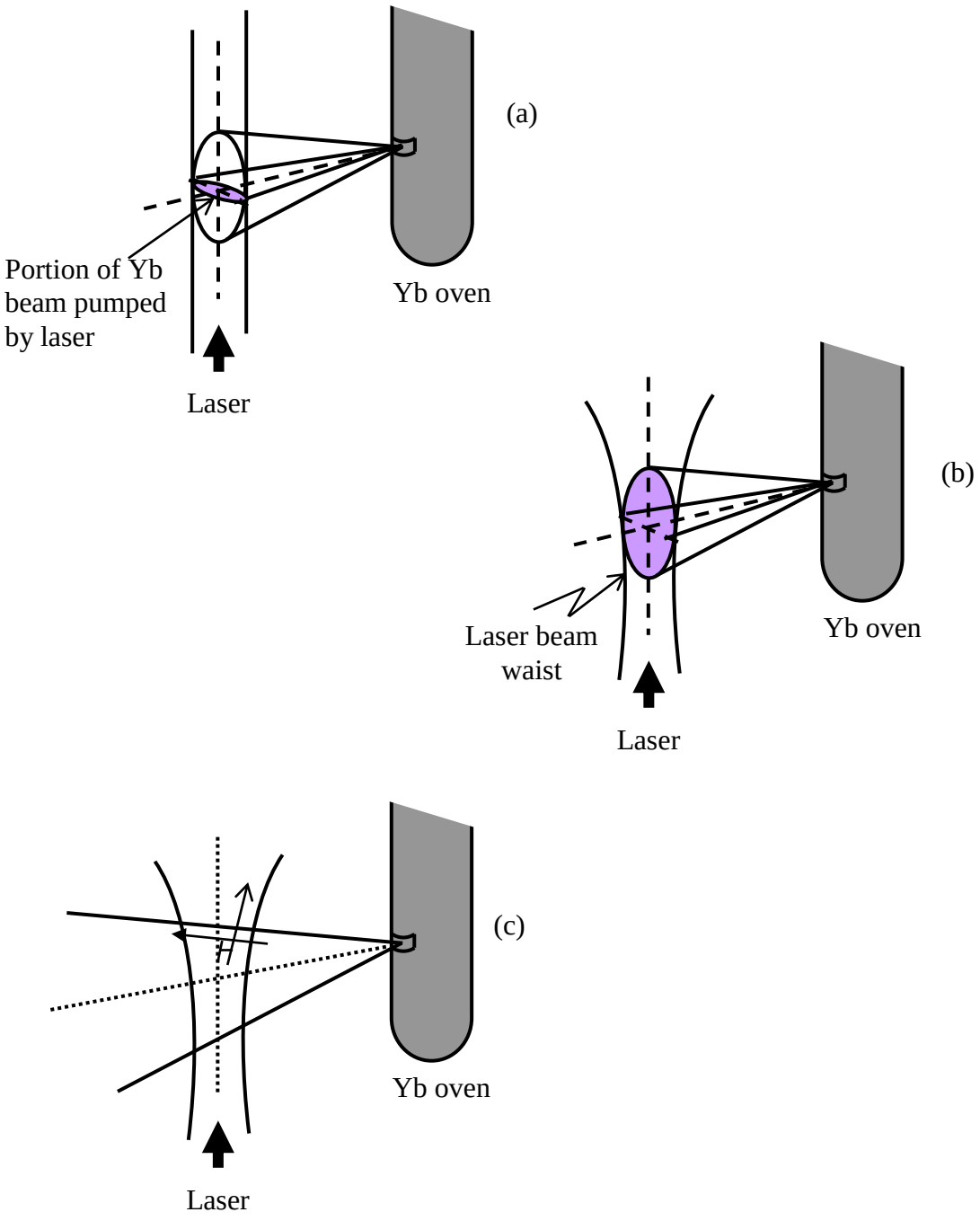

Figure 6.3: (a) A small portion of the atomic beam (shaded) intersecting perpendicularly to the laser beam. (b) Because of the fanned laser beam, a larger portion of the atomic beam (shaded) intersects the laser beam perpendicularly. (c) Fanned laser beam geometry, showing that for any divergent atomic trajectory there is a perpendicular pump beam trajectory.

The most efficient and ideal way to pump the atomic beam is to produce an atomic beam without any divergence at the interaction region where it intersects perpendicularly with the laser beam. Practically, the atomic beam has considerable divergence. With a diverging atomic beam source, only a portion of the atomic beam will be able to be pumped. This is shown in Figure 6.3(a) where a portion of the atomic beam (shaded) intersecting the laser beam perpendicularly is pumped. To make the optical pumping condition as efficient as possible, a diverging (fanned) pump beam using cylindrical lenses was produced. Two lenses, one cylindrical (f=15cm) and the other spherical (f=25cm) were placed in the path of the laser beam before it entered the vacuum chamber. The cylindrical lens transformed the incoming laser beam into a fanned beam and then the spherical lens focused the fanned beam to a waist near the interaction region as shown in Figure 6.3(b). A much greater portion of the atomic beam (shaded) then intersected perpendicularly with the laser beam. The effect of increasing the pumping efficiency is shown in Figure 6.3(c), where ideally there should be a perpendicular pump beam trajectory for any divergent atomic trajectory. This technique maximized the achievable excited state population fraction to about 3 – 6% in the present experiments.

6.3 Experimental Setup

The general setup for the experiment in the AMO laboratory is described in detail in Chapter 3. In this experiment involving electron atom collisions in laser-excited ytterbium, the electron detector was mounted on the turntable and the high resolution gun (HRG) was fixed perpendicular to the PMT axis inside the vacuum chamber. A Faraday

cup was mounted on the electron detector. The single-tube metal vapour oven was used to produce the ytterbium atomic vapour beam. The laser, tuned to 556 nm for optical pumping of the $^3P_1$ state, was incident from below. The experimental schematic is shown in Figure 6.4.

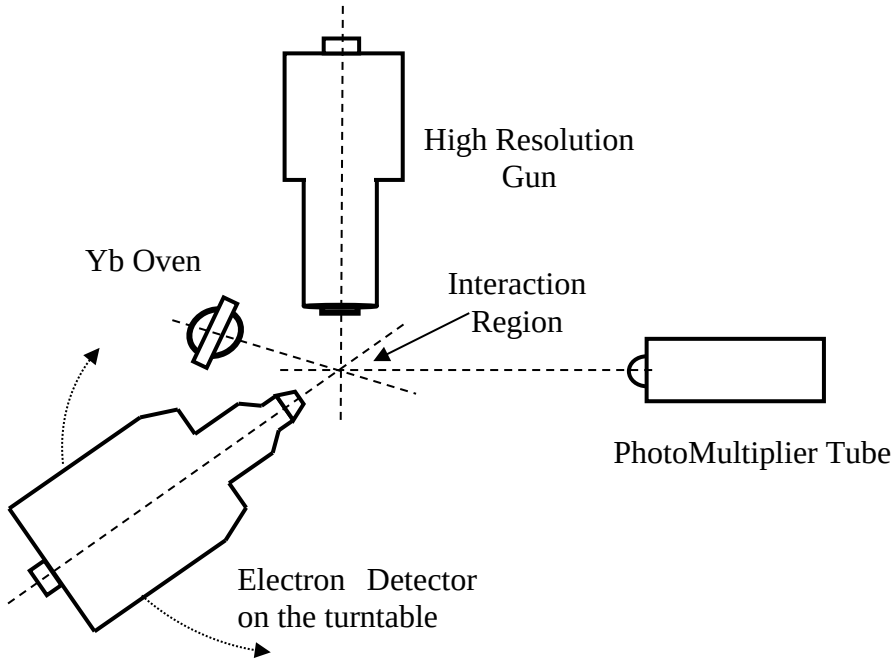

Figure 6.4: Setup for the ytterbium cross-beam experiment (Top-view; elements are arranged in the horizontal plane).

Initially the current was maximized on the Faraday cup by tuning the HRG potentials and deflectors. Current measured at the Faraday cup was between 300 – 500 nA for incident electron energies in the range of 10 – 30 eV. The HRG energy resolution was determined to be 200 mV at FWHM. The high resolution gun impact energy calibration was carried out with use of the helium 1S $2s^2$ ^2S elastic scattering resonance feature at 19.37 eV [Shultz1973].

The laser beam was linearly polarized for these experiments, with the plane of polarization adjusted via an optical assembly under computer control, as in Chapter 5. The geometry of the setup is shown in Figure 5.7, reproduced here for reference in Figure 6.5. The component of the laser polarization parallel to the electron beam denoted by L0, selects the m=0 sublevel of the $^3P_1$ state and the perpendicular component of the laser polarization denoted by L90 selects the combination of m=±1. As seen in Figure 6.5 the fluorescence detection axis was at 90° to the electron beam axis; these two axes define the electron-photon plane. The 399 nm fluorescence polarization components were measured with respect to the electron-photon plane. The designation, P0 refers to detection of polarization parallel to the electron-photon plane, and P90 refers to detection of polarization perpendicular to the electron-photon. P0 and P90 correspond to orientations of the PMT polarizer pass-axis as indicated in Figure 6.5.

Magnetic substates of the $^3P_1$-state corresponding to the selected laser polarizations are shown in Figure 6.6a. The four possible combinations determined by the laser and PMT polarizer orientations can be written as L0P0, L90P0, L0P90 and L90P90 and are shown in Figure 6.6b where p_x, p_y and p_z represent the p-orbitals as discussed in Chapter 2 in Figure 2.2.

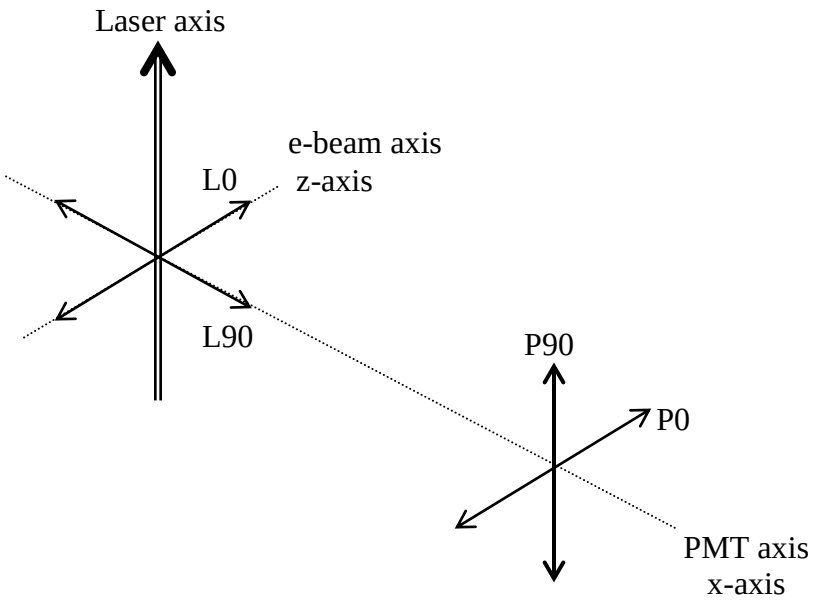

Figure 6.5: Geometry from the laser-pumped Yb experiments. The 556 nm laser polarizations L0 and L90 and the PMT polarizer pass-axes P0 and P90 for measuring the 399 nm polarization are shown.

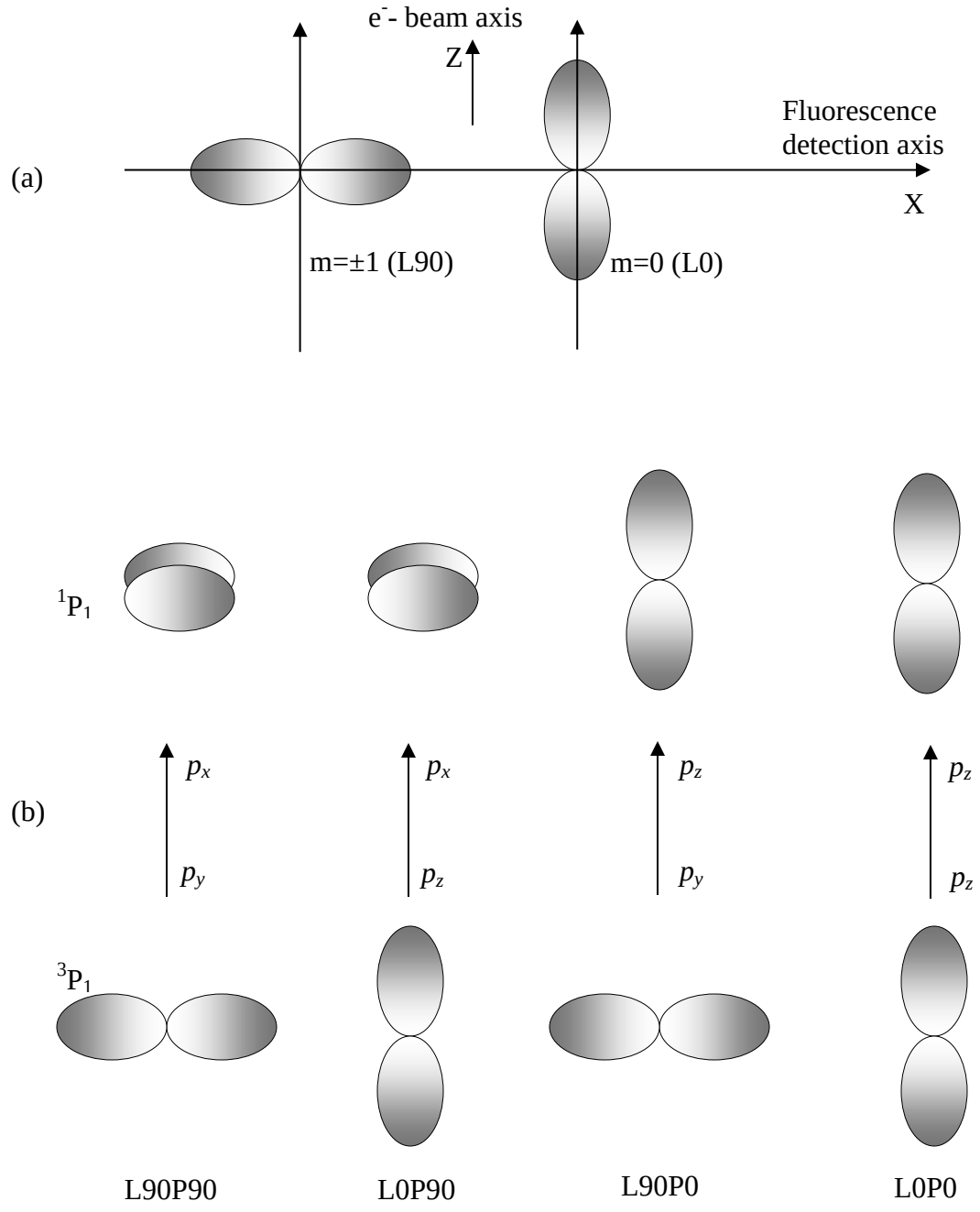

Figure 6.6: (a) Showing magnetic substates corresponding to laser polarizations. (b) Electron impact excited transitions for four possibilities determined by the laser and fluorescence polarizations.

A sequence of filters (Figure 3.16) was arranged in front of the PMT to block the laser induced fluorescence at 556 nm and transmit the 399 nm photon of interest from the $^1P_1 - {}^1S_0$ transition. The transmission graph for the 400 nm line filter is shown in Figure 6.7. An unresolved line visible at 399.09 nm, corresponding to the $(6p^2)^3P_2 \rightarrow (6s6p)^3P_2$ transition, falls within the 5 nm FWHM passband of the line filter; however this was safely ignored, as the relative intensity of 399.09 nm line with respect to the 398.9 nm line of interest is known to be just 5% [http://physics.nist.gov].

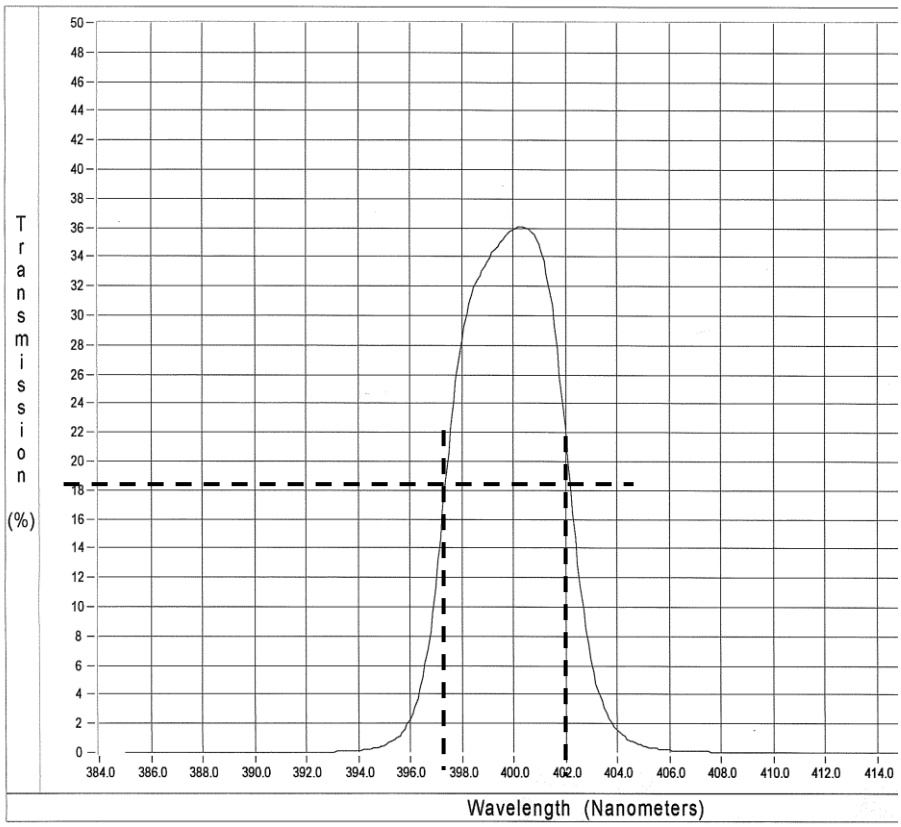

Figure 6.7: Transmission graph of the 400 nm line filter [Andover Corporation: www.andcorp.com].

6.3.1 Data Acquisition

In this experiment the laser polarization states L0 and L90 were selected by the λ/2-plate, and the 399 nm fluorescence polarization states P0 and P90 by orientation of the PMT polarizer. The multi-channel-scaler (MCS) based data acquisition system was used to collect and process the data. A measurement protocol was developed to include all combinations of laser and fluorescence polarizations and redundant checks. Table 6.2 shows the measurement sequence used in the current experiment. The experiment was carried out for five electron impact energies from 10 – 40 eV.

Table 6.2: Measurement Scheme: L0 and L90 denote laser polarization parallel and perpendicular to the electron beam direction, while P0 and P90 denote the polarizer oriented parallel and perpendicular to the electron-photon plane.

Data Sequence Number	Laser Polarization Configuration	399 nm Fluorescence Polarization Configuration	Comments	Electron Gun ON / OFF
1	L0	P0		ON
2	L0	P90		
3	L90	P90		
4	L90	P0		
5	Loff	P0		
6	Loff	P90		
7	L0	P0	redundant	
8	L0	P0		OFF
9	L0	P90		
10	L90	P90		
11	L90	P0		
12	Loff	P0		
13	Loff	P90		
14	L0	P0	redundant	

Summarizing the measurement protocol, the initial atomic $^3P_1$ target state for electron excitation was prepared by laser pumping the ground state atoms to the $^3P_1$ state. When the laser polarization was selected parallel (L0) to the electron beam, the magnetic

sublevel m=0 of the target $^3P_1$ state was populated, and when the laser polarization was selected perpendicular (L90) to the electron-beam, magnetic sublevels m=±1 of the target $^3P_1$ state were populated. Similarly, rotating the polarizer in front of the PMT by another stepper motor selects the polarization state of the final atomic $^1P_1$ state from which the photon was emitted. P0 corresponds to magnetic sublevel m=0, and P90 corresponds to a mixture of m=±1 magnetic sublevels of the final atomic state $^1P_1$. Example magnetic sublevel transitions from the $^3P_1$ to the $^1P_1$ state are shown in Figure 6.8.

The data collection was achieved by simultaneously acquiring the scattered electron energy loss spectrum (EELS) in one MCS and photon counts in another MCS. The EELS was used in the measurement of population determination of the target ytterbium state while the photon count rate was used in studying the polarization phenomena and in calculating the integral cross section of the 399 nm line.

A sample ytterbium EELS for electron incident energy of 30 eV at scattering angle of 15° with laser ON and laser OFF, is shown in Figure 6.9 (note the logarithmic intensity scale of Figure 6.9a). Compared to the spectra of Chapter 5, the much better energy resolution (200 meV) of the high resolution gun is apparent. Feature D at 3.11 eV indicates the $^1S_0 - {}^1P_1$ electron excitation which was used to determine the target ^3P state population as discussed in Section 6.5.1; the peak is clearly resolved, but the very small target population (of ~4%) is also apparent, in contrast to barium experiments reported in Chapter 5 (Figure 5.8). For efficiency of data taking, the EELS spectrometer was “parked” on the 3.11 eV scattering peak for the population determination in the ytterbium experiments reported here.

A typical fluorescence data sequence is shown in Figure 6.10, also at 30 eV. The dwell time of the MCS system was 200 ms/channel, indicating counting rates in the range of 200 Hz with the electron gun ON and 60 Hz with the gun OFF. Compared to the situation with barium (Figure 5.9) a much more stable photon signal is evident. With background determined from the electron gun OFF values, signal to background on the order of 2.5:1 is observed in this case.

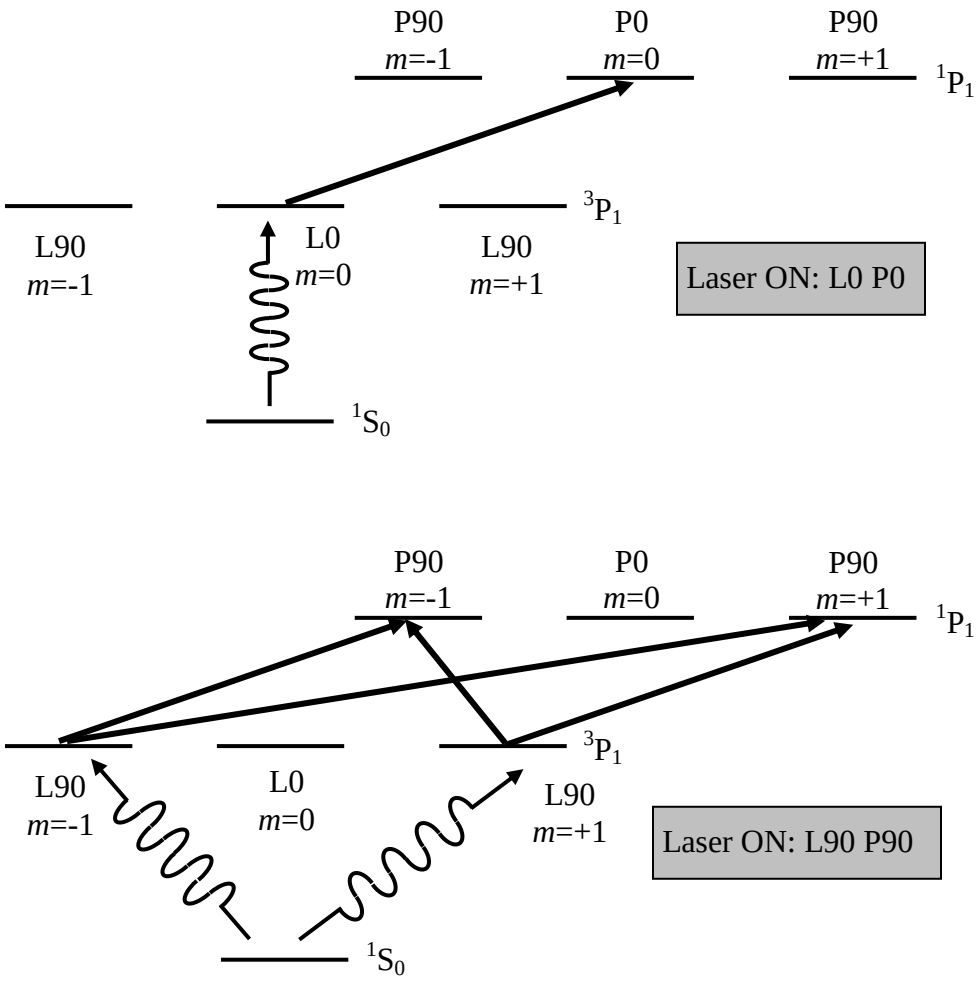

Figure 6.8: Sample magnetic sublevel transitions from $^1S_0$ to $^3P_1$ by laser pumping (wiggly arrows) and then electron excitation from target $^3P_1$ state to $^1P_1$ state (solid arrows).

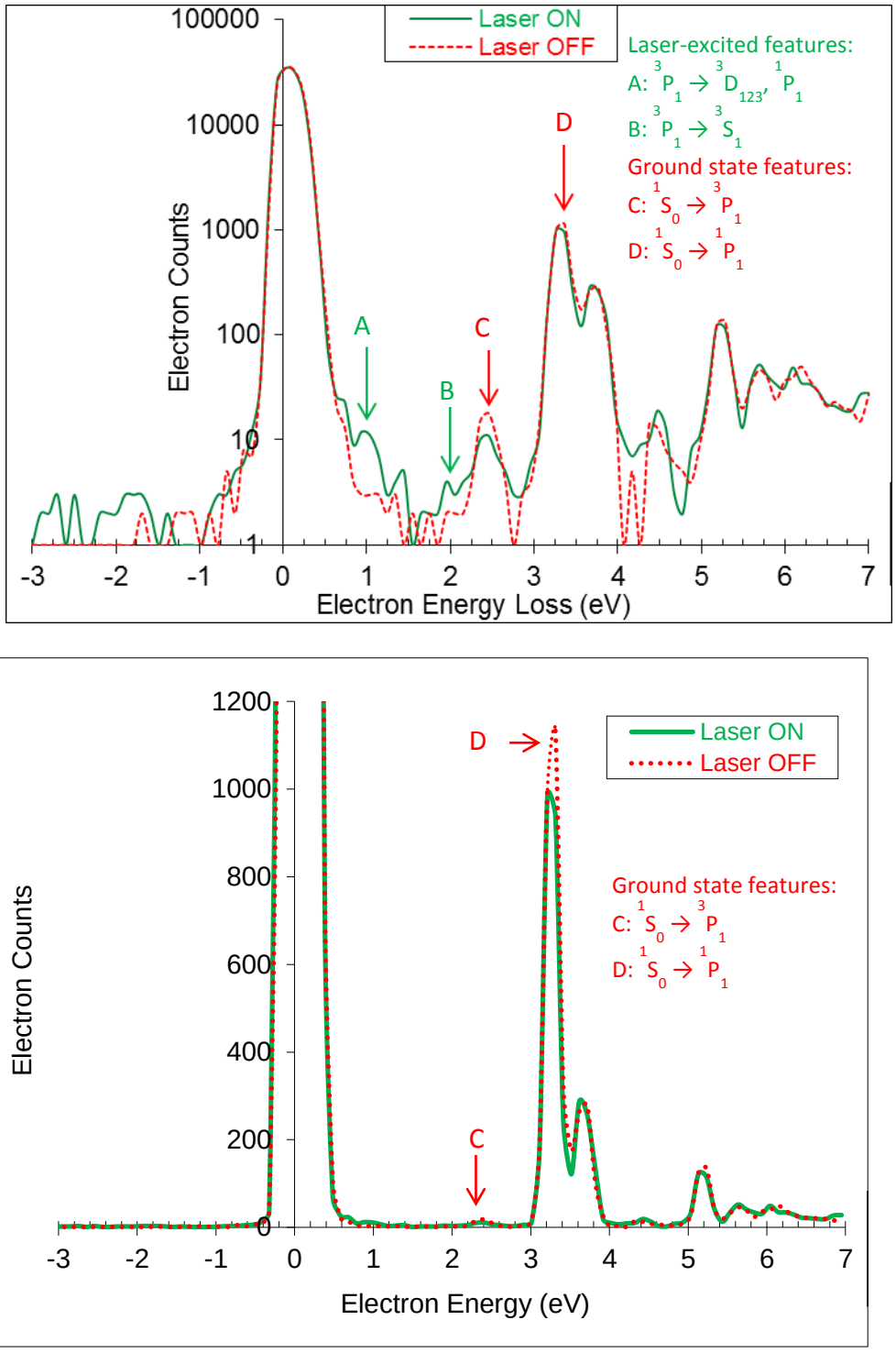

Figure 6.9: (a) Sample ytterbium EELS for electron incident energy of 30 eV at scattering angle of 15° with laser ON and laser OFF; note the logarithmic vertical scale. (b) region of the peaks of interest with a linear vertical scale.

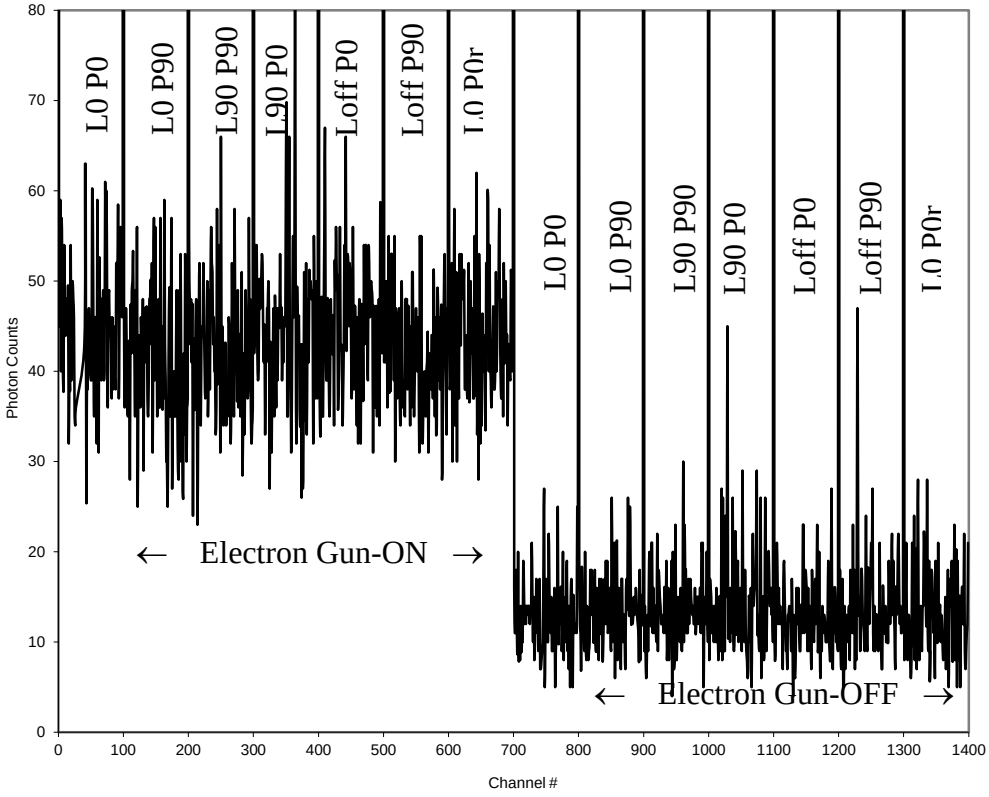

Figure 6.10: Typical 399 nm fluorescence data sequence for 30 eV electron incident energy.

6.3.2 Calibrations of Laser and Fluorescence Angles

For calibrating the laser polarization orientation Lψ, the same approach was used as for barium in Chapter 5. The laser induced fluorescence (LIF) at 556 nm was observed by the PMT system through highly attenuating neutral density filters with the PMT polarizer fixed. A stepping motor controlling a $\lambda/2$ plate rotated the plane of polarization of the laser beam. The measured laser induced fluorescence (LIF) intensity as a function of the laser polarization orientation is shown in Figure 6.11. The minima and maxima indicate the alignment of the laser polarization parallel and perpendicular to the PMT axis

respectively, as illustrated in Figure 6.5. The sinusoidal intensity function, Equation (4.6), was fitted to the data of Figure 6.11 to determine the polarization and locations of intensity maxima and minima. Using statistical error bars $\sqrt{N}$ for each data sample, the fit yielded $\frac{\chi^2}{df}$ of 7.8 with polarization of 0.54±0.01. The minima and maxima positions occur at channel 5 and 55 respectively with a periodicity of 100 channels.

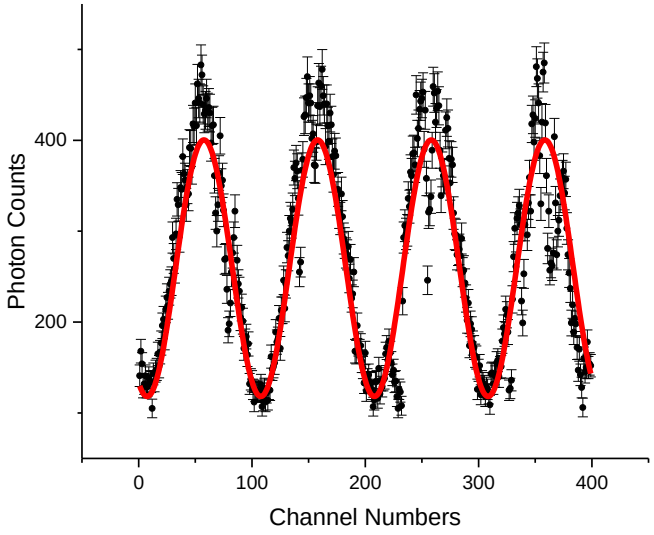

Figure 6.11: Measured 556 nm laser induced fluorescence (LIF) intensity as a function of the laser polarization orientation. The solid curve is a fit to the data. Horizontal axis: 1 channel number = 1.8°.

Similarly, in order to calibrate the fluorescence Pϕ angles, the PMT polarizer was rotated by its associated stepper motor to obtain the LIF sinusoidal intensity function for a fixed laser polarization direction. Figure 6.12 shows the measured LIF as a function of PMT polarizer angle. From these measurements, the polarizer angle settings for P0 and P90 were determined. The sinusoidal intensity function, Equation (4.6), was fitted also to the data of Figure 6.12, to determine the polarization and locations of intensity maxima and

minima. Using statistical error bars $\sqrt{N}$ for each data sample, the fit yielded $\frac{\chi^2}{df}$ of 3.5 with polarization of 0.43±0.01. The minima and maxima positions occur at channel 190 and 360 respectively with a periodicity of 355 channels.

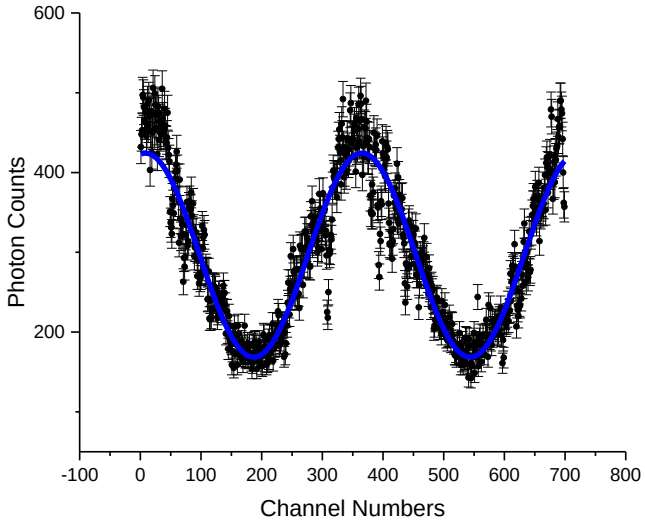

Figure 6.12: Measured and fitted 556 nm laser induced fluorescence (LIF) intensity as a function of the PMT polarizer orientation. Horizontal axis: 1 channel number = 0.51°.

The laser induced fluorescence (LIF) measurements in Figure 6.11 and Figure 6.12 were nominally set up with the PMT polarizer angle adjusted for maximum intensity during the laser scan, and with the laser polarization angle set for maximum intensity during the PMT scan. Ideally both sets of scans should yield the same value of the LIF polarization. A misalignment of the fixed polarization axis for either case yields a measurement that is systematically low by a factor of $\cos^2\alpha$ where α is the angle between

the actual and optimal alignment settings. Taking the alignments to be optimal for Figure 6.11, $P_{LIF} = 0.54 \pm 0.01$ was taken for the measurements.

6.4 Derivations of Equations for Relative Population of the Laser-Excited $^3P_1$ state and Relative Cross Section

In the following sections, the population (Φ) of the laser-excited ytterbium $^3P_1$ state is discussed, followed by a discussion of determination of the relative cross section $\sigma_{PS} = \frac{\sigma_P}{\sigma_S}$ for the 399 nm line transition excited by electron impact out of the $^3P_1$ state.

6.4.1 Population of the Optically Pumped ^3P state

In Chapter 5, the fractional population of the metastable D state in barium was determined from the difference in the counting rate of an EELS feature when the laser was ON and OFF. Here, the fractional population of the optically pumped $^3P_1$ state in ^{174}Yb is determined in a similar way. Let the fractional population of atoms in the $^3P_1$ state be denoted by:

$$\Phi = \frac{N_P}{N}, \tag{6.1}$$

with $N_S + Np = N$, (6.2)

where N is the total atomic target population, N_S is the ground-state $^1S_0$ population, and N_P is the $^3P_1$ state population. The relevant quantities are labelled in Figure 6.13 for convenient reference.

Since the ground state ($^1S_0 - {}^1P_1$) transition at 3.11 eV is the most intense ground state excitation peak in the EELS spectrum (Figure 6.9), it is the optimal transition for determining Φ. The EELS spectrometer was tuned to accept scattered electrons with 3.11 eV energy loss, and their rate is denoted by $i(3.11)$. With this notation, the derivations of Equations (5.7) – (5.11) carry over to the present case in the same form, yielding:

$$\Phi = 1 - \frac{i_{ON}(3.11)}{i_{OFF}(3.11)}. \qquad (6.3)$$

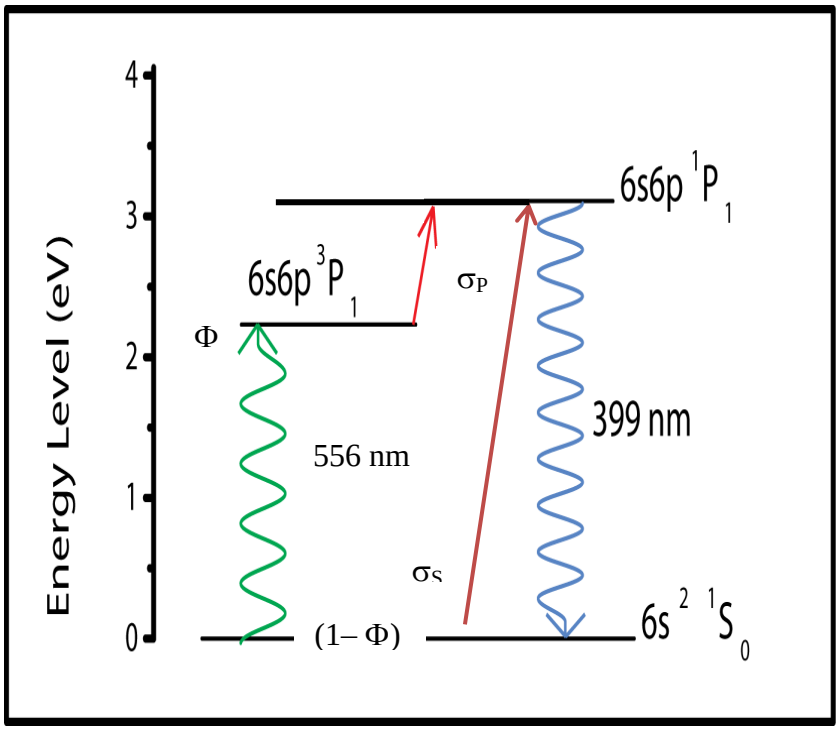

Figure 6.13: Low lying energy level diagram of ytterbium showing the optical pumping transition to the $^3P_1$-state (556 nm) and the radiative decay of the $^1P_1$ state (399 nm) studied in this chapter. Electron excitation cross sections are indicated by solid arrows. The relative populations of the $^1S_0$ and $^3P_1$ target states are $(1 - \Phi)$ and Φ respectively.

It should be noted that a previous study [Hein2010] from this AMO laboratory was carried out using both ground-state peaks, ($^1S_0 \rightarrow {}^1P_1$) and ($^1S_0 \rightarrow {}^3P_1$) to determine the $^1P_1$-state relative population. If there were significant contributions from unresolved

peaks associated with the laser-excited $^1P_1$-state, there would be different relative excited state populations deduced from these two measurements. The measured excited state population from both the ground-state peaks agreed well, justifying the use of the 3.11 eV ($^1S_0 \rightarrow {}^1P_1$) peak for population determination in the present study.

6.4.2 Relative 399 nm Line Excitation Cross Section for Electron Excitation from the $^3P_1$ state

The relative line excitation cross section, $\sigma_{PS} = \frac{\sigma_P}{\sigma_S}$ was determined in a similar way as carried out in Chapter 5 for $\sigma_{DS} = \frac{\sigma_D}{\sigma_S}$ in barium. The laser ON fluorescence signal for laser state L(Ψ) and fluorescence polarizer state P(Φ) is given by:

$$I_{ON}^{L\psi P\phi} = K'[(1-\Phi^{L\psi})\sigma_s^{P\phi} + \Phi^{L\psi}\sigma_P^{L\psi P\phi}], \tag{6.4}$$

where K′ is an experimental proportionality constant accounting for the laser intensity, the incident electron flux, the atomic target density, the PMT solid angle, fluorescence detection efficiency and data acquisition time. σ_s and σ_p are the electron excitation cross sections as indicated in Figure 6.13.

When the laser is OFF, Φ=0, and Equation (6.4) becomes:

$$I_{OFF}^{P\phi} = K'\sigma_s^{P\phi}. \tag{6.5}$$

Since the photon observation angle is 90° in this series of measurements, the polarization-averaged ground state cross section is given by:

$$\langle\sigma_s\rangle \equiv \frac{\sigma_s^{P0} + 2\sigma_s^{P90}}{3}. \tag{6.6}$$

Using Equations (6.5) and (6.6), the polarization-averaged ground-state fluorescence signal can be defined as:

$$\langle I_{OFF} \rangle \equiv K' \langle \sigma_s \rangle \equiv \frac{I_{OFF}^{P0} + 2I_{OFF}^{P90}}{3}. \tag{6.7}$$

Dividing Equation (6.4) by Equation (6.7):

$$\frac{\mathrm{I}_{\mathrm{ON}}^{\mathrm{L}\psi\mathrm{P}\phi}}{\langle I_{OFF} \rangle} = \frac{[\,(1-\Phi^{\mathrm{L}\psi})\sigma_s^{\mathrm{P}\phi} + \Phi^{\mathrm{L}\psi}\sigma_P^{\mathrm{L}\psi\mathrm{P}\phi}]}{\langle \sigma_s \rangle}. \tag{6.8}$$

Rearranging Equation (6.8) gives the relative cross section $\sigma_{PS}^{\mathrm{L}\psi\mathrm{P}\phi}$ as:

$$\sigma_{PS}^{\mathrm{L}\psi\mathrm{P}\phi} = \frac{1}{\Phi^{\mathrm{L}\psi}\langle I_{OFF} \rangle}\left[\mathrm{I}_{\mathrm{ON}}^{\mathrm{L}\psi\mathrm{P}\phi} - \left(1-\Phi^{\mathrm{L}\psi}\right) I_{OFF}^{\mathrm{P}\phi}\right]. \tag{6.9}$$

The above Equation (6.9) gives the relative line emission cross section in terms of the fluorescence intensities and the relative population of the laser excited $^3P_1$-state, determined from the EELS data through Equation (6.3).

6.4.3 Correction for Laser Polarization

Ideally the 556 nm laser induced fluorescence (LIF) should be 100% polarized, indicating 100% laser polarization, but in the present experiment the polarization was significantly lower (54%±1% as seen in Figure 6.11). Assuming that the LIF and laser polarizations were identical, the measured relative cross sections obtained from Equation (6.9) were corrected for the laser polarization using the following relation [Hein2010]:

$$[\sigma_{PS}^{L\psi P\phi}]_{Measured} = P_{Laser}[\sigma_{PS}^{L\psi P\phi}]_{True} + (1 - P_{Laser})[\sigma_{PS}^{P\phi}]_{Average}, \tag{6.10}$$

with $P_{Laser} = P_{LIF}$ assumed and where $[\sigma_{PS}^{L\psi P\phi}]_{True}$ is the corrected relative cross section reported in the present work as $\sigma_{PS}^{L\psi P\phi}$ and $\left[\sigma_{PS}^{P\phi}\right]_{Average} = \frac{\sigma_{PS}^{L0P\phi} + \sigma_{PS}^{L90P\phi}}{2}$.

6.5 Data Analysis

The data analysis was carried out separately for the electron data and the photon data. From the electron data, the population of the laser-excited target ^{3}P-state was determined. The ^{3}P-state population was used along with the photon data to determine the cross sections. These two data analyses are described first, and then the analysis for determining the relative cross section is described.

6.5.1 Electron Data Analysis

As discussed in Section 6.4.1, the depletion ratio of the 3.11 eV EELS peak with laser ON and laser OFF determines the laser-excited ^{3}P-state population, the target state of interest for electron excitation studies. For each of the five electron impact energies studied, there were approximately 60 measurement data files, and each data file contained 14 separate experimental configurations (Table 6.2). With the EELS spectrometer parked at 3.11 eV, the MCS acquisition system recorded the integral of the 3.11 eV peak directly, greatly simplifying the analysis as compared to Chapter 5. Since the fluorescence polarization state was irrelevant for this purpose, averages over P0 and P90 configurations were taken for each laser polarization setting.

Sample data are shown in Figure 6.14 and Figure 6.15, which are analogous to Figure 5.15 for the barium measurements. Each point consists of 100 samples at 200 ms/sample for an acquisition time of 20 s; hence, the detected 3.11 eV electron energy loss rates were approximately 1 – 2 kHz. Figure 6.14 shows a subset of 4 data runs at 15 eV electron energy. The smallness of the target populations is apparent from the relatively tiny changes in integrated electron rate for the different laser configurations. Most data at most energies are similar to Figure 6.14. Figure 6.15 shows a subset of the 10 eV EELS data where, in contrast, the tiny target populations are superposed on a linearly drifting EELS signal. The cause of the linear drifts at 10 eV is not known.

In order to extract target populations from the 10 eV EELS data, a linear fit was first made to the total EELS counts versus data sequence number, and the counts were adjusted relative to the average value measured in sequence state number 4. This procedure was applied to EELS data at all energies, although the only significant corrections were at 10 eV.

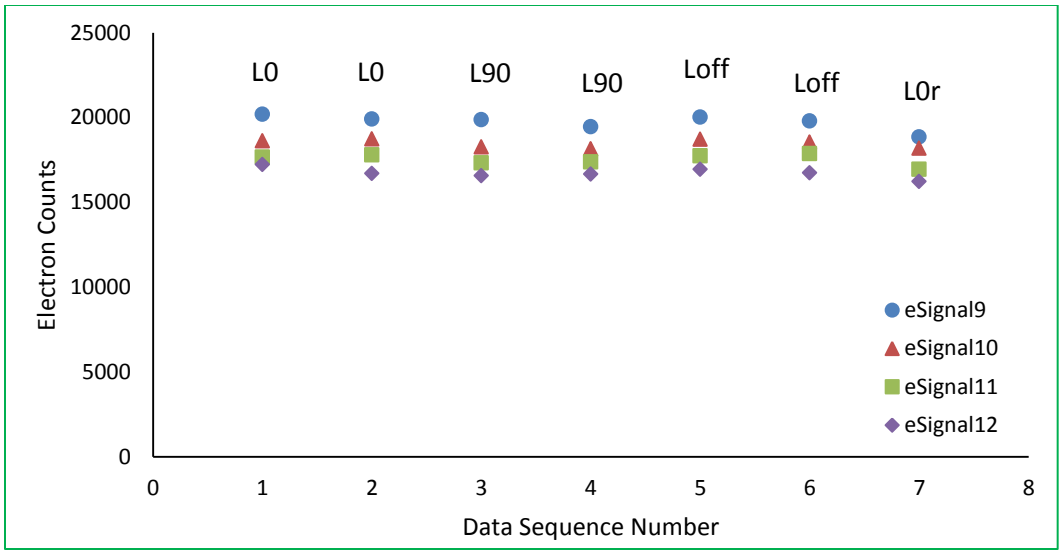

Figure 6.14: Integrated 3.11 eV EELS counts for a subset of typical data runs at 15 eV. The sample intervals correspond to the data sequence of Table 6.2.

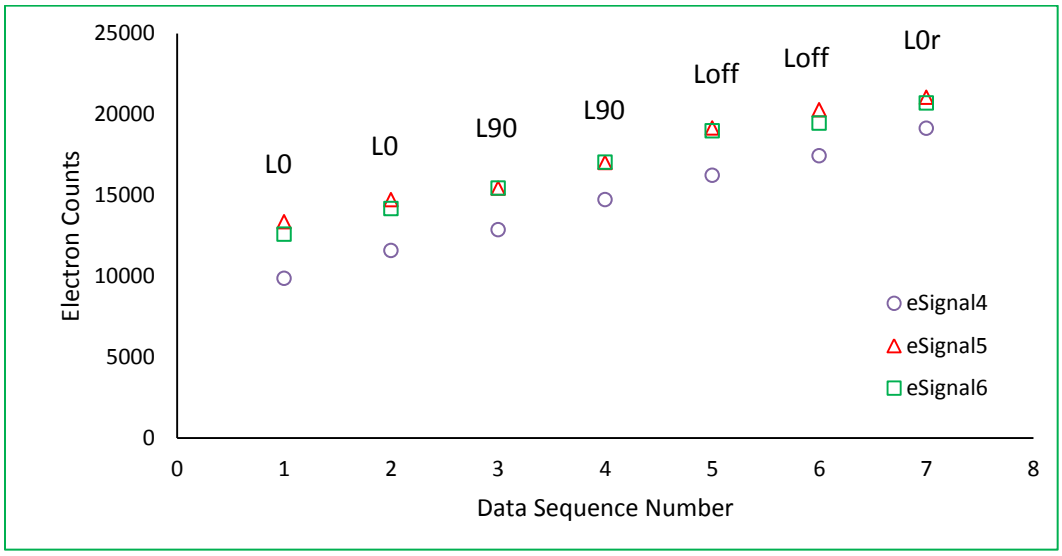

Figure 6.15: Integrated 3.11 eV EELS counts for a subset of typical data runs at 10 eV. The sample intervals correspond to the data sequence of Table 6.2.

Figure 6.16 and Figure 6.17 illustrate the laser-excited target P state populations at 10 and 30 eV calculated by using Equation (6.3). As seen in the figures, the populations are small and laser polarization state-dependent. Typical statistical errors $\delta\Phi = 0.006$ are obtained from counting statistics for each measurement. The scatter in the data points is much larger than the individual error bars, likely due to instability in the actual population values. The correction for EELS linear time drift is very significant at 10 eV and almost undetectable at 30 eV, which is more typical of the full Yb data set.

It can be seen in Figure 6.16 and Figure 6.17 that the laser-excited target ^{3}P-state populations are not the same for the two laser polarization orientations, i.e. $\Phi^{L0} \neq \Phi^{L90}$ for a given electron energy, and also there are some unphysical negative population measurements. To characterize the excited state target populations at each electron incident energy all runs with populations < 0 were first discarded and a weighted mean of all remaining measurements was calculated, according to the procedure described in Section 4.4. The weighted mean accounts appropriately for the different uncertainties in the individual measurements. The reduced χ^2 of the measurements was also calculated. To account for additional non-statistical spread in the data, the uncertainty in the weighted mean was scaled up by a factor[33] of $\sqrt{\frac{\chi^2}{df}}$. An additional cut on populations < 0.01 was made, with very little difference in the results. These cuts, together with the smaller data set at 40 eV eliminated most of the measurements at that energy.

Overall findings for the target state populations are listed in Table 6.3. The average target population achieved for this set of experiments was just over 3%. The

[33] This procedure is equivalent to assigning the statistical error in the mean from the calculated standard deviation and dividing by $\sqrt{N-1}$ for N measurements.

target populations should be independent of electron beam energy, but since the measurements were carried out at different times and were set up separately, they would not be necessarily be identical. Considering systematic trends, the populations Φ^{L0} and Φ^{L90} are generally different for a given electron beam energy. The 10 eV data are anomalous in that $\frac{\Phi^{L0}}{\Phi^{L90}} = 1.6$ whereas for all other energies this ratio is less than 1. It is not clear why this ratio would vary between measurement sets; the variation may be indicative of a systematic error that is not understood.

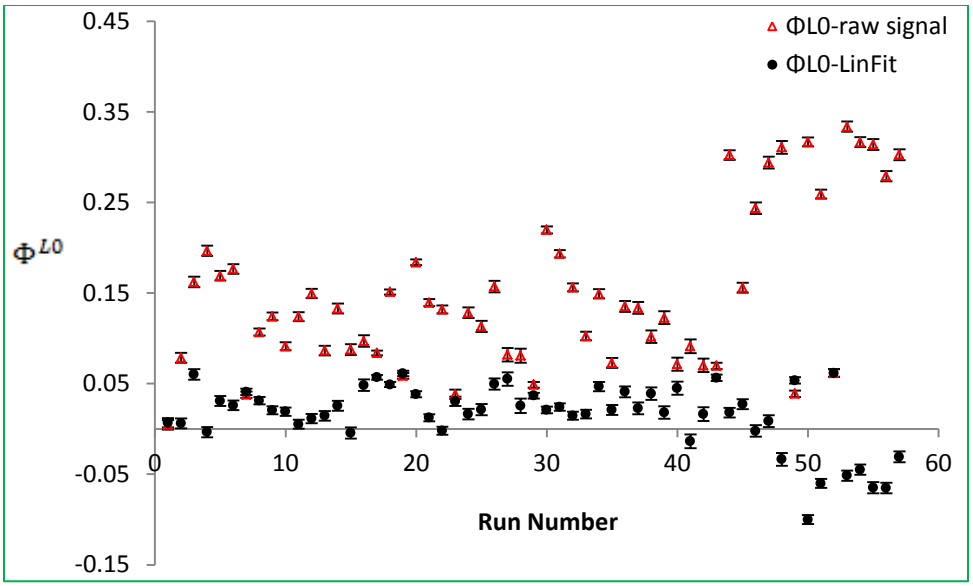

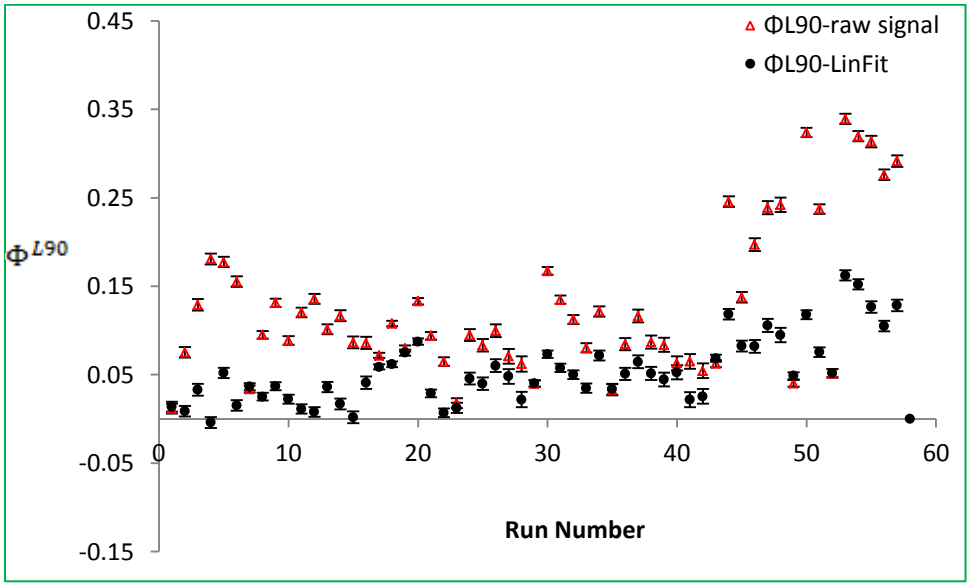

Figure 6.16: Target P state populations versus run number for all 10 eV data. Top panel: L0 configuration; bottom panel: L90 configuration. The raw data are corrected for a linear drift with time as explained in the text.

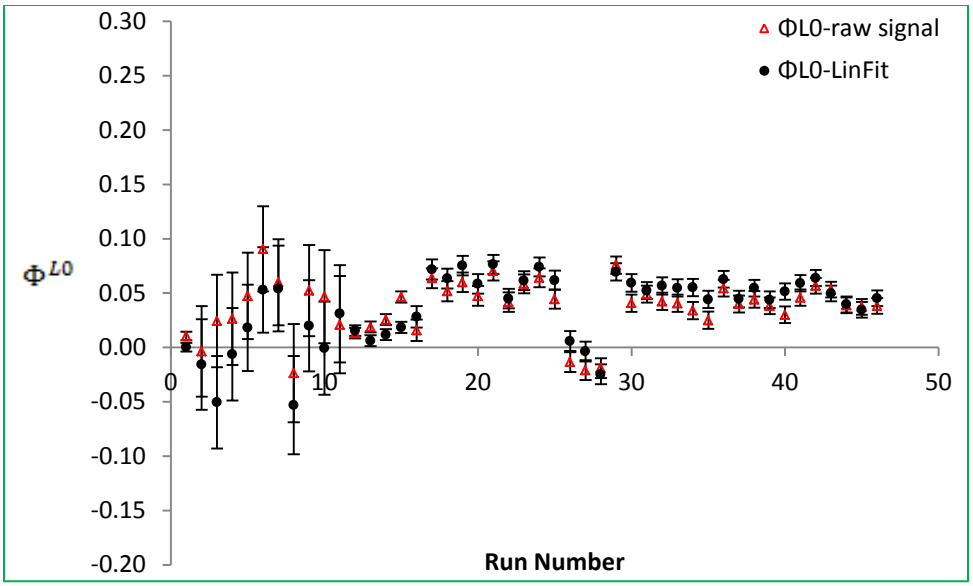

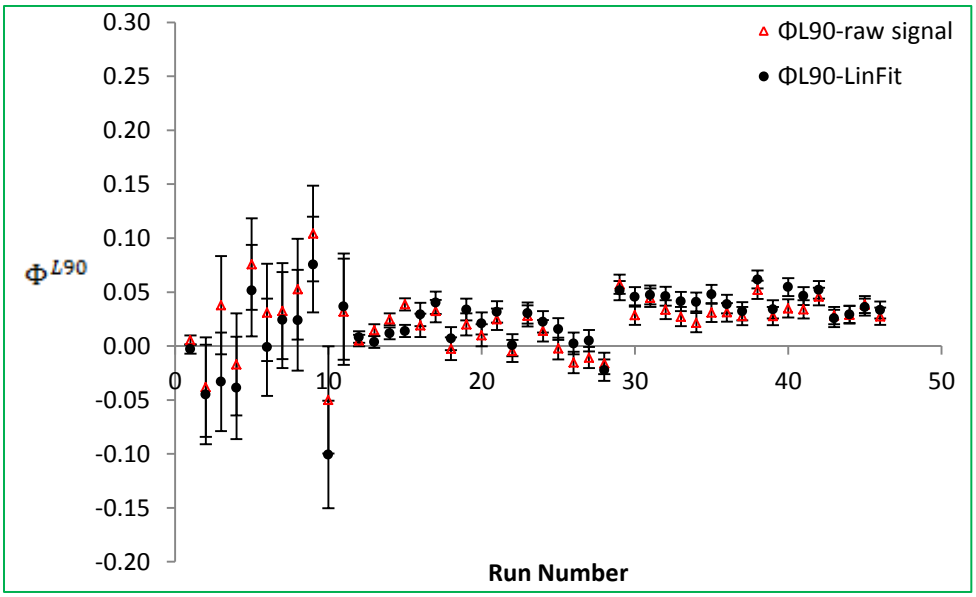

Figure 6.17: Target P state populations versus run number for all 30 eV data runs. Top panel: L0 configuration; bottom panel: L90 configuration. Populations calculated from the raw data and corrected for small linear drifts in time are almost identical in this case.

Table 6.3: Weighted average laser-excited ^{3}P state target populations for both laser polarizations.

Electron Energy (eV)	Cuts	Φ^{L0} Wt. Avg.	$\frac{\chi^2}{df}$	df	Φ^{L90} Wt. Avg.	$\frac{\chi^2}{df}$	df
10	$\Phi < 0$	0.035 ± 0.003	15.1	42	0.057 ± 0.005	41.3	52
	$\Phi < 0.01$	0.037 ± 0.003	14.0	39	0.060 ± 0.003	39.2	49
15	$\Phi < 0$	0.036 ± 0.003	35.7	60	0.030 ± 0.004	55.8	57
	$\Phi < 0.01$	0.036 ± 0.003	35.7	60	0.032 ± 0.004	55.8	54
20	$\Phi < 0$	0.032 ± 0.003	16.6	39	0.014 ± 0.001	2.9	36
	$\Phi < 0.01$	0.032 ± 0.003	16.2	38	0.017 ± 0.001	2.3	28
30	$\Phi < 0$	0.044 ± 0.004	7.7	36	0.029 ± 0.003	4.0	36
	$\Phi < 0.01$	0.046 ± 0.003	6.0	35	0.035 ± 0.003	2.4	32
40	$\Phi < 0$	0.026 ± 0.002	3.8	14	0.007 ± 0.001	0.7	7
	$\Phi < 0.01$	0.026 ± 0.002	3.8	14	0.011 ± 0.0001	N/A	1

6.5.2 Photon Data Analysis

Recall that photon data were collected simultaneously along with the corresponding electron data in a separate MCS. The photon analysis was carried out by first summing all counts in a given measurement configuration for each data run. Figure 6.18(a) shows typical photon summed counts at 30 eV for a particular data run, and Figure 6.18(b) shows the corresponding background-subtracted photon-summed signal. The integration time is 20 s for each data point (100 channels x 200 ms/channel). Error bars are based on counting statistics for the summed photon counts in each data sequence state.

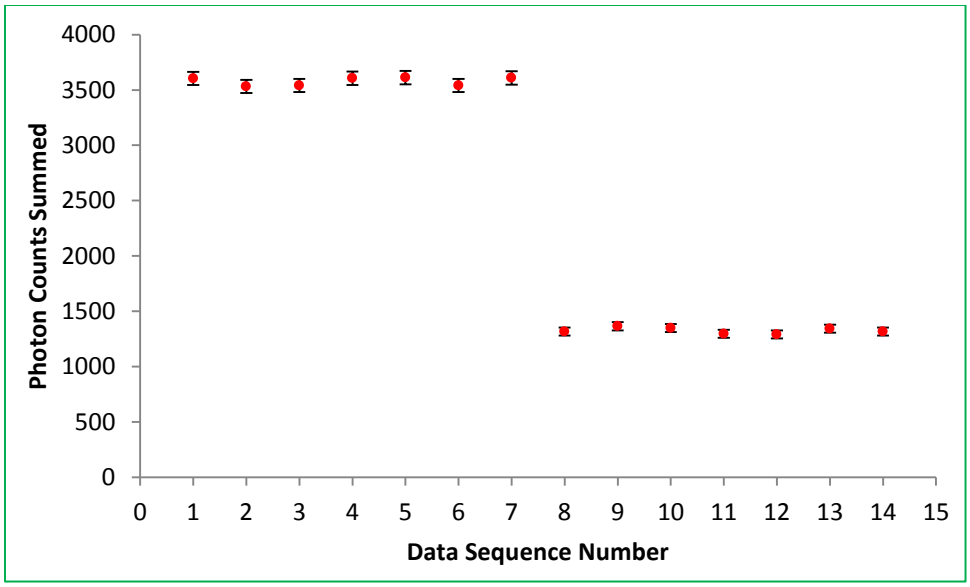

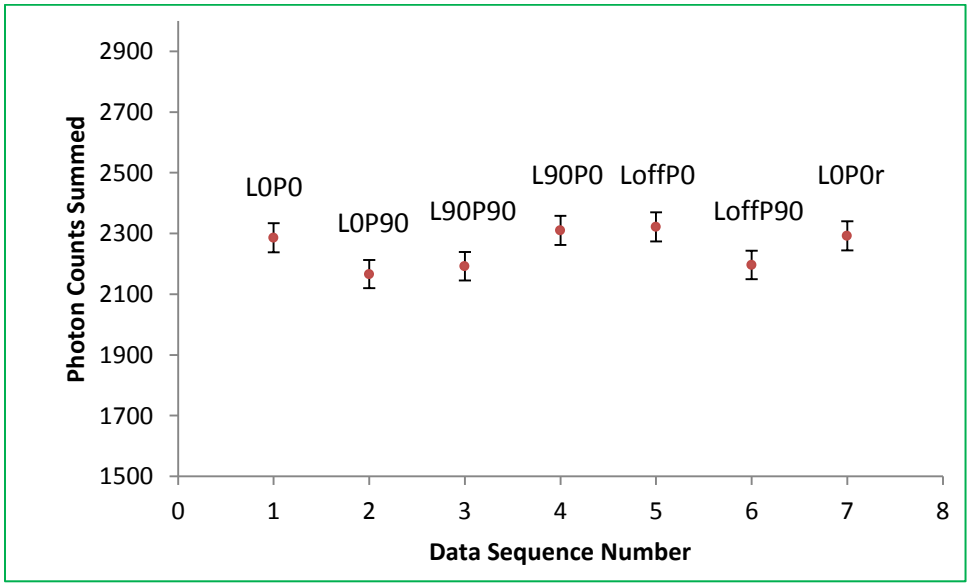

Figure 6.18: Summed photon counts for a typical data run at 30 eV versus data sequence number, with labels corresponding to Table 6.2. Integration time: 20 s per state. Panel (a) Full 14-state data sequence; panel (b) Background-subtracted counts obtained by subtracting gun OFF from gun ON data.

The signal to background ratio is vastly improved here for the ytterbium experiments over the situation of Chapter 5 for barium. Figure 6.19 shows the signal to background ratio for the L90P90 configuration for all data runs at 10 eV, which is characteristic of all the data sets. The signal to background ratio is very stable and was typically in the range of 1.0 – 1.5.

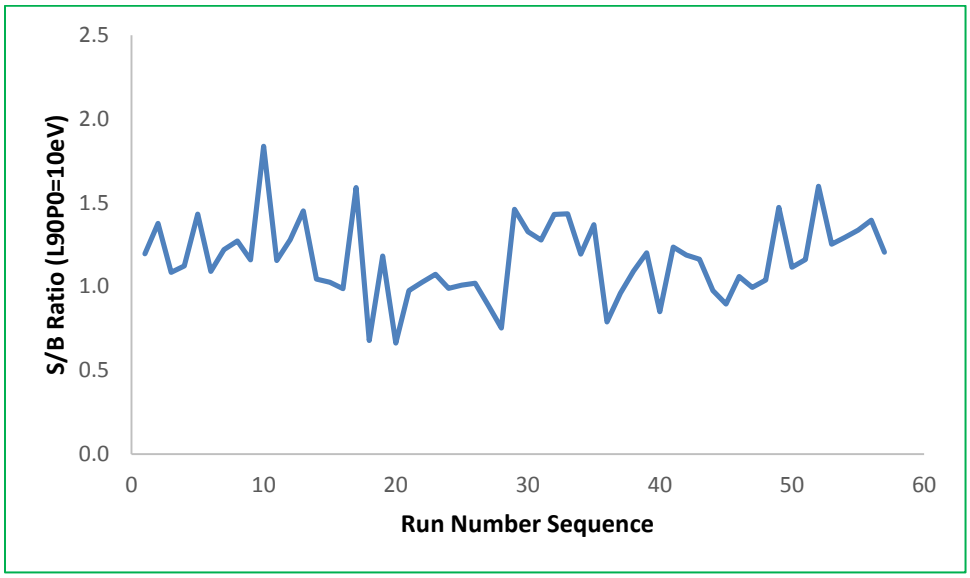

Figure 6.19: Photon signal to background ratio for the L90P90 configuration at 10 eV indicating a very stable photon signal in ytterbium.

6.5.3 Calculation of the Relative Cross Section

After calculating the relative populations of the laser-excited ^{3}P state and analyzing the photon data, the relative cross sections (RCS) were calculated. This was done for each of the four laser and 399 nm fluorescence polarization combinations on a measurement by measurement basis for all energies using Equation (6.9), which is reproduced below for discussion:

$$\sigma_{PS}^{\mathrm{L}\psi\mathrm{P}\phi} = \frac{1}{\Phi^{\mathrm{L}\psi}\left\langle I_{OFF}\right\rangle}\left[\mathrm{I}_{\mathrm{ON}}^{\mathrm{L}\psi\mathrm{P}\phi} - \left(1-\Phi^{\mathrm{L}\psi}\right) I_{OFF}^{\mathrm{P}\phi}\right]. \tag{6.9}$$

Here, *ON* and *OFF* refer to the 556 nm pumping laser. The difficulty of extracting reliable values of $\sigma_{PS}^{\mathrm{L}\psi\mathrm{P}\phi}$ from the data is apparent when one reflects upon the very small target population values, Φ~0.03 as measured by the electron data, and the comparable values of the 399 nm photon data rates I_{ON} and I_{OFF}. To deduce a positive RCS, the measured quantity $I_{ON}^{L\psi P\phi}$ must be larger than $(1-\Phi^{L\psi})I_{OFF}^{\mathrm{P}\phi}$. Physically it is observed that the I_{OFF} rates, which are proportional to the rate of electron excitation of the ($^1S_0$ – $^1P_1$) transition, are almost the same as the I_{ON} rates, which are proportional to the sum of electron excited ($^1S_0$ – $^1P_1$) and ($^3P_1$ – $^1P_1$) transition rates. The ($^3P_1$ – $^1P_1$) transition is electric dipole forbidden and is allowed only due to intercombination radiative processes, so its cross section σ_P is unusually small.

To illustrate the competing factors in detail, the ratio $\frac{I_{ON}}{I_{OFF}}$ is plotted for all runs in the L0Pϕ configurations at 20 eV in Figure 6.20. From Equation (6.9), the condition for a positive value of the relative cross section, $\sigma_{PS}^{\mathrm{L}\psi\mathrm{P}\phi} > 0$ can be expressed as: $\frac{I_{ON}^{L\psi P\phi}}{I_{OFF}^{P\phi}} > (1 - \Phi^{L\psi})$. For the data plotted in Figure 6.20, the weighted average Φ^{L0} = 0.032 (Table 6.3) and therefore a positive RCS requires the ratio $\frac{I_{ON}^{L\psi P\phi}}{I_{OFF}^{P\phi}} > \left(1 - \Phi^{L\psi}\right) = 0.968$. In Figure 6.20 a) the solid line indicates the average of the $\frac{I_{ON}^{L0P0}}{I_{OFF}^{P0}}$ ratio, which is equal to 0.976, while the dashed line shows the minimum $\frac{I_{ON}^{L0P0}}{I_{OFF}^{P0}} > 0.968$ ratio for the RCS to be positive; since 0.976 > 0.968, σ^{L0P0} is expected to be positive. On the other hand, in Figure 6.20 b)

the average of the $\frac{I_{ON}^{L0P0}}{I_{OFF}^{P0}}$ ratio is equal to 0.960; since 0.960 < 0.968, σ^{L0P90} is expected to be negative.

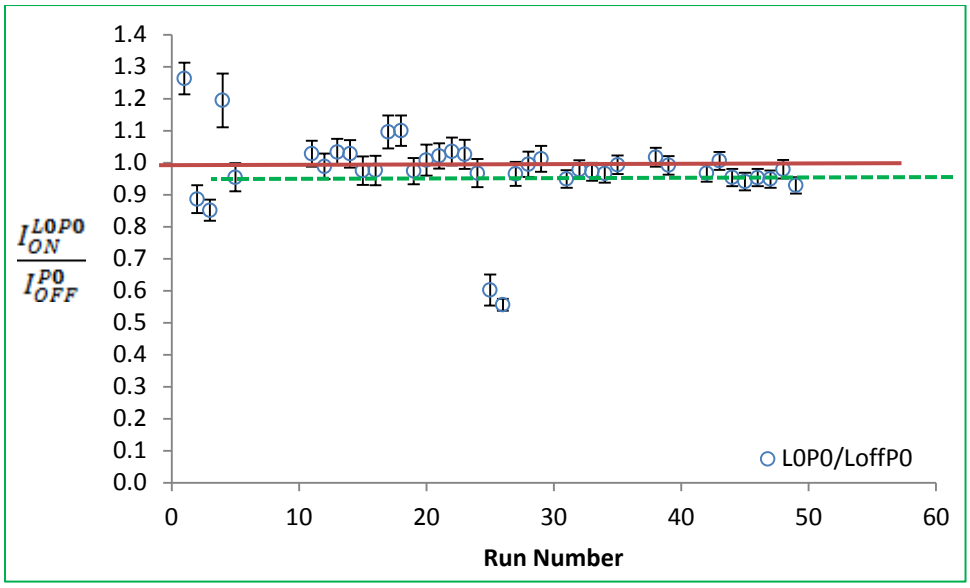

(a)

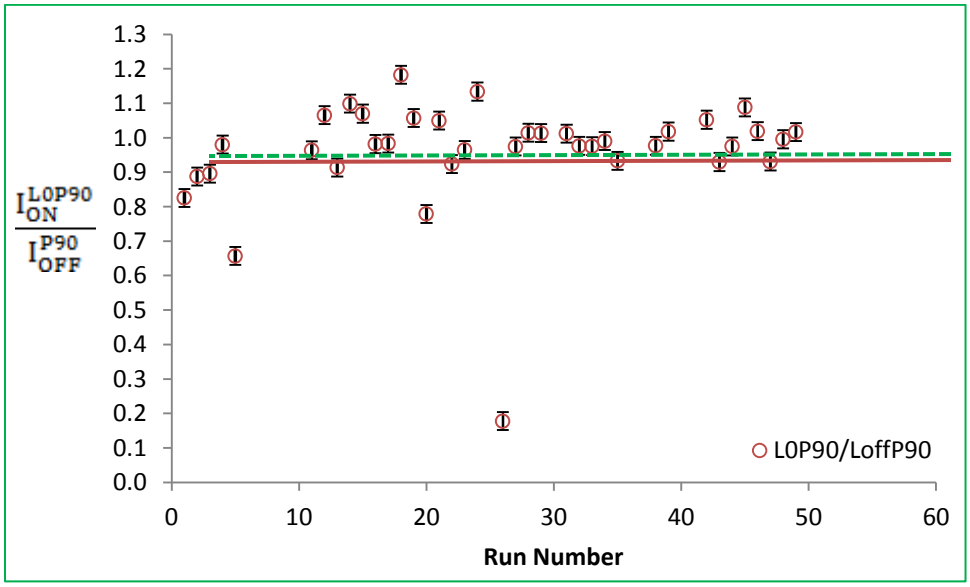

(b)

Figure 6.20: Photon signal ratio for 20 eV (a) $\frac{I_{ON}^{L0P0}}{I_{OFF}^{P0}}$ and (b) $\frac{I_{ON}^{L0P90}}{I_{OFF}^{P90}}$, indicating the laser ON and OFF photon signals very similar i.e. $I_{ON}^{L\psi P\phi} \sim I_{OFF}^{P\psi}$. The solid line indicates the average of the $\frac{I_{ON}^{L\psi P\phi}}{I_{OFF}^{P\phi}}$ ratio while the dash line shows the minimum $\frac{I_{ON}^{L\psi P\phi}}{I_{OFF}^{P\phi}}$ ratio for the relative cross section to be positive.

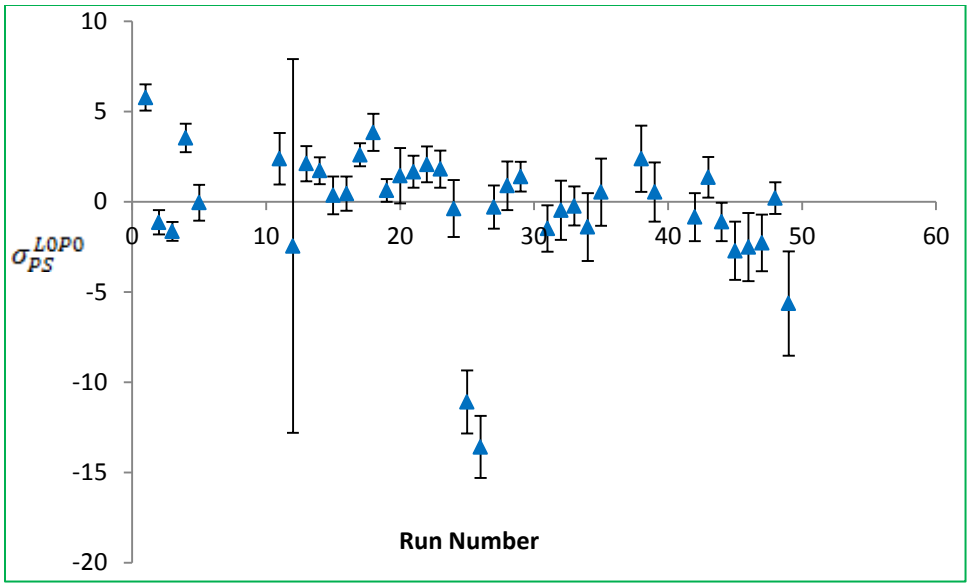

(a)

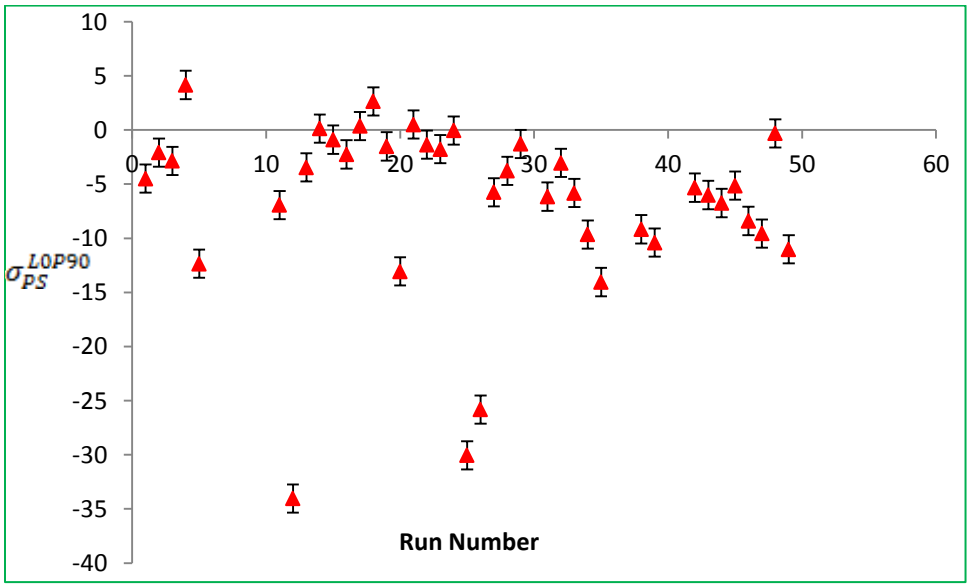

(b)

Figure 6.21: Relative cross section (RCS) at 20 eV of (a) σ_{PS}^{L0P0} showing a positive RCS and (b) σ_{PS}^{L0P90} showing a negative RCS i.e. for the same datasets as in Figure 6.20 (a) and (b) respectively.

Graphs of the measured relative cross sections (RCS) for all data in a particular configuration versus run number are shown in Figure 6.21, which is for the same datasets as in Figure 6.20. The difference between the analysis of Figure 6.21 and the illustration of Figure 6.20 is that the population values for each data run were used in their respective RCS evaluation. It can be seen in Figure 6.21 that the individual RCS are very small, and there are some anomalies with negative values of the RCS, some of which can also be seen in Figure 6.20. The σ_{PS}^{L0P0} values are mostly positive, while σ_{PS}^{L0P90} values are consistently negative. This could be due to either a systematically under estimated $^3P_1$ state population, or inconsistent laser ON and OFF photon measurements, or some other unidentified systematic error which is not presently understood. A weighted mean of the measurements was calculated, accounting appropriately for the different uncertainties in the individual measurements, and the reduced χ^2 of the measurements was also calculated. To account for additional non-statistical spread in the data, the uncertainty in the weighted mean was scaled up by a factor of $\sqrt{\frac{\chi^2}{df}}$. The results for all energies are presented in Table 6.4.

6.6 Results

The relative 399 nm line emission cross sections $\sigma_{PS}^{L\psi P\phi}$ for electron excitation from the ^{174}Yb $(6s6p)^3P_1$ state to the $(6s6p)^1P_1$ state for the various laser and fluorescence polarization configurations for the five energies studied are plotted in Figure 6.22. Here, the analysis as described in Section 6.5 is presented, which found unphysical negative cross sections for some configurations and energies. The error bars in the figures

correspond to the statistical uncertainties in the measurements as described in Section 6.5. The much larger uncertainty for the 40 eV data is attributed to a much smaller data set at that energy.

Table 6.4: Weighted average relative cross sections and $\frac{\chi^2}{df}$ for the reduced data set, after discarding runs with unphysical negative ^{3}P state cross sections and with Φ<0.01.

ElectronEnergy (eV)	Polarization Configuration	Reduced Data Set	
		RCS	$\frac{\chi^2}{df}$
10	L0P0	0.37 ± 0.33	4.3
	L0P90	-5.22 ± 0.63	11.3
	L90P90	0.62 ± 0.15	23.1
	L90P0	2.89 ± 0.28	9.4
15	L0P0	0.89 ± 0.26	2.8
	L0P90	-2.75 ± 4.0	4.8
	L90P90	0.40 ± 0.28	2.3
	L90P0	3.29 ± 0.51	6.8
20	L0P0	0.64 ± 0.43	6.9
	L0P90	-3.12 ± 0.69	12.2
	L90P90	0.72 ± 0.89	3.6
	L90P0	7.07 ± 0.79	2.8
30	L0P0	0.60 ± 0.21	3.8
	L0P90	-0.46 ± 0.23	2.9
	L90P90	0.82 ± 0.23	1.7
	L90P0	2.16 ± 0.28	1.8
40	L0P0	0.31 ± 0.33	1.8
	L0P90	0.10 ± 0.43	1.8
	L90P90	0.12 ± 3.48	0.7
	L90P0	-1.89 ± 2.25	0.7

The L90 cross sections are generally positive and larger for the P0 configuration than for P90. The 20 eV data point for L90P0 is a factor of two higher than the other energies; otherwise the L90 data are roughly constant with energy with the P0 cross sections approximately twice the size of the P90 ones. The L0 cross sections are consistent with zero or negative, indicating a systematic problem of unknown origin at

least for this configuration. The L0 and L90 cross sections could be in principle be different because of their selectivity in populating different magnetic sublevels of the $^3P_1$ state. In particular, L0P0 selects an m=0 to m=0 transition, while L90P0 connects a superposition of ($^3P_1$, m=+-1) to ($^1P_1$, m=0) as illustrated in Figure 6.8.

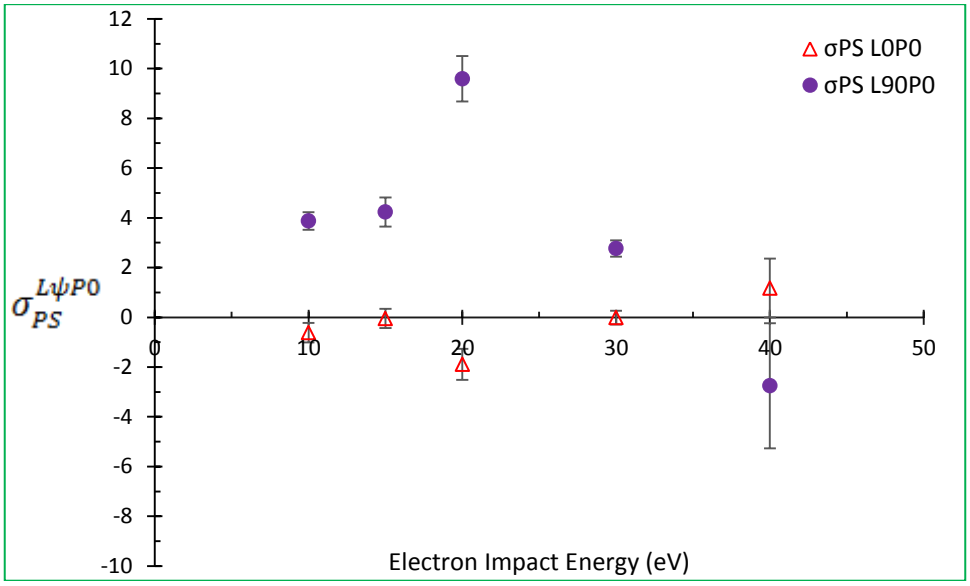

(a)

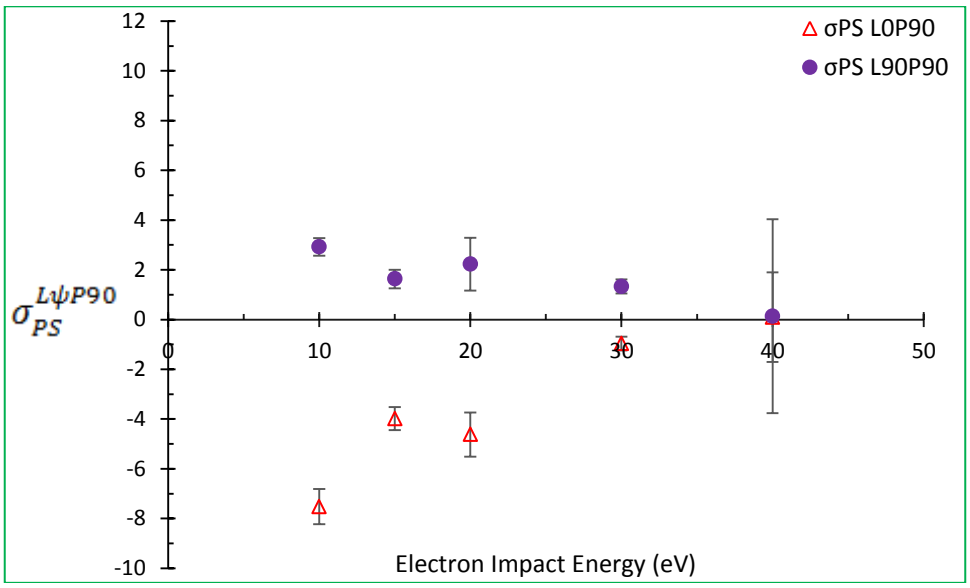

(b)

Figure 6.22: Relative 399 nm line emission cross section $\sigma_{PS}^{L\psi P\phi}$ for different laser and fluorescence polarization configurations, (a) P0 configuration (b) P90 configuration.

The cross sections of Figure 6.22 (a) and (b) with negative contributions accepted at face value are averaged over the fluorescence polarizations via:

$$\sigma_{PS}^{L\psi} = \frac{1}{3}\left[\sigma_{PS}^{L\psi P0} + 2\sigma_{PS}^{L\psi P90}\right], \tag{6.11}$$

and averaged over the laser polarizations via:

$$\sigma_{PS}^{P\phi} = \frac{1}{2}\left[\sigma_{PS}^{L0P\phi} + \sigma_{PS}^{L90P\phi}\right]. \tag{6.12}$$

The results of both averages are plotted in Figure 6.23. When averaging over the fluorescence polarizations, Figure 6.23 a) shows $\sigma_{PS}^{L90} > \sigma_{PS}^{L0}$, and σ_{PS}^{L90} is positive, except at 40 eV where it is consistent with zero. When averaging over the laser polarizations as plotted in Figure 6.23 b), $\sigma_{PS}^{P0} > \sigma_{PS}^{P90}$, and σ_{PS}^{P0} is positive, except at 40 eV where it is consistent with zero.

To obtain the relative emission cross section for excitation of the $^1P_1$ state from the laser-excited $^3P_1$ state, an average of all the polarizations and a sum over all the datasets is made. Averaging over the laser and fluorescence polarizations gives the result:

$$\sigma_{PS} \equiv \frac{\sigma_P}{\sigma_S} = \frac{1}{2}[\sigma_{PS}^{L0} + \sigma_{PS}^{L90}] = \frac{1}{3}[\sigma_{PS}^{P0} + 2\sigma_{PS}^{P90}], \tag{6.13}$$

which is plotted in Figure 6.24. Again, in this calculation the negative cross sections are included at face value at this stage. The results for σ_{PS} are generally positive or consistent with zero when averaged as described above. However, the inclusion of negative cross section measurements in the averaging process is not strictly physically reasonable. An approach for addressing this problem is discussed in the next section.

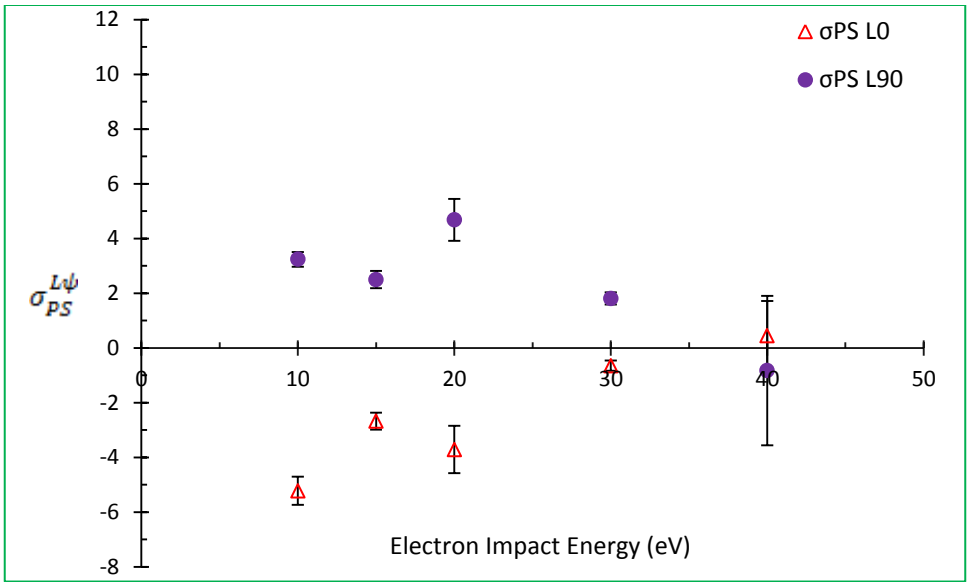

(a)

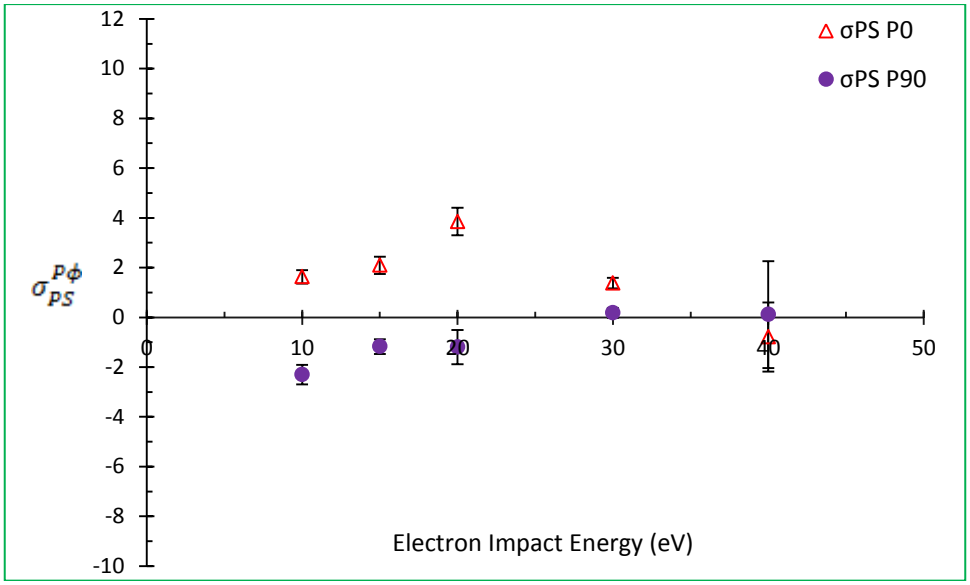

(b)

Figure 6.23: Relative line emission cross section out of the $^3P_1$ state averaged over (a) fluorescence polarization and (b) Laser polarization.

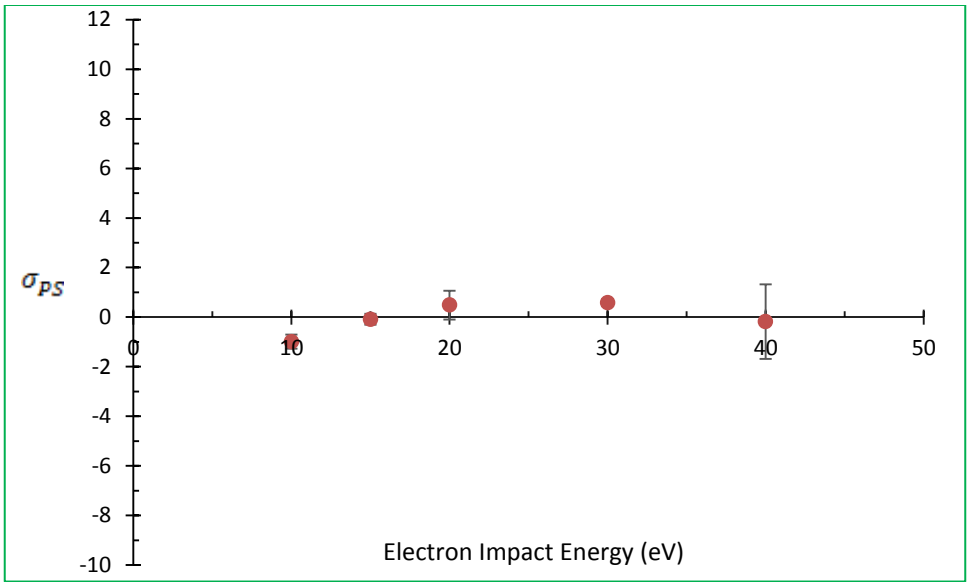

(a)

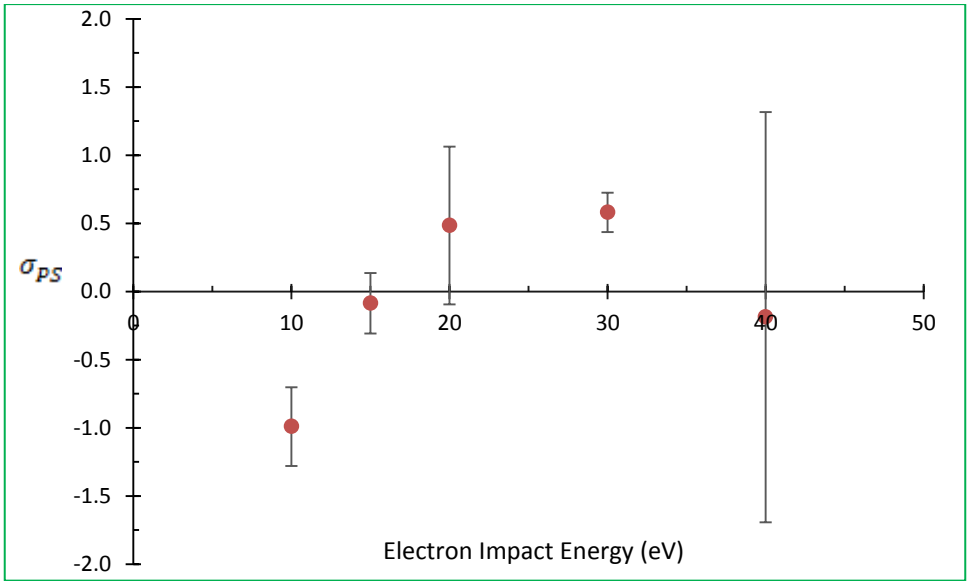

(b)

Figure 6.24: Relative line emission cross section averaged over both laser and fluorescence polarizations. (a) same scale as Figure 6.23 (b) same data, expanded vertical scale.

6.7 Discussion

As reported in Section 6.6, for the very small target populations and the P-state electron excitation cross sections that were studied, the measured relative line emission cross sections $\sigma_{PS}^{L\psi P\phi}$ yielded unphysical negative results for some configurations and beam energies. Likely, the sensitivity of the experimental setup was not sufficient for reliable measurements of cross sections that are this small. However the data can be used to establish limits for comparison with theory.

A reasonable approach is to set all negative partial cross sections to zero and recalculate the average. The results are compared with the original experimental average (including negative contributions) in Figure 6.25. In this 'forced zero' approach, the average relative cross sections are larger, on the order of 1.0, and are roughly constant with energy. It should be noted that the measured results correspond to the relative line emission cross section; the comparison with theory will be discussed in the next section.

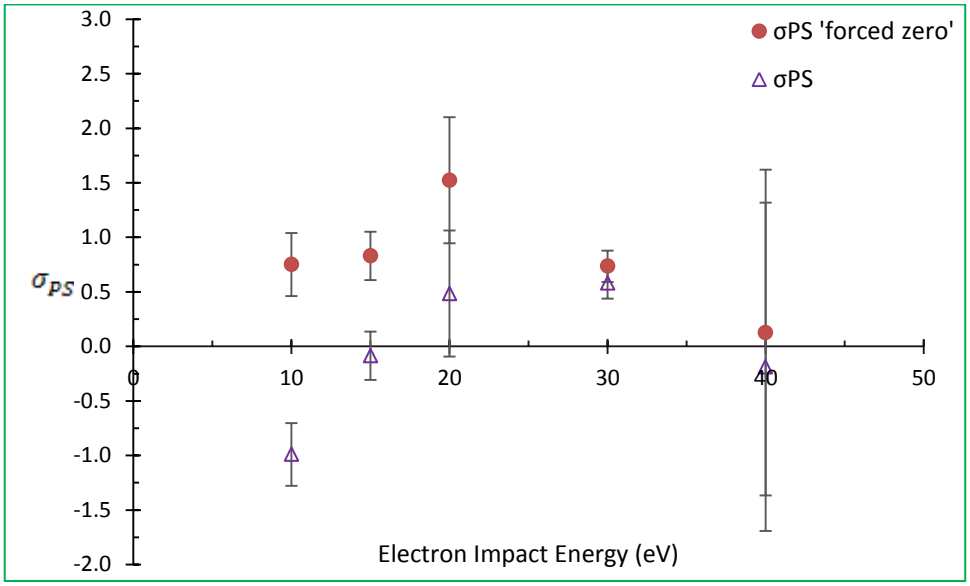

Figure 6.25: Relative cross section averaged over both laser and fluorescence polarizations. Solid symbols: 'forced zero' calculation as discussed in the text; open symbols: original calculation including negative contributions.

6.7.1 RCCC-Model Calculations

Prior to completing the present measurements, there were no available predictions for σ_{PS} from theory. In 2014, Bostock et al. (Bostock2014b) provided unpublished new calculations in the fully relativistic theoretical RCCC model which are presented here in Figure 6.26. Note that the vertical scale of Figure 6.26(a) for σ_S is 10x larger than Figure 6.26(b) for σ_P.

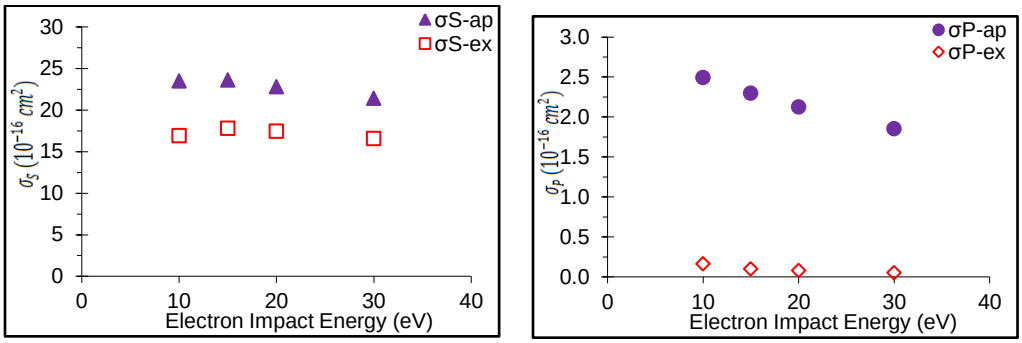

(a) (b)

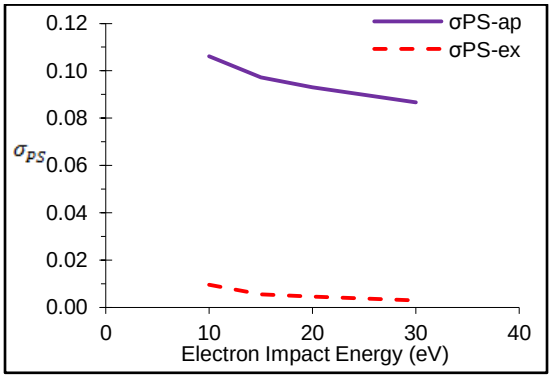

(c)

Figure 6.26: Theoretical cross sections for the transitions of interest calculated in the RCCC model [Bostock2014b]. Each panel shows both apparent (solid symbol/line), and the excitation (open symbol/dash line) cross sections. (a) σ_S (b) σ_P (c) σ_{PS}.

In the present study the measured line emission cross section and apparent cross section are the same, as there is no branching ratio to be considered. Looking first at the predictions for the apparent cross sections (solid symbols in Figure 6.26), it can be seen that the ground state excitation σ_S is expected to be about 10x as large as σ_P.

A comparison of the apparent (solid symbols/solid line) and excitation (open symbols/ dash line) cross sections indicates the contribution of cascading from higher levels. The relative cascading contribution $(\sigma_{ap} - \sigma_{ex})/\sigma_{ex}$ is about 25% of the σ_S cross section while it is almost 100% of the σ_P cross section. This large predicted cascading contribution to σ_P implies that most of the 399 nm fluorescence would have been due to electron excitation of higher energy states which fed the ^1P state as they decayed, rather than due to direct excitation of the ^1P state from the laser-excited ^3P target state in the measurements reported here. Hence, it was decided to restrict the experimental conclusions to the apparent cross sections only for these transitions.

6.7.2 Comparison for the Relative Cross Section $\sigma_{PS\text{-}ap}$

In this section, the apparent relative cross section data are compared with the only available RCCC model theoretical calculations. The theoretical prediction of σ_{PS} by the RCCC model is shown Figure 6.26(c); again for this relative cross section, the cascading contribution dominates.

The comparison between theory and experiment is shown in Figure 6.27. The RCCC model calculations of the relative cross section σ_{PS} are 10x smaller than the 'forced zero' calculation of σ_{PS} found by experiment. The present experimental σ_{PS} is almost within the limits of experimental error bars of the 10x-rescaled RCCC model. No uncertainty was provided for the RCCC model calculations. There are no other

measurements of σ_{PS} (or σ_P) in ytterbium that could be used to compare with the present data. Note that the RCCC model calculations have been done very recently and have not been yet been published; the authors have not yet been informed of the final results from this thesis.

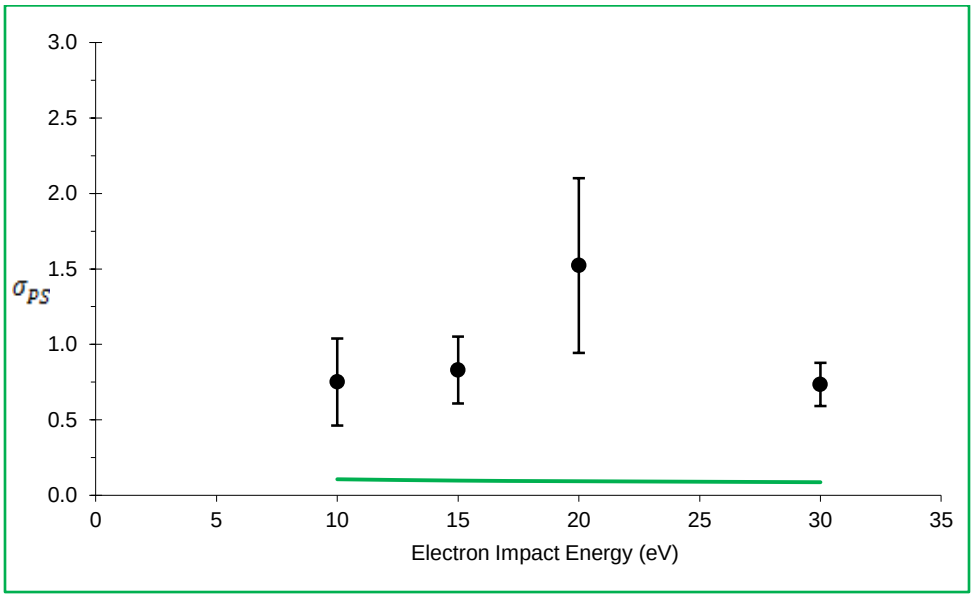

(a)

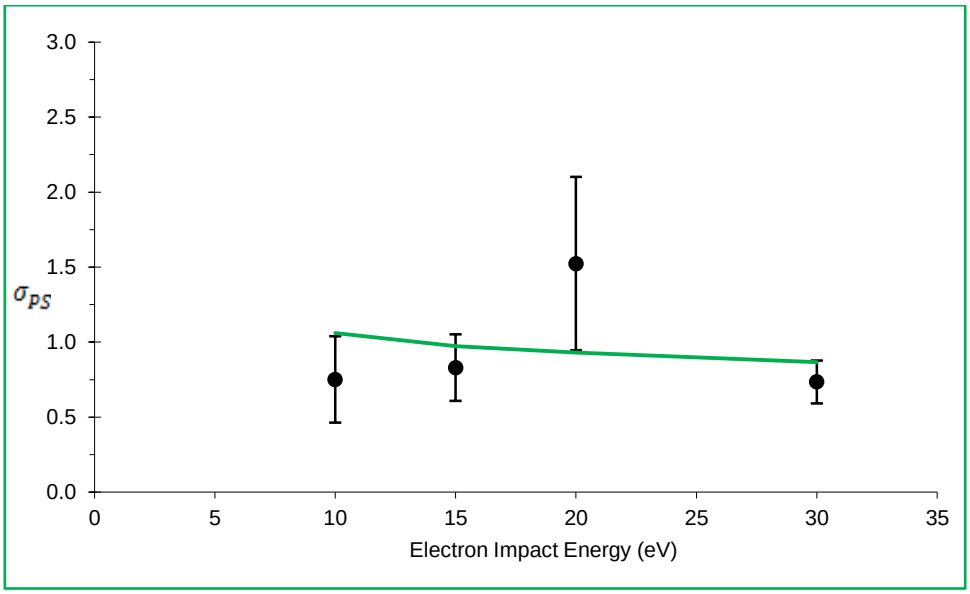

(b)

Figure 6.27: The apparent relative cross section $\sigma_{PS\text{-}ap}$ of ytterbium (a) Comparison between present work (data points) and RCCC theory (solid line) [Bostock2014b], (b) Comparison between present work and the RCCC prediction rescaled by a factor of 10.

6.7.3 The Apparent Cross Section $\sigma_{P\text{-}ap}$

The apparent cross section for the $(6s6p)^3P_1 \rightarrow (6s6p)^1P_1$ transition $\sigma_{P\text{-}ap}$ can be determined by multiplying the relative cross section σ_{PS} by existing values of $\sigma_{S\text{-}ap}$ for the $(6s^2)^1S_0 \rightarrow (6s6p)^1P_1$ transition. $\sigma_{S\text{-}ap}$ was taken from previous experimental work of Shimon [Shimon1981] and Predojevic [Predojevic2005a], and also from the theoretical models RDW [Srivastava1995], UDW [Johnson1998] and RCCC [Bostock2014b]. These $\sigma_{S\text{-}ap}$ are plotted in Figure 6.28. Unfortunately, existing experimental values for $\sigma_{S\text{-}ap}$ disagree by a factor of 2, while theoretical predictions vary by a factor of 3. Hence, the estimate of $\sigma_{P\text{-}ap}$ obtained by rescaling $\sigma_{S\text{-}ap}$ encounters a significant additional uncertainty.

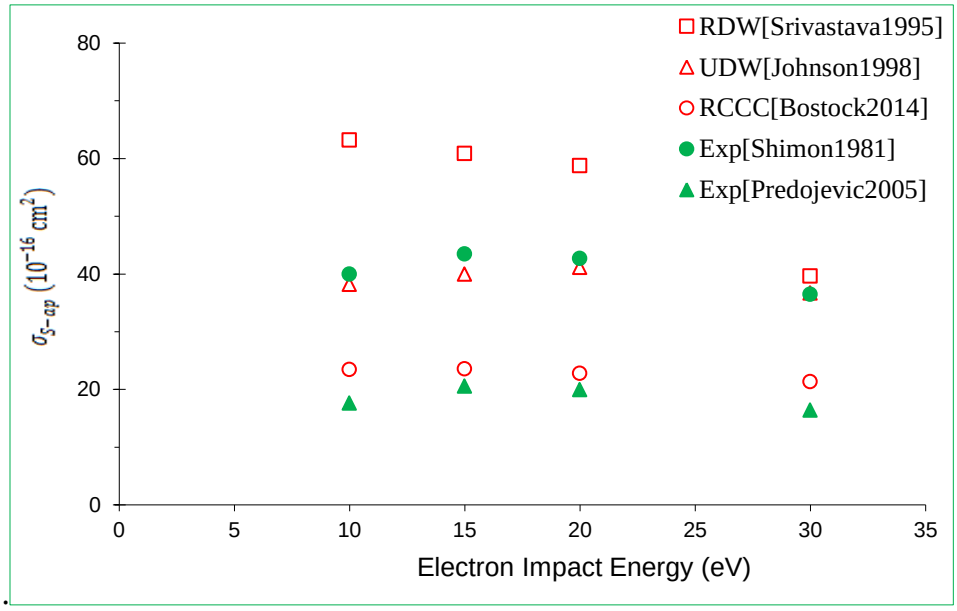

Figure 6.28: Ground state excitation cross section $\sigma_{S\text{-}ap}$ from previous experimental works and theoretical models. Open symbols: theory; closed symbols: experiment.

From Figure 6.28 it can be seen that the RDW model (being based on a non-relativistic approach) disagrees most significantly with other works especially at lower energies and should not be considered in determining $\sigma_{P\text{-}ap}$. The UDW model agrees well

with the experimental work of Shimon et al. [Shimon1981], while RCCC model agrees well with the more recent experimental work of Predojevic et al. [Predojevic2005]. Thus the two data sets give a range of $\sigma_{S\text{-}ap}$.

The present work $\sigma_{P\text{-}ap}$ was obtained by multiplying the measured $\sigma_{PS\text{-}ap}$ with the average of the two published data sets of $\sigma_{S\text{-}ap}$. These are tabulated in Table 6.5 and are plotted in Figure 6.29. Figure 6.29 shows the present work and the range of $\sigma_{P\text{-}ap}$ (dashed line) deduced from these measurements in comparison with RCCC model [Bostock2014b]. The normalization uncertainty $\Delta\sigma_{norm}$ is calculated applying half the difference between the two sets of experimental measurements used in the normalization. The solid line at the bottom of the figure shows the RCCC model prediction for $\sigma_{P\text{-}ap}$. Despite the large range in the normalized results, theory remains ~10x smaller than experiment in this case.

Table 6.5: Apparent cross section $\sigma_{P\text{-}ap}$ of $(6s6p)^3P_1 \rightarrow (6s6p)^1P_1$ transition after normalizing the present data of σ_{PS} with $\sigma_{S\text{-}ap}$. Also shown are the limits of normalization along with errors.

E_e (eV)	Present work σ_{PS}	$\sigma_{P\text{-}ap} \pm \Delta\sigma_{exp} \pm \Delta\sigma_{norm}$ (x 10^{-16} cm^2) normalized to average of σ_S of [Shimon1981] and [Predojevic2005a]
10	0.75 ± 0.29	$22 \pm 8 \pm {}^{7}_{9}$
15	0.83 ± 0.22	$27 \pm 7 \pm {}^{9}_{10}$
20	1.52 ± 0.58	$48 \pm 18 \pm {}^{17}_{17}$
30	0.73 ± 0.14	$19 \pm 4 \pm {}^{8}_{7}$
40	0.13 ± 1.5	N/A

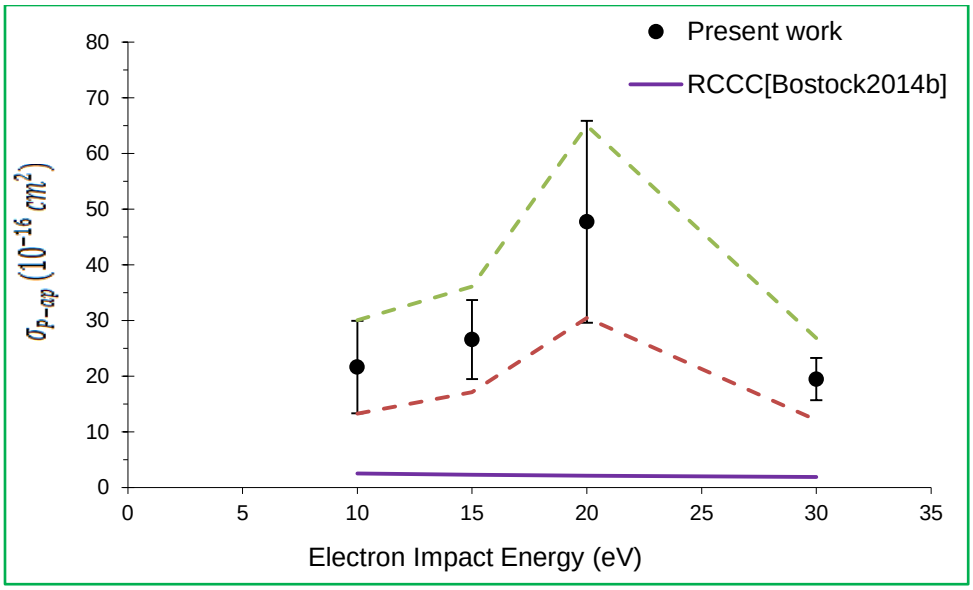

Figure 6.29: Present work apparent cross section $\sigma_{P\text{-}ap}\pm\Delta\sigma_{exp}$ (solid symbol) for the $(6s6p)^3P_1\rightarrow(6s6p)^1P_1$ transition in ytterbium obtained by multiplying the present σ_{PS} by average of previously measured σ_S, compared to the RCCC model prediction (solid line). The dashed lines show the independent normalization error $\Delta\sigma_{norm}$.

6.8 Summary and Conclusion

In this chapter, the electron impact excitation of the laser excited ytterbium $(6s6p)\ ^3P_1$ state has been studied by measuring the intensity of the 399 nm line emission from the $(6s6p)\ ^1P_1$ state to the ground level. The 399 nm line emission cross section σ_{PS} for electron excitation of the laser-excited $^3P_1$ state was measured relative to the excitation out of the ground state. This measured σ_{PS} appears to be too small to measure reliably with the current experimental setup, as evidenced by finding unphysical negative cross sections in some laser polarization configurations. Also, fluctuations in the measurements exhibited larger $\sqrt{\frac{\chi^2}{df}}$ than could be understood based on a thorough examination of the known statistical errors. In order to obtain reasonable limits on the measured cross

sections, a ‘forced zero’ method was applied, in which the negative cross sections were set to zero numerical value. This allowed to set an experimental lower limit on the cross section σ_{PS} which was found to be 10x larger than the only available RCCC model value [Bostock2014b].

Alternatively, the measured cross section σ_{PS} with negative contributions at face value can be estimated by the limits determined by their error bars. A 1σ error band plot of σ_{PS} is shown in Figure 6.30 along with the original measured σ_{PS} and the RCCC model predictions. Recall that the EELS yields showed a significant and systematic linear drift in time for 10 eV data, which was corrected in the analysis; this should be borne in mind when considering the impact of the 10 eV point in Figure 6.30. Also, the data set was very small for 40 eV, resulting in the larger error bars at that energy. The other points represented about 7 hours of data taking; with the present setup, the longest feasible measurement time would be around 9 hours before the laser system would need to be shut down and completely retuned. It can be seen that due to the very small values of σ_{PS}, the sensitivity of the experimental apparatus would have to be improved for more reliable measurements.

Nonetheless the current experimental data provide the first electron excitation cross section estimate of the Yb $(6s6p)^1P_1$ state from the laser-excited $(6s6p)^3P_1$ state. It was compared with the only available theoretical RCCC-model [Bostock2014b]. Improvement of the experimental technique and further refinement of the theory are both needed to make progress in this challenging field.

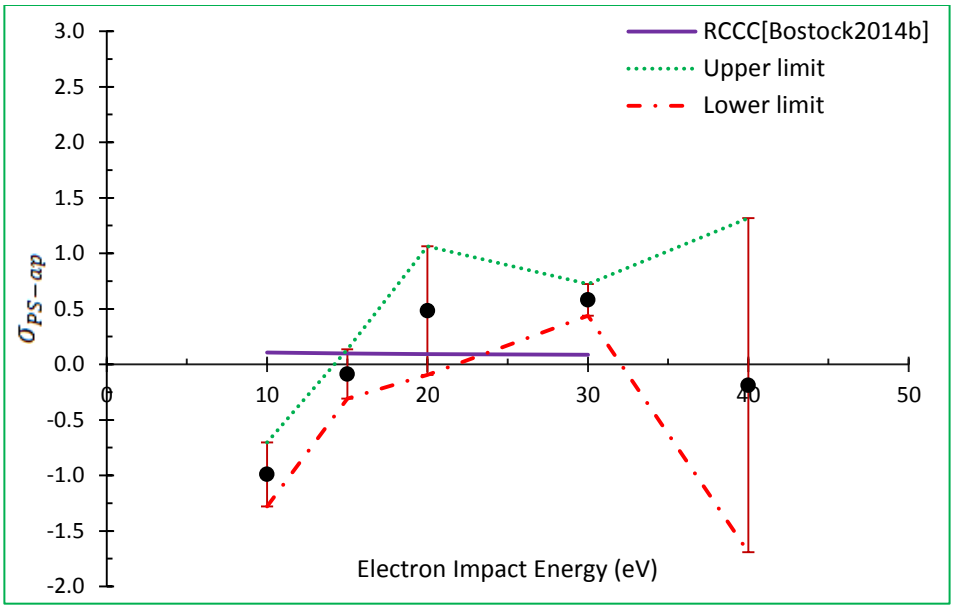

Figure 6.30: Limits of the measured σ_{PS} defined by their error bars along with the RCCC-model calculated values.

Also earlier from this AMO lab, electron-impact excitation from laser excited $^3P_1$ state has been carried out for 20 eV electron energy [Hein2011a]. The $^3P_1 \rightarrow {}^1P_1$ and $^3P_1 \rightarrow {}^3D_{1,2,3}$ electron impact excitation processes in ytterbium cannot be resolved due to the close proximity of these final state energy levels. The present work measurements and in addition to the new Bostock theory [Bostock2104b] both indicate that $^3P_1 \rightarrow {}^1P_1$ would have made a negligible contribution to the Hein work [Hein2011a].

Chapter 7

Conclusion and Summary

Three experiments were reported in this thesis. All involved the detection of fluorescence photons from decays of states in heavy atoms excited by electron bombardment. The goal of the experiments was to infer total cross sections for electron excitation of selected states in barium and ytterbium. The range of electron beam energies (10 – 50 eV) was chosen to challenge relativistic theories at an intermediate energy above threshold for excitation of the states of interest. The experimental techniques relied on previous measurements for absolute normalization; measured branching ratios were used to convert the line emission cross section to the level apparent cross section, and theoretical models were used to account for cascade feeding from higher states to achieve the level excitation cross section.

The experiments described in Chapter 4 involved excitation from the ground state of barium to the low lying $(6s6p)^1P_1$ (2.24 eV) and $(6s7p)^1P_1$ (3.54 eV) states. Measurements of the decay fluorescence at 554 nm and 583 nm respectively were used to determine the relative emission cross sections and ultimately the electron excitation cross section of the 3.54 eV state. Unexpected difficulties included a large photon background at both wavelengths and the surprising discovery that the photon signal rates did not scale with the inelastic electron rate measured in the EELS spectrometer. The later precluded

the intended use of the EELS spectrum for counting rate normalization purposes. Despite these challenges, it was possible to reproduce previously published results for the 583 nm line emission cross section, although with larger than intended error bars. A comparison with new and previously unpublished relativistic calculations by Bostock et al. as well as earlier published calculations was made; results are of the same order of magnitude but experimental uncertainties precluded definitive conclusions from being drawn. For future work, it is recommended that the 'blended' contributions from lines close to 583 nm due to other electron-excited transitions be measured separately to obtain the 'true' excitation cross section of barium $(6s7p)\ ^1P_1$ level out of the ground state.

The experiments of chapters 5 and 6 involved electron scattering from excited states of barium and ytterbium respectively. The excited target states were prepared by optical pumping with a linearly polarized laser beam. EELS spectra were analyzed to infer relative population of the excited target states in each case, as required for normalization purposes. For the Ba experiments of Chapter 5, relative target state populations of the metastable $(5d6p)^1D_2$ states at the 20% level were obtained, while in the case of Yb, the lower relative abundance of the most abundant isotope for optical pumping limited the target state populations to a few percent.

The laser-excited target state barium experiments, like the ground state measurements of Chapter 4, were subject to large photon backgrounds, with a signal to background ratio on the order of 10%. The ytterbium measurements on the other hand, as reported in Chapter 6, exhibited much better photon signal to background ratios on the order of 1.0. In all three experiments, the photon data exhibited short timescale fluctuations consistent with counting statistics, yet the run-to-run variations in both

photon and scattered electron rates were much larger, characteristic of time-varying experimental conditions which limited the statistical precision of the results.

The excited state studies of Ba and Yb produced new results in an area that is particularly challenging to both experiment and theory. The excitation cross section for the $(6s5d)^1D_2 \rightarrow (6s7p)^1P_1$ transition in Ba had not been measured previously; results are about a factor of 5 smaller than predicted by the latest relativistic RCCC calculations of Bostock et al. The apparent cross section for the $(6s6p)^3P_1 \rightarrow (6s6p)^1P_1$ transition in Yb had not been measured previously; results are about a factor of 10 larger than recent calculations of Bostock et al., which were only available after the measurements had been completed.

Both sets of excited state measurements (chapters 5 and 6) featured studies of laser polarization dependence of the relative emission cross section. Weighted averages of many experimental runs were combined to deduce the physics results of interest. These larger data sets exhibited nonstatistical variations, and it was necessary to impose data quality cuts to eliminate large fluctuations and in some cases unphysical data (e.g. negative target population measurements). The Yb data set was particularly challenging to analyze, with unphysical negative partial cross sections persisting in several data configurations, even after reasonable data quality cuts were imposed. In hindsight, the Yb target populations were simply too low, in light of the experimental conditions and the very small predicted cross sections for the transition of interest, to yield reliable results by this experimental method. Nonetheless, the theoretical calculations do indicate cross sections about an order of magnitude smaller than observed.

Experimental work was carried out in the Atomic Molecular Optics (AMO) laboratory in the department of Physics and Astronomy, University of Manitoba. Most of the measurements were taken in 2010 – 2011; the laboratory has not been operational since that time.

Reflecting upon the experimental situation described in this work, it is possible to identify ways in which apparatus might be improved as well as to suggest some technical studies that could be undertaken to hopefully improve the success of new measurements of this type. In the former category, it became clear during the data analysis that time-varying experimental conditions led to non-statistical variations in the measurements, for both photon and scattered electron data. The introduction of additional monitoring signals to be incorporated in the data stream would help to diagnose and stabilize the experimental conditions. For example, a Faraday cup could be installed downstream of the interaction region to monitor the electron beam current; temperature and pressure sensors could be read out as an indicator of the atomic beam conditions, and a signal to monitor the pump laser beam intensity could be added to the data stream. A modification to the data acquisition system in order to record continuous time series data rather than accumulated spectra would allow more precise tracking of experimental conditions in the offline analysis effort. An automated system could be introduced for changing the two line filters in front of the PMT in sequence to allow for more rapid alternation between the 554 nm and 583 nm photon measurements for the barium studies. The problem of the slipping PMT polarizer motor drive could be mitigated by installing an optical shaft encoder and logging the measured phase of the polarizer shaft rather than relying on the stepping motor channels to determine the polarizer orientation.

Considering additional experimental studies that could be done to optimize the data taking conditions, a very important contribution could be made by tracking down and hopefully eliminating the large photon backgrounds that were observed at 554 nm and 583 nm in the barium experiments. Development of a suite of measurements to characterize and monitor the atomic beam density and ultimately demonstrate an absolute normalization between photon and electron counting rates would address the normalization issue encountered in Chapter 4 and would also shed light on the reliability of the target state population measurements in chapters 5 and 6. Improvements to the laser polarization and an increase in the laser power could improve the sensitivity of the excited target state experiments, although if the Bostock et al. calculations are correct, the Yb excited state cross sections are probably too small to be reliably measured by these techniques even with the suggested technical improvements. Ultimately one could consider implementation of an electron-photon coincidence measurement, which would eliminate all backgrounds and would uniquely identify the transition of interest. The rate for such experiments would be extremely low however, which is why they have not been previously attempted. On the theoretical side, it is hoped that the recent calculations will soon be published and that the authors may be able to suggest some new experimental studies that would be technically feasible, to explore the validity of the new RCCC model.

References

Aleksakhin I S, Zapesochnii I P, Garga I I and Starodub V P (1975). Opt. Spectrosc. **38** 126.

Aleksakhin I S, Zagrebin S B, Ozolinsh D A, Samson A V, Shafranosh I I and Shishova T A (1983). Opt. Spectrosc. **53** 222.

Allen L H (1984). *Physics of Thermal Gaseous Nebulae*, **v112** of *Astrophysics and Space Science Library* (Reidel, Boston, 1984), pp. 26—30 and 116—146.

Andersen N, Gallagher J W and Hertel I V (1988). Phys. Rep., **165** 1.

Andover Corporation: www.andcorp.com.

Becker K H, McCurdy C W, Orlando T M, and Rescigno T N (2000). Current status and future perspectives of electron interactions with molecules, clusters, surfaces, and interfaces [Workshop on *Fundamental challenges in electron-driven chemistry*; Workshop on *Electron-driven processes: Scientific challenges and technological opportunities*] http://www.osti.gov/scitech/ servlets/purl/809935.

Bernius M T, Man K F and Chutjian A (1988). Rev. Sci Instrum **59** 2418.

Bhattacharya A K (1997). J. Appl. Phys. **137** 299.

Bizzarri A and Huber M C E (1990). Phys. Rev. A **42** 5422.

Blum K and Kleinpoppen H (1979). Physics Reports **52** 203.

Blum K (1981). *Density Matrix Theory and Application. Physics of Atoms and Molecules*. Plenum Press.

Boffard J B, Lagus M E, Anderson L W and Lin C C (1999a). Phys. Rev. A **59** 4079.

Bogaerts A and Gijbels R. (1995). Phys. Rev. A **52** 3743.

Bostock C J (2010). PhD thesis. http://espace.library.curtin.edu.au/cgi-bin/espace.pdf?file=/2010/12/22/file_1/150426

Bostock C J (2014a). Private communication - calculations of Ba RCCC-model.

Bostock C J (2014b). Private communication - calculations of Yb RCCC-model.

Bray I, Fursa D V, Kheifets A S and Stelbovics A T (2002). Journal of Physics B **35** R117.

Bray I and Fursa D V (2011). J. Phys. B: At. Mol. Opt. Phys. **44**, 061001(3pp).

Burke P G, Joachain C J (Eds.) (1997): *Photon and Electron Collisions with Atoms and Molecules.* Plenum Press.

Cahuzac Ph (1968). Phys. Lett. A **27** 473.

Chapman S C (1989), J. Geophys. Res. **94** 227.

Chen S T and Gallagher A (1976). Phys. Rev. A, **14** 593.

Chutjian A (1979). Rev. Sci Instrum **50** 347.

Clark R E H, Abdallah Jr J, Csanak G and Kramer S P (1989). Phys. Rev. A **40** 2935.

Csanak G, Taylor H S and Yaris R (1971a). Phys. Rev. A **3** 1322.

Csanak G, Taylor H S and Yaris R (1971b). Adv. At. Mol Phys. (ed. Bates D R) **7** 287.

Csanak G and Cartwright D C (1988). Phys. Rev. A **38** 2740.

Delcroix P, Ferreira C M and Ricard A. (1976). *Metastable atoms and molecules in ionized gases*. Chapter-5 of *Principles of Laser Plasmas* (ed. Bekefi G) NewYork: Wiley.

Drake G W F, edited by (2006). *Handbook of Atomic, Molecular, and Optical Physics*. Springer.

Fabrikant I I (1980). J. Phys B: At. Mol. Opt Phys. **13** 603.

Fano U and Macek J H (1973). Rev. Mod. Phys. **45** 553.

Faraday Michael (1933). *Faraday's Diary. IV*, Nov. 12, 1839 - June 26, 1847 (Thomas Martin ed.). London: George Bell and Sons, Ltd. Paragraph 7504-7718.

Fursa D V, Trajmar S, Bray I, Kanik I, Csanak G, Clark R E H, Abdallah Jr J (1999). Phys. Rev. A **60** 4590.

Fursa D V, Bray I, Csanak G, Clark R E H, Abdallah Jr J, Kanik I and Trajmar S (2002). Phys. Rev. A **65** 032723(7pp).

Fursa D V (2014). Private communication.

Grynberg G, Aspect A and Farbre C, Cambridge University Press 2010. Introduction to Quantum Optics. p. 123.

Hanne G F, McClelland J J, Scholten R E and Celotta R J (1993). J. Phys B: At. Mol. Opt Phys. **26** L753.

Heddle D W O and Gallagher J W (1989). Reviews of Modern Physics **61** 221.

Hein J D (2010). *PhD Thesis, University of Manitoba*. http://mspace.lib.umanitoba.ca/

Hein J D, Ududec C, Sasaki D K and Zetner P W (2010). J. Phys. B: At. Mol. Opt. Phys. **43**, 185206(10pp).

Hein J D, Kidwai S, Zetner P W, Bostock C, Fursa D V, Bray I, Sharma L, Srivastava R and Stauffer A (2011a). J. Phys. B: At. Mol. Opt. Phys. **44**, 015202(9pp).

Hein J D, Kidwai S., Zetner P W, Bostock C, Fursa D V, Bray I, Sharma L, Srivastava R and Stauffer A (2011b). J. Phys. B: At. Mol. Opt. Phys. **44**, 075201(7pp).

Henry R J W and Kingston A E (1988). *Advances in Atomic and Molecular Physics,* eds. Sir. *D.* Bates and B. Bederson, Academic Press Inc., London.

Herman H W and Hertel I V (1980). J. Phys B: At. Mol. Opt Phys. **13** 4285.

Hertel I V and Stoll W (1977). Adv. At. Mol. Phys **13** 1113.

Hoffmann D, Feng P and Walker T (1994). Journal of Optical Society of America B **11** 712.

Jensen S, Register D, and Trajmar S (1978). J. Phys. B **11**, 2367.

Jiang T Y, Shi Z, Ying C H, Vuskovic L. and Bederson B (1995). Phys. Rev. A **51** 3773.

Johnson P V, Li Y, Zetner P W, Csanak G, Clark R E H and Abdallah Jr J. (1998). J. Phys B: At. Mol. Opt Phys. **31** 3027.

Johnson P V, Eves B, Zetner P W, Fursa D and Bray I (1999). Phys. Rev. A **59** 439.

Johnson P V, Spanu C, Li Y and Zetner P W (2000). J. Phys B: At. Mol. Opt Phys. **33** 5367.

Johnson P V, Spanu C and Zetner P W (2001). J. Phys B: At. Mol. Opt Phys. **34** 4311.

Johnson P V, Zetner P W, Fursa D and Bray I (2002). Phys. Rev. A **66** 022707 (pp12).

Johnson P V and Zetner P W (2005). J. Phys B: At. Mol. Opt Phys. **38** 2793.

Kazakov S M and Khristoforov O V (1983). Sov. Phys. JETP **57** 290.

King G C M, Adams A and Read F H (1972). J. Phys. B: At. Mol. Opt. Phys. **5** L254.

Klimkin V G (1975). Sov. J. Quantum Electron **5** 326.

Krivchenkova V. S. and Khakaev A.D (1975), Opt. Spectrosc. **39** 123.

Kulaga D, Migdalek J and Bar O (2001). J. Phys B: At. Mol. Opt Phys. **34** 4775.

Lamb W E (1957). Phys. Rev. **105(2)** 559.

Lagus M E, Boffard J B, Anderson L W and Lin C C (1996). Phys. Rev. A **53** 1505.

Law M R and Teubner P J O (1995). J. Phys B: At. Mol. Opt Phys. **28** 2257.

Letokhov V S (1979). Nature **277** 605.

Li Y and Zetner P W (1996). J. Phys B: At. Mol. Opt Phys. **29** 1803.

Li Y and Zetner P W (1994a). J. Phys B: At. Mol. Opt Phys. **27** L293.

Li Y, Wang S, Zetner P W and Trajmar S (1994b). J. Phys B: At. Mol. Opt Phys. **27** 4025.

Li Y and Zetner P W (1995). J. Phys B: At. Mol. Opt Phys. **28** 5151.

Lin C C and Anderson L W (1991). Adv. At. Mol. Opt. Phys. **29**, 1.

Lockwood R B, Sharpton F A, Anderson L W and Lin C C (1992a). Physics Letter A **166** 357.

Lockwood R B, Anderson L W and Lin C C (1992b). Z. Phys. D: Atoms, Molecules and Clusters **24** 155.

Lukomski M, MacAskill J A, Seccombe D P, McGrath C, Sutton S, Teeuwen J, Kedzierski W, Reddish T J, McConkey J W and van Wijngaarden W A (2005). J. Phys B: At. Mol. Opt Phys. **38** 3535.

MacAskill J A, Kedzierski W, McConkey J W, Domyslawska J, Bray I (2002). J Elec. Spec. Rel. Phenom. **123** 173.

Macek J and Hertel I V (1974). J. Phys. B: At. Mol. Opt. Phys. **7** 2173.

Mandy J A, Romanyuk M I, Papp F F and Shpenik O B 1993 *Proc. 18th Int. Conf. on the Physics of Electronic and Atomic Collisions (Aarhus)* ed T Andersen, B Fastrup, F Folkmann and H Knudsen (Bristol: Hilger) p167.

Massey, H. S. W., McDaniel, E. W. and Bederson, B. edited by (1982a). *Applied Atomic Collision Physics*, **vol 5**: *Special Topics* (Academic, New York, 1982).

Massey, H. S. W. and Bates, D. R. edited by (1982b). *Applied Atomic Collision Physics*, **vol 1**: *Atmospheric Physics and Chemistry* (Academic, New York, 1982).

Massey, H. S. W. and Bates, D. R. edited by (1982c). *Applied Atomic Collision Physics*, **vol 3**: *Gas Lasers* (Academic, New York, 1982).

McCavert P and Trefftz E. (1974). J. Phys. B: At. Mol. Opt. Phys. **7** 1270.

McDaniel E W (1989). *Atomic Collisions – Electron and Photon Projectiles*. John Wiley and Sons.

McFarland R H (1967). Phys. Rev. **156** 55.

Mikosza A G, Hippler R, Wang J B and Williams J F (1996). Phys. Rev. A **53** 3287.

Mildren R P, Brown D J W, Carman R J, and Piper J A (1995). Opt. Commun. **120** 112.

Mildren R P, Brown D J W, Carman R J, and Piper J A (1997a). IEEE J. Quantum Electron. **33** 1717.

Mildren R P, Brown D J W, Carman R J, and Piper J A (1997b). J. Appl. Phys. **82** 2039.

Mildren R P, Brown D J W, Carman R J, and Piper J A (1997c). Opt. Commun. **137** 299.

Moore C (1958). Atomic *Energy Levels as Derived from Analysis of Optical Spectra (US National Bureau of Standards Circular 467)*, **vol III**, Washington DC: US Govt. Printing Office.

Niggli S and Huber M C E (1987). Phys. Rev. A **35** 2908.

NIST - http://physics.nist.gov/PhysRefData/ASD/lines_form.html

Oppenheimer JR (1927a). Z. Phys. **43** 27.

Oppenheimer J R (1927b). Proc. Nat. Acad. Sci. **13** 800.

Oppenheimer J R. (1928). Phys. Rev. **32** 361.

Pandey K, Singh A K, Kumar P V K, Suryanarayana M V and Natarajan V (2009). Physical Review A **80** 022518 (pp6).

Penny W G (1932). Proc. Nat. Acad. Sci. **18** 231.

Percival I C and Seaton M J (1958). Phil. Trans. R. Soc. A, **251** 15.

Piech G A, Lagus M E, and Anderson L W (1997). Phys. Rev. A **55** 2842.

Piech G A, Chilton J E, Anderson L W, and Lin C C (1998). J. Phys. B: At. Mol. Opt. Phys. **31** 859.

Predojevic B, Sevic D, Pejcev V, Marinkovic B P, and Filipovic D M (2005a). J. Phys. B: At. Mol. Opt. Phys. **38** 1329.

Predojevic B, Sevic D, Pejcev V, Marinkovic B P and Filipovic D M (2005b). J. Phys. B: At. Mol. Opt. Phys. **38** 3489.

Rall D L A, Sharpton F A, Schulman M B, Anderson L W, Lawler J E and Lin C C (1989). Phys. Rev. Lett. **62** 2253.

Register D F, Trajmar S, Jensen S W and Poe R T (1978). Phys. Rev. Lett. **41** 749.

Register D F, Trajmar S, Csanak G, Jensen S W, Fineman M A and Poe R T (1983). Phys. Rev. A **28** 151.

Sang R T, Farrell P M, Madison D H, MacGillivray W R and Standage M C (1994). J. Phys B: At. Mol. Opt Phys. **276** 1187.

Scholten R E, Lorentz S R, McClelland J, Kelly M H and Celotta R J (1991). J. Phys B: At. Mol. Opt Phys. **24** L653.

Schultz G J (1973). Rev. Mod. Phys. **45** 378.

Selvin J (1984). Reports on Progress in Physics **47(5)** 461.

Shimon L L, Golovchak N V, Garga I I and Kurta I V (1981). Opt. Spectrosc. **50** 571.

Shuk R W and Szuszgzewiez E P (1991). J. Geophys. Res. **96** 1337.

Simons D J, Pongratz M B, Smith G M, and Barasch G E (1981). J. Geophys. Res. **86** 1576.

Smirnov Y M (2003). Opt. Spectrosc. **94** 332.

Srivastava R, Zuo T, McEachran R P and Stauffer A D (1992a). J. Phys B: At. Mol. Opt Phys. **25** 3709.

Srivastava R, McEachran R P and Stauffer A D (1992b). J. Phys B: At. Mol. Opt Phys. **25** 4033.

Srivastava R, McEachran R P and Stauffer A D (1995). J. Phys B: At. Mol. Opt Phys. **28**, 885.

Starodub V P (1998), J. App. Spectrosc. – Brief Communications **65** 449.

St.John R M, Miller F L, Lin C C (1964). Phys. Rev. A **134 A** 888.

Taylor J R (1997): *An Introduction to Error Analysis*. University Science Books.

van Raan A F J, DeJonkh J P, VanEck J, Heideman H G M (1971). Physica **53** 45.

van Wijngaarden W A and Li J (1995). Can. J. Phys. **73** 484.

van Zyl B, Dunn G H, Chamberlain G and Heddle D W O (1980). Phys. Rev. A **22** 1916.

Walker T, Feng P, Hoffmann D and Williamson R S (1992). Phys. Rev. Lett. **69** 2168.

Wang S, Trajmar S and Zetner P W (1994). Phys B: At. Mol. Opt Phys. **27** 1613.

Wescott E M, Stenbaek-Nielsen H C, Hallinan J J, Deehr C S, Romick G J, Olson S V, Roederer J G, and Sydora R (1980). Geophys. Res. Lett. **7** 1037.

Wescott E M (1993). J. Geophys. Res. **98** 3711.

Williams J F and Willis B A (1975). J. Phys. B: At. Mol. Opt. Phys. **8** 1641.

Williams J F (1976). J. Phys. B: At. Mol. Opt. Phys. **9** 1519.

Williams J F (1988). J. Phys. B: At. Mol. Opt. Phys. **21** 2107.

Winske D (1988). J. Geophys. Res. **93** 2539.

Woodgate G K (1970). *Elementary Atomic Structure* - McGraw Hill.

Yang C M and Rodrigez A E (1992). Wright Laboratory, Report TR-92-006, Wright Patterson AFB, Ohio.

Zetner P W, Li Y and Trajmar S (1992). Phys B: At. Mol. Opt Phys. **25** 3187.

Zetner P W, Li Y and Trajmar S (1993). Phys. Rev. A **48** 495.

Zetner P W, Trajmar S, Wang S, Kanik I, Csanak G, Clark R E H, Abdallah Jr J and Nickel J C (1997). J. Phys. B: At. Mol. Opt. Phys. **30** 5317.

Zetner P W, Trajmar S, Kanik I, Wang S, Csanak G, Clark R E H, Abdallah Jr J, Fursa D and Bray I. (1999). J. Phys B: At. Mol. Opt Phys. **32** 5123.

Zetner P W, Johnson P V, Li Y, Csanak G, Clark R E H and Abdallah Jr J. (2001). J. Phys. B: At. Mol. Opt. Phys. **34** 1619.

Zetner P W and Johnson P V (2006). J. Phys B: At. Mol. Opt Phys. **39** 455.

Zuo T, McEachran R P and Stauffer A D (1991). J. Phys B: At. Mol. Opt Phys. **24** 2853.